THE UNIVERSITY OF READING

Department of Meteorology

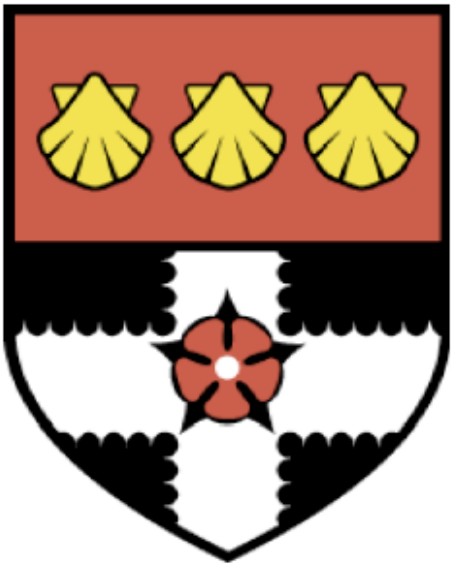

# Ocean Model Uncertainty and Time-Dependent Climate Projections

**Christopher Metcalfe Brierley**

A thesis submitted for the degree of Doctor of Philosophy

December 2006

## Declaration

"I confirm that this is my own work and the use of all material from other sources has been properly and fully acknowledged"

Chris Brierley

# Abstract

Atmosphere-ocean general circulation models are the best tools available to provide policy-relevant predictions of the climate's response to a change in the amount of atmospheric $CO_2$. They include parameterisations of physical processes that cannot be resolved explicitly. There is uncertainty in the numerical values (parameters) involved in the parameterisation of ocean physics. This is called ocean model uncertainty. This thesis is the first investigation of the effects of ocean model uncertainty in a complex climate model.

A database of ocean parameters and their uncertainty ranges has been created through expert elicitation for a complex model (HadCM3). A perturbed physics ensemble has been created from the highest priority parameters. This ensemble represents an upper bound of ocean model uncertainty. Each ensemble member has been run to a preindustrial quasi-steady state. The effects of ocean model uncertainty on the long-term climate state are presented and quantified. There is surface temperature uncertainty of greater than 2.5°C at high latitudes.

A climate change experiment was performed with $CO_2$ increasing by 1% per year. The effects of ocean model uncertainty on the climate change signal can be detected above natural variability. The global mean effects are compared to those seen from other sources of uncertainty. The regional patterns of the effects on the surface climate change signal are quantified: they are over 100% of the ensemble mean signal in regions of strong vertical ocean heat transfers. Effects on the vertical structure of the ocean are also quantified. The effects of ocean model uncertainty on the slowdown of the thermohaline circulation are investigated. Analysis of the evolution of ensemble spread with increasing $CO_2$ reveals an anti-correlation between the preindustrial global mean temperature and the transient climate response. This is mediated by variations in ocean heat uptake processes and climate feedbacks in approximately equal measure.

# Acknowledgements

I would like to thank Alan Thorpe and Mat Collins for their unswerving commitment to this project. They were both in Reading when they proposed this project, and had both left well before it ended. However, they still devoted their time to provide me with help and guidance. Thank you to Malcolm MacVean, who kindly performed the model runs on which the majority of this thesis is based. I would also like to thank NERC and climate*prediction*.net for providing the funding for this project. There is long list of ocean modelling experts, who also deserve thanks. They patiently explained parameterisation scheme to me, as well as providing the uncertainty ranges on which this work is based.

A PhD is not only a thesis and the results contained within: it also represents over three years of education and experience. Many thanks are owed to the Royal Berkshire Hospital, the University Health Centre and Jane, Vicki and Laura without whom I may not have lasted the three years. I would like to thank the Department of Meteorology for assisting greatly with my education over the past years. The varied residents of 2u07 also deserve thanks. They have made coming into work every day a pleasure rather than a chore. Finally, special thanks go to Marsha, who has experienced every high and low with me. And even let me play frisbee in my spare time, rather than spend it with her.

Thank you all.

# Contents

# CHAPTER 1

# Introduction

## 1.1 Motivation

The Earth's climate is the mean state of its weather. Climate fluctuates because of internal variability and changes in response to external influences, such as changes in the level of greenhouse gases (such as $CO_2$) in the atmosphere. Humans are causing an increase in greenhouse gas levels through a variety of means, such as the use of fossil fuels and deforestation. The Earth will warm in response to this, although not uniformally. Complex numerical models (called atmosphere-ocean general circulation models and abbreviated to AOGCMs) can be created to provide projections of the future climate.

Many factors combine to make the features of these projections uncertain. These factors can be categorised as being scenario, initial condition and AOGCM uncertainties. The last of these categories, AOGCM uncertainty, has only recently started to be systematically explored (Murphy *et al*. (2004), Stainforth *et al*. (2005) and Collins *et al*. (2006)). The effects of uncertainties relating to the parameters in the physical parameterisations in the ocean model was not known prior to this study. This thesis describes the creation and properties of an ensemble that samples the maximum bound of the effects of parameter uncertainty in the physics parameterisations in the ocean model (referred to as "ocean model uncertainty" throughout this thesis).

This thesis is divided into 7 chapters, each of which tackle an individual element of ocean model uncertainty. This first chapter acts as an introduction and literature review. It will introduce the climate system, and then go on to explain the role of the ocean in it. There then follows a brief description

of climate change (a more comprehensive description of the common features of climate projections will be provided later in section 5.2, which compares the ensemble mean climate change to that shown in the literature). The introduction will then describe the different sources of uncertainty in climate projections, followed by a discussion of previous studies that investigate AOGCM uncertainty. The final section of this introductory chapter presents the aims of this thesis.

Chapter 2 presents a description of ocean parameters in the third version of the Hadley Centre's coupled model (HadCM3). The maximum uncertainty in each parameter is also quantified by the provision of a range of plausible values. Chapter 3 describes the creation and evaluation of an ensemble that samples ocean model uncertainty. It also shows the effects of ocean model uncertainty on the long term preindustrial climate state. Chapter 4 looks at effects of ocean model uncertainty on the global mean transient climate response to an increase in $CO_2$, and compares them to the effects from other sources of uncertainty. Chapter 5 extends this analysis by looking at the effects of ocean model uncertainty on the spatial patterns of the climate change signal. Chapter 6 looks at the temporal evolution of the ensemble spread of global average temperature under increasing $CO_2$ (rather than looking at the effects on the climate change signal as in the previous two chapters). The thesis will conclude in chapter 7 with a summary of the findings of this work and a further discussion leading to suggestions for future work that needs to be conducted in this area.

## 1.2 The climate system

The weather experienced at an individual location on the globe is influenced by many factors, and can not be predicted in detail more than a week or two ahead. This is due to the chaotic, non-linear features of the system (Lorenz, 1967). However, the long term statistics of the weather can be modelled: these statistics are referred to as the climate. Different properties of the Earth determine the climate. These properties are inter-connected to each other, leading to the idea of the Earth as a "climate system"

composed of various components. These components are the atmosphere, the hydrosphere (primarily the ocean), the cryosphere, the biosphere and the land surface. They are shown schematically in figure 1.1 from Baede *et al.* (2001). Each component has its it own timescales. This thesis is concentrating on projections of climate change over the next 80 years. So, for example, ice sheet changes will not be important over this timescale (Church *et al.*, 2001), and will not be modelled in this thesis.

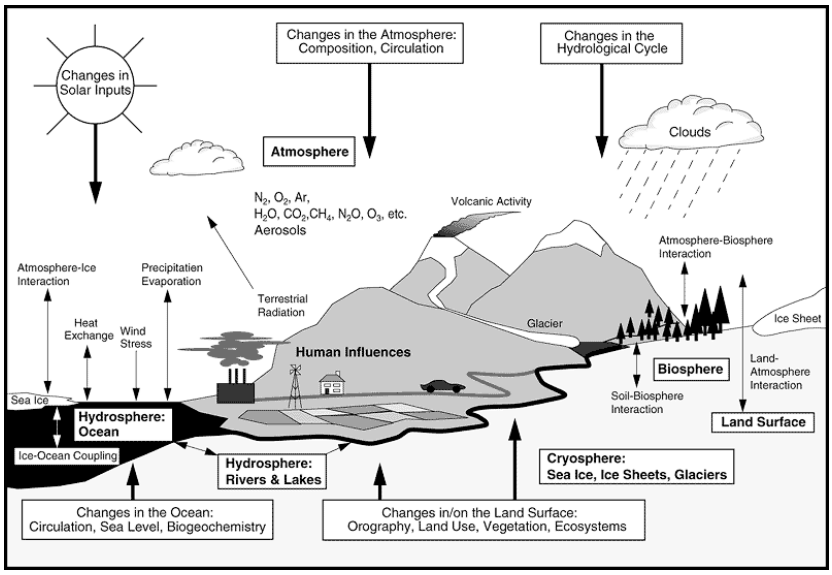


**Figure 1.1** *A schematic view of the components of the global climate system (bold), their processes and interactions (thin arrows) and some aspects that may change (bold arrows). Presented as figure 1.1 in Baede* et al. *(2001).*

The atmosphere is the most rapidly changing component of the climate system. It equilibriates in approximately 20 years to any imposed changes (Williams *et al.*, 2001). The equilibrium climate system is often described by its energy balance (Gill, 1982). Most energy is input in the tropics as shortwave solar radiation, and either reflected back out to space or absorbed. The absorbed energy is re-emitted as longwave radiation across the surface of the whole Earth. This means that the extra-tropics has a net loss of energy. Internal circulations exist in the climate system to transport energy from its arrival point in the tropics poleward so that it can be lost to space. The atmosphere and ocean circulations combine to transport this energy (see figure 1.2).

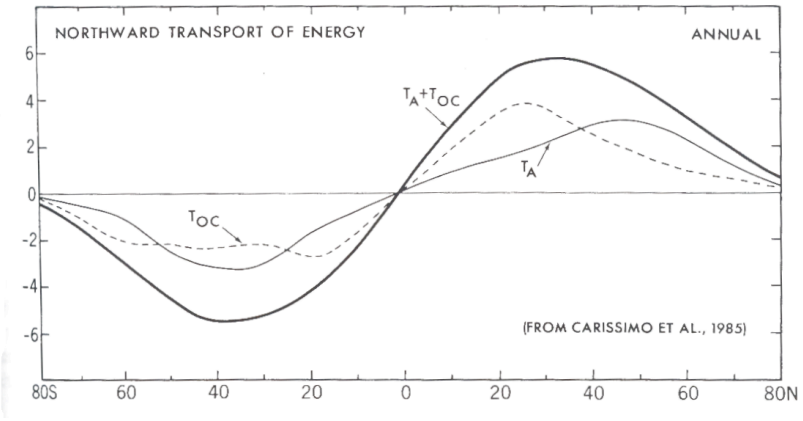


**Figure 1.2** *The northward transport of energy in the climate system (vertical scale in $10^{15}$ Watts). The thick solid line shows the total energy transport ($T_A + T_{OC}$), the thin solid line is contribution from the atmosphere ($T_A$) and the dashed line is the contribution from the ocean ($T_{OC}$). Presented as figure 13.17 in Peixoto and Oort (1992), but created with data from Carissimo* et al. *(1985).*

### 1.2.1 The role of the ocean

The ocean is a large transporter of heat poleward, as well as storing large quantities of heat. The relative heat capacity of sea-water to air is such that a 2.5m depth of the ocean stores the same amount of heat as the whole depth of the atmosphere (Gill, 1982). Unlike the atmosphere, sea water is not transparent, so energy is only added to the ocean at the surface, causing a very stable stratified ocean (Sprintall and Cronin, 2001).

The ocean contains a series of basin-wide, wind-driven gyre circulations: polar gyres in the North Atlantic and North Pacific, sub-tropical gyres in the midlatitudes and the equatorial circulation near the equator (see figure 1.3). These gyres are formed by Sverdrup balance (Sverdrup, 1947), with a western boundary current (Stommel, 1948). They are most obvious in the Northern Hemisphere, where the landmasses form continuous basin edges, but also exist in the Southern Hemisphere subtropics. The Southern Ocean does not have a gyre circulation, as it is not constrained to an individual basin - it flows unimpeded around the globe in the Antarctic Circumpolar Current (ACC).

Whilst there are several large wind driven circulations, overturning circulations dominate the poleward heat transport .They are driven by density variations and collectively called the thermohaline circula-

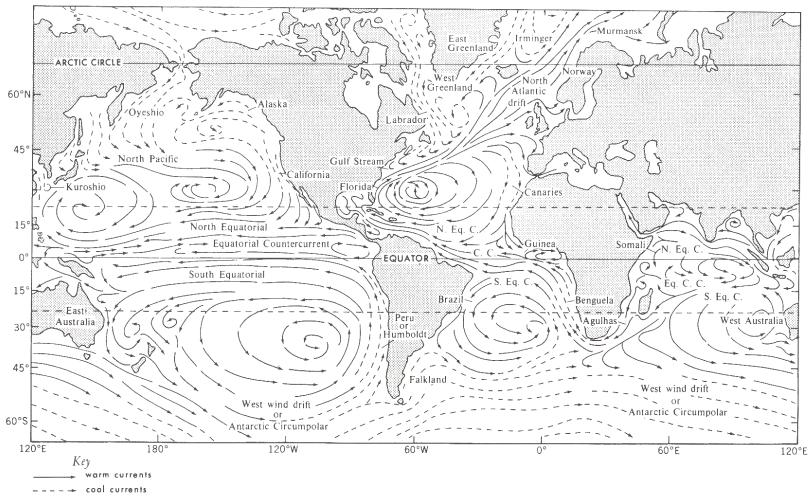


**Figure 1.3** *A schematic showing the major surface currents in the ocean. Published as figure 8.1 in Peixoto and Oort (1992).*

tion (THC, Stommel (1961)). A schematic of this circulation is shown in figure 1.4. It shows the few small areas of the ocean in which penetrative deep convection occurs in yellow. These are the Ross and Weddell Seas in the Southern Ocean and regions of the North Atlantic. The thermohaline circulation keeps the North Atlantic surface air temperature over 4°C warmer than it would be otherwise (Vellinga and Wood, 2002).

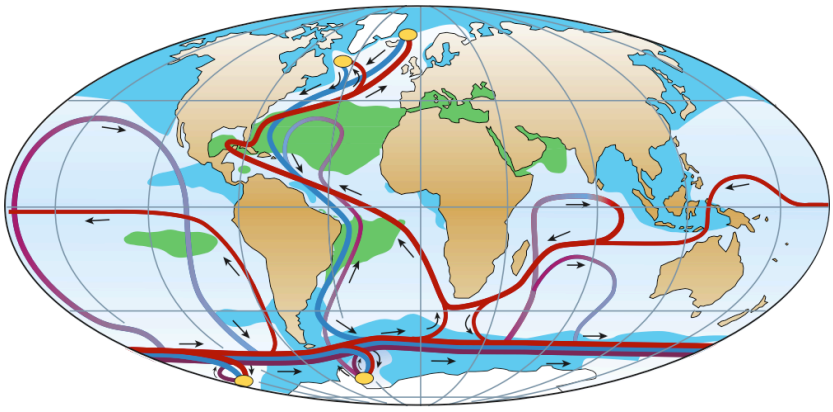

**Figure 1.4** *A schematic of the thermohaline circulation. Red lines are warm surface currents, blue lines are cold deep currents. The yellow areas indicate sinking regions. Areas with a sea surface salinity above 36psu are shaded green and areas below 34psu a light blue. Taken from Rahmstorff (2002) but based on data presented in Broecker* et al. *(1990).*

### 1.2.2 What is climate change?

It has long been established that changes in the amount of $CO_2$ in the atmosphere will cause changes in the Earth's temperature (Tyndall (1865) and Arrhenius (1896)). An increase in $CO_2$ will change the optical properties of the atmosphere, leading to a greater proportion of longwave radiation being absorbed and re-radiated back to the surface (see the "greenhouse warming" box in Thorpe (2005) for a succinct mathematical description of this process). A change in the energy balance of the Earth caused by a change in the radiative properties of the atmosphere is called an "imposed radiative forcing" (Ramaswamy *et al*., 2001). Calculating the temperature changes expected in response to changes in $CO_2$ quantities was considered a theoretical exercise, until Callendar (1949) suggested that the emissions of $CO_2$ resulting from industrialisation were leading to an observable increase in temperature. Plass (1956) recalculated the radiative transmission profiles with advanced knowledge of the absorption spectra, and showed that $CO_2$ could cause temperature changes greater than 1 °C per century. However, it was expected that the ocean would absorb most anthropogenic (resulting from human activities) $CO_2$ , until the work of Revelle and Suess (1957) showed this would not be the case. Since the 1950s, the importance of anthropogenic global warming has been slowly understood; first amongst scientists and now amongst the general populace.

The primary tools for investigations into the climate system are numerical models. As computers have become faster, numerical models have become more sophisticated, and so our understanding of the climate system has increased. Manabe and Wetherald (1967) devised a method of computing a moist atmospheric profile. They calculated that the Earth would warm by 2.36 °C in response to a doubling of $CO_2$. This is considered to be the first in a long line of physically realistic climate projections of the impact of increasing $CO_2$ (Weart, 2004). The advent of atmosphere-ocean general circulation models (AOGCMs) allowed the three dimensional pattern of changes in climate to be assessed (e.g. Manabe and Wetherald (1975) and Hansen *et al*. (1981a)). This study will be using the third generation of the Hadley Centre's Coupled Model (HadCM3), which is described in detail in section 2.3.2. A more

substantial and detailed description of the expected climate impacts of increasing $CO_2$ is given in sections 5.3 - 5.8. The major features of the surface temperature changes are an amplification of the warming in the Arctic, greater warming over land than ocean, and a minimum of warming in the Southern Ocean.

The time-dependent, rather than equilibrium, response to an imposed radiative forcing (such as that caused by an increase in $CO_2$ ) depends on the speed at which the climate system can restore radiative balance as well as the magnitude of the equilibrium response. The speed of the response depends primarily on the heat capacity of the climate system, and the time taken for thermal contact to be established with the atmosphere (Hansen *et al.*, 1981b). The vast majority of additional heat storage observed in the past fifty years has occured in the ocean (see figure 1.5). This shows that the effectiveness of the mixing processes that transport heat into the interior ocean is important in determining the time-dependent response of the climate response. AOGCMs capture these processes sufficiently to simulate the observed pattern of recent warming and to attribute it to anthropogenic causes (Barnett *et al.*, 2005).

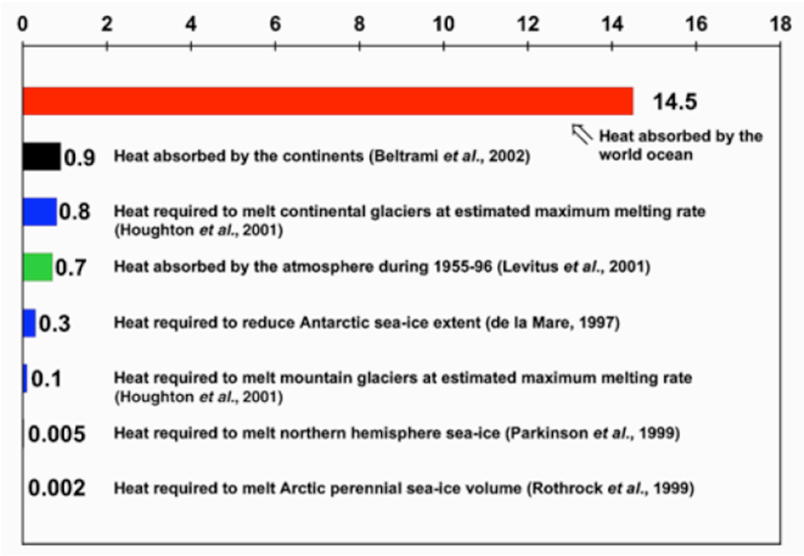


**Figure 1.5** *The heat storage of the climate system from 1955-1998 ($10^{22}$ J.). The world ocean accounts for 85% of the heat storage. Presented as fig. 3 in Levitus* et al. *(2005) - the references are included in the bibliography, except for the information about glacier heat absorption which is contained instead in Folland* et al. *(2001a).*

## 1.3 Uncertainty

The Intergovernmental Panel on Climate Change (IPCC) was established by the international community in 1988 in response to growing concern about climate change. It produces a regular comprehensive review of climate science. The most recent report was the third assessment report (TAR) produced in 2001, although a fourth (known as AR4) is in production. Different AOGCMs give a range of climate projections. The IPCC report has collected and combined these projections to give an idea of the uncertainty in them. The term "projections" is used to emphasise that they are not predictions of what will happen, but only show what would occur if certain events occur. Figure 1.6 is an example of the range in projections of the global mean surface temperature until 2100.

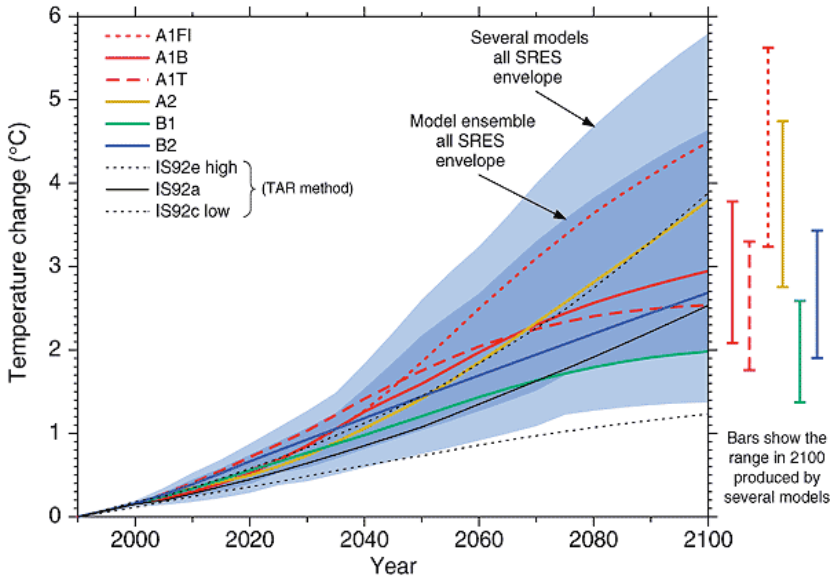


**Figure 1.6** *Global mean temperature change as projected by a simple climate model that emulates the responses of AOGCMs by varying certain parameters. The different solid lines represent ensemble mean projections for a variety of scenarios. The dark blue region shows the range of projections from a single parameter setting, but with the full set of 35 scenarios. The light blue region shows the full range of projections found by varying both parameters and scenarios. The bars on the right show the range of projections from a single scenario at 2100. Shown as figure 9.14 in Cubasch* et al. *(2001).*

The range in the projections arise due to uncertainties from a variety of sources - the scenario, the initial conditions and the AOGCM itself. The rest of this section will describe each of these three uncertainties in turn, followed by a description of their relative importance. The various forms of uncertainties are summarised in figure 1.7.

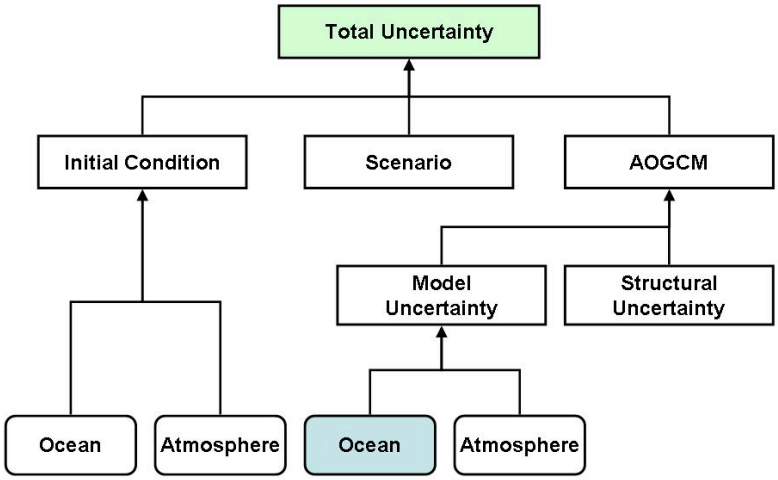


**Figure 1.7** *A schematic showing the various forms of uncertainty involved in climate predictions. The blue box shows ocean model uncertainty - the facet of uncertainty that this thesis explores.*

### 1.3.1 Scenario uncertainty

Variations in the amount of $CO_2$ in the atmosphere cause variations in the climate system by changing the Earth's energy balance (sec. 1.2.2). There are many other possible causes for changes in the energy balance, for example, changes in the amount of solar radiation reaching the Earth and emissions from volcanic eruptions. Some uncertainty in climate projections is a direct consequence of uncertainty in the imposed forcings, and is termed scenario uncertainty. An example of this is given as the dark blue wedge in fig. 1.6. This wedge shows the range in global mean surface temperature as a result of scenario uncertainty. In this case, the scenario uncertainty is sampled by considering each possible scenario proposed by the IPCC Special Report on Emissions Scenarios (SRES, Nakićenović *et al.* (2000)). These scenarios are created by considering varying population and economic projections, and the amount of anthropogenic gas emissions these projections would imply. The (anthropogenic) scenario uncertainty, shown by the blue wedge, is as important as all other uncertainties combined for a single scenario (shown as the bars to the right hand edge of fig. 1.6) for the global mean surface temperature. The scenario uncertainty relating to volcanic eruptions is large on annual timescales,

because of the lack of predictability of volcanic eruptions. The scenario uncertainty, especially the anthropogenic component, is different from the other forms of uncertainty, because humans have a direct choice of which scenario to follow. The scenario uncertainty can be significantly reduced if humans choose to reduce it by regulating the levels of greenhouse gas emission.

It is not an aim of this thesis to investigate scenario uncertainty, which is related to fields as varied as demography and economics as well as climate science. The IPCC devotes a whole chapter to climate scenario development and scenario uncertainty (Mearns *et al*., 2001). The effects of scenario uncertainty will be removed from this study by considering only a single scenario. The scenario chosen is that used in the second phase of the Coupled Model Intercomparison Project (CMIP2, Meehl *et al*. (1997) and Meehl *et al*. (2000)) so that comparison to those results can be made. The scenario is described in detail in section 4.2. All the results presented in this study should be considered projections of the climate state if this scenario occurs, rather than predictions of what will occur in future.

### 1.3.2 Initial condition uncertainty

It has long been known that the precise evolution of the weather in a numerical weather forecast depends on the initial state of the atmosphere (e.g. Thompson (1957)). A misrepresentation of the atmospheric state exists at all spatial scales because of a lack of observations, observational error and the finite grid resolution of the numerical model used to represent the atmosphere. This misrepresentation is called an initial condition error (Palmer, 2000). The error can grow rapidly, leading to a loss of predictability on timescales of days. A suite of methods for dealing with this error growth have been developed that allow routine weather prediction out to 10 days (e.g. Tracton and Kalnay (1993) and Molteni *et al*. (1996)). All the methods involve determining a set (ensemble) of plausible initial conditions. The methods vary in the technique used to optimise the sampling of the uncertainty. Each initial condition is integrated forward to create an individual prediction (an ensemble member). These

are considered equally likely to occur and are combined to form a probabilistic prediction.

Atmosphere initial condition uncertainty is the dominant source of uncertainty in weather forecasts and saturates in amplitude over a few days. However, initial condition uncertainty in the ocean and other slowly varying features of the climate system will cause some uncertainty on much longer timescales (e.g. decadal predictability in the THC, Griffies and Bryan (1997)). Collins and Allen (2002) show that initial condition uncertainty is important for climate predictions on decadal timescales. This realisation has lead to a development of operational decadal prediction systems. On longer timescales, the influence of initial condition uncertainty becomes harder to differentiate from uncertainty related to the preference of an AOGCM for its own equilibrium state, rather than the observed initial conditions. This latter form of uncertainty is related to AOGCM uncertainty, because the equilibrium state is determined by the model parameters and structure.

### 1.3.3 AOGCM uncertainty

Climate projections are performed with the aid of AOGCMs. The complexity of an AOGCM is determined by the computing resources available to perform the projection. Although computing resources have increased exponentially since the 1960s, there will always be a finite resource available for the creation of climate projections. This means that AOGCMs require a finite resolution (and a variety of other approximations and assumptions) that leads to uncertainty in climate projections.

Climate projections on centennial timescales cannot be easily verified. Weather forecasts can be verified by comparing many different forecasts to the observed weather state at that time. It is not possible to use the same methodology with centennial climate projections (although it has been used with some success for decadal predictions through hindcasts). However, it is clear that using an incorrect model will give an incorrect projection. A realistic model should give a realistic projection. However, it is not always possible to determine whether an AOGCM provides an incorrect or a realistic representation

of the climate system. The state of the climate system is so multi-faceted, that determining it precisely through observations is impossible. It is also not precisely known which elements of the climate system dominate the predictability on centennial timescales. These elements are the most important to represent accurately in AOGCMs used for climate projections. As it is not known precisely what these elements are, it is not possible to define a single criterion that will measure whether an AOGCM is a realistic representation of the climate state. Many AOGCMs have representations of the climate state that are considered plausible according to some possible criteria.

Different AOGCMs give different, but similarly plausible, representations of the climate system and its evolution. This ambiguity leads to uncertainty in climate projections. The numerical model used in this study is an AOGCM, so this form of uncertainty shall be termed "AOGCM uncertainty" to prevent confusion with "model uncertainty", which is defined as a subset of AOGCM uncertainty in this thesis.

### 1.3.4 The division of AOGCM uncertainty into structural and model uncertainties

AOGCM uncertainty arises from the misrepresentation of the climate system in the numerical model. The misrepresentation of the climate systems occurs for a variety of reasons. It is possible to subdivide AOGCM uncertainty, according to its cause, into structural uncertainty and model uncertainty.

Model uncertainty is the uncertainty that arises from the modelling of processes that are not explicitly resolved in the AOGCM. Important physical processes occur on scales less than the grid resolution. Their effects need to be included in the AOGCM, so their impacts on larger scales must be parameterised. These parameterisations include numerical values, called parameters, that are uncertain. Model uncertainty can therefore be defined as "the uncertainty arising from the inclusion of uncertain parameter values in physical parameterisations." This thesis aims to explore and quantify the model uncertainty in the ocean model. Chapter 2 involves many examples of physical parameterisations and

their associated parameters.

Structural uncertainty is uncertainty arising from choices and assumptions made during the model development. These choices and assumptions will have an impact on how the model is structured, hence the name "structural uncertainty". An example of a structural choice made in the model development would be the resolution of the AOGCM. The resolution determines whether physical processes are explicitly resolved or need to be parameterised. Other examples of structural choices are the vertical coordinate system, whether the AOGCM is a spectral or gridbox model, the method of parameterisation chosen, and whether flux adjustments are used (the latter choice is discussed further in section 2.7).

### 1.3.5 Relative importance of different forms of uncertainty

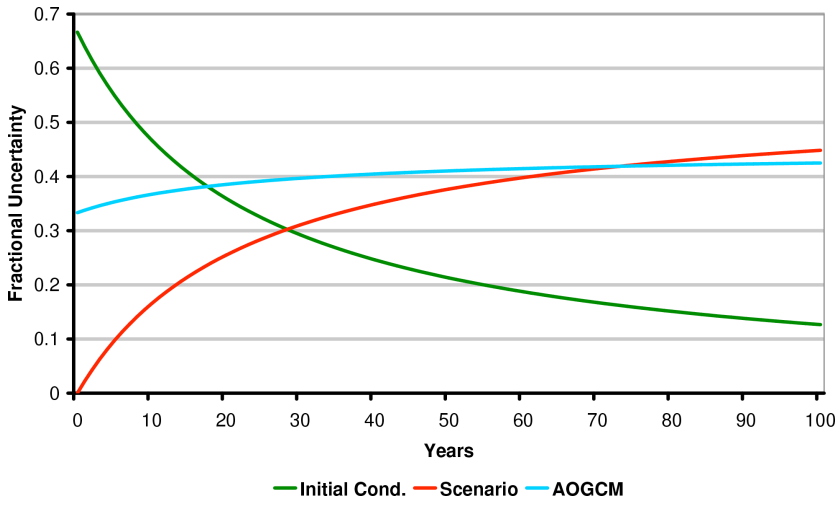


**Figure 1.8** *A schematic showing the fraction of the total uncertainty in climate projections arising from initial condition uncertainty (green), scenario uncertainty (red) and AOGCM uncertainty (blue). The data is approximated from the global mean surface temperature change in AOGCM runs and is assumed to combine linearly, which is not the case. However, it does illustrate the timescales over which the different sources of uncertainty are important.*

It is essential to understand which uncertainties are the most important at different time horizons. This can not be truly determined until each individual uncertainty has been quantified, and their interactions with each other understood. However, some studies have looked at the relative magnitudes

of the different sources of uncertainty (e.g. Collins and Allen (2002)). Initial condition uncertainty dominates the total uncertainty in the initial period (the first decade), although AOGCM uncertainty is also important. Seasonal and decadal predictions need to include both initial condition and AOGCM uncertainty (Palmer *et al.*, 2004). The relative importance of the initial condition uncertainty reduces as the time horizon increases. The scenario uncertainty becomes steadily more important with longer timescales, and dominates for century-long predictions. AOGCM uncertainty is important for all time horizons, and dominates for projections of a few decades. AOGCM uncertainty is poorly understood in comparison to both scenario and initial condition uncertainty. However, several attempts have been made to investigate and quantify AOGCM uncertainty.

Figure 1.8 is a schematic representation of the relative importance of the different uncertainties in determining the global mean surface temperature. Although the data are derived from a AOGCM studies, the sampling of the respective uncertainty is sub-optimal, so the figure should only be treated as a schematic Three ensembles of climate projections have been used to represent the different uncertainties. Initial condition uncertainty is represented by the average of the range of an ensemble of three HadCM3 runs using the A2 scenario (Hulme *et al.*, 2002). It is assumed to be constant in time. The AOGCM uncertainty is represented by an initial spread of 0.3 °C (half that of the initial condition uncertainty). This uncertainty then linearly increases to fit the spread of the AR4 multi-model ensemble at seventy years (shown in fig. 7 of Collins *et al.* (2006)). The scenario uncertainty is represented by the difference between the A1F1 and B1 projections. These projections were performed with HadCM3 by Johns *et al.* (2003). They only provide data for the 2040s and 2080s, so a linear approximation to this data has been used in figure 1.8. The uncertainty from each source is presented as a fraction of the total combined uncertainty (the uncertainties would be expected to interact with other, but for this figure they are assumed to be independent). Although none of these measures sample their respective uncertainty comprehensively, they do give an idea of the relative importance of the different sources of uncertainty on the global mean surface temperature. Other variables, and regional averages may have a different division of the relative uncertainty.

## 1.4 Previous investigations of AOGCM uncertainty

The primary constraint faced when investigating AOGCM uncertainty is access to a finite computing resource. There are two approaches that can be taken to address this problem. One approach is to use less complex models that require less computing time. The advantage to this approach is that it allows comprehensive sampling of uncertainty space. However, it requires some knowledge to constrain the simple model's parameters. This approach also runs the risk of using a model that is so simple, the results do not provide useful information about the climate system (for example, by missing out important feedbacks).

### 1.4.1 Ensembles of opportunity

The second approach is to use the selection of AOGCMs that have been developed by various modelling groups around the world. This approach has the advantage that the computation is outsourced to the modelling groups. This approach has been used by the IPCC, which has collected and presented the results from many modelling groups. However until the third report, the modelling groups were using an assortment of scenarios. This meant that AOGCM uncertainty could not be isolated from the scenario uncertainty

Meehl *et al*. (1997) proposed an intercomparison of AOGCM time-dependent climate responses as the second phase of the Coupled Model Intercomparison Project (CMIP2). To this end, they defined a single scenario that should be performed by all participating modelling groups. A selection of variables from each AOGCM projection has been collected in an central database, and is available to all climate researchers (http://www-pcmdi.llnl.gov/).

The ensemble created by these projections is an "ensemble of opportunity" (Allen and Stainforth, 2002). The ensemble distribution of the global mean temperature change for the CMIP2 ensemble is shown in figure 1.9. It shows a spread in response, however this spread is only a selection of possible

responses. It may not cover the full range of possible responses, and does not provide a probability distribution.

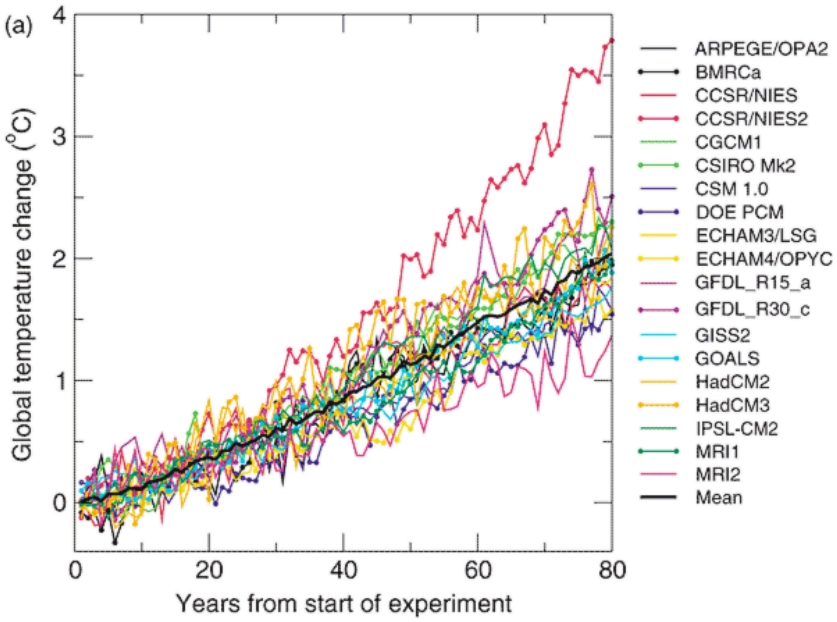


**Figure 1.9** *The time evolution of the globally averaged temperature change relative to the control run of the CMIP2 simulations (in °C). Presented as figure 9.3 in Cubasch* et al. *(2001).*

However it is the only resource available to investigate AOGCM uncertainty into the regional features of climate change. It also does not require additional AOGCM integrations, and so can be researched without access to supercomputing facilities. It has recently been used for studies into fields as varied as sea ice changes (Flato and Participating CMIP Modelling Groups, 2004) and tropical Pacific warming (Collins and the CMIP Modelling Groups, 2005).

An "ensemble of opportunity" has been used to incorporate AOGCM uncertainty into seasonal forecasts by the DEMETER project at the European Centre for Mediumrange Weather Forecasting (ECMWF, Palmer *et al.* (2004)). DEMETER combines initial condition ensembles from 7 different AOGCMs to form a single ensemble, from which probabilistic forecasts can be made. They found that the multi-model system gave some additional predictive skill compared to a single model.

### 1.4.2 Simpler, cheaper models

An alternative approach is to use simple models, that are computationally cheap to run. This allows a thorough investigation of the model parameters to be performed. This method has exchanged an opportunistic investigation of the full AOGCM uncertainty for a proper quantification of the model uncertainty. The structural component of the AOGCM uncertainty is not included. With such simple models, the structural uncertainty may be large.

An example of such a method is the work of Forest *et al*. (2002) (updated by Forest *et al*. (2006)). A 2D model with three tunable parameters (Sokolov and Stone, 1998) is used to simulate the climate of the 20th century. An optimal detection technique is then used compare these simulations to observations, leading to the computation of a joint probability distribution function (PDF) for the three parameters. Frame *et al*. (2005) show that the results from this methodology are highly sensitive to prior assumptions made about the method of combining the information by the researchers. They suggest that ensembles should be created for a particular forecast quantity, and the prior distribution should be uniform in that forecast quantity.

Hargreaves and Annan (2006) have performed a forecast for the THC change using an efficient 3D ocean-climate model (Edwards and Marsh, 2005). They have used a version of the ensemble Kalman filter method (used in probabilistic weather forecasting to optimally sample the initial condition uncertainty) to tune multiple model parameters to obtain a large ensemble that has many plausible representations of the THC. This is an advance on the study of Edwards and Marsh (2005), which used the same model, but did not optimise the model tuning. Edwards and Marsh (2005) rather created a large ensemble of model with multiple semi-random parameter perturbations. These simple model studies present an idea of the model uncertainty involved in climate projections. However, they have an increased, yet unquantified, amount of structural uncertainty and may have important feedbacks missing. For example, the ensemble spread in Edwards and Marsh (2005) of the transient climate

response (TCR, the change in global mean surface air temperature for the 20 years centred on the year of doubling of $CO_2$ (Cubasch *et al.*, 2001)) is a third of that seen in the CMIP2 ensemble (Collins *et al.*, 2006).

### 1.4.3 AOGCM perturbed parameter ensembles

Allen (1999) proposed that AOGCM uncertainty could, and should, be sampled systematically (rather than by using ensembles of opportunity). The only obstacle was a lack of computing resources to tackle the problem. Allen (2003) then showed that this obstacle could be overcome by using distributed computing techniques to use the public's personal computers to perform the large numbers of integrations necessary. Simultaneously, the Met. Office started to tackle the problem, using a reprioritisation of research directions to make the necessary computing resources available.

The long term aim of both groups is a probabilistic climate prediction; however they have both started with simpler problems. Both groups are using a single AOGCM, and have taken the decision to tackle the model uncertainty component of AOGCM uncertainty. Murphy *et al*. (2003) compiled a database of parameters in the atmosphere model and their associated uncertainty ranges, through consultation with experts. Stainforth *et al*. (2005) and Murphy *et al*. (2004) both used this database to perturb the atmosphere parameters to sample the model uncertainty in the atmosphere component of the AOGCM (subsequently called the "atmosphere model uncertainty"). Both studies used a mixed-layer only ocean model (a slab ocean) coupled to the perturbed atmospheres to determine the equilibrium change in global mean surface temperature caused by a doubling of $CO_2$ (climate sensitivity). Murphy *et al*. (2004) perturbed a single parameter to its maximum plausible extent to create each perturbed model version. Stainforth *et al*. (2005) perturbed multiple parameters simultaneously, and found a larger spread in climate sensitivity.

Collins *et al*. (2006) created an ensemble of multiply perturbed atmosphere and coupled them to an

ocean model (creating perturbed versions of HadCM3). The multiple perturbations were chosen in such a way that parameter space is systematically sampled. They then performed a transient climate change scenario (using the CMIP2 scenario). This experiment design allowed Collins *et al*. (2006) to quantify the effects of atmosphere model uncertainty on time-dependent climate. Many of their results will be included in this thesis for comparative purposes.

## 1.5 The aims of this thesis

Several recent studies have investigated the effects of atmosphere model uncertainty on the climate response to an increase in $CO_2$ in HadCM3 (Murphy *et al*. (2004), Stainforth *et al*. (2005) and Collins *et al*. (2006)). The effects of ocean model uncertainty on HadCM3's climate response are not known. This thesis aims to correct that by performing a similar style of experiment to that of Collins *et al*. (2006). They created a perturbed physics ensemble that samples atmosphere model uncertainty, then performed an idealised increasing $CO_2$ experiment with each ensemble member. The ensemble spread is a measure of the effects of atmosphere model uncertainty.

Chapter 2 and the first half of chapter 3 will describe the creation and evaluation of a perturbed physics ensemble that samples ocean model uncertainty. Chapter 2 will present a database of ocean physics parameters and their uncertainty ranges. This database has been created by expert elicitation and complements the atmosphere parameter database of Murphy *et al*. (2003). A seven member ensemble has been created by perturbing the most important parameters to their extreme plausible values. The initialisation and a simple evaluation (through comparison to observations) of this ensemble will be presented in sections 3.1 - 3.4. The ensemble spread shows the magnitude of effects of ocean model uncertainty. The later part of chapter 3 will present the effects of ocean model uncertainty on HadCM3's representation of the long-term preindustrial climate state, by analysing the ensemble spread without any imposed increases in $CO_2$.

The rest of the thesis will describe the effects of ocean model uncertainty on HadCM3's time-dependent response to increasing $CO_2$ concentrations. This will be achieved by the analysis of the climate change signal for each ensemble member, which is defined as the change in climate for the twenty years centred about the time of $CO_2$ doubling. The spread in the climate change signals (as opposed to the actual ensemble spread) has been quantified for various other sources of uncertainty (e.g. Cubasch *et al*. (2001) and Collins *et al*. (2006)). Chapter 4 will quantify the global mean effects of ocean model uncertainty by analysing the signal spread. It will also compare the effects of ocean model uncertainty to those of other sources of uncertainty. The spatially varying effects of ocean model uncertainty on the climate change signal will also be investigated. These include regional effects in the surface temperature and precipitation fields, depth varying effects in the ocean and effects on the thermohaline circulation. This forms an initial quantification of the effects of ocean model uncertainty on the climate change signal.

The ensemble spread in the increasing $CO_2$ experiment should be investigated (as well as the signal spread). This can be thought of as investigating the response of ocean model uncertainty to increasing $CO_2$, as opposed to investigating the response of the effects of increasing $CO_2$ to ocean model uncertainty. It will be shown that the ensemble spread reduces as $CO_2$ increases. Chapter 6 will look for an explanation for this reduction.

# CHAPTER 2

# A database of ocean parameters and their uncertainty ranges

## 2.1 Introduction

A climate model, due to its resolution, does not explicitly resolve all the important physical processes. Parameterisations try to model the effects of unresolved processes and their feedbacks on the resolved variables. In general, these parameterisations can not be determined precisely from theory or from observations. This study attempts to understand and investigate uncertainties related to the parameter values contained in the parameterisations of physical ocean processes.

Research has already been undertaken to estimate the effects of atmosphere model uncertainty. Climate*prediction*.net (Stainforth *et al*., 2005) and the Quantifying Uncertainty of Model Predictions team at the Met. Office (QUMP, Murphy *et al*. (2004)) have utilised an atmospheric model with a mixed layer ocean (Pope *et al*. (2000) and Williams *et al*. (2001)) to investigate the uncertainty in the doubled $CO_2$ climate sensitivity caused by atmosphere model uncertainty. The parameter perturbations identified for their work are only relevant to the atmospheric component of the AOGCM. They identified twenty-nine perturbations (see Murphy *et al*. (2004) supplementary table 2 for a full list of these). The nature of the mixed-layer only ocean means that these studies can only determine equilibrium responses rather than replicate time-dependent changes. A dynamical ocean model is required to make a projection of time-dependent climate change, and will contain its own model uncertainties.

The first stage in investigating the ocean model uncertainty is to identify the parameters that contain uncertainties that could have an impact on the climate system in general and on its response to increas-

ing $CO_2$ specifically. This chapter identifies each of the relevant parameterisations and the uncertainty contained within them. Section 2.2 explains the process, through which the parameters were identified. Sections 2.4 to 2.9 describe the parameters and the possible perturbations that could be made to them. The computer resources required to attempt every perturbation are not available to this study. Therefore a hierarchy of perturbations is required. Whether a parameter is considered to be important to investigate it has been mentioned in the relevant section of this chapter. Some element of the hierarchy of the perturbations is also shown by the priority columns in the summary tables (section 2.10).

## 2.2 The expert elicitation used to create the database

The method used to create the database of ocean physics parameters and determine their uncertainty ranges is similar to that followed by Murphy *et al*. (2003) to determine the atmospheric parameter perturbations used by Murphy *et al*. (2004) and Stainforth *et al*. (2005). It can be can be divided into the following three steps:

1. Identification of the major components of the model physics.
2. Experts (usually the authors of the code) asked to provide plausible upper and lower limits for key parameters in each model component.
3. Subjective judgement used to constrain the list of parameters to manageable proportions. This expertise comes from previously performed model tuning exercises.

The first step, identification, was achieved at a group discussion attended by the majority of experts listed in table 2.2. The 15 most important processes were identified, of which some were later discounted. All the possible perturbations within those important processes were listed. A range of values was found for each parameter. This range came preferentially from papers containing estimates of the

parameters derived from observations. However when observational studies were unavailable, first the literature surrounding the parameterisation scheme, then the experts who implemented the scheme into the ocean model were consulted. This information was then distributed to physical oceanographers and climate modellers for validation of the ranges and to check that no parameterisations had been overlooked. A prioritisation was decided upon through discussions with the Met. Office's Oceans and Climate division. Table 2.2 lists the names of all the experts who were involved in creating this parameter database. This method of consulting experts is referred to as expert elicitation.

| **Expert Consulted** | **Institution** |
|---|---|
| David Acreman | Met. Office |
| Myles Allen | Oxford University |
| Helene Banks | Met. Office |
| Ben Booth | Met. Office |
| Jo Brown | Reading University |
| Mat Collins | Met. Office |
| Stephen Cusack | Met. Office |
| Nick Faull | Oxford University |
| Dave Frame | Oxford University |
| Peter Gent | N. C. A. R. |
| Chris Gordon | Met. Office |
| Jonathan Gregory | Reading University |
| Chris Jones | Met. Office |
| Ann Keen | Met. Office |
| Peter Killworth | Southampton Oceanography Centre |
| David Marshall | Reading University |
| John Marshall | M. I. T. |
| Syukuro Manabe | G. F. D. L. |
| Anne Pardaens | Met. Office |
| Malcolm Roberts | Met. Office |
| David Sexton | Met. Office |
| Michael Vellinga | Met. Office |
| Richard Wood | Met. Office |
| Kuniko Yamazaki | Oxford University |

**Table 2.1** *People involved in the elicitation process*

The rest of this chapter describes individual parameterisation schemes and the ranges determined for the parameters involved within them. Section 2.4 deals with horizontal mixing, whilst section 2.5 treats vertical mixing, including the mixed layer. Changes in bathymetry and marginal sea outflows are covered in section 2.6. Section 2.7 details possible perturbations to the derivations of any flux

adjustments. Different numerical solvers for the advection scheme are covered in section 2.8, and the penetration of solar radiation in section 2.9. Tables summarising the perturbations can be found in 2.10

It is important to note that two slightly different ocean models are being considered in this chapter: HadCM3 (Gordon *et al*., 2000) and its lower ocean resolution form HadCM3L (Jones and Palmer, 1998). The models are substantively similar, only the horizontal resolution and any resolution dependent parameters are different. This parameter database has been created for the use of climate*prediction*.net and QUMP (the two groups currently studying model uncertainty in AOGCMs).

The reason for using the two models is the different computer resources of Climate*prediction*.net and QUMP. QUMP has access to large memory storage facilities and supercomputers, but relatively little processing time. Climate*prediction*.net can produce hundreds of thousands of model runs, but each model run will be performed on a volunteer's personal computer. This means that the storage and transmission of large amounts of data is unfeasible. Climate*prediction*.net is therefore using HadCM3L, which is faster and outputs less data, whilst QUMP is using the full version of HadCM3, due to its better representation of regional features. Whenever the resolution will be an issue in a parameterisation it will be mentioned and two differing databases have been produced. A description of the models follows in section 2.3.

## 2.3 Description of the Hadley Centre coupled model

HadCM3 is the Hadley Centre's third coupled model. It has been used for both climate analysis and projections. Projections from it are presented in the IPCC's third assessment report (Cubasch *et al*., 2001). HadCM3L was developed for work including an interactive carbon cycle. It is HadCM3 with a lower resolution ocean component. The atmospheric component (common to both) is described in section 2.3.1. Then the ocean component of HadCM3 is described in section 2.3.2 followed by a

section detailing the differences between HadCM3 and HadCM3L (section 2.3.3).

### 2.3.1 The atmospheric component

The atmospheric component of HadCM3 is based on a quasi-hydrostatic approximation to the full primitive equations in spherical polar co-ordinates (Johns *et al*., 1997). It is a gridpoint model with an Arakawa B grid with a horizontal spacing of $2.5° \times 3.75°$ and 19 sigma levels in the vertical. The time step is 30 minutes.

It involves a radiation scheme with 14 spectral bands, which allows the spectral properties of different gases to be represented (Edwards and Slingo, 1996). There is a prognostic cloud scheme that interacts with the radiation scheme, a parameterisation of the orographic and gravity wave drag, and a land surface scheme (MOSES) that includes stomatal dependence on temperature, $CO_2$ and vapour pressure deficit (Cox *et al*., 1999).

A sulphur cycle model is also included in the version of HadCM3 used for this study. This involves consideration of the production, transportation and deposition of five different forms of sulphur from natural and anthropogenic sources (Jones *et al*., 2001).

The systematic biases in the atmospheric model are described by Pope *et al*. (2000). The most significant errors for this work are thought to be a cold bias over the north Pacific, and a warm bias over the Southern Ocean and tropical oceans. A zero-layer sea ice model is also included, and the effect of sea ice formation and melt on the ocean salinity is parameterised (Gordon *et al*., 2000).

### 2.3.2 The ocean component of HadCM3

The ocean component of HadCM3 is a gridpoint model with 20 fixed depth levels. The horizontal grid has of $1.25° \times 1.25°$, meaning that the ocean has six gridboxes for each atmospheric gridbox. The

vertical levels are chosen to have higher resolution near the surface, see table 2.2. The bathymetry is taken from a 1/12°resolution dataset, and is smoothed onto the model grid. The Greenland-Iceland-Scotland ridge has been excavated to allow a through-flow similar to observations (Gordon *et al.*, 2000). The land-sea mask is represented at the atmosphere's 2.5°$\times$ 3.75°resolution. The model has a rigid lid, which means that the volume of the ocean is fixed, and that the freshwater flux does not lead to changes in the volume of the water column. The freshwater flux is therefore converted into an equivalent salinity flux to help close the global salinity budget. The accumulation of snow on Greenland and Antarctica would lead to a global salinity drift (due to the lack of iceberg calving in the model), so an appropriate freshwater flux is applied uniformally over the areas of the adjacent ocean where icebergs occur. Closing the salinity budget is important, because normally HadCM3 does not have flux adjustments. The other important ocean parameterisations are described in more detail in the following sections.

The atmosphere and ocean components are coupled every 24 hours. The ocean variables are interpolated from, or averaged onto, a 2.5°$\times$ 3.75°resolution to allow the smooth transfer of the information.

### 2.3.3 Differences between HadCM3 and HadCM3L

HadCM3L is a low resolution ocean version of HadCM3 that was developed for use with an interactive carbon cycle model to offset the extra computational expense (Cox *et al.*, 2000). The resolution of the ocean is 2.5°$\times$ 3.75°like the atmosphere. The same parameterisation schemes are used as HadCM3, however the Gent and McWilliams (1990) scheme has a spatially constant coefficient, unlike HadCM3 (discussed further in 2.4.3). Originally HadCM3L required flux adjustment to reproduce the observed sea ice distribution in the Arctic, which allowed the possibility of a periodically synchronous spin up (Jones and Palmer, 1998). However, Jones (2003) found that HadCM3L could be run without flux adjustments, if the flow across the Greenland-Iceland-Scotland ridge was increased. This can be obtained by removing Iceland and excavating the ridge to a the depth of 800m. Climate*prediction*.net

| Level Number | Upper Boundary (m) | Depth (m) | Lower Boundary (m) |
|---|---|---|---|
| 1 | 0.00 | 5.0 | 10.0 |
| 2 | 10.0 | 15.0 | 20.0 |
| 3 | 20.0 | 25.0 | 30.0 |
| 4 | 30.0 | 35.1 | 40.2 |
| 5 | 40.2 | 47.9 | 55.5 |
| 6 | 55.5 | 67.0 | 78.5 |
| 7 | 78.5 | 95.8 | 113. |
| 8 | 113.0 | 138.9 | 164.8 |
| 9 | 164.8 | 203.7 | 242.6 |
| 10 | 242.6 | 301.0 | 359.4 |
| 11 | 359.4 | 447.1 | 534.7 |
| 12 | 534.7 | 666.3 | 797.9 |
| 13 | 797.9 | 995.6 | 1193.2 |
| 14 | 1193.2 | 1501.0 | 1808.5 |
| 15 | 1808.5 | 2116.0 | 2423.8 |
| 16 | 2423.8 | 2731.0 | 3039.0 |
| 17 | 3039.0 | 3347.0 | 3654.3 |
| 18 | 3654.3 | 3962.0 | 4269.5 |
| 19 | 4269.5 | 4577.0 | 4884.8 |
| 20 | 4884.8 | 5193.0 | 5500.0 |

**Table 2.2** *The depth of the 20 vertical levels in HadCM3 and HadCM3L*

uses HadCM3L without Iceland (this configuration is referred to as FAM1 in Jones (2003)).

## 2.4 Parameters for lateral mixing

The ocean is in a dynamic equilibrium in the sense that the energy absorbed from the winds at the surface is dissipated throughout the ocean (Colling, 2002). The primary method of this energy dissipation is through the turbulent motion of the ocean currents. This turbulence is characterised by mesoscale eddies that have a length scale of 50-200km. This means that they will be contained within 1 gridbox and their mixing effect must be parameterised. This is done by modelling the process as a diffusion with an associated eddy diffusivity (rather than the well observed molecular diffusivity, Griffies (2004)). The stratification of the ocean means that influence of eddy mixing is much greater horizontally than vertically. Therefore HadCM3 separates diffusion into a lateral component and a much smaller vertical component. It uses a variety of parameterisations to calculate these separate

components, but all are based on the diffusion equation:

$$\frac{dQ}{dt} = -K\nabla Q \tag{2.1}$$

where $Q$ is the quantity being diffused, $\nabla$ is the spatial derivative and $K$ is the constant of proportionality. There are two quantities that need to be diffused: momentum and tracers (such as temperature and salinity). They are treated separately and the constants of proportionality have different names: viscosity, $\nu$, for momentum diffusion and diffusivity, $K$, for tracer diffusion.

### 2.4.1 Horizontal viscosity

The diffusion of momentum is parameterising an eddy frictional force, namely the effect of turbulence on the speed of the flow. The value of the viscosity is primarily determined by two factors; a desire to reduce grid scale noise in the narrow western boundary currents and secondly to prevent instability in the diffusion calculation near the north pole. A latitude dependent viscosity is used for the latter reason:

$$\nu_H(y) = \nu_H(1 + cos(y)) \tag{2.2}$$

where $y$ is the latitude and $\nu_H$ is a constant. The value of $\nu_H$ in HadCM3 of $300\mathrm{m}^2\mathrm{s}^{-1}$ is within the range determined by observational studies (except for its artificial latitude dependence, which is included for numerical stability).

The magnitude of the horizontal viscosity in HadCM3L is 50 times that of HadCM3. This is primarily due to the timestep constraints imposed by topographic instability (the rigid lid cannot capture the effects of currents encountering steep bathymetry (Killworth, 1987)). The value of viscosity in HadCM3L is much larger than observations imply, but is also the lowest value required to constrain the noise with a reasonable timestep. The horizontal viscosity should not be investigated with HadCM3L, because the reduction in viscosity required for the value to agree with observations would mean that the model would be numerically unstable.

However perturbing the horizontal viscosity would have physical meaning in HadCM3 and should be included in studies at this resolution. The range of viscosities should include 1000 and $2000 \mathrm{m}^2\mathrm{s}^{-1}$ (Bell, 1994). This perturbation should not be given a high priority, because of the model may have increasing computational modes (due to either the misrepresentation of the frictional boundary currents or to the use of centred differencing), which would need to be investigated before inclusion in the ensemble.

### 2.4.2 Isopycnal diffusion

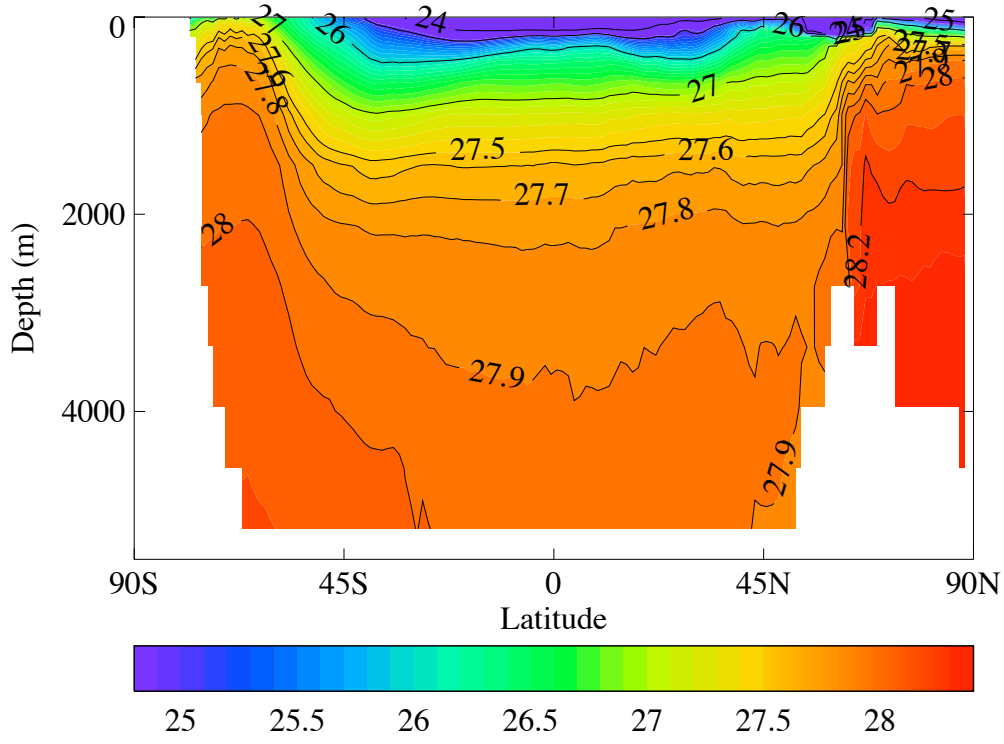


**Figure 2.1** *The stratification of the ocean in HadCM3. A zonal mean cross-section of the global ocean, showing the potential density, $\rho_\theta$. The units are $\sigma_\theta$, equal to $\rho_\theta - 1000 kgm^{-3}$. The contours show lines of constant potential density, isopycnals.*

The stratification of the ocean is not uniform with depth; lines of constant density (isopycnals) slope because of the combined effects of temperature and salinity (see figure 2.1). The vertical gradient of the isopycnals is greatest in the high latitudes, especially in the Southern Ocean. Eddies are observed

to occur along isopycnal surfaces rather than truly horizontal ones. Mixing which occurs perpendicular to isopycnal surfaces is called diapycnal mixing.

Mixing along isopycnal surfaces can transport heat vertically if the isopycnals are not completely horizontal. HadCM3 computes the isopycnal surfaces, then parameterises the effects of eddies as a diffusion by determining the gradient of temperature and salinity on the isopycnal. It can then calculate the horizontal and vertical components of any tracer movements. This is necessary, because of the importance of the vertical heat fluxes in the energy budget of the Southern Ocean (Gregory, 2000). Figure 2.2 is a schematic to show how this upward heat transport can exist. Isopycnal diffusion is very important in determining the water properties of the deep ocean, by controlling the flow of heat and salinity from the high latitudes, in the regions of subduction and sloping isopycnals (Griffies, 2004).

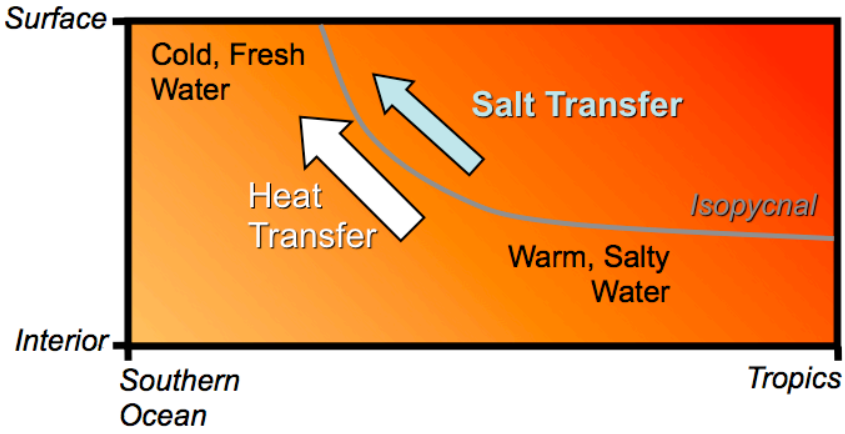


**Figure 2.2** *A schematic showing the upwards diffusion of heat along isopycnals. As water get either saltier or colder is becomes denser. At colder temperatures, salinity effects on the density dominate the temperature effects. The leads to the isopycnals sloping. There is transfer of both heat and salt along the isopycnal. These transfers will have a vertical component.*

HadCM3 does allow the possibility of the isopycnal diffusion coefficient, $K_I$, to change with depth, but it is kept constant in the standard parameter set-up. This depth variation is achieved by specifying the ocean surface and floor values of $K_I$. The coefficient decreases with depth from one value to the other with a scale depth of 50m. So it is possible to change the profile of the variations with depth by adjusting ocean surface and floor values (and possibly the scale length as well). The effects

of changing this depth profile are felt to be less than the effects of changing the value of a constant $K_I$ by Richard Wood (who implemented the depth variation). Therefore in this study the isopycnal diffusion will have a constant value everywhere. Huang *et al*. (2003) uses a range for $K_I$ of 500m$^2$s$^{-1}$ to 2000m$^2$s$^{-1}$ for their study into the uncertainty of subgrid-scale eddy mixing in an idealised ocean model. However, this range does not cover the lower range of the observed ocean floor values that are given by Bell (1994). The uncertainty range for a single global value should encompass all the observations. Therefore the range to be investigated will be from 200m$^2$s$^{-1}$ (observed at depth) and 2000m$^2$s$^{-1}$ (observed at the surface). The value of $K_I$ used in HadCM3 is 1000m$^2$s$^{-1}$.

### 2.4.3 Sub grid scale stirring

Gent and McWilliams (1990) provide a parameterisation of the eddy mixing effect caused by baroclinic instability on the water properties. They do this by including a diffusion of the thickness of the isopycnic levels. The rate of this diffusion is determined by a constant of proportionality called the thickness diffusivity, $K_{THK}$.

The Visbeck *et al*. (1997) scheme determines the thickness diffusivity at every point in the ocean according to the large scale features of the flow. This scheme gives a better representation of the physical process, because it allows the baroclinic regions of the ocean (such as the western boundary currents) to have different eddy mixing than the rest of the ocean. The value of the thickness diffusivity is given by

$$K_{THK} = \alpha_{VIS} \frac{f}{\sqrt{Ri}} l^2 \tag{2.3}$$

where $f$ is the Coriolis force, $Ri$ is the Richardson number, $l$ is the eddy transfer length, which is the width of the baroclinic zone. The constant of proportionality, $\alpha_{VIS}$, is $0.015 \pm 0.005$ according to Visbeck *et al*. (1997). The Richardson number is a measure of the stratification of the flow and is given by

$$Ri = \frac{-g\frac{d\rho}{dz}}{\rho_0(\frac{dU}{dz}^2 + \frac{dV}{dz}^2)} \tag{2.4}$$

where $\rho$ is the potential density, $\rho_0$ is a reference density level, and U and V are horizontal velocities.

A background thickness diffusivity, $K_{THK,bg}$ is applied everywhere in addition to the values returned by the Visbeck *et al*. (1997) scheme. It dominates $K_{THK}$ for the majority of the ocean. The purpose for this background value is noise reduction and it does not have a physical basis. HadCM3 uses a value of $350 m^2 s^{-1}$, whilst a subsequent eddy permitting model developed by the Hadley Centre uses $150 m^2 s^{-1}$. The preferred background value would be zero, so this is the bottom of the range proposed.

The Visbeck *et al*. (1997) scheme is not used in HadCM3L. This is because the lower resolution prevents certain elements of the flow to be accurately determined. In HadCM3L, the Gent and McWilliams (1990) scheme is used with constant thickness diffusivity globally. It is typical of a value returned by the Visbeck *et al*. (1997) scheme for the Antarctic circumpolar current. The scheme is particularly successful in low resolution models. It has been suggested that it compensates for the poor gyre transports in these models. The value for the thickness diffusivity is too large in the majority of low resolution models compared to the results of the Visbeck *et al*. (1997) scheme. Therefore, the proposed minimum for $K_{THK}$ in HadCM3L is a reduction to HadCM3's $K_{THK,bg}$.

None of the perturbations relating to the parameterisation of Gent and McWilliams (1990) have been given a high priority by the experts consulted, yet the inclusion of the scheme greatly improved the simulations of climate models. This is not contradictory, because the anticipated effects of perturbing the parameters within their uncertainty ranges was thought by the experts to be much less than the complete removal or inclusion of the Gent and McWilliams (1990) scheme. In light of the results presented later in this thesis, these priorities and the manner of implementing the perturbations may need to be re-evaluated. There is some compensation by the Gent and McWilliams (1990) diffusion for the effects of the perturbed isopycnal diffusion on the heat uptake due to increased $CO_2$. Yet in some formulations of the Gent and McWilliams (1990) scheme the value for the thickness diffusivity is forced to be the same as for the isopycnal diffusivity, notably the Modular Ocean Model (Griffies *et al.*, 2004). These coupled perturations may not allow such compensation to occur and therefore, in

the work of climate*prediction*.net, the two diffusivity coefficients have been perturbed simultaneously, and by the same magnitude.

## 2.5 Parameters for vertical mixing

Although the vast majority of mixing from mesoscale eddies occurs along isopycnal surfaces, there is still eddy mixing across the isopycnals (called diapycnal mixing). There is also some molecular scale mixing. Mixing from both these sources are parameterised together.

There are 4 schemes available to perform the vertical mixing in HadCM3: Pacanowski and Philander (1981), Peters *et al*. (1988), Large *et al*. (1994) and a prescribed vertical diffusion. The latter scheme defines both the vertical diffusivity of tracers and momentum as constant values. It is outdated and should not be used in current modelling studies. The first two schemes are K-theory schemes, which means that they diffuse depending on the stratification of the fluid. They do this by determining the Richardson Number ($Ri$, eq. 2.4), which defines the relative importance of buoyancy to shear in the fluid, and so determines the possibility of turbulence. The Large scheme treats the ocean surface as a fluid boundary layer and uses a formulation analogous to that used in the atmospheric part of the model.

### 2.5.1 K-theory mixing

The purpose of the "K-theory" mixing scheme (Pacanowski and Philander, 1981) is to allow the vertical viscosity and diffusivity to depend on the local properties of the ocean. The Richardson number is a way of quantifying the relative stratification and buoyancy properties of the water (see eq. 2.4). Equation 2.5 determines the vertical viscosity (vertical mixing of momentum, $\nu$) by relating it to the Richardson number of the water. Equation 2.6, which determines the vertical tracer diffusivity, $K_V$, requires knowing the viscosity from eq. 2.5.

$$\nu_V = \frac{\nu_{V,0}}{(1+\alpha Ri)^n} + \nu_{V,bg} \tag{2.5}$$

$$K_V = \frac{\nu_V}{1 + \alpha Ri} + K_{V,bg} \tag{2.6}$$

In the above equations, $\nu_{V,bg}$ and $K_{V,bg}$ are background values of viscosity and diffusivity, $\alpha$ and $n$ are tunable parameters, and $\nu_{V,0}$ is the co-efficient of vertical mixing of momentum dependent on the Richardson number. Compared to the effects of the background diffusion parameters and the size of $\nu_{V,0}$, the two tunable parameters are insignificant (Pacanowski and Philander, 1981). Pacanowski and Philander (1981) suggest a range for $\nu_{V,0}$ from model tuning experiments of of $5 \times 10^{-3}$ to $15 \times 10^{-3}\mathrm{m}^2\mathrm{s}^{-1}$. It is felt that they over-estimated the value of $\nu_{V,0}$. Their range has been changed to $3 \times 10^{-3}$ to $8 \times 10^{-3} m^2 s^{-1}$ during the expert elicitation. Both ranges contain the value of $5.5 \times 10^{-3} m^2 s^{-1}$ used in HadCM3.

Bell (1994) suggested a range for the background vertical viscosity of $5.0 \times 10^{-5}\mathrm{m}^2\mathrm{s}^{-1}$ to $1.0 \times 10^{-4}\mathrm{m}^2\mathrm{s}^{-1}$. HadCM3 uses a smaller value of $1.0 \times 10^{-5}\mathrm{m}^2\mathrm{s}^{-1}$, because subsequent studies have shown these estimates to be too high for HadCM3, although $1.0 \times 10^{-5}\mathrm{m}^2\mathrm{s}^{-1}$ is still used by Griffies *et al*. (2004). The range for $\nu_{V,bg}$ determined by the expert elicitation exercise is $0.5 \times 10^{-5}\mathrm{m}^2\mathrm{s}^{-1}$ to $8.0 \times 10^{-5}\mathrm{m}^2\mathrm{s}^{-1}$.

The vertical diffusivity tends to be set to the background value for the majority of the ocean, due to the high Richardson number. In the mixed layer, the mixing of tracers is subsequently performed by the Kraus and Turner (1967) scheme (see section 2.5.5 for a description), so any diffusivities calculated for the mixed layer are irrelevant. Observations of deep ocean diffusivities do not correspond to those determined by the K-theory scheme (Rickard, 1999). HadCM3 uses the observations of Kraus (1990) to provide a depth increasing background diffusivity, $K_{V,bg}$ to overcome this misrepresentation (Gordon *et al*., 2000). Other modelling studies have used values as low as $0.5 \times 10^{-5} m^2 s^{-1}$. However, a subsequent study by Ledwell *et al*. (1993) measured the surface diffusivity as $1.0 - 1.5 \times 10^{-5}\mathrm{m}^2\mathrm{s}^{-1}$, agreeing with the profile of Kraus (1990). The influence of any diffusion changes within the K-theory scheme are thought to occur primarily in the equatorial undercurrent. Further considerations about the background diffusivity are described in section 2.5.3. The values in tables 2.9 and 2.8 were proposed

by Richard Wood and are based on the observations of the vertical diffusivity at the surface and at depth. The models require the surface value and the increase per metre to be specified, rather than a surface and a bottom value. The ranges and the increase per metre are shown in table 2.3.

| **Range** ($m^2s^{-1}$) | **Surface value** ($m^2s^{-1}$) | **Depth increase** ($m^2s^{-1}m^{-1}$) |
|---|---|---|
| $0.5 \times 10^{-5} - 4.0 \times 10^{-5}$ | $5.0 \times 10^{-6}$ | $7.0 \times 10^{-9}$ |
| $1.0 \times 10^{-5} - 15 \times 10^{-5}$ | $1.0 \times 10^{-5}$ | $2.8 \times 10^{-8}$ |
| $2.0 \times 10^{-5} - 50 \times 10^{-5}$ | $2.0 \times 10^{-5}$ | $9.6 \times 10^{-8}$ |

**Table 2.3** *The depth profiles for $K_{V,bg}$ proposed by Richard Wood. The first column presents the ocean surface and floor values. The second columns provide the required information to implement these changes in HadCM3.*

### 2.5.2 Peters *et al.* (1988)

The Pacanowski and Philander (1981) scheme does not quite recreate the correct structure at the base of the equatorial thermocline at low Richardson numbers. Peters *et al.* (1988) suggest the addition of a correcting term with a power Richardson number dependence to the Pacanowski and Philander (1981) equations. As this is only an additional term, the uncertainty ranges for the diffusivities are unchanged from those in section 2.5.1. This scheme switch should be given a low priority, because its likely impacts will be limited to the equatorial undercurrent.

### 2.5.3 Problems during accelerated spinups

It is possible to use an accelerated method of bringing HadCM3L to an equilibrium (Jones and Palmer, 1998). This would use the distorted physics technique of Bryan (1984), which allows a longer timestep, and therefore has a significant reduction in computer time required. Wood (1998) has found some problems with using this technique with a complicated model such as either HadCM3 or HadCM3L. There is interaction between the implicit diffusion solver, the mixed layer model and the vertical tracer diffusion, which creates a dependence of the model equilibrium below the tropical

mixed layer on the timestep used. This timestep sensitivity can be removed by removing any one of the three interacting schemes. As stated in section 2.5.2, only the tracer diffusivities in the tropical undercurrent are affected by the K-theory mixing. Therefore a modification has been made to HadCM3L, which removes the K-theory tracer effects (i.e. equation 2.6 is replaced by $K_V = K_{V,bg}$). The Richardson number in the deep ocean is large, so this effect is not too drastic. However it does show that the background diffusivity is a high priority perturbation to include.

### 2.5.4 Large *et al.* (1994)

The Large *et al*. (1994) scheme treats the ocean mixed layer as a boundary layer. It comes in two different flavours; full (cubic) and a quadratic form. They both involve using a vertical diffusion scheme to find the diffusivity, $K_V$, at all depths. Then a mixed layer depth can be found by comparison with the surface forcing conditions (determined by the wind mixing energy or the wind stress). Using a shape function, $G(z)$, the diffusivity throughout the boundary layer is found and matched up with diffusivity at the mixed layer depth.

The full Large scheme approximates the shape function, $G(z)$, with a cubic equation. One of the advantages is its application to both momentum and tracer movements. This means that the full Large scheme provides a more accurate representation of the surface currents. However experience with the full Large scheme has found that it under-performs with wind-driven stable layers, particularly those in the Southern Ocean around March (Rickard, 1999).

The Quadratic Large scheme approximates the shape function with a quadratic, such that $G(z) = 1 + a_2(z)^2$. This is computationally cheaper that the full Large scheme, but has the problem that it reproduces the near surface vertical tracer structure so poorly that a mixed layer scheme must also be applied. However the two schemes combined create a similar structure of the surface currents and properties as observations.

Both of the boundary layer schemes have two available tunable parameters associated with the manner in which the bottom of the boundary layer is determined. The Richardson number throughout the column is calculated, and the edge of the boundary layer is defined as the depth at which the Richardson number equals a critical value, $RI_{CRIT}$. Rickard (1999) suggests a standard value of 0.3, which falls within the range of 0.25 to 0.5 suggested by Large *et al*. (1994). HadCM3 also specifies a maximum depth of the oceanic boundary layer, $D_{max}$. The boundary layer depth calculated can not exceed this maximum, even if the critical Richardson number occurs below it. Large *et al*. (1994) state there is no need for a maximum boundary layer depth, yet in HadCM3 it is specified at 80m for numerical reasons (Rickard, 1999). It is suspected that the model will not be overly sensitive to realistic perturbations to this parameter, hence it should be given a low priority in the experiments.

### 2.5.5 The mixed layer model

For a certain depth the ocean is well mixed, with the whole layer having very similar density and temperature. The depth of the mixed layer changes throughout the year, and even throughout the day. The mixed layer is formed by enough energy being added to the surface, to overcome the potential energy of the existing stratification. A reduction in the energy input will lead to the base of the mixed layer re-stratifying.

The energy is added to the ocean surface by the penetration of solar radiation (determined by the ocean colour - see section 2.9), sensible heat flux, latent heat flux and mechanical mixing caused by the action of the wind. The energy added by the wind, called wind mixing energy, penetrates furthest into the ocean and is therefore the most dominant process.

When used, the full boundary layer scheme will model the mixed layer accurately enough. However, the quadratic Large scheme will not mix the near-surface tracers sufficiently, and another scheme must be used to perform this mixing. Kraus and Turner (1967) proposed a scheme from bulk physical

properties to perform this mixing. It can also be used without the Large boundary layer schemes described above.

The Kraus and Turner (1967) scheme is not able to parameterise any deep convection that does not stretch upto the surface, because of its top-down formulation. The parameterisations of Roussenov *et al*. (1995) and Rahmstorf (1993) are used by HadCM3 to model deep convection. They both mix the water column over a single timestep.

The wind mixing energy used for the mixed layer calculation, $W_{surf}$, is a function of the velocity of the wind (calculated at 10m in HadCM3), $V_{10m}$ :

$$W_{surf} = \lambda W_{10m} = \lambda \frac{(\rho_{air} C_D)^{3/2}}{\rho_{water}^{1/2}} V_{10m}^3 \tag{2.7}$$

where $\rho_{air}$ is the density of air, $\rho_{water}$ is the density of sea water, $C_D$ is the surface drag co-efficient. $\lambda$ is the "wind mixing fraction" and corrects for the height difference in the calculation. The ocean and atmosphere models interact every 24 hours, so $W_{surf}$ is a daily average. To improve biases seen in previous model setups the wind mixing energy is calculated every timestep in the atmosphere model and then averaged over the 24 hours (this is denoted $W_{10m}$ in the above equation).

As well as the input of energy at the surface, the depth profile of the wind mixing energy is important. The reduction of energy with depth is modelled using an exponential decay length, $\delta$:

$$W_n = [W_{n-1} - \Delta P_{n-1,n}] exp(\frac{-z_n}{\delta}) \tag{2.8}$$

where $W_{n-1}$ is the wind mixing energy available at the previous (shallower) level, $z_n$ is the thickness of the level and $\Delta P_{n-1,n}$ is the change in potential energy between the two levels. This essentially parameterises a background dissipation of turbulent kinetic energy.

The two parameters can, and should, be varied simulataneously to define a depth profile, which simulates observed data. Davis *et al*. (1981) used such a technique to find the combination of parameters that modelled a year of observations from Ocean Weather Station Papa, in the North Pacific. The values they determined for $\lambda$ and $\delta$ (0.7 and $100m$ respectively) are used in HadCM3. Subsequent work

| $\lambda$ | $\delta$ (m) | Mean MLD error (m) | RMS MLD error (m) |
|---|---|---|---|
| 0.7 | 100 | -26 | 29 |
| 0.5 | 50 | -4 | 15 |
| 0.3 | 100 | -5 | 11 |

**Table 2.4** *Mixed layer parameter combinations of $\lambda$ and $\delta$ with their associated mixed layer depth (MLD) errors (Acreman, 2005)*

has explored the accuracy of a variety of combinations for the model (Acreman, 2005). Two possible combinations, which have better simulations of the OWS Papa have been chosen as perturbations. They are shown in 2.4, along with the errors in mixed layer depth between the parameter set and the observations calculated by Acreman (2005). These parameter changes seem to make a large change to the mixed layer depth, and should be given a high priority.

Some turbulent energy will be transmitted from the mixed layer through the thermocline to the upper levels of the deep ocean, driving some deep convection. This is parameterised by passing a fraction, $\epsilon$, of the turbulent kinetic energy of the bottom level of the mixed layer to the next level down. Bell (1994) suggests a range for this parameter of $0.13 - 0.17$, the standard value for HadCM3 is $0.15$. The experts give this parameter a low priority, because the amount of turbulent energy in the bottom level of the mixed layer is itself small.

## 2.6 Bathymetry

The shape of an ocean basin affects the flow in that basin. The flow of water from marginal seas (those which are not freely mixed with the oceans) can also affect the circulation. The flow of water from the marginal seas of the Mediterranean and the Hudson Bay is important for the salinity of the North Atlantic. There are two schemes for parameterising this flow in HadCM3. The diffusive scheme (Diff.) compares the water properties for specified gridpoints in the Atlantic and the Mediterranean and diffuses a flow between them. The advective (Adv.) scheme imposes a flow of 0.4 Sv from the Mediterranean and 0.8 Sv from the Hudson Bay into the Atlantic. These flow strengths are based upon

observations, although the Mediterranean volume transport is lower than recent observations.

## 2.7 Haney forcing and flux adjustments

A problem found when coupling AOGCMs together is that the fluxes derived from the atmosphere are not necessarily those required to sustain a realistic ocean state, and vice versa. The surface heat and freshwater fluxes from the atmosphere can be adjusted before being input to the ocean model to combat this problem. These flux adjustments are required by most low resolution models, such as HadCM2 (Johns *et al.*, 1997). However the improvements made when creating HadCM3 mean that flux adjustments are not necessary to attain a realistic climate state (see Gordon *et al.* (2000) for more details).

A lack of flux adjustment does not mean that a model is correct, because there could be a compensation of errors. The parameter perturbations could break this balance, by correcting one error but not affecting the compensating error. Therefore Collins *et al.* (2006) used flux adjustments for HadCM3, because although they are intentionally breaking the balance, the perturbations are all plausible and they want every model to have realistic climate states. HadCM3L also does not need flux adjustments (see section 2.3.3 for an explanation of how this is possible), but will be run with flux adjustments by climate*prediction*.net for the same reasons as Collins *et al.* (2006). The ensemble used in the next chapters will not use flux adjustments to constrain the control climates (section 3.2): partly to see if a perturbed ensemble without flux adjustments is possible and because partly this study is concerned with the deep ocean processes such as the thermohaline circulation, which can be adversely affected by flux adjustments (Marotzke and Stone, 1995). This decision does mean more processing power must be expended in spin-up to achieve a stable surface climate.

To create the flux adjustment field for the model, the model's surface conditions are compared to a climatology.

$$\mathrm{F}_{applied} = \mathrm{F}_{model} - \beta_{HANEY}(\mathrm{SST}_{model} - \mathrm{SST}_{climatology}) \tag{2.9}$$

The strength of this comparison is controlled by the Haney relaxation coefficient, $\beta_{HANEY}$. A weaker coefficient allows the model to vary further from the climatology. It will a have large influence in the initial state of the model, because of its importance in determining the flux adjustments. The Haney parameter, $\beta_{HANEY}$, can be thought of as an equivalent relaxation timescale,

$$\tau = \frac{\rho_{water} c_p d}{\beta_{HANEY}} \tag{2.10}$$

where $\rho_{water}$ is the density of water, $c_p$ is the heat capacity of seawater, and $d$ is a depth for the surface waters. The standard value, 163 $\mathrm{Wm}^{-2\circ}\mathrm{C}^{-1}$, is equivalent to 1 week with depth of 25m. No observational range of uncertainty exists for this parameter, because it is a modelling construct. The range in table 2.8 represents a timescale from 2 days to a fortnight as these timescales have been used in global modelling studies (although timescales of a month or more have been used in regional models).

## 2.8 Advection

The numerical scheme used to perform the advection is a structural aspect of the model. There are two available numerical methods for tracer advection in HadCM3: the second order centred difference scheme and the third order QUICK method. Using a fourth order advection scheme has also been suggested, and has been incorporated into a more advanced ocean model at the Hadley Centre. The advection process is divided into a horizontal and vertical component for both salinity and temperature. Changing the advection scheme would lead to interesting numerical changes, but these could also be problematic by causing the model to be numerically unstable. There is a also chance that changing the advection scheme could mean that it is impossible for the coupled system to have an equilibrium state.

| **Water Type** | **R** | $\zeta_1$**m** | $\zeta_2$**m** |
|---|---|---|---|
| Type IA | 0.62 | $\frac{5}{3}$ | $\frac{1}{20}$ |
| Type IB | 0.67 | 1 | $\frac{1}{17}$ |
| Type II | 0.77 | $\frac{2}{3}$ | $\frac{1}{14}$ |

**Table 2.5** *Water Type parameters determined by Paulson and Simpson (1977)*

The advection scheme used in the model is an example of the structural uncertainty in a model, and this thesis is concerned with ocean *model* uncertainty. Hence, advection will not be included in the study.

## 2.9 Solar radiation

The amount of solar radiation penetrating into the ocean is a driver for the mixed layer, through both the Large and Kraus-Turner schemes (see sections 2.5.4 and 2.5.5 respectively). This is dependent on the water colour (modified through biology for example). The different types of water were classified by Jerlov (1968), ranging from clear (type I) to a much murkier colour (type III). HadCM3 assumes that sea water is the same type all over the globe, and that the incoming solar only arrives at short or long wavelengths. A set of three parameters are used to represent this solar penetration: the depth penetration of red light, $\zeta_1$; the depth penetration of blue light, $\zeta_2$ and the ratio of the amount of incident solar radiation at red wavelengths to blue wavelengths, $R$. Paulson and Simpson (1977) determined the values for these parameters from observational studies of the different water types (see Table 2.5). A spatial distribution of the different types was determined by Simonot and le Treut (1986) - type III water exists primarily in sub polar regions, and type I water only in the tropical Pacific. HadCM3 uses water type IB, although a similar area of the globe is type IA and type II (Simonot and le Treut, 1986). Therefore these are the suggested perturbations.

### 2.9.1 Implementation of water type changes in HadCM3

HadCM3's atmospheric radiation code divides the radiation into shortwave (200nm-689nm) and longwave (689nm-5000nm). These definitions are different from the red and blue light definitions used by Paulson and Simpson (1977) to calculate the parameter settings in table 2.5. To compound the problem, the shortwave radiation is input into ocean as visible light, whilst the longwave is transferred as heat (the majority of longwave radiation is infra-red). The settings for type IB water in HadCM3 are therefore thought to be $R = 0$ and $\zeta_2 = 1/17m$, on the assumption that any red light does not penetrate far enough to be of consequence (note that $\zeta_1$ is irrelevant when $R = 0$).

However this is only an approximation. The ocean carbon cycle model has been found to be sensitive to the light penetration (Palmer and Totterdell, 2001). Changes were implemented to improve the accuracy of the light penetration into the ocean carbon cycle model. Different settings have been also proposed by Storkey (2001) for the ocean forecasting model, because of its much higher vertical resolution. It is felt the impact on the ocean circulation of these changes will not be significant as the variations in water type. To implement the water type changes, $\zeta_2$ should be changed to the values in the right-hand column in table 2.5 and $R$ should be kept as zero.

## 2.10 Summary

This chapter describes a database of ocean parameters in HadCM3 and HadCM3L along with their uncertainty ranges. The parameters and their ranges have been described individually in previous sections, and now need to be combined together. The most succinct method of summarising this chapter is to collate all the information into a series of tables.

A brief description of the most important parameterisations in HadCM3 and HadCM3L can be found in table 2.6. The parameters within those schemes are shown in 2.7. Table 2.8 lists the parameters

| **Physical Process** | **Description/Process Affected** | **Author** |
|---|---|---|
| Horizontal Eddy Viscosity | Currents | |
| Isopycnal Diffusion | Tracers on Isopycnals | Griffies *et al*. (1998) |
| Sub Grid Scale Stirring | Eddies in baroclinic instability | Gent and McWilliams (1990) |
| Spatial Eddy Variations | Varies coefficients in eddy scheme | Visbeck *et al*. (1997) |
| K-Theory Vertical Mixing | Vertical tracer profile | Pacanowski and Philander (1981) |
| Adjusted K-Theory Mixing | Vertical tracer profile at low $Ri$ | Peters *et al*. (1988) |
| Boundary Layer | Computes a fluid boundary layer | Large *et al*. (1994) |
| Quadratic Boundary Layer | Modifies the surface currents | Large *et al*. (1994) |
| Mixed Layer | Creates bulk mixed tracer layer | Kraus and Turner (1967) |
| Marginal Sea Outflow | North Atlantic salinity and THC | Gordon *et al*. (2000) |

**Table 2.6** *A list of the important parameterisations in the ocean component of HadCM3 and HadCM3L*

in HadCM3 and gives the uncertainty range for them. The first column of this table gives an idea of the magnitude of the expected effects on climate change of implementing the perturbations by assigning them each a priority. Table 2.9 is the equivalent table for HadCM3L. There are 3 high priority parameters to perturb. They are the same for both HadCM3 and HadCM3L

| Description | Scheme Involved In | Parameter Name |
|---|---|---|
| Momentum Diffusivity | Horizontal Eddy Viscosity | $\nu_H$ |
| Tracer Diffusivity | Isopycnal Diffusion | $K_I$ |
| Constant thickness diffusivity | SGS Stirring | $K_{THK}$ |
| Coefficient of thickness diffusivity dependence on Richardson No. | Visbeck Eddy Scheme | $\alpha_{VIS}$ |
| Background thickness diffusivity | Visbeck Eddy Scheme | $K_{THK,bg}$ |
| Coefficient of viscosity dependence on Richardson No. | K-Theory Vertical Mixing | $\nu_{V,0}$ |
| Background viscosity | K-Theory Vertical Mixing | $\nu_{V,bg}$ |
| Background diffusivity (depth dependent) | K-Theory Vertical Mixing | $K_{V,bg}$ |
| Critical Richardson No. to define bottom of boundary layer | Boundary Layer | $Ri_{CRIT}$ |
| Maximum boundary layer depth | Boundary Layer | $D_{max}$ |
| Windstress Scaling | Kraus Turner Mixed Layer | $\lambda$, $\delta$ |
| Energy for deep ocean convection | Kraus Turner Mixed Layer | $\epsilon$ |
| Strength of coupling to climatology | Flux adjustment values | $\beta_{HANEY}$ |
| Water Colour | Penetration of solar radiation | Water Type |

**Table 2.7** *A description of the parameters contained in the database.*

| HadCM3 | | | | | |
|---|---|---|---|---|---|
| *Priority* | **Parameter** (units) | **Low** | **Intermediate/ Switch Options** | **High** | **Sect.** |
| m | $\nu_{\mathbf{H}}$ ($m^2s^{-1}$) | 1000 | 2000 | **3000** | 2.4.1 |
| h | $\mathbf{K_I}$ ($m^2s^{-1}$) | 200 | **1000** | 2000 | 2.4.2 |
| l | $\alpha_{\mathbf{VIS}}$($m^2s^{-1}$) | 0.010 | **0.015** | 0.020 | 2.4.3 |
| m | $\mathbf{K_{THK,bg}}$($m^2s^{-1}$) | 0.0 | 150 | **350** | 2.4.3 |
| *l* | ***K-Theory Vertical Mixing*** | | ***Norm.****/Adj.** | | *2.5.1 / 2.5.2* |
| m | $\nu_{\mathbf{V,0}}$ ($\times 10^{-3}m^2s^{-1}$) | 3.0 | **5.5** | 8.0 | 2.5.1 |
| m | $\nu_{\mathbf{V,bg}}$ ($\times 10^{-5}m^2s^{-1}$) | 0.5 | **1.0** | 8.0 | 2.5.1 |
| h | $\mathbf{K_{V,bg}}$ ($\times 10^{-5}m^2s^{-1}$) | $0.5-4$ | $\mathbf{1.0-15}$ | $2-50$ | 2.5.3 |
| *l* | ***Boundary Layer*** | | ***Quad.****/full*† | | *2.5.4* |
| l | $\mathbf{Ri_{CRIT}}$ (dimensionless) | 0.25 | 0.3 | **0.5** | 2.5.4 |
| l | $\mathbf{D_{max}}$ (m) | 60 | **80** | 100 | 2.5.4 |
| h | $\lambda$, $\delta$ (fraction,m)* | 0.3, 100 | 0.5, 50 | **0.7, 100** | 2.5.5 |
| l | $\epsilon$ (fraction)* | 0.13 | **0.15** | 0.17 | 2.5.5 |
| *l* | ***Marginal Sea Outflow*** | | ***Diff.****/Adv.*‡ | | *2.6* |
| l | $\beta_{\mathbf{HANEY}}$ ($Wm^{-2\circ}C^{-1}$) | 81 (2 dy) | 163 (1wk) | 572 (2 wk) | 2.7 |
| m | **Water Type** | II | IB | IA | 2.9 |

*"Norm." means the Pacanowski and Philander (1981) scheme is being used, "Adj." refers to adjustment proposed by Peters *et al*. (1988). †When the "full" scheme is used as opposed to the quadratic approximation the mixed layer scheme should not be applied. ‡Either a diffusive scheme or an advective scheme will be used.

**Table 2.8** ***HadCM3 parameter database with uncertainty ranges*** *- those in italics are logical switches. For continuously varying parameters, the upper and lower bounds are shown, as well as an intermediate value. For switches, the two options available are shown. The standard value is highlighted in bold font. The section which describes the perturbation is shown in the column labelled* ***Sect.*** *An indication of the expected importance of the different perturbations is provided by the priority column: h = high priority, m = medium priority, l = low priority.*

| HadCM3L | | | | | |
|---|---|---|---|---|---|
| *Priority* | **Parameter** (units) | **Low** | **Intermediate/ Switch Options** | **High** | **Sect.** |
| h | $\mathbf{K_I}$ ($m^2s^{-1}$) | 200 | **1000** | 2000 | 2.4.2 |
| l | $\mathbf{K_{THK}}$ ($m^2s^{-1}$) | 350 | 675 | **1000** | 2.4.3 |
| *m* | ***Visbeck Scheme*** | | *On*/***Off**** | | *2.4.3* |
| *l* | ***K-Theory Vertical Mixing*** | | ***Norm.***/*Adj.*† | | *2.5.1 / 2.5.2* |
| m | $\nu_{\mathbf{V,0}}$ ($\times 10^{-3} m^2s^{-1}$) | 3.0 | **5.5** | 8.0 | 2.5.1 |
| m | $\nu_{\mathbf{V,bg}}$ ($\times 10^{-5} m^2s^{-1}$) | 0.5 | **1.0** | 8.0 | 2.5.1 |
| h | $\mathbf{K_{V,bg}}$ ($\times 10^{-5} m^2s^{-1}$) | $0.5-4$ | $\mathbf{1.0-15}$ | $2-50$ | 2.5.3 |
| *m* | ***Boundary Layer*** | | ***Quad.***/*full*** | | *2.5.4* |
| l | $\mathbf{Ri_{CRIT}}$ (dimensionless) | 0.25 | 0.3 | **0.5** | 2.5.4 |
| l | $\mathbf{D_{max}}$ (m) | 60 | **80** | 100 | 2.5.4 |
| h | $\lambda$, $\delta$ (fraction, m)** | 0.3, 100 | 0.5, 50 | **0.7, 100** | 2.5.5 |
| l | $\epsilon$ (fraction)** | 0.13 | **0.15** | 0.17 | 2.5.5 |
| *l* | ***Marginal Sea Outflow*** | | *Diff.*/***Adv.***‡ | | *2.6* |
| l | $\beta_{\mathbf{HANEY}}$ ($Wm^{-2\circ}C^{-1}$) | 81 (2days) | 163 (1wk) | 572 (2wk) | 2.7 |
| m | **Water Type** | II | IB | IA | 2.9 |

*When "off" means Gent and McWilliams (1990) is being used and when applied uses HadCM3 standard values (see table 2.8). †"Norm." means the Pacanowski and Philander (1981) scheme is being used, "Adj." refers to adjustment proposed by Peters *et al*. (1988). ** When the "full" scheme is used as opposed to the quadratic approximation the mixed layer scheme cannot be applied. ‡Either a diffusive scheme or an advective scheme will be used.

**Table 2.9** ***HadCM3L parameter database with uncertainty ranges*** *- those in italics are logical switches. For continuously varying parameters, the upper and lower bounds are shown, as well as an intermediate value. For switches, the two options available are shown. The standard value is highlighted in bold font. The section that describes the perturbation is shown in the column labelled* ***Sect.****. An indication of the expected importance of the different perturbations is provided by the priority column: h = high priority, m = medium priority, l= low priority.*

# CHAPTER 3

# The effects of oceanic perturbations on the control climate

## 3.1 Introduction

The previous chapter investigated the plausible ranges for different parameters in the ocean model of HadCM3 and HadCM3L. These ranges are the extreme values each of the parameters over which the parameterisation is still a reasonable representation of the physics involved. Just presenting a range of parameter values does not show the impact of that uncertainty. There is some knowledge of the probable impacts of each parameter perturbation. This knowledge has been used to provide a prioritisation of the parameter perturbations. The changes to the three high-priority parameters are expected, by the experts consulted, to have the largest effects to the time-dependent response to an increase $CO_2$ in both models.

A perturbed ocean physics ensemble has been created to sample the ocean model uncertainty. It has been created by perturbing the highest priority parameters to the extreme values of their uncertainty range. Section 3.2 goes into the ensemble design in further detail. Each ensemble member has a 500 year "spin up" followed by an 80 year "control" run - both with constant preindustrial levels of $CO_2$. Section 3.3 describes the spin ups and the rest of the chapter describes the long term preindustrial climates as seen in the control runs. A model version that is not able to accurately replicate current climate could be expected to provide an inaccurate projection of future climate change. Thus section 3.4 presents a comparison of each ensemble member to climate observations.

An analysis of the ensemble spread in the control runs is equivalent to an analysis of the effects of

| Run Name | Isopycnal Diffusivity ($m^2s^{-1}$) | Vertical Background Diffusivity ($\times 10^{-5} m^2 s^{-1}$) | Mixed Layer (ratio,m) |
|---|---|---|---|
| STD | 1000 | 1.0-15 | $\lambda$=0.7, $\delta$=100 |
| LowISO | **200** | 1.0-15 | $\lambda$=0.7, $\delta$=100 |
| HighISO | **2000** | 1.0-15 | $\lambda$=0.7, $\delta$=100 |
| MedLAM | 1000 | 1.0-15 | **$\lambda$=0.5, $\delta$=50** |
| LowLAM | 1000 | 1.0-15 | **$\lambda$=0.3, $\delta$=100** |
| LowVDIFF | 1000 | $\mathbf{0.5-4}$ | $\lambda$=0.7, $\delta$=100 |
| HighVDIFF | 1000 | $\mathbf{2.0-50}$ | $\lambda$=0.7, $\delta$=100 |

**Table 3.1** *The perturbed ocean physics model versions. The non-standard parameter values are shown in bold font.*

ocean model uncertainty on the long term preindustrial state of the climate system. The work will be primarily devoted to understanding the spatial patterns of uncertainty in the surface temperature, but will also include depth profiles and climate indices such as the thermohaline circulation.

## 3.2 Ensemble design

An ensemble of model versions with perturbed ocean physics parameterisations is needed to investigate the uncertainty of the ocean model physics. Such an ensemble has been created using the high priority perturbations determined in chapter 2. The ensemble consists of seven members; six versions of HadCM3 with a single physics perturbation and a version of HadCM3 with the standard parameter settings. The values of the ocean parameters for each model version are shown in table 3.1.

The ensemble has been created by Malcolm MacVean using the ECWMF supercomputer for the Met. Office's QUMP project. Flux adjustments were not used in the ensemble, although they would guarantee a preindustrial climate similar to observations. There were two reasons for not using them. Firstly, they are not physical and could introduce further errors. Secondly, it was unknown whether an unflux-adjusted ensemble would produce stable ensemble members. It can now be categorically stated that it does. Section 2.7 involves a further discussion of flux adjustments. This decision means that a large amount of time has to be invested in letting the models approach their equilibria. A spin up period

of 500 years was chosen from investigation of the standard model, after which the model is deemed to be in quasi-equilibrium. The behaviour of the model versions as they approach their equilibria is discussed in section 3.3.

The lack of flux adjustments may result in the model climatology drifting to an unrealistic state. This means that each model version must be verified as having a realistic climate state before its acceptance into the ensemble. This verification is performed through a comparison of the model version's preindustrial climate to observations. This is covered in section 3.4 and will conclude that every model version provides a similarly plausible representation of the current climate.

This does not mean that the control states of the model versions are identical, just that no ensemble members can be ruled out as being unduly unrealistic, which for these purposes shall be defined as having mean biases that are significantly larger than that of the standard model. The rest of the chapter is devoted to looking at the spread across the ensemble in the control runs and hence the effect of model uncertainty on the equilibrium climate state.

## 3.3 Approach to model equilibrium

All of the model versions were started from the observed and analysed global ocean temperatures and salinities of Levitus and Boyer (1994) , the sea ice distribution from Rayner *et al*. (2003) and a state of no motion. To get appropriate initial mixed layer depths, monthly mean fields are used rather than annual averages. Data for September was used as opposed to any other month, because it is the month with the least changes in sea ice (being minimum in the Northern Hemisphere and the maximum in the Southern Hemisphere).

Each model version was run for 500 years, after which it was deemed "spun up". Some residual climate drift can still be seen in the 80 year control run. However the computing resources required to reach an actual equilibrium, should one even exist, are too prohibitive. This residual drift is less than

the changes caused by an increase in $CO_2$ that will be shown in next chapter.

Figure 3.1 shows the evolution throughout the spin up and control run of the 1.5m surface air temperature, top of the atmosphere (TOA) net flux imbalance and change in ocean heat content (change in energy of the ocean per $m^2$ of its surface). It can be seen that there is an initial positive TOA flux imbalance for every model version. This is because the atmosphere starting state is taken from the end of the multi-millenial integration of HadCM3 performed by Gordon *et al*. (2000) and described in more depth by Collins *et al*. (2001). This integration does not include an interactive sulphur cycle, whilst all the model versions presented here include the parameterisation of Jones *et al*. (2001). This parameterisation interactively calculates the concentrations of natural sulphate aerosols and then advects those aerosols around to create varying spatial fields. The sulphur cycle used in Gordon *et al*. (2000) has specified spatially varying aerosol distributions that are constant in time. One of the features of these specified distributions is a difference between the amount of aerosol over the land and ocean. The ratio of these amounts was a parameter tuned during model development, so that HadCM3 reached a radiative balance. By introducing the interactive scheme, this radiative balance is broken and a new balance must be found. The reason for including the interactive sulphur scheme in the model is for intercomparison reasons: Collins *et al*. (2006) included the scheme (and perturbed parameters in it). As we intend to compare our results for ocean model uncertainty to the results for atmosphere model uncertainty (determined by Collins *et al*. (2006) from an experiment of similar design) it seems consistent to use the same AOGCM. They found that inclusion of the interactive sulphur cycle leads to a TOA heat flux imbalance of approximately 1.5 $Wm^{-2}$. This value is similar to the initial TOA flux imbalance seen in the ocean ensemble presented here.

The initial positive TOA flux imbalance causes an increase in the global mean temperature and the ocean heat content from the start of the integration. The majority of the surface temperature warming occurs in the first 100 years, however the increase in ocean heat content is still occuring after 500 years. The drift in heat content at the start of the integration is comparable with the increase caused

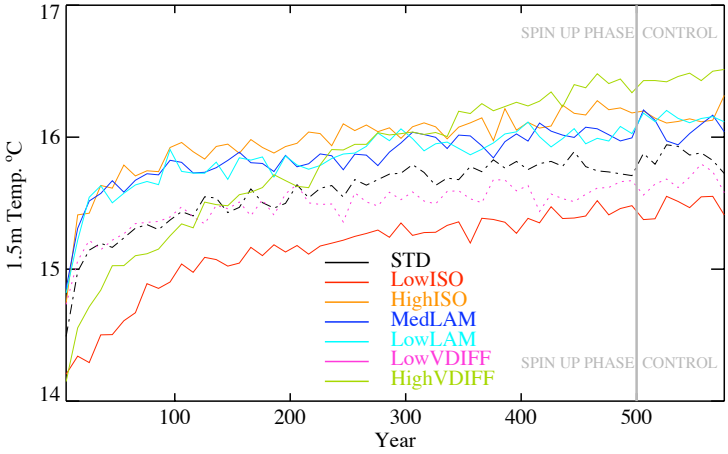


(a)

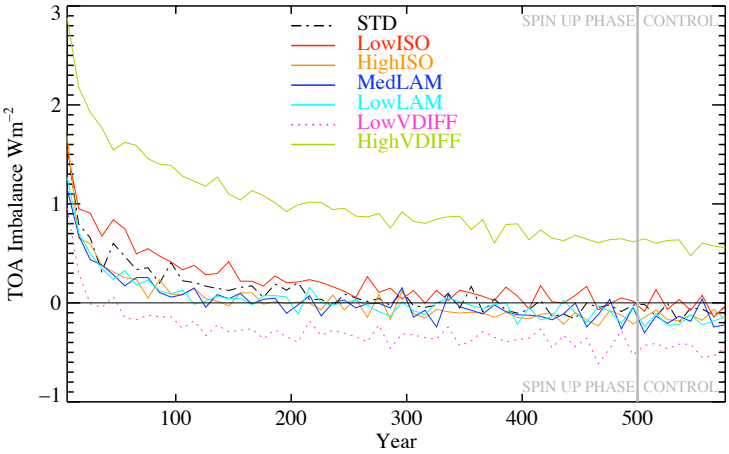


(b)

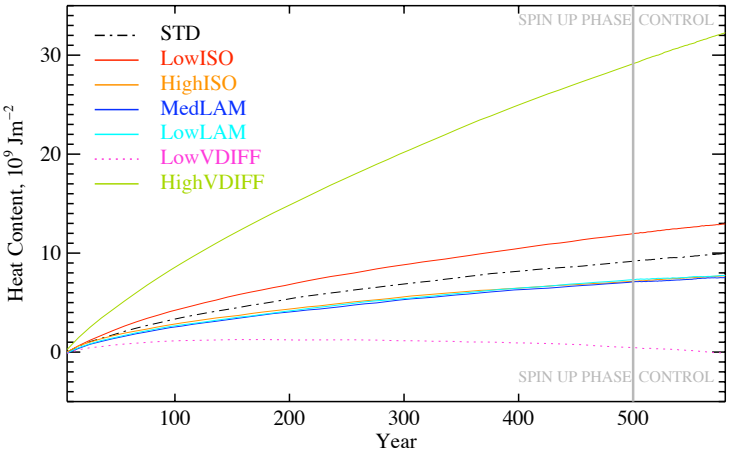


(c)

**Figure 3.1** *Timeseries of the model spin up. (a) shows the global mean 1.5m air temperature for each model version, (b) shows the top of the atmosphere flux imbalance, and (c) shows the change in global mean ocean heat content from Levitus and Boyer (1994). HighISO,MedLAM and LowLAM are all overlaid on (c). The grey bar indicates the boundary between the spin up period (years 1-500) and the control run (years 501-580).*

by the increasing $CO_2$ content for every model version showing that a spin up is essential. This is the case for surface temperature as well. It can also be seen in fig. 3.1 that the model versions do not have the same control climates. The global mean 1.5m air temperature differs by approximately 1°C. The ocean heat content varies by $30 \times 10^{10}$ $Jm^{-2}$, which is approximately equal to 10 times the increase in heat content seen during the increasing $CO_2$ experiment.

### 3.3.1 Depth variation of the climate drift

The global mean heat content is directly proportional to the depth integral of the temperature change, so the fact that the heat content is still drifting whilst the surface temperature seems settled implies that there is a depth variation of the climate drift. Changes in surface temperature do not travel instantaneously throughout the ocean, and can take hundreds of years to percolate to the deepest regions of the ocean. Figure 3.2 shows the drift in the heat content of each model level throughout the control phase of the experiment for each model version (calculated using a linear regression onto the annual heat content timeseries).

It can be seen from fig. 3.2 that the top five model levels (the mixed layer, which is approximately the top 50m) shows small drifts in the heat content. The drift increases below this layer, as the thermocline sinks from the observed state (all the model versions have a deeper global mean thermocline, shown in figure 3.3). HighVDIFF has large drifts throughout the deep ocean, whilst most of the model versions do not exhibit large drifts below 2000m. It can be seen from this figure that the drift in the surface climate is much smaller than the drifts at depth.

## 3.4 Model validation

The previous section has shown that the model versions do not have the same control climate. This implies some possible problems. No observations exist about the future evolution of the climate

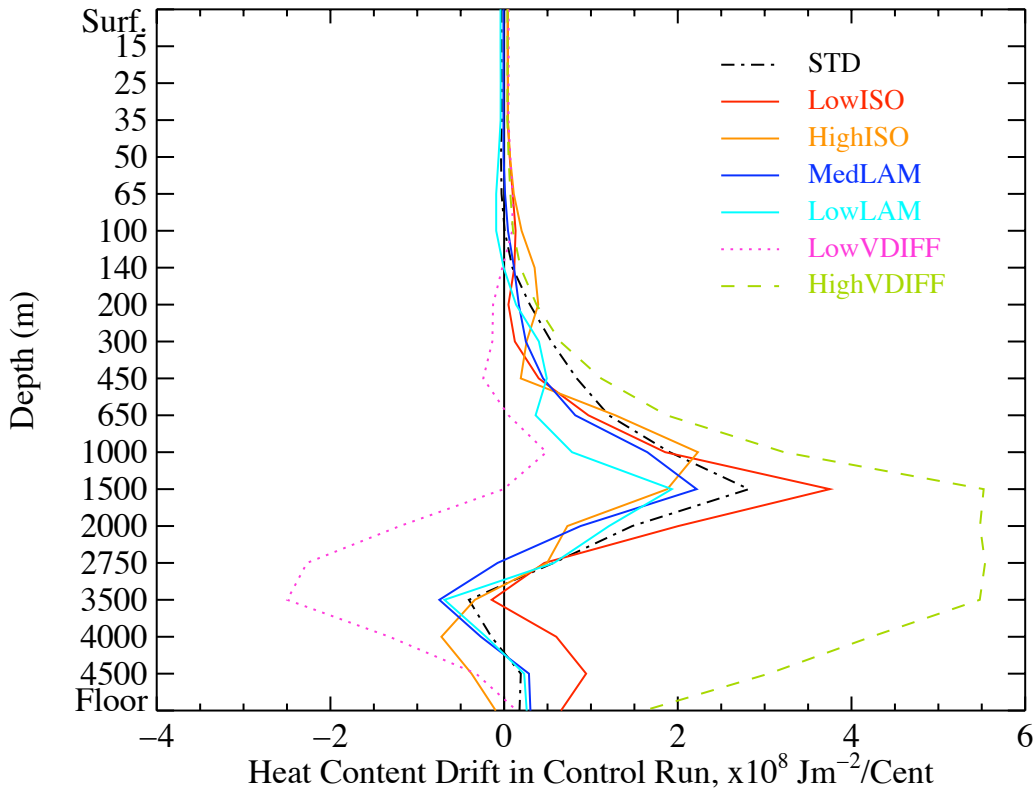


**Figure 3.2** *The climate drift in the control run of each model version. The vertical coordinate is uniform in model level, although the respective depths are shown. The drifts shown are calculated as the slope of the line of best fit of the heat content timeseries.*

system (hence the interest in creating climate projections). This lack of observations means that the accuracy of a model's projection must be verified in other ways. The main method of verification is by comparison of a model's simulation of the current climate state to observations. Model evaluation is so important that the IPCC's most recent assessment report devotes 54 pages to it (McAvaney *et al.*, 2001), compared to 57 pages presenting the global results of climate projections (Cubasch *et al.*, 2001).

The square root of the global mean squared error (rms error) is a simple and effective method of quantifying the difference between a model global field and observations of that field, and is calculated by:

$$RMS\ Error = \sqrt{\langle \left( [Model]_{501}^{580} - Obs \right)^2 \rangle_{global}} \tag{3.1}$$

where $\langle Field \rangle_{global}$ means the global mean of the $Field$. $[Model]_{501}^{580}$ is a spatially varying time

| Dataset | Variable | Resolution | Reference |
|---|---|---|---|
| Legates-Willmott | Surface Air Temperature | 0.5°x 0.5° | Legates and Willmott (1990) |
| CRU | Surface Air Temperature | 5°x 5° | Jones *et al*. (1999) |
| CMAP | Precipitation | 2.5°x 2.5° | Xie and Arkin (1996) |
| HadSLP2 | Mean Sea Level Pressure | 5°x 5° | Allan and Ansell (2006) |
| ERA-15 | Mean Sea Level Pressure | 2.5°x 2.5° | Gibson *et al*. (1999) |
| ERBE | Outgoing longwave radiation | 5°x 5° | Barkstrom (1984) |
| ERBE | Net Top of the Atmosphere Flux | 5°x 5° | Barkstrom (1984) |
| HadISST | Sea Surface Temperature | 1°x 1° | Rayner *et al*. (2003) |
| Levitus | Sea Surface Temperature | 1°x 1° | Levitus and Boyer (1994) |
| Levitus | Sea Surface Salinity | 1°x 1° | Levitus and Boyer (1994) |
| Levitus | Ocean Potential Temp., $\theta$ | 1°x 1° | Levitus and Boyer (1994) |
| Levitus | Ocean Salinities | 1°x 1° | Levitus and Boyer (1994) |

**Table 3.2** *The observational datasets used for the model evaluation.*

average over the 80 years of the control run. A selection of datasets for various climate variables were used for the model evaluation. The datasets are shown in table 3.2, along with their resolution. The observed datasets are not on the same grid as the model. Therefore, it has been necessary to interpolate onto the larger grid before the rms error can be calculated. This interpolation will introduce some small inaccuracies, but these are unavoidable. The control integrations are performed with preindustrial levels of $CO_2$, but accurate observations of this period do not exist: present day observations are used instead. Table 3.3 show the rms errors between the model version and observations.

If it is assumed that the standard model version provides a realistic simulation of the current climate, then any "similar" model version should also give a realistic simulation. The assumption that the standard model version provides a realistic simulation is a reasonable one to make, because the model (HadCM3, both with and without the interactive sulphur cycle) has been often used for climate experiments, and extensive knowledge of its biases exists (e.g. McAvaney *et al*. (2001) and Collins *et al*. (2001)). However defining "similar" is difficult: there are many different measures of error and the rms error is only one possible example. The rms error can be thought of as a distance between the model simulation and the observations in a many dimensional phase space. A similar rms error implies that a model is a similar distance from the observations. A simple definition of "similar" would be that the difference in the error between a model version and the standard model version is an order

| Variable | Source | STD | Low Iso | High Iso | Med LAM | Low LAM | Low Vdiff | High Vdiff |
|---|---|---|---|---|---|---|---|---|
| 1.5m temperature (°C) | CRU | 2.54 | 2.32 | 2.78 | 2.72 | 2.77 | 2.46 | 3.03 |
| 1.5m temperature (°C) | Legates Willmott | 3.83 | 3.66 | 3.97 | 3.90 | 3.92 | 3.74 | 4.15 |
| Precipitation ($mm/day$) | CMAP | 1.60 | 1.62 | 1.60 | 1.49 | 1.50 | 1.68 | 1.50 |
| Surface Pressure ($Pa$) | ERA 15 | 411 | 413 | 411 | 414 | 411 | 418 | 407 |
| Surface Pressure ($Pa$) | HadSLP2 | 435 | 436 | 436 | 437 | 435 | 440 | 430 |
| Outgoing Longwave ($W/m^2$) | ERBE | 13.4 | 13.1 | 13.7 | 13.6 | 13.6 | 13.4 | 13.7 |
| Net TOA Flux ($W/m^2$) | ERBE | 12.4 | 12.5 | 12.4 | 12.1 | 12.1 | 13.0 | 11.4 |
| Sea Surface Temperature (°C) | HadISST2.1 | 3.05 | 2.93 | 33.18 | 3.15 | 3.17 | 3.00 | 3.34 |
| Sea Surface Temperature (°C) | Levitus | 2.03 | 1.86 | 2.20 | 2.16 | 2.19 | 1.94 | 2.41 |
| Sea Surface Salinity ($PSU$) | Levitus | 2.21 | 2.33 | 2.13 | 2.27 | 2.27 | 2.44 | 2.07 |
| Ocean $\theta$ (°C) | Levitus | 1.22 | 1.37 | 1.18 | 1.17 | 1.18 | 1.19 | 2.05 |
| Ocean Salinity ($PSU$) | Levitus | 0.47 | 0.49 | 0.45 | 0.49 | 0.49 | 0.51 | 0.43 |

**Table 3.3** *Global root mean squared errors between an 80 year average for each model version and observations for selected variables. The observations are detailed in table 3.2.*

of magnitude less than the errors in the standard model version. Table 3.4 investigates this for each perturbed model version, by showing the fractional root mean squared error,

$$Fractional\ RMS\ Error = \frac{\sqrt{\langle [Pert_i]_{501}^{580} - [STD]_{501}^{580} \rangle_{global}}}{\sqrt{\langle [STD]_{501}^{580} - Obs \rangle_{global}}} \tag{3.2}$$

where $Pert_i$ is the perturbed model version and $STD$ is the standard model version.

The fractional differences in the atmospheric variables are within an order of magnitude of the standard model for all the model versions, except HighVDIFF's surface air temperature if the CRU observations are used. Therefore the atmosphere model climates are all similar, implying all the model versions should be accepted into the ensemble. This is not the case for ocean temperatures (although it is true for the salinities). HighVDIFF has a sea-surface temperature field that (like the surface air temperature) is not similar if one dataset is used, but is classified as similar with another dataset. The ocean potential temperatures for HighVDIFF are different from the STD model version, as is LowISO.

The depth profiles of the different model versions are shown in figure 3.3, along with the Levitus and

| Observed Dataset | LowISO | HighISO | MedLAM | LowLAM | LowVDIFF | HighVDIFF |
|---|---|---|---|---|---|---|
| Legates-Willmott | -0.05 | 0.03 | 0.02 | 0.02 | -0.03 | 0.08 |
| CRU | -0.09 | 0.09 | 0.07 | 0.09 | -0.03 | **0.19** |
| CMAP | 0.01 | 0.00 | -0.07 | -0.06 | 0.05 | -0.06 |
| ERA 15 | 0.00 | 0.00 | 0.00 | -0.00 | 0.02 | -0.01 |
| HadSLP2 | 0.00 | -0.00 | -0.00 | -0.00 | 0.00 | -0.00 |
| ERBE - OLR | -0.02 | 0.02 | 0.02 | 0.02 | 0.00 | 0.02 |
| ERBE - TOA | 0.00 | -0.00 | -0.03 | -0.02 | 0.05 | -0.08 |
| HadISST | -0.04 | 0.04 | 0.03 | 0.04 | -0.02 | 0.09 |
| Levitus - SST | -0.09 | 0.08 | 0.05 | 0.07 | -0.05 | **0.16** |
| Levitus - SSS | 0.05 | -0.04 | 0.03 | 0.03 | 0.10 | -0.06 |
| Levitus - $\theta$ | **0.12** | -0.04 | -0.04 | -0.04 | -0.02 | **0.68** |
| Levitus - sal. | 0.03 | -0.05 | 0.03 | 0.03 | 0.08 | 0.10 |

**Table 3.4** *The fractional root mean squared error as computed from equation 3.2. The values shown are the difference due to the perturbation, normalised by the error of the standard model. The values shown in bold are those where the difference between the perturbed model and the standard model is greater than 10% of the error of the standard model.*

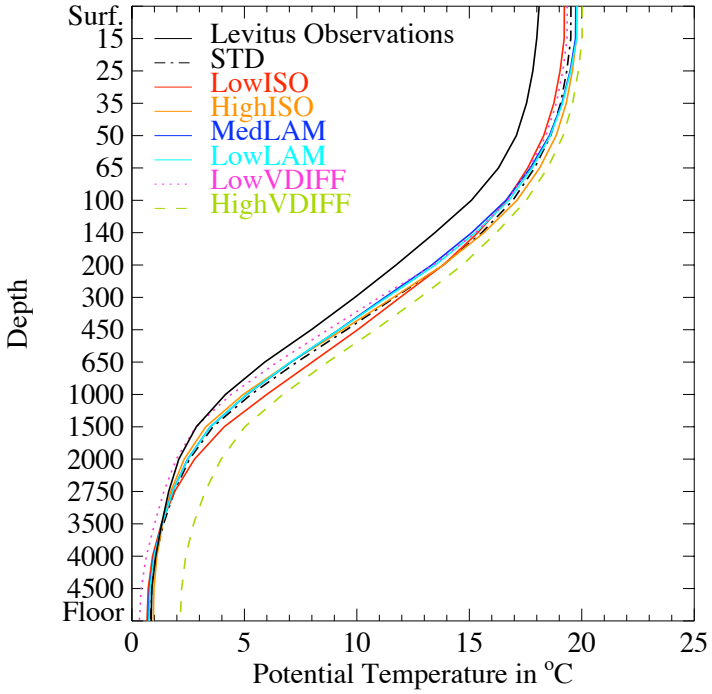


**Figure 3.3** *The global average potential temperature for each model level in the ocean. The values shown are the mean of all 80 years in the control, for each model version. The solid black line shows the Levitus and Boyer (1994) observations interpolated on the same vertical grid.*

Boyer (1994) observations. It can be seen that the top 50m of the ocean is similarly inaccurate in each model version compared to the observations. However in the deep ocean most model versions agree more or less with the observations. The exception to this is HighVDIFF. The rms error values

have been weighted according to the volume encompassed, so the errors of the four lowest levels are equal in weight to the other 16. Unfortunately, the deep ocean is the region were the uncertainties in the observations are largest and the sampling used to create the observational climatology may cause some errors (Gregory *et al*., 2004b). This means that the relative distance of the temperature errors in HighVDIFF might not be as large, as implied by this analysis.

### 3.4.1 Conclusions from the model evaluation

One test of whether a model will produce a plausible future climate projection is whether that model has a plausible representation of the current climate state. Investigating whether AOGCMs have plausible current climate states is a large research field, with many possible metrics to answer the question. That sort of investigation is not the main subject of this thesis. It is necessary that unrealistic model versions do not get included in the investigation of the ensemble spread, because it could give an inflated impression of the amount of uncertainty in climate projections. A simple test has been devised to investigate if a model version has a plausible current climate state. It starts from the assumption that the standard model has such a state. Any model version with differences from STD that are an order of magnitude less than that of STD from the observations are considered to be similar to STD, and therefore also have a plausible control climate state. All of the model versions have a surface climate that is similar by this definition for all tested variables (at least according to one observed dataset). However, the interior of the ocean in both LowISO and HighVDIFF are not similar.

The rest of this thesis assumes that all the model versions are equally plausible, because they all have similar surface climates. There is little evidence to either support or contradict this assumption, and in fact there are many different suggestions as to the important aspects of the climate system that must be modelled correctly. Murphy *et al*. (2004) have proposed a "climate prediction index" that quantifies the similarity of a modelled climate to observations. It has been designed to weight different models when creating a probability distribution function. This ensemble has only seven members, so the

creation of a probability distribution function is not feasible. That it has been assumed that all the model versions are equally probable, should be taken into consideration in all of the future work.

Some of the work relating to the transient climate response (which will be presented in the next chapter) has been presented by Collins *et al*. (2007). This paper also introduces some further AOGCM integrations to investigate the validity of this assumption. HighVDIFF has been replicated with flux adjustments to maintain a base climate that is closer to observations. Although the additional flux adjustments did change the transient climate response of HighVDIFF, it did not change the qualitative conclusions from the research.

Although this is true for the surface climates, it may not be a valid conclusion for analysis involving the deep ocean (Collins *et al*. (2007) analyse no ocean interior quantities). Both HighVDIFF and LowISO do not have ocean interiors that are similar to the standard model's. However the same assumption - that they are both plausible representations of the observed climate system - is made for the resulting analysis. This assumption was only made after the analysis of the surface temperature changes showed that ensemble spread is small. This was partly made to make the thesis self-consistent, and partly made because an exaggerated ensemble spread should be easier to detect, and hence easier to determine from whence it had arisen. As all the model versions are to be considered equal members of the ensemble, they shall henceforth be referred to as "ensemble members".

## 3.5 Ensemble spread in the preindustrial climate due to ocean model uncertainty

The perturbations to the ocean physics parameterisations effect the long term preindustrial climate of HadCM3. The previous section presented a comparison between the climates of the different ensemble members and observations of the real world. It concluded that all ensemble members are plausible representations of the real climate. The ensemble members are not identical though. The differences

between them arise from ocean model uncertainty. Analysis of the ensemble spread is therefore a quantification of the effects of ocean model uncertainty. Such an analysis may also hint at the role of ocean physics in determining the preindustrial climate.

An example of the different preindustrial climates is shown in figure 3.4. The ensemble mean sea surface temperature (SST) is shown as the top left panel; the other panels show the deviations of each ensemble member from the ensemble mean. Green indicates a small, but detectable change. The black contour is the zero line, showing the sign of these small changes. An area is only coloured if its change is "detectable" from modelled internal variability, and therefore an actual effect of ocean model uncertainty. This detection will be discussed in more detail in the following section.

Figure 3.4 shows that the differences between the SST of the standard model version and the ensemble mean are small, and mainly negative. This implies that that the effect of the perturbations is roughly symmetric around the standard model (see section 3.5.5). The impacts of reducing isopycnal diffusivity are larger than increasing it, but seem to have a similar spatial pattern. The SST differences from perturbations to the vertical diffusivity have similar patterns, to each other and to the spatial pattern of the effects of perturbing isopycnal diffusivity. These patterns are strikingly close to those of the ensemble spread that will be shown in figure 3.7. The largest changes are occuring in the Southern Ocean and the North Atlantic, and tongues spread equatorwards along the eastern boundary. The two mixed layer perturbations do not show the same SST pattern as the other perturbations. They are both changes in the same direction, because both perturbations are improvements on the standard mixed layer parameterisation. The spatial patterns are similar, but not identical. Both mixed layer perturbations are lacking the large changes in the Southern Ocean seen in the other perturbations. MedLAM has stronger changes near the equator than LowLAM .

Looking at a combination of 8 panels of SST patterns is not a convenient method of investigating the ensemble spread. Therefore, all of the panels will be condensed into a single diagnostic for each variable. These figures show the range across the ensemble at each grid point, and will be used

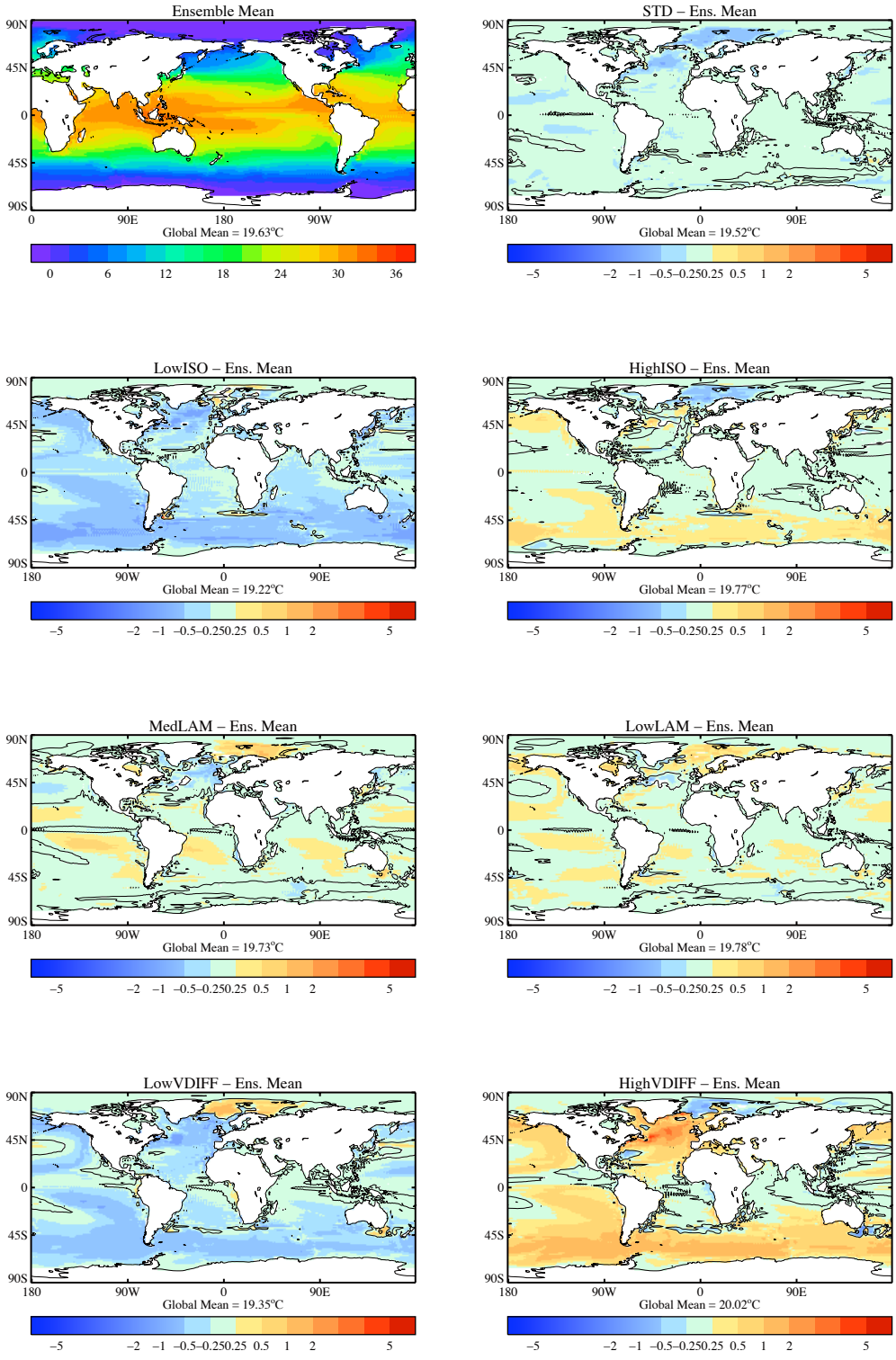


**Figure 3.4** *Preindustrial sea surface temperature patterns. The top left panel shows the ensemble mean pattern; the other panels are the difference between a single ensemble member and the ensemble mean. An area is only shaded if it is significantly different from the deviations expected by internal variations at the 5% level. The black contour shows a deviation of 0. The modelled internal variability can be seen in figure 3.5.*

extensively throughout the rest of this chapter and in chapter 5. The range is taken as the diagnostic of the ensemble spread, because the design of the ensemble samples the maximum effects of ocean model uncertainty (see section 4.4.2 for further discussion of this point). It is important to remember that even if the 7 ensemble members had the same preindustrial climate state, there would be some ensemble spread due to the system's internal variability. Only a spread which is larger than the internal variability can be said to be caused by the ocean model uncertainty.

### 3.5.1 Natural variability and significance

Each run of the same model may give different results even though the external factors are identical, because the non-linear nature of the climate system will create some internal variability. This internal variability is sometimes called natural variability, because the variations come about naturally and are not caused by anthropogenic activity. It is hard to determine the magnitude of internal variability at 80 year timescales from observations of the climate system, because the observational record does not stretch back far enough. However the internal variability of the model can be estimated by running the model for a long time period with no imposed changes.

A multi-thousand year integration of HadCM3 has been performed by the Hadley Centre to look at the internal variability of the model (Collins *et al.*, 2001). The data from this run is available from the British Atmospheric Data Centre (BADC) at www.badc.nerc.ac.uk. This integration does not include an interactive sulphur cycle. The final 500 year segment of this integration has been used to estimate the standard deviation of the modelled internal variability at an 80 year timescale for each gridpoint:

$$\sigma_{80yr} = \sqrt{\Sigma_{i=0,10,20...420} \frac{\left([x]_i^{i+80} - \overline{x}\right)^2}{n-1}} \tag{3.3}$$

where $x$ is the detrended variable (to account for any linear drifts which still exist in the integration), $\overline{x}$ is the average value for all 500 years, $\{x\}_i^{i+80}$ is the mean value of $x$ between the years $i$ and $i+80$. $n$ is the number of samples, 43 in this case. Figure 3.5 shows an example of this product: the standard deviation of modelled internal variability in sea surface temperature on 80 year timescales.

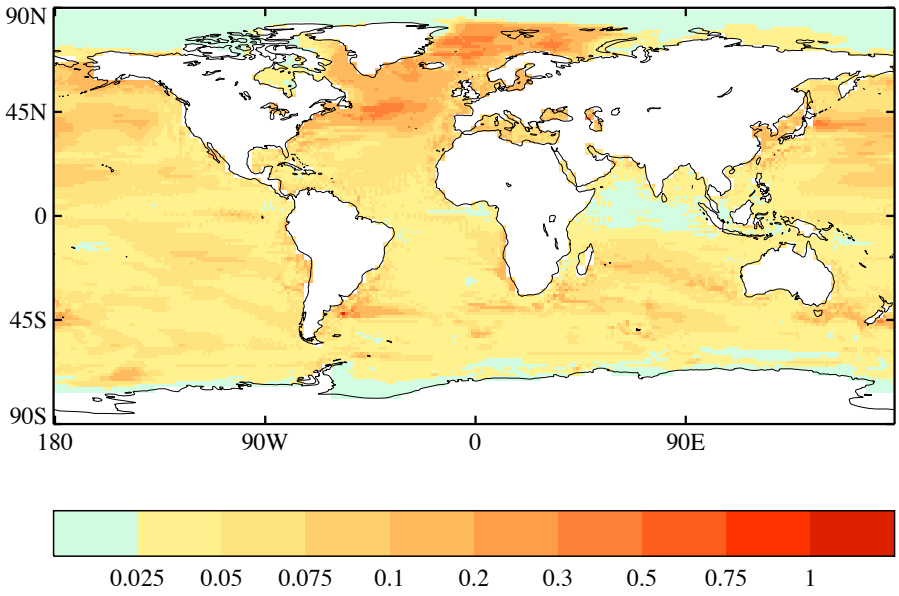


**Figure 3.5** *The standard deviation of modelled internal variability in the sea surface temperature on 80 year timescales (in °C) computed from a millenia long control run of HadCM3. Note the non-linear colour scale.*

The standard deviation of the ensemble can also be computed. An F-test can be used to test whether the standard deviations from two samples are likely to have come from the same population, at the 5% confidence interval. The spread of the ensemble can only be proved to be a consequence of the physics perturbations, if the spread is both larger in magnitude, and not drawn from the same population as the modelled internal variability. In the following analysis the spread is only shown where it fulfils these criteria (except where explicitly stated).

The multi-thousand year control integration was performed without an interactive sulphur cycle. This thesis assumes that this difference does not have an effect on the internal variability of HadCM3. This assumption can be simply tested by using an F-test as described above to determine whether the variances in global mean annual surface temperature for both STD and the control run are distinguishable.

They are not distinguishable at even the 50% significance level, leading to the conclusion that the assumption that the long control run without an interactive sulphur cycle is a fair source for estimates of modelled internal variability.

The F-test methodology is not appropriate to test whether the difference between individual ensemble members is likely to arisen from internal variability alone. In these instances, the modelled internal variability is assumed to be a Gaussian distribution with the standard deviation computed by equation 3.3. 95% of individual samples taken from this distribution will fall within 2 standard deviations of the mean value. Therefore if the difference between 2 ensemble members (or an ensemble member and the ensemble mean) is greater than 2 standard deviations of internal variability, then the difference is "detectable" at the 5% confidence level.

### 3.5.2 Ensemble spread in surface temperature and precipitation

Figure 3.6 shows the range of the 1.5m air temperature for each gridbox in the control climates. The majority of the world is detectably affected by ocean model uncertainty at the 5% confidence level. The largest ensemble spread in temperature occurs in the high latitudes and can be over 5°C. This spread occurs primarily over regions of strong vertical heat transfers within the ocean, but is probably also related to variations in the sea ice edge.

The ensemble spread in preindustrial surface air temperature is less over the land than the ocean, except for Antarctica. This is perhaps to be expected as perturbations were made only to the ocean rather than the atmosphere. Yet there is a greater area of the ocean where the ensemble spread is not detectable, than over the land. The detectable ensemble spread is a minimum in the equatorial regions of the oceans. The difference in the spread of the North Pacific storm track and the North Atlantic storm track region seems to imply that the ocean model uncertainty is not having large effects on the stormtracks, and that the large spread in the North Atlantic is associated with the large vertical ocean

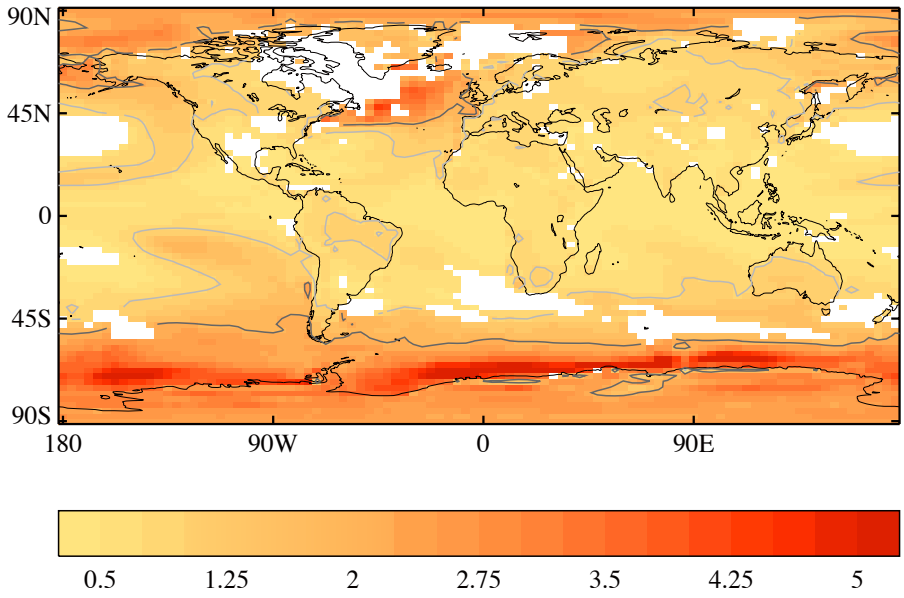


**Figure 3.6** *Ensemble spread in preindustrial surface air temperature. The ensemble spread is only shown if the standard deviation of the ensemble is significantly different to the standard deviation expected from internal variability. The light grey contour is at 1°C, and the black contour is at 2.5°C.*

heat transports in this region. Tongues of large ensemble spread extend equatorward along the eastern side of the ocean basins, although they are most obvious in the Pacific. The natural variability in the tropics is small in comparison to the high latitudes (fig. 3.5), so the numerically small ensemble spread in the tropics may also be important.

Figure 3.7 shows the ensemble spread of sea surface temperature. The spatial pattern is similar to that of the surface air temperature (which is unsurprising as they are in direct contact over the majority of the ocean). The internal variability in SST is half that seen in surface air temperature, so more of the spread is detectable in fig. 3.7, than in fig. 3.6. The tongues of larger spread in the eastern Pacific are again clearly visible. The spread in SST in the Southern Ocean is 25% less than in the surface air temperature. Sea ice forms a barrier that prevents close contact between the atmosphere

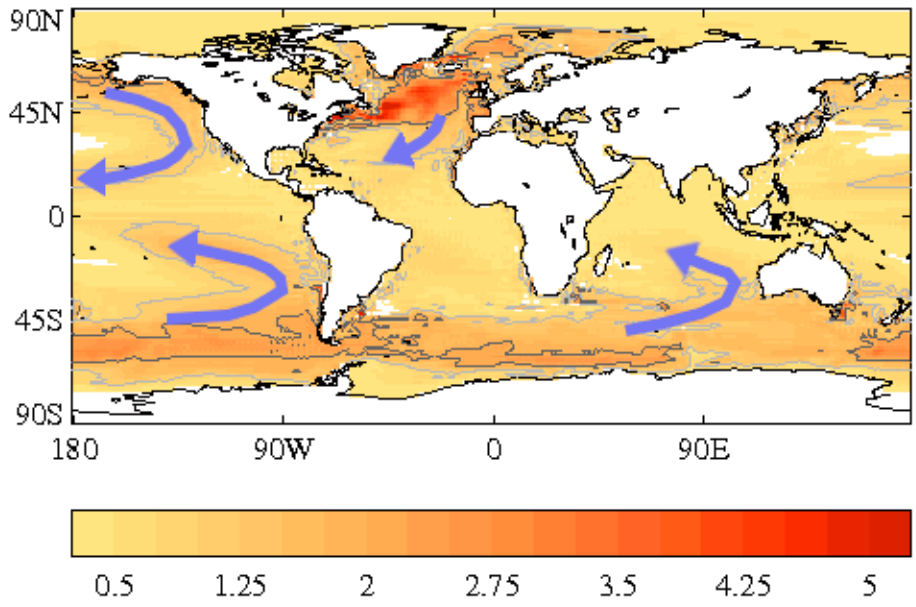


**Figure 3.7** *The range of the control mean sea surface temperature in the ensemble. The range is only shown if the standard deviation of the ensemble is significantly different to the standard deviation expected from internal variability. The light grey contour is at 1°C, and the black contour is at 2.5°C. The blue arrows indicate the tongues of uncertainty, which will be discussed in section 3.5.4.*

and the ocean, meaning that changes in the atmospheric temperatures are not communicated to the ocean surface. The smaller SST spread in the Arctic (compared to the surface air temperature) also occurs because of the sea ice cover (sea ice will be analysed in section 3.5.9).

The other main climate variable concentrated upon in climate change research is precipitation (e.g. in Cubasch *et al.* (2001)). Figure 3.8 shows the precipitation of the ensemble. The ensemble mean pattern is shown in panel (a) and is similar to the preindustrial pattern from standard HadCM3 (Pope *et al.*, 2000). The tongues of large uncertainty seen in the surface temperature relate to areas of low precipitation over the ocean. The ensemble spread is shown in panel (b) as a percentage change in the ensemble mean rainfall for that location.

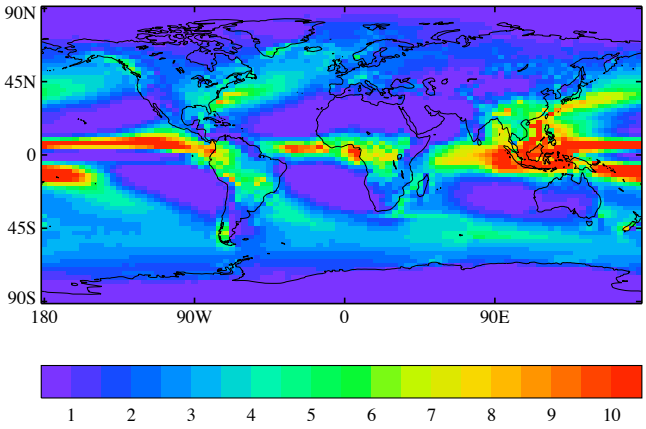


(a) Ensemble Mean Pattern

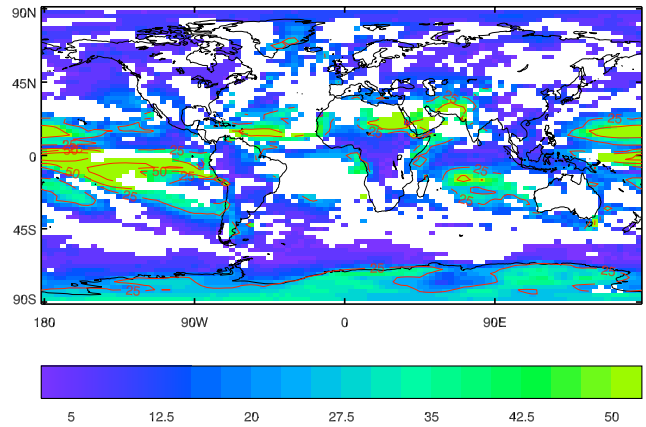


(b) Ensemble Spread

**Figure 3.8** *Precipitation in the ensemble. (a) is the ensemble mean precipitation pattern in mm per day. (b) is the ensemble range, and is expressed as a percentage of the ensemble mean precipitation. The red contours show a range of 25%, 50% and 100% of the ensemble mean pattern.*

There are many regions across the globe, where the ensemble spread in precipitation is not detectable from the modelled internal variability (these are the regions that are not coloured in fig.3.8(b)). However, there is detectable spread in the tropics, especially the Pacific. This spread seems to occur between the high precipitation areas (the inter-tropical convergence zones, ITCZs) and the low rainfall areas over the oceans. The ensemble spread in precipitation is probably related to uncertainty in the location and width of the ITCZs, which could be influenced by the warmth of the underlying sea-surface (Yao and Del Genio, 2002).

### 3.5.3 Uncertainty in the Southern Ocean and North Atlantic

The Southern Ocean and North Atlantic are the areas of the largest vertical heat transfers in the global ocean (Gregory, 2000) and the parameterisation of heat transfer has large impacts there (Guilyardi *et al.*, 2001). The primary role of the ocean in transient climate change is as a large heat sink. The perturbations chosen to form this ensemble are thought by the experts consulted, to regulate the vertical heat transfer and therefore determine the amount of heat that can be stored in the ocean. It is not a surprising result that the largest ensemble spread in temperature exists in the regions of the largest vertical heat transport. The magnitude of the ensemble spread (and therefore the effects of ocean model uncertainty) was not previously known, and has been shown to be up to 5°C in the North Atlantic and around the maximum sea-ice edge in the Southern Ocean.

### 3.5.4 Tongues of uncertainty

There is large surface temperature ensemble spread in the subtropical high pressures - identified in fig. 3.7 by blue arrows. The reason for these areas of uncertainty is not as obvious as the uncertainty in the regions of strong vertical heat transfer. There are several possible explanations for the uncertainty in these regions.

The eastern side of an ocean basin has a deeper mixed layer than elsewhere at the same latitude, due to the strong trade winds above it (de Boyer Montégut *et al.*, 2004). One of the physics perturbations in the ensemble is to the mixed layer parameterisation. This raises the possibility that the mixed layer parameters will effect the area, whilst the other perturbations will not. The recent figures looked at the spread of the ensemble, so the pattern could be a composite of different patterns from the different parameter perturbations. Another possible explanation is that the uncertainty in the surface temperature forms in the high latitudes and then is advected equatorwards in the subtropical gyre (see fig. 1.3 for a schematic of the ocean currents.).

This can be investigated by returning to the sea surface temperature changes shown by the individual ensemble members (figure 3.4). The mixed layer perturbations do show changes in equatorial regions without the large changes in the Southern Ocean seen in the other ensemble members. They do however both show ensemble spread upstream in the eastern boundary currents, which could be advected along into the tropical regions. It is important to remember that under advection spread does not need to gradually decay. Ensemble spread is not a conserved quantity and there can be regions of growth as well as decay. The decay of spread in the western side of the tropical ocean may not occur at the same rate that spread is being advected into the region, leading to a build up of spread. The largest temperature differences in the equatorwards currents occur in ensemble members with large changes at the high latitudes. It is therefore most probable that the large ensemble spread is caused by advection. A similar feature was found by Guilyardi *et al*. (2001). They also reached the conclusion that the feature was caused by advection from high latitudes.

### 3.5.5 Proportionality of perturbation effects on the sea surface temperatures

At the beginning of this section on the ensemble spread, it was shown in figure 3.4 that the effects of increasing the isopycnal and vertical diffusivities have a similar pattern, but an opposite sign to the effects from reducing the relevant diffusivity. It is interesting to investigate whether the effects of the

ocean perturbations are proportional. If the consequences of perturbations to a single parameter are non-proportional, then it might imply that there are non-proportional combinations between multiple parameter changes (such as seen by Stainforth *et al*. (2005)). The relationships can be tested using the global mean values. This is shown in figure 3.9 where the global mean SST changes are compared to the parameter perturbation. It seems as if both panels have a straight line relationship. However the sparsity of data points means it is impossible to disprove that a more complex relationship exists.

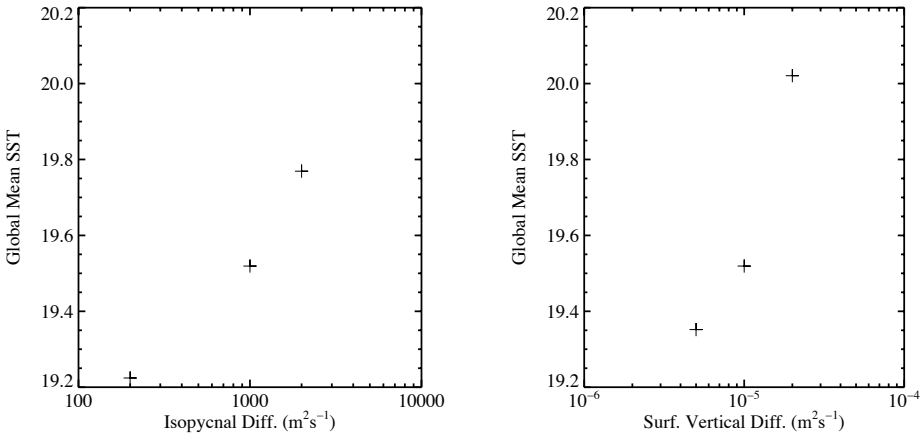


(a) (b)

**Figure 3.9** *The relationships between global mean sea surface temperature in the control run and (a) isopycnal diffusivity and (a) vertical diffusivity.*

To overcome the problem of the small amount of information, it is possible to investigate the proportionality of the spatial patterns of the effects of the perturbations. A proportionality ratio, $r_{prop}$, can be defined as the ratio of the effect of increasing the parameter by a defined proportion to the effect of decreasing the parameter by the same proportion,

$$r_{prop} = \frac{a+b}{2 \times STD} \times \frac{T(x,y)_{K=a} - T(x,y)_{K=STD}}{T(x,y)_{K=STD} - T(x,y)_{K=b}} \tag{3.4}$$

where $T(x,y)_{K=i}$ is the spatially varying field of the sea surface temperature averaged over the control run for ensemble member in which the respective diffusivity, $K$, takes the value, $i$. $r_{prop}$ is equal to unity if the effect of doubling $K$ is the same as the effect of halving it. A ratio greater than one means that the effect of increasing the diffusion is greater than the effect of reducing it.

Figure 3.10 shows the spatial distribution of the ratio of the effects of the positive and negative pertur-

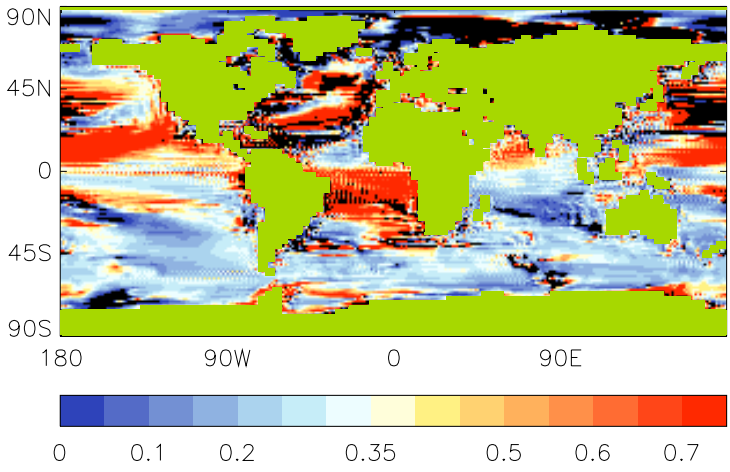


(a) Isopycnal Diffusivity - Ratio of Global Mean Values = 0.34

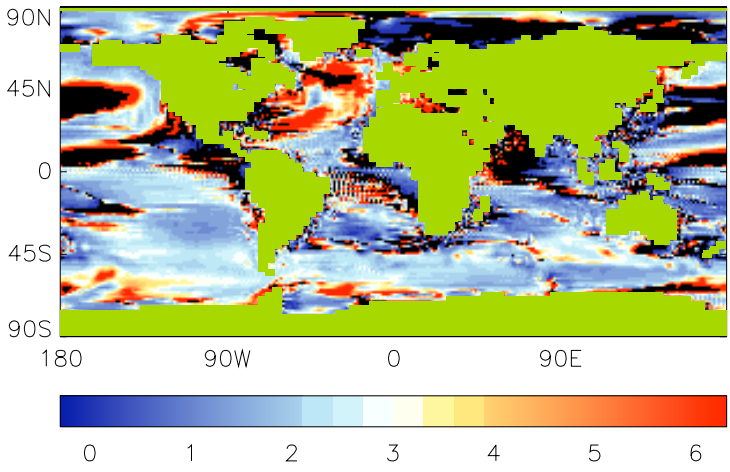


(b) Vertical Diffusivity - Ratio of Global Mean Values = 3.0

**Figure 3.10** *The proportionality ratio, $r_{prop}$, of the effects of changes in diffusivity as calculated by equation 3.4 for (a) isopycnal diffusivity and (a) vertical diffusivity. The ratios for the global mean effects are 0.34 and 3.0 respectively.The colour schemes are centred on these value, with red indicating that increasing the diffusivity has stronger effects than the global mean, and blue indicating that reducing the diffusivity has stronger effects. Black areas are those that have a negative ratio. This indicates that both increasing and reducing the diffusivity have the same effect. The land is shown in green.*

bations for both isopycnal diffusivity (a) and background vertical diffusivity (b). If there is complete proportionality then the ratio will be a globally constant value. It can be seen that this is not the case. The colour scales have been chosen so that they are centred on $r_{prop}$ for the global mean values pre-

sented in fig. 3.9 (0.34 and 3.0 for the isopycnal and vertical diffusivity respectively). A region is coloured black if the ratio is negative. This implies that the effects of both an increase and a reduction are in the same direction from STD, and so no proportionality can possibly exist.

It can be seen by the large variations in the colour in both fig. 3.10(a) and 3.10(b) that neither parameter has spatially uniform linear changes. Some regions of the globe show no proportionality, with both high and low values of diffusion causing similar changes in sea surface temperature.

### 3.5.6 Surface salinity changes

The previous sections have mainly concentrated on identifying and explaining the preindustrial surface temperature effects of ocean model uncertainty. It has been shown in figure 3.7 that there is ensemble spread in the preindustrial distribution of precipitation in the perturbed ocean physics ensemble. This spread, along with spread in the amount of surface evaporation (not presented in this thesis), combines to produce ensemble spread in the sea surface salinity (SSS). This is shown in figure 3.11.

The most striking difference between the effects on SSS and the effects on temperature is the fact that the largest SSS effects are not located in the Southern Ocean. The largest spread occurs in the Arctic ocean. The reason for this large spread is uncertain. It could be related to sea ice uncertainty through a processes such brine rejection (Weeks, 2001), however the lack of large spread in the Southern Ocean may refute this. There is ensemble spread underneath the tropical convection zones (namely the maritime continent, the Gulf of Guinea and the upwelling region off the coast of Ecuador). These regions exhibited small ensemble spread in precipitation as a percentage of the ensemble mean pattern (fig. 3.8b). As they are regions with large amounts of mean precipitation (fig. 3.8a), the small percentage spread must equate to a large absolute ensemble spread in precipitation compared to elsewhere on the globe.

There is large ensemble spread in SSS underneath the North Atlantic storm track. This region has the

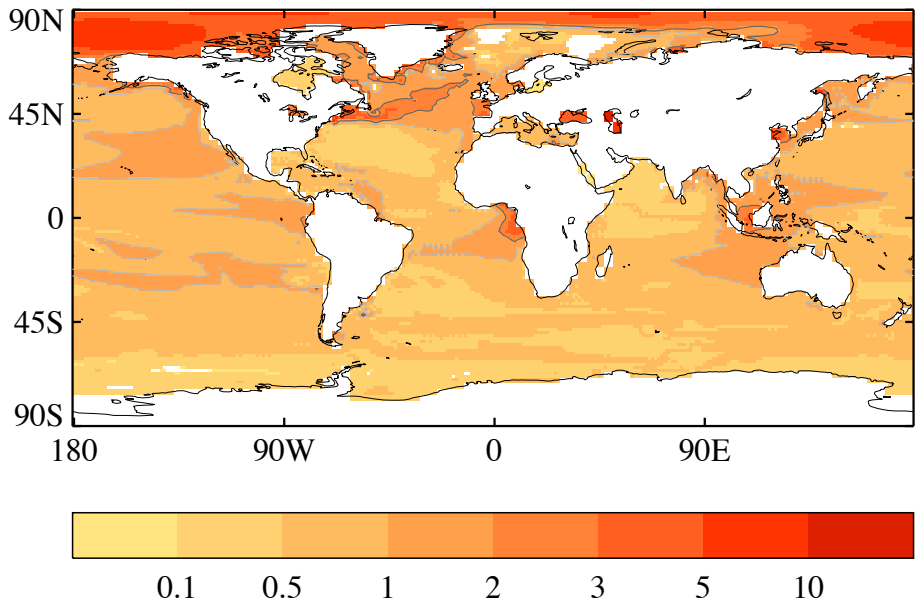


**Figure 3.11** *The ensemble range in sea surface salinity. The light grey contour shows a range of 1, and a dark grey contour shows a range of 2. Areas are only coloured if the ensemble variance is different from that expected from internal variability at the 5% confidence level.*

largest spread in SST (fig. 3.7), yet there is not detectable spread in precipitation over this region. The ensemble spread in SSS could come from a variety of sources. The spread in SST could indicate a large ensemble spread in evaporation over the region (warmer surface air can extract more moisture according to the Clausius-Clapeyron equation (Houghton, 2002)). There is a large amount of natural variability in precipitation in this area, so the ensemble spread in precipitation could be having detectable effects without being detectable itself. Finally, the spread in SST and SSS could both be caused by different strengths of northward flow along the western boundary. The area of large spread extends up to the Greenland-Iceland-Scotland ridge, meaning that the different strength flows may be associated with spread in the strength of the thermohaline circulation (which will be investigated in section 3.5.11).

### 3.5.7 Depth-varying changes

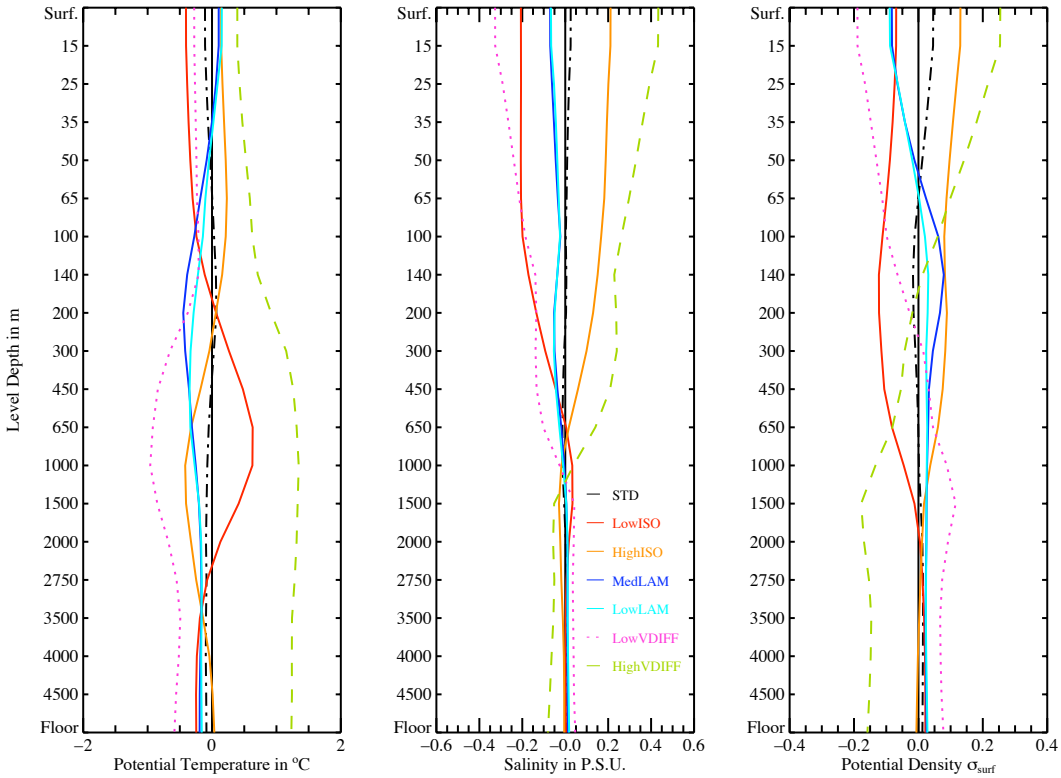


**Figure 3.12** *Global mean depth profiles. The left panel shows the depth variation of the potential temperature (also shown in fig. 3.3 compared to the observations of Levitus and Boyer (1994)). The middle panel shows the salinity profile in practical salinity units (PSU). The right panel shows how the changes in temperature and salinity combine to the effect the density profile of the ocean. Each profile is shown as deviations from the ensemble mean.*

There is ensemble spread in the preindustrial surface climate in the perturbed ocean physics ensemble. However, the perturbations were chosen to effect the vertical heat transfer of the model (chapter 2), and have been shown in section 3.4 to give different temperature profiles from those observed by Levitus and Boyer (1994). Figure 3.12 shows each ensemble member's global mean potential temperature profile, global mean salinity profile and global mean density profile as a deviation from the ensemble mean profiles.

It was noted in section 3.4 that the ensemble members were similarly inaccurate near the surface and that HighVDIFF was over 1°C warmer at depth. This is visible in fig. 3.12 as HighVDIFF's temperature anomalies diverge from the ensemble mean at roughly 300m. LowVDIFF diverges in a similar depth and at a similar rate, however the anomalies reduce near the ocean floor. This is consistent with

weaker vertical transports as the anomalies do not have time to travel so deep. The ensemble members that do not have perturbations to the vertical diffusivity all have some depth compensation occuring. This is not exact compensation as the thin, surface layers show smaller anomalies than those at some thicker, deeper layer. However, such patterns are consistent with a constrained surface heat input along with changes in the vertical heat transports, because the heat is residing in different levels of the ocean.

The anomalous salinity profiles are shown in the middle panel of fig. 3.12. The quantity of both salt and water in HadCM3 is almost constant (Gordon *et al*., 2000), so the profiles show exact compensation of salinity. The anomalies in the ocean interior are small in magnitude, but encompass a large volume of water. They also seem to be uniform at depths below 1500m. The 2 mixed layer perturbations cause nearly identical anomalies and the 2 lines are overlaid in this panel.

Potential temperature and salinity anomalies combine to form anomalies in the potential density. An increased salinity corresponds to denser water, whilst an increased temperature corresponds to lighter water. In the upper ocean for all four diffusivity perturbations, the changes in potential temperature and salinity are of the opposite sense. This partial density compensation probably occurs because the density is more constrained than either the temperature or the salinity changes, because water sinks or rises to its level of neutral buoyancy. A similar process does not occur for either temperature or salinity alone. The salinity changes always dominate in the final density anomaly in the upper ocean. The mixed layer perturbations do not show this density compensation in the top 4 layers of the ocean, but do show compensation to some degree below that. Interestingly the potential temperature anomalies dominate the salinity changes below 65m for the mixed layer perturbations. Only the vertical diffusivity perturbations change the potential density profile beneath 1000m, and therefore have a significant effect on the global mean density. This is through their large influence on the potential temperature profile at these depths.

### 3.5.8 Global mean heat transfers

The rate of potential temperature change from each parameterisation at each grid point in the ocean can be diagnosed from the model. These heating rates can be used to calculate a global mean vertical heat flux between model levels,

$$F(Z) = \rho c_p \left\langle \int_{-H}^{Z} \frac{d\theta}{dt} dz \right\rangle_{Globe} \tag{3.5}$$

where $\rho$ is the average density of sea water (taken to be 1026 kgm$^{-3}$), $c_p$ is the specific heat capacity of water at a constant pressure (3988 Jkg$^{-1}$°C$^{-1}$ in HadCM3), $\frac{d\theta}{dt}$ is the diagnosed heating rate (computed for each time step, but averaged over the 80 years of the control run), $\int_{-H}^{Z} dz$ is the vertical integral from the bottom of the ocean up to level $Z$ and $\langle\rangle_{Globe}$ means taking the horizontal average over the whole globe (Gregory, 2000). The global mean vertical heat fluxes derived in this manner for a selection of physical processes in the ocean model are shown in figure 3.13.

The ensemble mean heat balance is shown in the top left panel. Advection causes a downwards heat flux at all depths, as does vertical diffusion. This is expected as it has already been shown that the potential temperature of the ocean reduces with depth (figure 3.12). Any vertical circulation must advect the same amount of water upwards, as downwards, but the water travelling upwards will have a lower temperature, than the water sinking - leading to a net downwards heat flux on the global mean. The heat flux diffused vertically is proportional to the vertical temperature gradient, so must always lead to a net downwards flux, because the temperature is always colder below. In equilibrium, the net heat flux downwards must equal the net heat flux upwards. All of the ensemble members are close to equilibrium (compared to their starting conditions). The downwards heat flux from advection and vertical diffusion, must be balanced by an upwards heat flux from other processes: namely isopycnal diffusion, convection, mixed layer physics and the sub-grid-scale stirring parameterisation of Gent and McWilliams (1990). Combined these six processes determine the heat balance below the seasonally

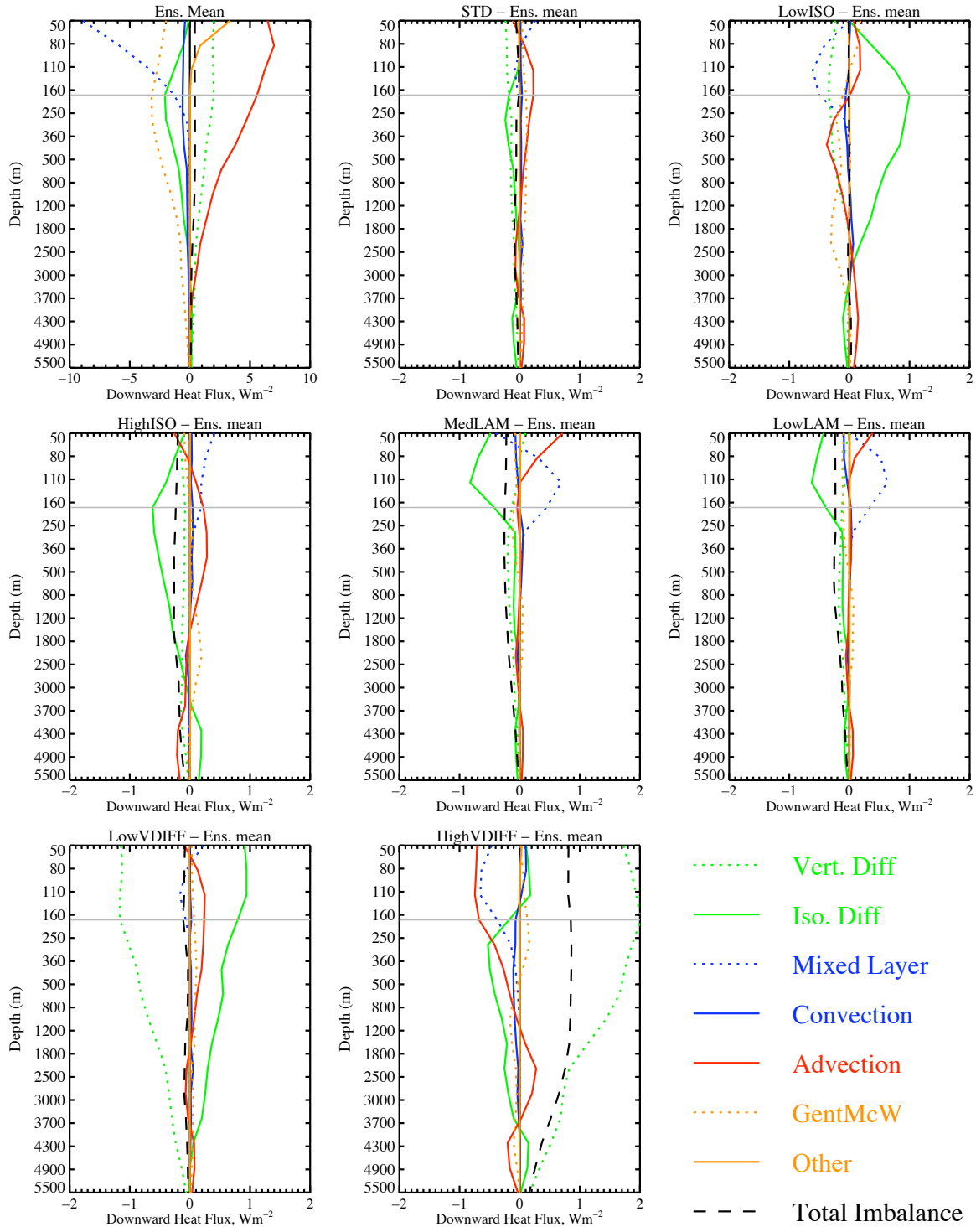


**Figure 3.13** *The global mean vertical heat flux from various processes ($Wm^{-2}$ of the world ocean). The top left panel shows the ensemble mean heat balance. The other panels show the difference in the heat balance for each ensemble member from the ensemble mean. The vertical axis is linear in model level, however some significant depths are shown. The key for each of the different lines is in the bottom right corner. The grey line indicates the boundary between the upper and lower ocean (Gregory, 2000)*

effected surface layer (defined as 160m in HadCM3 by Gregory (2000)). Other processes such as the penetration of solar radiation will effect the surface layers - they are included as "Other" on the figures. Isopycnal diffusion causes an upwards flux of heat, because of sloping of the isopycnals in high latitudes (solid green line; further explanation of this upwards heat flux and a schematic are presented in section 2.4). The largest cause of upwards vertical heat flux on the ensemble global mean is the parameterisation of sub-grid-scale eddy stirring devised by Gent and McWilliams (1990). This parameterisation diffuses the thickness of an isopycnal along the isopycnal. It therefore causes a net flow upwards, because of the slope of the isopycnals in the high latitudes (for reasons similar to the isopycnal diffusion itself). Convection occurs when cold, dense water sinks, and is replaced by warm water from depth. Although it causes large heat transfers locally, it only occurs infrequently and in limited locations, so causes a small effect on the global mean heat balance. The mixed layer parameterisation acts to bring heat up to the surface on the global mean. At times when the sea surface is warmer than the air above (e.g. winter), the ocean will lose heat from the sea surface to the atmosphere. This surface heat loss causes the surface water to become denser and sink being replaced by warmer water from deeper within the mixed layer. This mixing is what is being parameterised by the mixed layer scheme, and hence the net heat flux is upwards. The same balance of processes is maintained in every ensemble member, yet the perturbations do alter the heat transports of the individual processes.

The perturbations to the isopycnal diffusivity cause changes to the amount of heat transported vertically by the isopycnal diffusion parameterisation. This change in heat transport is balanced by different processes at different depths. The increase/reduction in the isopycnal diffused heat is compensated for by an increase/decrease in heat flux from the mixed layer scheme in the upper ocean (above the grey line,160m), then a decrease/increase in the heat flux downwards from advection down to 800m. The Gent and McWilliams (1990) scheme then compensates for it between 800m-2500m, with the advection compensating for any changes below that.

The mixed layer perturbations both reduce the heat loss from the mixed layer. This effect is maximised at a depth of 100m. The mixed layer only reaches such depths in the high latitudes (de Boyer Montégut *et al.*, 2004). This means that the majority of the heat loss at 100m from the mixed layer physics occurs in the high latitudes. However the mixed layer perturbations both reduce the depth of the mixed layer in the high latitudes, which must lead to a reduction in heat loss (i.e. an increase in downward heat flux) at these depths. The shallower mixed layer means that the isopycnals slope more than on the ensemble mean (the height of the top of the isopycnal slope has risen). This means that the reduction in mixed layer heat loss below 50m is compensated for by an increase in upwards heat transfer from the isopycnal diffusion.

Increasing or reducing the vertical diffusivity causes a corresponding change in the amount of heat being transported by the vertical diffusion parameterisation. These 2 perturbations cause the largest reorganisations of the heat transports. The climate drift in HighVDIFF (sec. 3.5.8) can be seen by the fact there is still a 1 $Wm^{-2}$ imbalance throughout the top 2000m, which reduces near the ocean floor. HighVDIFF has a top of the atmosphere imbalance of 0.6 $Wm^{-2}$ (see figure 3.1). This corresponds directly to the 0.8 $Wm^{-2}$ surface imbalance shown in figure 3.13, because fig. 3.13 is calculated as Watts per square metre of the ocean surface (rather than square metre of the Earth's surface). The ocean only covers 70% of the model's surface layer. The processes that attempt to balance out the vertical diffusion changes are not the same for the two perturbations. A reduction in vertical diffusivity is compensated for by an reduction in upwards heat flux from isopycnal diffusion throughout the column. This is probably because the interior waters, whose heat is being diffused upwards along the isopycnals, are colder because of the reduced heat diffused vertically into them in the interior. An increase in vertical diffusivity causes increased upwards isopycnal diffusion below 200m for a similar reason. Above 200m, there is an increase in the heat loss from the base of the mixed layer, as well as a reduced advection of heat downwards. These two changes are related to the changes in the temperature profile of HighVDIFF, seen in fig. 3.12. The temperature gradient in the thermocline has been reduced, because of the relative warming of the water at the bottom of the mixed layer to

that at the top. A reduced temperature gradient will result in less heat being transferred downwards by advection, if the global overturning circulation strength is kept constant. Warmer waters at the bottom of the mixed layer will allow more heat to be transported upwards by the turbulent mixing parameterised by the mixed layer scheme.

Analysis of the vertical heat transports from individual processes has shown that each of the parameter perturbations changes the vertical heat flux caused from its respective parameterisation. There are also compensating changes that occur to balance the imposed change in heat flux. The compensating changes have a simple explanation for both the vertical diffusivity and mixed layer perturbations. The changes in vertical diffusivity act to strengthen or weaken the vertical temperature gradient, which affects the heat flux from other process. The mixed layer perturbations cause shallower mixed layers in the high latitudes, leading to reduced heat loss from the mixed layer parameterisation. This is compensated for by an increase in isopycnal diffusion, caused by steeper sloping of the isopycnals in this region. The compensating changes for the isopycnal parameter perturbations occur from different sources at different depths and therefore can not be simply explained in a global mean sense.

### 3.5.9 Sea ice distributions

The largest ensemble spread in the surface air temperature occurs in the Southern Ocean and in the Arctic. It was stated that this is related to uncertainty in the sea ice distributions of the ensemble. The long term mean annual maximum and minimum sea ice extent for each ensemble member is shown in figure 3.14. The extent is calculated by creating a logical mask of sea ice coverage for each month. A gridpoint is considered ice-covered if the fractional coverage exceeds 0.15 (McAvaney *et al.*, 2001). The maximum and minimum were taken from these monthly masks (Flato and Participating CMIP Modelling Groups, 2004).

The maximum sea ice extent in the Arctic is similar for all the ensemble members, although High-

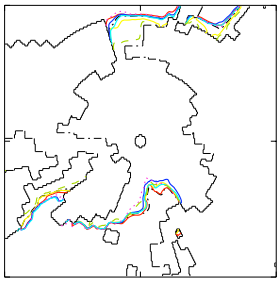

(a) Maximum - Arctic

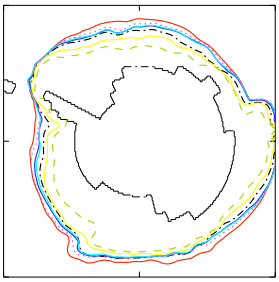

(b) Maximum - Antarctic

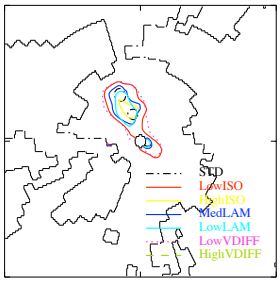


(c) Minimum - Arctic

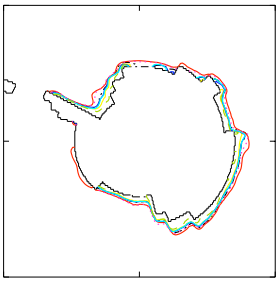

(d) Minimum - Antarctic

**Figure 3.14** *The long term mean annual maximum and minimum sea ice extent for each ensemble member.*

| Sea Ice Extent ($10^6 Km^2$) | STD | Low ISO | High ISO | Med LAM | Low LAM | Low VDIFF | High VDIFF | Obs. | Int. Var. |
|---|---|---|---|---|---|---|---|---|---|
| NH Maximum | 15.7 | 16.0 | 15.0 | 15.7 | 15.8 | 15.8 | 13.8 | 14.4 | 0.15 |
| NH Minimum | 0.2 | 1.4 | 0.2 | 0.6 | 0.4 | 1.7 | 0.0 | 7.7 | 0.11 |
| SH Maximum | 18.0 | 21.8 | 16.1 | 19.6 | 19.6 | 20.4 | 12.9 | 20.4 | 0.12 |
| SH Minimum | 2.2 | 3.3 | 1.7 | 2.0 | 2.0 | 2.8 | 1.0 | 3.8 | 0.04 |

**Table 3.5** *The maximum and minimum sea ice extents for Northern and Southern hemisphere. The observations are from a climatological (1961-1991) year from the HadISST data set (Rayner* et al.*, 2003). The modelled internal variability on 80 year timescales and from a millenial control integration of HadCM3 is also shown.*

VDIFF has less coverage in the Bering Sea. All the ensemble members show only a small amount of permanent sea ice in the Arctic: all are less than the observed minima. Table 3.5 gives the area covered by this sea ice extent. Most of the northern hemisphere minima are an order of magnitude less that the observed extent, and HighVDIFF shows complete summer melt. This is interesting as it shows especially high sensitivity of the summer sea ice to global warming (the annual global mean surface air temperature of HighVDIFF is only 2°C warmer than the observations of Legates and Willmott (1990)). Holland *et al*. (2006) find abrupt reductions in the summer sea ice occuring near this temperature rise in a set of transient climate projections. The long spin up period would have allowed any such abrupt changes to have occured, which may explain the apparent high sensitivity of the summer sea ice.

There are large differences within the ensemble in the maximum ice extent in the Southern Ocean. They occur directly underneath the area of large ensemble spread in surface air temperature, confirming the amplification of uncertainty in air temperature by the maximum sea ice extent.

### 3.5.10 Ensemble spread in the Antarctic circumpolar current

The ensemble spread in the maximum sea ice extent in the Southern Ocean could be related to changes of circulation in region. The Southern Ocean is dominated by the Antarctic Circumpolar Current (ACC), which circles the globe at 60°S. The strength of the ACC is commonly used in model evalua-

tion studies and ranges from 10-236 Sv in models included in the last IPCC report (McAvaney *et al.*, 2001). Observed estimates range from 123 Sv (Whitworth and Petersen, 1985) to 135 Sv Cunningham *et al.* (2003). The strength of the ACC has been found for all the ensemble members by calculating the volume transport across 69°W in the Drake Passage. The figures are shown in table 3.6, along with other climate indices.

| **Climate Index** | **STD** | **Low ISO** | **High ISO** | **Med LAM** | **Low LAM** | **Low VDIFF** | **High VDIFF** | **Obs.** | **Int. Var.** |
|---|---|---|---|---|---|---|---|---|---|
| Antarctic Cirumpolar Circulation (Sv) | 218 | 235 | 208 | 228 | 227 | 220 | 218 | 123-135 | 2 |
| Thermohaline Circulation (Sv) | 19 | 18 | 18 | 18 | 19 | 17 | 25 | 15-20 | 0.3 |
| Interannual var. of SAT (°C) | 0.14 | 0.14 | 0.13 | 0.17 | 0.15 | 0.14 | 0.12 | 0.12 | 0.02 |
| Decadal THC var. (Sv) | 0.8 | 0.5 | 0.5 | 0.5 | 0.4 | 0.5 | 0.7 | n/a | 0.2 |

**Table 3.6** *The value of selected climate indices across the ensemble. The method of calculation and the sources for the observed values are given in the relevant text. A standard deviation of the modelled internal variability (int. var.) of a long HadCM3 run is given, to allow assessment of the significance of the changes seen in the variables.*

Every ensemble member has a stronger ACC than observed, although there is no correlation between the ACC strength and the maximum ice extent. A stronger ACC has been shown to cause greater ocean heat uptake under an increasing $CO_2$ scenario, because it increases the amount of deep water being ventilated in the Southern Ocean (Russell *et al.*, 2006). Therefore the ocean heat uptake in the ensemble may be unrealistically large, and hence the ensemble spread may be unrealistic. However, the enhanced ACCs would act to enhance any ensemble spread, which will make any effects of ocean model uncertainty easier to detect.

### 3.5.11 Thermohaline circulation

The thermohaline circulation (THC) and its behaviour under climate change scenarios has been studied extensively since Stommel (1961) showed that it may have multiple stable equilibria, and that variations in the climate could change in which equilibrium the circulation resided. The long term

mean strength of the thermohaline circulation is shown in table 3.6. It is calculated as the maximum of the zonal mean meridional overturning in the North Atlantic. The thermohaline circulation has a large natural variability on interdecadal through to centennial timescales (Dong and Sutton (2005) and Vellinga and Wu (2004)). This complicates the determination of the mean state from observations. All of the ensemble members have THCs that are within observational estimates (Bryden *et al.*, 2005; Schmitz, 1996), except HighVDIFF which is a little strong (although even that is within the range found in other modelling studies (Gregory *et al.*, 2005a)).

Bryan (1987) showed that in a simple model the strength of the thermohaline circulation (THC) was proportional to the cube root of the vertical diffusivity. Although, the difference between the thermohaline strength of STD and HighVDIFF is approximately consistent with this relationship, the difference in THC strength between LowVDIFF and STD is not. Contrary to this view, Gregory (2000) proposed that the isopycnal diffusivity was the dominant factor in setting the strength of the thermohaline circulation, because of its control of the upward heat transfer in the Southern Ocean. This does not seem to the case either, as the 3 ensemble members with different values of isopycnal diffusivity have very similar THC strengths. Gnanadesikan (1999) suggested that the strength of the thickness diffusivity in the Gent and McWilliams (1990) scheme, is a driving factor in setting the strength of the thermohaline circulation. This parameter has not been perturbed in the ensemble: it is calculated depending on the local flow conditions (Visbeck *et al.*, 1997). Thorpe *et al.* (2001) show that the decadal strength of the THC in HadCM3 is proportional to the depth integrated meridional density gradient. The 80 year average THC strength in this ensemble does not show such a relationship, although this is could have been anticipated, because the perturbations are known to effect the thermohaline circulation.

All of above discussion concerns solely the strength of the THC, rather than the spatial characteristics of the circulation. The reason for this decision rests primarily on the fact that a similar analysis can not performed for the climate change signal. The ensemble mean spatial pattern climate change signal is shown in figure 5.11. It is barely detectable at depth (which is why fig. 5.11 does not incorporate

any significance testing). The uncertainty in this signal will therefore also be very hard to detect, and hence analyse.

### 3.5.12 Changes in internal variability from parameter perturbations

Changes in the long term mean state may not be the only effect of ocean model uncertainty - the internal variability could also be effected. Future work looking at the response of the model to an increase in $CO_2$ will require statistical testing, to determine if the observed changes could have arisen from internal variability. If the internal variability of each ensemble member is different, then this may be hard to perform. This section will investigate if there are any changes in modelled internal variability across the ensemble. It will concentrate on the global mean surface temperature and the thermohaline circulation, because both of these features will be investigated in detail later in this thesis.

McAvaney *et al*. (2001) contains an analysis of the global mean surface temperature variability of the CMIP models (Bell *et al*., 2000). The primary aim of the work of Bell *et al*. (2000) was to compare the modelled internal variability to that of observations. In this thesis, the aim is to investigate the effect of ocean model uncertainty on the modelled climate state; so a simpler analysis has been performed. The interannual standard deviations of the global mean surface air temperature for each ensemble member are presented in table 3.6. The "observed" value presented in table 3.6 is the standard deviation of the linearly detrended global mean surface temperature of Hansen *et al*. (1999). The internal variability is computed by sub-dividing the millenia-long HadCM3 control run in 80 year segments and then calculating the standard deviation of global mean surface temperature between them. An f-test could be used to determine whether the interannual variability of the ensemble member is significantly different from the standard ensemble member, however this test would not take account of the possible existence of long timescale variations in variability. Such long timescale variations exist in HadCM3 as shown by the modelled internal variability of the 80 year segments in the control run in table 3.6. The internal variability is different between the ensemble members, but only in the the case

of MedLAM is this difference greater than 1 standard deviation of long term variability away from STD. Even MedLAM is only $1\frac{1}{2}$ standard deviations away from STD, so these differences also can not be considered significant. The conclusion is that the ensemble does not show detectable effects of ocean model uncertainty on the interannual variability of the global mean surface temperature.

It has been shown that the parameter perturbations have an effect on the long term mean strength of the thermohaline circulation (THC). The THC is also known to have large decadal variability (Dong and Sutton, 2005). Observational estimates of this variability are hard to make, because of the short length of the observational record. The standard deviation of the decadal variability in each of the ensemble members is shown in table 3.6. It can be seen that the variability in STD is largest, however all the perturbations are within 2 standard deviations of the long timescale internal variability (from the HadCM3 millenia-long run). Therefore, it can not be verified that these variations are caused by the parameter perturbations.

The largest mode of internal variability in the climate system is the El Niño-Southern Oscillation (ENSO). It has a period of 3-7 years, and so a twenty year sample, so as will be used to calculate the climate change signal, would not provide reliable statistics of future ENSO. The aim of this thesis is to investigate the effects of ocean model uncertainty on time-dependent climate change. Therefore, the investigation of ENSO statistics in the control run (if there are any) cannot have an equivalent investigation under climate change, and so will not be included in this thesis.

## 3.6 Conclusions

The previous chapter presented a selection of possible parameters that could be perturbed in HadCM3 and gave a maximum and minimum plausible value for each parameter. The parameters were given a priority according to their expected effects on transient climate change. This chapter has presented a seven member ensemble that has been created to sample the ocean model uncertainty. This ensemble

contains 6 perturbed ensemble members in which the 3 high priority parameters to the maximum and minimum of their uncertainty ranges. The ensemble also contains an ensemble member with the standard parameter settings. These seven model versions have been spun-up for 500 years, after which the drift in the surface climate is small compared to the effects of increasing $CO_2$ by 1% per year.

Once a model version has been spun up, a further 80 years of integration of each model version has then been performed with preindustrial levels of $CO_2$ as a control run. A simple measure has been used to verify that each model version is able to realistically simulate the climate system, under the assumption that the standard HadCM3 is suitable for climate projections. Each model version has a plausible simulation of current climate, however some of the ocean temperatures of HighVDIFF are too high, and should be treated with caution in subsequent work. It is essential, that all ensemble members have plausible simulations of current climate, because it is a necessary, but not sufficient, condition for an accurate projection of future climate change. This model verification has shown that all the ensemble members are suitable to assess the effects of ocean model uncertainty on time-dependent climate change.

The ensemble spread in the control runs is a measure of the effects of ocean model uncertainty on the preindustrial climate state. The majority of this chapter has been devoted to the analysis of ensemble spread in the control run. This analysis has quantified the effects of ocean model uncertainty on the preindustrial climate state.

Ocean model uncertainty causes uncertainty in the surface air temperature that can be detected from natural variability across the majority of the globe (both over land and ocean). The largest uncertainty is in high latitudes and is amplified by interactions with the sea ice edge. The largest uncertainty in the sea surface temperature is greater than 2.5°C. This occurs in the Southern Ocean and North Atlantic. These are both regions of strong vertical heat transports. There are also “tongues” of uncertainty in the equatorward portion of the subtropical ocean gyres. The effect of individual perturbations to the climate state has been also been investigated. None of the parameters have a linear relationship in

the spatial pattern of surface temperature changes. There is also detectable ensemble spread in the precipitation and sea surface salinity that is caused by ocean model uncertainty.

Ocean model uncertainty has effects throughout the depth of the ocean. It affects both the global mean potential temperature and salinity profiles. The surface changes in potential temperature and salinity have opposite effects on the density of the mixed layer for all the perturbed diffusion parameters. None of the ensemble members show a vertically consistent change in density (i.e. an anomalously dense surface will have anomalously light water underneath it). These effects have been explained in terms of the major sources of vertical heat flux. All of the perturbed parameters impose a change in the individual parameterisation's vertical heat flux. These changes cause changes in the vertical heat flux from other process to restore the oceans vertical heat budget. A different compensating mechanism occurs for each parameter.

The ensemble spread in a variety of other climate variables has been investigated. There is uncertainty in both the sea ice extent and the Antarctic circumpolar current, although the variations are not correlated. An increase in vertical diffusion causes an increase in the strength of the thermohaline circulation, whilst the other perturbations do not have significant consequences. Ocean model uncertainty can not be shown to have effects on the interannual variability of either the global mean surface air temperature or the thermohaline circulation. This verifies that only a single measure of internal variability is required for statistical significance testing of the ensemble spread.

This chapter has documented the creation and evaluation of an ensemble that samples the ocean model uncertainty in time-dependent climate projections. Although it has looked at the effects of ocean model uncertainty on the preindustrial climate, the ensemble has not been created explicitly to sample the ocean model uncertainty in the quasi-equilibrium climate state. The next chapter will describe the results of a time-dependent climate change experiment: the purpose for which the ensemble described in this chapter has been created.

# CHAPTER 4

# Global mean ensemble properties under a doubling of $CO_2$

## 4.1 Introduction

The previous chapter describes an ensemble created to sample ocean model uncertainty. The ensemble consists of the standard set up of HadCM3 (Gordon *et al.*, 2000) and 6 members with perturbations to parameters involved in the parameterisations of the ocean physics. The perturbations are shown in table 3.1, and have an effect on the long term climate state of HadCM3 when no change in forcing has been imposed and with preindustrial levels of $CO_2$. The ensemble spread between these long term climate states represents the uncertainty in the preindustrial state caused by ocean model uncertainty. It has been explored in the previous chapter.

The climate of the real world does not reside in such a state, because there is always a changing external forcing being applied. This forcing of climate change could come from natural sources (e.g. changes in the incoming solar radiation and aerosol particles from volcanic eruptions) or from anthropogenic changes to the land surface or the chemical composition of the atmosphere. The large heat capacity of sea water and the slow ocean currents mean that the ocean plays an important role in determining the time-dependent response of the climate system to an imposed forcing. Ocean model uncertainty may lead to some uncertainty in the time-dependent response. The size of this uncertainty is not known. An idealised time dependent change in radiative forcing has been applied to the perturbed physics ensemble to quantify this uncertainty.

This chapter comprises a more detailed analysis of that contained in a paper that has been accepted to

be published by Journal of Climate as Collins *et al*. (2007). This paper also includes the results of some additional flux-adjusted model integrations, which will not be described in this thesis. The additional model integrations do not alter the conclusions given here, but rather confirms them by including an alternate version of HighVDIFF that has a more realistic simulation of the current climate. Inclusion of this flux-adjusted version of HighVDIFF, instead of the version of HighVDIFF presented here, further reduces the spread in the transient climate response. This paper also incorporates a discussion of possible alterations to the ocean convection scheme that could be made in an attempt to sample the uncertainty in implicit parameters in the physical parameterisations. A copy of this paper is included as appendix A.

This chapter will first describe the idealised forcing applied to the each model. There will then be a discussion of climate drifts and climate change, and methods to calculate them (section 4.3). The ensemble spread in the global mean temperature response caused by the physics perturbations will then investigated. This quantity will henceforth be known as the "signal spread" to differentiate it from the ensemble spread discussed in the previous chapter.

The signal spread will be compared to both the spread expected from internal variability and the signal spread found in other ensembles. The signal spread across the perturbed ocean physics ensemble is differentiable from internal variability (and so attributable to ocean model uncertainty), but less than that found in ensembles that sample atmospheric uncertainties. The rest of the chapter will discuss possible reasons for the smaller signal spread found in the perturbed ocean physics ensemble. There could be a compensation between different warming factors, which would act to reduce the signal spread. Measures of the strength of two warming factors will be introduced and their relative importance will be investigated.

## 4.2 The 1% per year scenario

A time-dependent climate change experiment has been performed for each ensemble member. An imposed radiative forcing is applied to the model by increasing the level of $CO_2$ in the atmosphere. The experiment consists of two 80 year model integrations: one in which the $CO_2$ increases incrementally by 1% every year and a control run where the $CO_2$ is kept at preindustrial levels. The control runs were the focus of the previous chapter. This scenario was performed by a selection of coupled climate models as the second phase of the Coupled Model Intercomparison Project (CMIP2, Meehl *et al.* (1997)). The amount of $CO_2$ in the atmosphere will reach twice the preindustrial level after 70 years. This rate of $CO_2$ increase is similar to the observed rate, and follows a "business as usual" scenario. The scenario is chosen partly because of its simplicity to apply, but more because it allows easier comparison to other model integrations and experiments.

## 4.3 Drifts and the climate change signal

The definition of a climate change is the "change between the initial state of the system and the state of the system subsequent to an imposed change in forcing". The climate system has internal variability around the true climate state. Two independent samples of the same climate state may have a different values, leading one to think that a change has occured. This internal variability can be thought of as unwanted "noise", which acts to disguise the change in the climate state (thought of as a "signal"). The only way to put a true value to the signal, without any noise being included is to take the initial and final climate states as being the mean of two infinitely long samples. This is because the noise from internal variability will diminish over very long timescales. However, it is not possible to get two infinitely long samples of the transient evolution of a system, as the evolution is described by snapshots of the response at a finite time. Any snapshot will include some effects of internal variability. To confuse the problem further, there may be some background "drift" in the control integration.

There are different techniques available to reduce the effects of drift and internal variability to get the best estimate of the climate change signal. There is no conventional method, and the IPCC is not explicit about the method used in any one chapter. The method depends on the opinion of the contributing researchers and all results are referred to as "climate change". In the rest of this section, some different possible methods will be discussed, along with explanations for the choice of methods to be used for the rest of this thesis. The following derivations will discuss the change in global mean temperature, although the methodology applies to every variable at every individual location. The transient climate response (TCR) is defined as the "global mean temperature change, which occurs at the time of $CO_2$ doubling for the specific case of 1%/yr increase of $CO_2$" by Cubasch *et al*. (2001). This definition does not explicitly state a time period over which the temperature change is calculated. However values stated by Cubasch *et al*. (2001) are derived from the CMIP2 modelling project, which only stored four 20-year means (Raper *et al*., 2002). Therefore Collins *et al*. (2006) refined the definition to be "the 20 year averaged global warming" centred "at the time of $CO_2$ doubling". This thesis will use 20 year averages, so that the results may be directly compared to these other studies.

The temperature in a model integration with increasing $CO_2$ can be thought of as consisting of the following elements:

$$T_{1\%}(t) = T_{eq} + \Delta T_{CO_2}(t) + Noise(t) + Drift(t) \tag{4.1}$$

where $T_{eq}$ is the initial equilibrium climate state, $\Delta T_{CO_2}(t)$ is the change in temperature due to an increase in $CO_2$: the climate change signal. $Noise(t)$ is the modelled internal variability, which reduces on longer timescales. $Drift(t)$ is the change in the temperature that occurs, because the model had not reached its equilibrium at the beginning of the integration. The majority of the properties are a function of time, $t$.

### 4.3.1 Small drift

The drift in the global mean annual temperature is small in the control runs compared to the increase in temperature seen in the increasing $CO_2$ run (section 3.3). Therefore the drift term can be ignored in equation 4.1. The signal, $\Delta T_{CO_2}(t)$, can then be approximated by:

$$\Delta T_{CO_2}(t) \approx T_{1\%}(t) - T_{eq} + Noise(t). \tag{4.2}$$

There is some noise in this equation, which arises from the effects of internal variability on the two other terms on the right hand side. The equilibrium temperature, $T_{eq}$, is not known. The best estimate of the equilibrium temperature is the mean value throughout the control run (i.e. years 501-580), because the internal variability decreases as the averaging period increases. Therefore the transient climate response is

$$TCR = [\Delta T_{CO_2}(t)]_{561}^{580} \approx [T_{1\%}(t)]_{561}^{580} - [T_{cont}(t)]_{501}^{580}\,, \tag{4.3}$$

where $[T]_{t_1}^{t_2}$ indicates the time average of $T$ between the years $t_1$ and $t_2$ and $T_{cont}(t)$ is the timeseries of $T$ in the control run. This method will be used throughout this chapter, because the drifts are small in the surface climate variables (as shown in section 3.3). This method is used by Johns *et al*. (2003) to create spatial patterns of climate change. However if there is a drift in the control simulations that is appreciable in size to the climate change signal (such as in the deep ocean in this ensemble) this approximation is not appropriate.

### 4.3.2 Including climate drift

If the climate system is drifting as well as responding to an increase in $CO_2$ then the two processes can be hard to disentangle. One possible simplification is to assume that the drift in the increasing $CO_2$ run is the same as that in the control run. Cubasch *et al*. (1992) investigated using two definitions of the climate signal. The climate drift in the control run can be removed using their second method:

taking the contemporaneous difference. However by using a shorter averaging period a larger amount of internal variability will be incorporated.

$$[\Delta T_{CO_2}(t)]_{561}^{580} \approx [T_{1\%}(t)]_{561}^{580} - [T_{cont}(t)]_{561}^{580}\,. \tag{4.4}$$

This method of calculating the climate signal will be used in chapter 5, because at depth and at regional scales the drift in the control climate is larger than the reduction in variability achieved by the longer averaging period. Another reason for using this method is to compare the spatial patterns of uncertainty with those shown by Cubasch *et al*. (2001), which are most likely calculated using this method.

### 4.3.3 Linear approximation

Both of the above approaches use only the information from the final quarter of 1% run. This could be seen as wasting the information from the previous 60 years. In fact, the second, contemporaneous method only uses a quarter of all the available information to calculate the climate change signal. Another possibility would be to assume that the climate change in response to a linear increase in forcing is itself linear (Gregory and Mitchell, 1997):

$$\Delta T_{CO_2}(t) = at \tag{4.5}$$

where $a$ is a constant of proportionality. There might still be climate drift, which again can be approximated as being the same as the drift in the control run. Therefore a timeseries can be computed that is a linear trend, with some noise from interannual variability.

$$\Delta T_{CO_2}(t) + noise(t) = T_{1\%}(t) - T_{cont}(t) \approx at \tag{4.6}$$

The coefficient $a$ can be calculated as a line of best fit using a least squares estimation method (Draper and Smith, 1998). The value of the climate change signal can then be estimated at time, t, even near the beginning of the experiment, when the signal is smaller than the noise from internal variability.

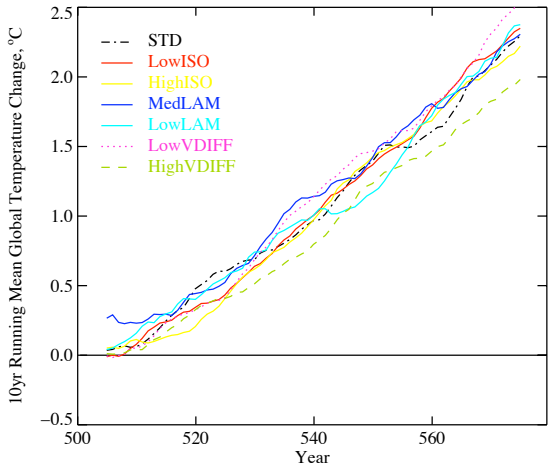


**Figure 4.1** *The global mean temperature change for each ensemble member (defined as the difference of the 1% run from the long-term mean of the control run). A 10 year running mean has been used to smooth the lines.*

The linear approximation method will not be used directly in this thesis, however it is analogous to the combined climate feedback parameter ($\Lambda$) and ocean heat uptake efficiency ($\kappa$) model of Gregory and Mitchell (1997). This model will be described in more detail in sections 4.6 and 4.7 where the constant of proportionality, $a$, is related to the sum of $\Lambda$ and $\kappa$.

## 4.4 Global mean response

The primary response of the climate system to an increase in $CO_2$ is a global warming. The increase in global mean temperature can be seen in figure 4.1, which shows a 10 year running mean of the difference in global mean temperature between the increasing $CO_2$ run and the mean of the control run for each ensemble member. It can be seen that the change in temperature is not the same in each ensemble member.

The transient climate response (TCR) is defined as the change in global mean surface air temperature for the 20 years centred on the year of doubling of $CO_2$ (Collins *et al.*, 2006). This is calculated as the difference between the average of the increasing $CO_2$ run in years 561-580 and the mean of the control

run (eq. 4.3). The TCR for each ensemble member is shown in table 4.1. The range of TCR across the ensemble is $1.8 - 2.3\,^{\circ}$C. This range is dominated by the ensemble members with perturbations to the vertical diffusivity. This table also shows the change in global mean annual average temperature in the control run caused by the perturbations. The effect of increasing $CO_2$ is approaching an order of magnitude larger than the effect of any of the perturbations on the equilibrium climate state. The average top of the atmosphere flux imbalance, $N$ and the effective climate sensitivity will be discussed in section 4.6.

| **Model Version** | $T_{CONT}$ (°C) | **TCR** (°C) | $N$ ($\mathrm{Wm}^{-2}$) | **Eff. Clim. Sens.** (°C) |
|---|---|---|---|---|
| STD | 15.9 | 2.1 | 1.4 | 3.4 |
| LowISO | 15.5 | 2.2 | 1.3 | 3.4 |
| HighISO | 16.2 | 2.1 | 1.3 | 3.0 |
| MedLAM | 16.1 | 2.1 | 1.4 | 3.4 |
| LowLAM | 16.1 | 2.2 | 1.3 | 3.3 |
| LowVDIFF | 15.7 | 2.3 | 1.3 | 3.6 |
| HighVDIFF | 16.5 | 1.8 | 1.4 | 2.9 |

**Table 4.1** *Global mean aspects of each model version. $T_{CONT}$ is long term average global mean surface temperature in the ensemble member's control run (see chapter 3). TCR is the transient climate response of the model version. $N$ is the average flux imbalance at the top of the atmosphere for the years 561-580. The effective climate sensitivity is the climate sensitivity of the model version for a doubling of $CO_2$ determined from the average of years 561-580.*

### 4.4.1 Natural variability

There are internal (or "natural") variations in the models due to the chaotic, nonlinear nature of the climate system. These natural variations happen on all timescales, so the variations in the TCR found in the ensemble might not be caused by the parameter perturbations. The natural variability in the model can be estimated. If it is found to be significantly smaller than the signal spread in TCR found in the ensemble, then there is confidence that the ocean model uncertainty is causing a signal spread in the transient climate response.

An estimate of the natural variability can be found from several sources. One possible source is the 580 years of data from the STD model spin up with a constant level of $CO_2$. However in the STD

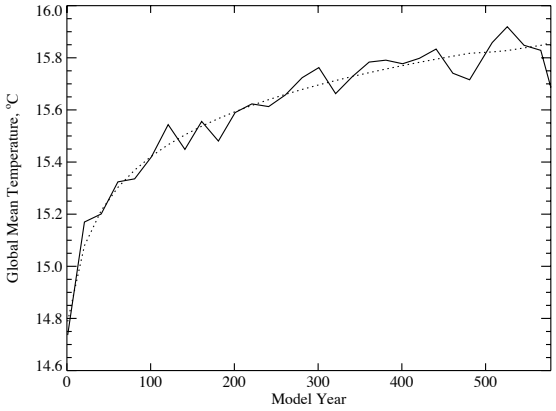


**Figure 4.2** *The evolution of 20 year averaged global mean temperature during the spinup of the standard model. The dotted line shows the logarithmic trendline that was removed when calculating the natural variability.*

model spin up, a drift in the climate state occurs. This climate drift can be seen in figure 4.2, which shows the 20 year average global mean temperature throughout the STD model's spin up. The dotted line shows the line $T = 0.26 \times log(t) + 287.33$, which was computed to be the line of best fit using a least squares regression. The differences between the logarithmic trend and the modelled global mean temperature form a distribution of modelled natural variability. The standard deviation of 20 year global average surface temperature for the standard model with constant $CO_2$ is $0.05$ °C. The distribution can be added to the ensemble mean TCR to give an estimate of the variations in TCR than could be expected from internal variability. This will be shown in figure 4.4 as the "natural var."

However this is only one possible estimate of modelled natural variability. Chapter 3 took its estimate of modelled internal variability from a millenia long simulation of HadCM3 (Collins *et al.*, 2001). The estimate of the modelled natural variability is $0.05$ °C from this 1000 year simulation. Section 3.5.12 showed that there is no detectable change in the preindustrial interannual variability between the ensemble members. This may not be the case on longer timescales. A method of estimating the modelled natural variability that accounts for this possibility is to use the seven control runs from the ensemble:

$$
\begin{aligned}
St.Dev. &= \sqrt{\overline{\overline{(20\ year\ anomalies)^2}}} \\
&= \sqrt{\overline{\overline{\left([GM_i]_t^{t+20} - [GM_i]_{501}^{580}\right)^2}}}
\end{aligned}
\tag{4.7}
$$

where $GM_i$ is the global mean field for the $i$th ensemble member, $[X]_t^{t+20}$ is the average of $X$ between $t$ and $t+20$, and $\overline{\quad}_i$ is the average over all the ensemble members. This method of using every ensemble member's control run also estimates the modelled natural variability to have a standard deviation of 0.05 °C.

If the modelled natural variability follows a normal distribution, then more than 95% of the samples will fall within $\pm 2$ standard deviations of the mean. The central limit theorem states that this is a fair assumption for a large sample sizes (von Storch and Zwiers, 1999). If each of the ensemble members were less than 2 standard deviations (0.1°C) from the ensemble mean, then the physics perturbations would not have a detectable effect on the TCR at the 95% significance level, because such deviations would be expected from the internal variability. Five of the seven ensemble members are within $\pm 2$ standard deviations of the ensemble mean and, therefore, have no detectable effect of the perturbations on the global mean temperature response. The TCR of both LowVDIFF and HighVDIFF fall outside that expected from modelled internal variability at the 5% confidence interval.

The size of a sample will have an effect on the sample's range assuming that it is taken from a probability distribution. This ensemble is considered a small sample, having only seven members. Therefore a test of spread that takes the sample size into account might be preferable. An F-test determines whether the variances of the perturbed ocean physics ensemble and the detrended internal variability distribution are indistinguishable at a 5% confidence level (further description of this statistical test is given in section 4.4.2). This test also confirms that the spread in TCR of the ensemble can not be explained by modelled internal variability.

Both of these measures show ocean model uncertainty causes detectable uncertainty in the time-

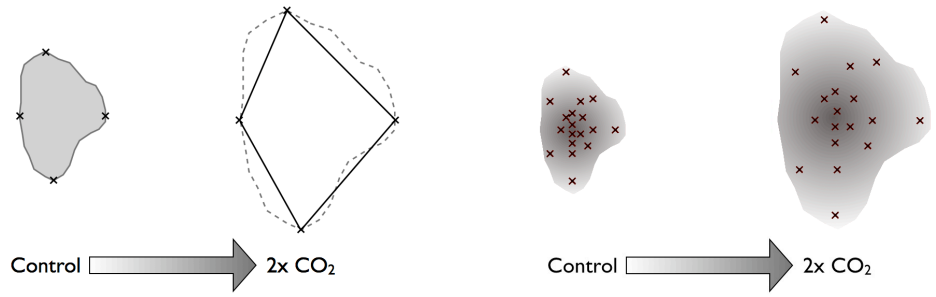


(a) Ocean ensemble (b) Atmosphere ensemble

**Figure 4.3** A schematic showing the different sampling methods. The ocean ensemble (a) samples only the maximum extent of the uncertainty and hence can only inform us about the maximum extent of the uncertainty at the time of doubled $CO_2$. The atmosphere ensemble (b) systematically samples all the uncertainty - obtaining information about the probability density function of the resulting uncertainty.

dependent global mean temperature response of HadCM3 at the 5% confidence interval.

### 4.4.2 Comparison with other ensembles

The signal spread in TCR from the ensemble must be compared to other temperature ranges to understand the importance of ocean model uncertainty in time-dependent climate change. Collins *et al.* (2006) have performed a similar experiment to quantify the atmosphere model uncertainty. They found a TCR range of $1.5 - 2.6$ °C, which is more than twice the range of the perturbed ocean parameter ensemble. There are some differences between their ensemble and the one presented in this thesis. Their ensemble consisted of 17 ensemble members: 16 perturbed members and the standard model configuration, compared to the 6 perturbed members and 1 standard model version of this ensemble. Collins *et al.* (2006) selected the perturbations for each model with the aim to evenly sample parameter space. This means that they used multiple parameter perturbations for each model, and did not always perturb the parameters to their maximum and minimum plausible values. The perturbed ocean ensemble is not expected to give an even sampling of parameter space, only to sample the furthest extent of the envelope. A schematic showing the effects of the sampling is shown as in figure 4.3.

The differences in the sampling methodology between this study and that of Collins *et al*. (2006) mean that the resultant uncertainties should also be different. This study is only an initial gauging of the ocean model uncertainty and aims to answer two major questions: can we detect the effects of ocean model uncertainty and how large are the effects of this uncertainty compared to those from other forms of uncertainty? Only the maximum linear extent of ocean model uncertainty is required to answer both of these questions. It should be noted here that multiple parameter perturbations would be expected to increase this range linearly (this is further discussed in section 4.5). Due to this sampling methodology, the range is the only statistical measure of spread with real value. However, with only seven ensemble members the ocean ensemble is small. For a normally distributed variable, the range will increase as the sample size increases. This would not be the case for the standard deviation, yet the ocean ensemble has been designed in a way that the standard deviation would not be representative of the sample. It would instead be a maximum bound of the standard deviation of the ocean ensemble, so risks over-estimating the spread of the ensemble.

The atmosphere ensemble was designed to answer different questions, so is sampled in a different way. It should have both a representative range and standard deviation. This thesis will compare both the range (possibly under-estimated in the ocean ensemble) and the standard deviation (possibly over-estimated in the ocean ensemble), when comparing relative magnitude of signal spreads. The spatial patterns of spread that are presented as a quantification of ocean model uncertainty show only the range. They should strictly be thought of as a spatial pattern of the maximum linear bound of the effects of ocean model uncertainty.

The scenario used in this experiment is the same as that used in CMIP2 (Meehl *et al*., 1997)), so the TCR spread in ensembles produced by CMIP2 can also be compared to that from the perturbed ocean ensemble. CMIP2 is an ensemble of opportunity (Allen and Stainforth, 2002). It is a multi-model ensemble that has not been explicitly designed to sample parameter space. Most climate models, whose data are used in the third and fourth assessments of the IPCC, are included in CMIP2.

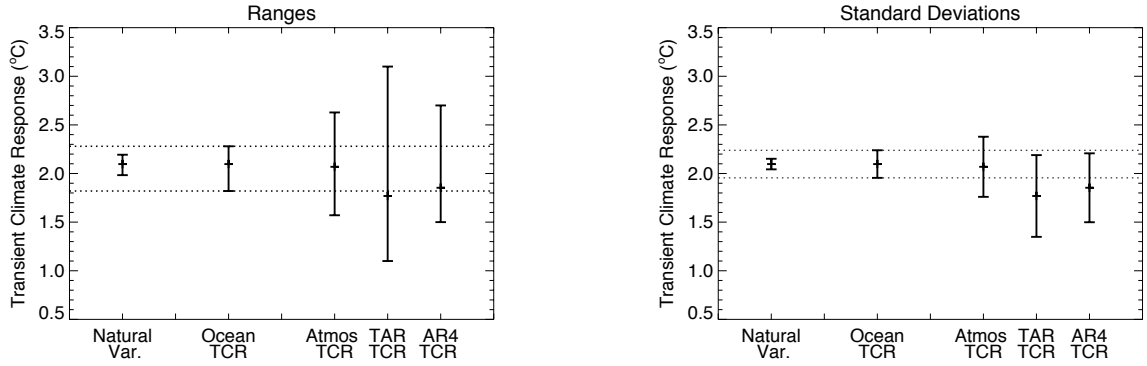


**Figure 4.4** *A comparison of the spread of transient climate response from a variety of sources. The left hand panel shows the spread as the range of response, whilst the right hand panel uses the standard deviation. The TCR spread found from the perturbed ocean physics ensemble is shown in centre of each panel (called Ocean. TCR). "Natural Var." is the variations in expected from internal variability dressed about the ensemble mean (described in section 4.4.1). On the right hand side of each panel are the spreads in TCR found by 3 other studies. "Atmos. TCR" is the range found by Collins* et al. *(2006) from an experiment of similar design, but investigating only atmospheric model uncertainty. "TAR TCR" and "AR4 TCR" are the ranges from models included in the 3rd and 4th assessments reports by the IPCC respectively. They are both AOGCM ensembles so include both atmosphere and ocean model uncertainty, along with structural and initial condition uncertainty. All ensembles use the 1% scenario.*

Figure 4.4 shows the results from a comparison of the TCR spread of the different ensembles for two methods of measuring the signal spread. The left hand panel shows the range of TCR from the four ensembles as well as the the 5-95% range expected from modelled internal variability. The range could be related to the ensemble size, so the right hand panel shows the mean $\pm 1$ standard deviation of the ensembles. The signal spread of the ocean ensemble is larger than that expected from modelled internal variability (described in the previous section) by both measures. The range of the atmosphere ensemble is twice as large as the ocean ensemble, however a larger range would be expected because of the larger sample size. The standard deviation from the atmosphere ensemble is also larger than the standard deviation from the ocean ensemble. The range and standard deviation of the TCR from the ocean ensemble are smaller than two CMIP2 ensembles. These CMIP2 ensembles are labelled "TAR" and "AR4", relating to the models used in the IPCC's third and fourth assessment reports respectively (Cubasch *et al.* (2001) and values shown in Collins *et al.* (2006)).

Whether the differences in the standard deviations between the ensembles are statistically significant

| Ocean ensemble compared to ... | Ratio of Variances | Critical Value |
|---|---|---|
| Natural Variability | 6.83 | 2.43 |
| Atmosphere | 4.73 | 3.94 |
| CMIP2, 3rd Assessment Report | 8.75 | 3.88 |
| CMIP2, 4th Assessment Report | 6.22 | 3.96 |

**Table 4.2** *Comparison of the ocean physics TCR ensemble spread to the spread from selected other ensemble spreads. If the ratio of the variances exceeds the critical value, then the null hypothesis that the samples could have the same variance is rejected at the 5% confidence level. Note: the ratio is always defined as the larger variance divided by the smaller.*

can be determined by using an F-test (von Storch and Zwiers, 1999). The F-distribution shows the probability of a ratio of variances occuring if the two samples were taken from the same probability distribution. The f-distribution depends on the size of each sample. Table 4.2 shows the ratio of the variance of the ocean ensemble to the other ensembles shown in fig. 4.4, along with the critical value from the appropriate f-distribution. If the ratio of variances is greater than the critical value then we reject the null hypothesis (that the samples come from the same probability distribution) at the 5% confidence level. The variance of every ensemble is significantly different from the ocean ensemble.

The spread of the TCR across the perturbed ocean physics ensemble represents the uncertainty in the transient response caused by ocean model uncertainty. By comparing the spread from the ocean ensemble to the spread in a perturbed atmosphere physics ensemble (Collins *et al.*, 2006), it is shown that the effect of ocean model uncertainty on the TCR is less than the effect of atmosphere model uncertainty. The spread in TCR in the ocean ensemble is less than in 2 different ensembles of opportunity, showing that the effect of ocean model uncertainty on the TCR is less than all AOGCM uncertainties combined (see section 1.3.3 for a description of the differences between AOGCM and model uncertainty). The conclusion that the effect of ocean model uncertainty on projections of the time-dependent global mean response of the climate system is relatively small is a major result of this thesis. The TCR signal spread is less than the ensemble spread in preindustrial global mean temperatures. This will be covered in more detail in chapter 6, which discusses the temporal evolution of ensemble spread.

## 4.5 Possible explanations for the relatively small response

In the previous sections it has been shown that the spread in transient climate response caused by ocean model uncertainty is smaller than the spread from other uncertainties, including atmosphere model uncertainty. It is important to investigate different possible reasons for this result. The most obvious conclusion is that the ocean model uncertainty is, itself, small in comparison to other uncertainties. This does not mean there is no structural uncertainty contained in the ocean model. This work has defined ocean model uncertainty as being the uncertainty related to the value of parameters in the ocean model. It has not investigated the variety of structural changes, such as increased resolution and different coordinate systems, that have been the cause of many improvements in ocean models over the past years. The ocean model uncertainty (from the parameter values) could be small, whilst the structural uncertainty is large.

Before it can be concluded that the ocean model uncertainty is indeed small, it must first be demonstrated that the reason for the small signal spread is not deficient sampling of the ocean model uncertainty. There could also be a compensation mechanism that is masking important regional uncertainty. There are three possible reasons for a deficient sampling of the ocean model uncertainty, and each will be discussed in turn.

### 4.5.1 Underestimates of the parameter ranges

The first possibility is that the ensemble created does not sample the full uncertainty contained in each of the perturbed parameters. This would occur if the perturbations made in the ensemble do not cover the full range of the individual parameters. This would imply errors in the results of the expert elicitation exercise presented in chapter 2, arising either from errors in the manner of determining and collating the expert opinions, the experts being too conservative, or from gaps in the experts' knowledge.

To investigate the possibility of conservative ranges being included in the ensemble, the experts were consulted again. The results were shown to them, and they were asked to reconsider the ranges suggested in light of the results. As the results imply that their field of expertise is not as important as other fields, it could have been expected that they would expand the ranges. This was not the case. Each range was reaffirmed, and it was stated that there could be no justification for expanding the ranges given our knowledge of the processes and the current observations. Future observations and scientific advances may alter the range of the parameters, so this possibility can never be discounted. However as research normally acts to reduce uncertainty rather than increase it, this possibility is considered an unlikely explanation for result of the relatively small ensemble spread.

### 4.5.2 Inconsequential parameters chosen

A second possibility for a deficient sampling of the ocean model uncertainty could be that the most important processes have not been perturbed. The experts were explicitly asked to suggest parameter perturbations to those processes that are most important in transient climate change in the model. These suggestions gave rise to the 3 parameters in the ocean ensemble being chosen. The experts (and by extension, the scientific community) may not know, which ocean parameters control the transient model response. There may also be important processes not included in this study, because they currently do not have any adjustable parameters associated with them. One such process is the convective adjustment, which is assumed to occur within one time-step in the ocean model. The possibilities for including a tunable timescale parameter into the convection parameterisation are briefly discussed in Collins *et al*. (2007). Consideration of different parameterisation schemes falls outside the scope of this thesis, but should be investigated in future studies.

However it is possible to investigate whether the most important physical processes in transient climate change have been perturbed. The rate at which the ocean transports heat into its deeper layers is the prime determinant of the surface warming experienced at any time in a climate change scenario

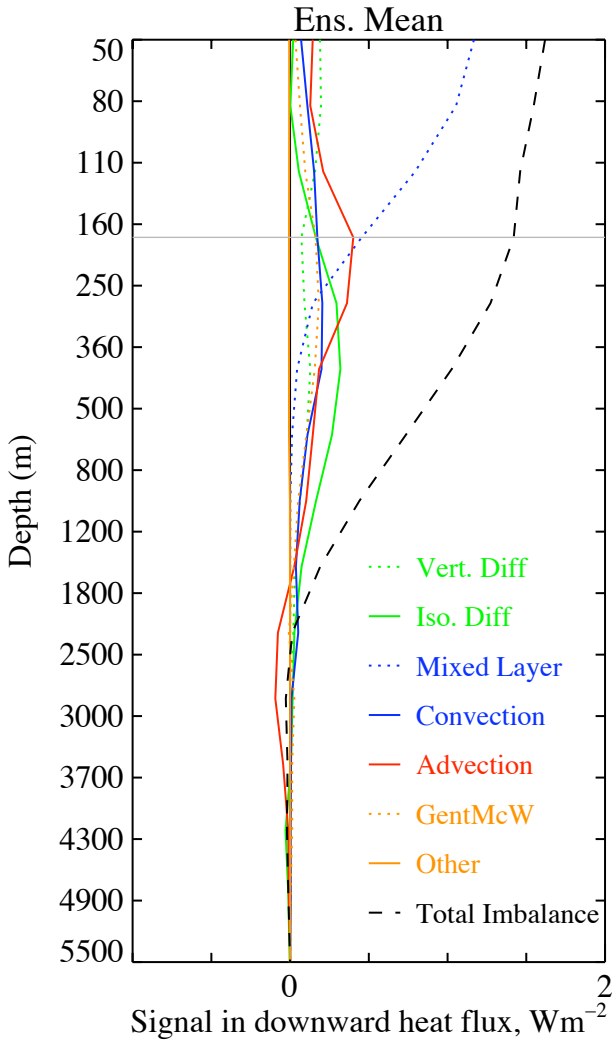


**Figure 4.5** *The ensemble mean additional downwards heat flux caused by an increase in $CO_2$, $Wm^{-2}$. The black line shows the total, and the coloured lines show the components from individual parameterisations. The anomalies of each ensemble member from this profile are shown in figure 5.23*

(Levitus *et al.*, 2005). Diagnostics that allow the estimation of vertical heat flux from individual parameterisation schemes were introduced in section 3.5.8. The diagnostics allow the relative size (and importance) of the additional vertical heat flux from the different physical processes to be determined. The ensemble mean additional heat fluxes are presented in figure 4.5 (analysis for individual ensemble members can be found later in section 5.14). It can be seen that the 3 processes that dominate the additional heat flux (albeit at different depths) are mixing in the mixed layer, advection and isopycnal diffusion. Of these three dominant processes, two have been perturbed.

Advection is explicitly resolved, so its parameterisation has not been perturbed. It is noted that making

different choices about the model resolution and time-step would probably change the advective heat flux, by explicitly resolving more or less motions. The resolution and time-step are structural choices, made during model development. They therefore fall outside the scope of this thesis.

### 4.5.3 Possible non-linear interactions

Each ensemble member has only a single perturbation. Multiple parameters be could perturbed simultaneously. This would probably expand the range slightly if the effects of the parameter perturbations combined linearly. The range in TCR is determined by the two perturbations in vertical diffusivity and the other perturbations have minor effects in comparison. This means that the range would not be greatly increased by multiple parameter perturbations combining linearly. However, the perturbations do not necessarily combine linearly: there could be feedbacks between their effects. This has been seen with atmospheric parameter perturbations (Stainforth *et al*., 2005). Section 3.5.5 has shown that the perturbations themselves are not linear, so it is a distinct possibility that the interactions between them are also non-linear. The only method to incorporate any non-linear feedbacks of ocean model uncertainty is to create an ensemble with all possible parameter combinations.

### 4.5.4 Possible compensation of warming factors

The climate's response to an imposed radiative forcing can be thought of as being controlled by two different factors. The additional heat at the surface must be lost. This occurs either by additional radiation back to space or by absorption into the deep ocean (both of which can be thought of as infinite heat sinks). The small spread in the transient climate response could be due a relationship between heat loss to the 2 different heat sinks. For example, a larger loss to space could be compensated for by a smaller loss to the deep ocean. Raper *et al*. (2002) noticed this form of compensation occuring (although not at a statistically significant level) from an analysis of the global mean response of the CMIP2 multi-model ensemble. They used the same form of analysis that will be performed here. They

also present several reasons for this compensation.

The ocean physics perturbations are expected to change the rate of heat transfer into the deep ocean (through design). Chapter 3 has shown that the ocean parameter perturbations also have an effect on the long term mean state of the modelled climate, notably different sea ice distributions. This suggests that there could also be changes in the heat loss to the space, which is related to the climate sensitivity.

## 4.6 Climate sensitivity

The climate sensitivity is defined as the equilibrium surface temperature response of the climate system to a doubling of $CO_2$, $\Delta T^{eq}_{2\times CO_2}$. When the climate sensitivity is estimated from a transient run it is known as the *effective* climate sensitivity. Collins *et al*. (2006) compared the results from a perturbed physics ensemble of coupled model integrations to integrations with the equivalent perturbations with a slab ocean (Murphy *et al*., 2004). They showed that the effective climate sensitivities of a perturbed physics ensemble are highly correlated to the climate sensitivities of the models run to equilibrium. The effective climate sensitivity can be determined by considering the global mean radiative balance:

$$N = Q - \Lambda \Delta T \tag{4.8}$$

where $N$ is the top of the atmosphere flux imbalance, $Q$ is the imposed radiative forcing, $\Delta T$ is the change in global mean temperature and $\Lambda$ is a constant of proportionality called the climate feedback parameter. $N$, $Q$ and $\Delta T$ can all be diagnosed directly for the ensemble. All quantities are calculated as the average of years 61-80 in the increasing $CO_2$ run less the average for the whole of the control run. This period is chosen for comparability with previous work. Using this averaging period means that the temperature change, $\Delta T$ is the TCR and the imposed forcing, $Q$, is that of doubling $CO_2$, $Q_{2\times CO_2}$. The transient climate response for each ensemble member is given in table 4.1, along with the corresponding value for $N$. $N$ is computed as the global mean of the imposed incoming short-wave solar radiation less the global mean of the outgoing modelled long wave and short wave radiation at

the top of the atmosphere. The climate sensitivity is defined as for the equilibrium change in response to a doubling of $CO_2$,

$$0 = Q_{2\times CO_2} - \Lambda \Delta T^{eq}_{2\times CO_2} \tag{4.9}$$

Using equation 4.9 to substitute for $\Lambda$ into equation 4.8 and then re-arranging, the effective climate sensitivity can be defined as,

$$\Delta T^{eq}_{2\times CO_2} = \frac{Q_{2\times CO_2} \times TCR}{Q_{2\times CO_2} - \left( \left[ \langle TOA_{1\%} \rangle_{globe} \right]^{580}_{561} - \left[ \langle TOA_{cont} \rangle_{globe} \right]^{580}_{501} \right)} \tag{4.10}$$

where $TCR$ stands for the transient climate response, $TOA$ is the net top of the atmosphere flux and $\left( \left[ \langle TOA_{1\%} \rangle_{globe} \right]^{580}_{561} - \left[ \langle TOA_{cont} \rangle_{globe} \right]^{580}_{501} \right)$ is referred to as $N$ in table 4.1. The forcing due to a doubling of $CO_2$, $Q_{2\times CO_2}$ is assumed to have a value of 3.74 $Wm^{-2}$, calculated using double radiation calculations (Williams *et al.*, 2001). Gregory *et al.* (2004a) suggest that $Q_{2\times CO_2}$ may differ slightly from this value, but the effect of variations in $Q_{2\times CO_2}$ have been shown to be small (Raper *et al.*, 2002).

The effective climate sensitivity ($\Delta T^{eq}_{2\times CO_2}$ from equation 4.10) is a measure of the total atmosphere and surface feedbacks in the system. The physical causes of the four major feedbacks that make up the climate feedback parameter (blackbody radiative feedback, water vapour, ice-albedo, clouds) should be unaffected by perturbing the ocean physics. It is expected the effective climate sensitivities to be the very similar throughout the perturbed ocean ensemble. Some differences in effective climate sensitivity would be expected from natural variability. The effective climate sensitivity for each of the ensemble members is shown in table 4.1. The climate feedback parameter can also be calculated directly from eq. 4.8:

$$\Lambda = \frac{Q_{2\times CO_2} - N}{TCR} \tag{4.11}$$

The values of the climate feedback parameter, $\Lambda$, for each ensemble member are given in table 4.3.

Figure 4.6 shows the range in effective climate sensitivity from the ensemble compared to ranges and standard deviations found from other studies and natural variability. The signal spread in effective

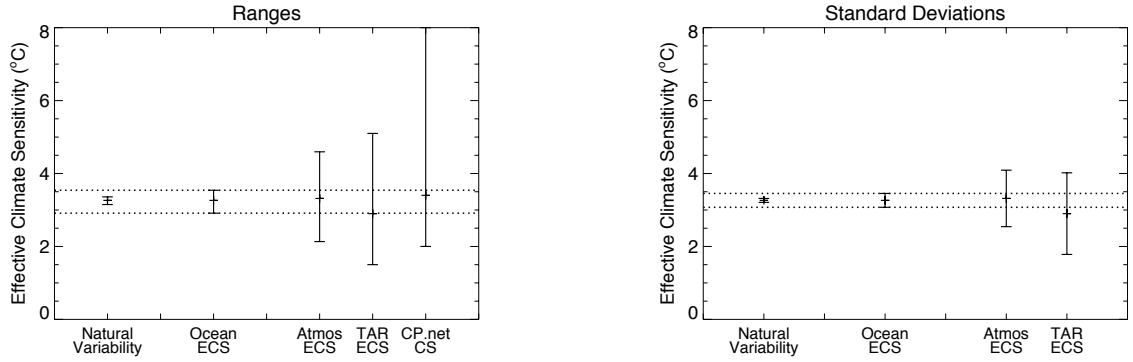


**Figure 4.6** *A comparison of the signal spread of effective climate sensitivity from the ensemble. The left hand panel shows the spread as the range, whilst the right hand panel uses the standard deviation. The spread found from the perturbed ocean physics ensemble is shown in the middle of each panel (called ocean ECS). "Natural Variability" is the variations in expected from internal variability described in section 4.4.1. On the right hand side are 3 ranges of climate sensitivity found by other studies. "ATMOS ECS" is the range found by Collins* et al. *(2006) from an experiment of similar design, but investigating only atmospheric model uncertainty. "TAR ECS"is the range of effective climate sensitivity from the 3rd assessments reports by the IPCC. "CP.net CS" is the 5-95% confidence interval of climate sensitivity (not computed from transient runs) found by climateprediction.net. This experiment only perturbed atmosphere and land surface parameters (Stainforth* et al.*, 2005).*

climate sensitivity across the ensemble is larger than that expected by natural variations alone, and therefore ocean model uncertainty has a distinguishable effect on the climate sensitivity. The effect of atmosphere model uncertainty on climate sensitivity has been examined by both Collins *et al*. (2006) and Stainforth *et al*. (2005). Both studies use perturbed physics ensembles; Collins *et al*. (2006) used an ensemble of 17 transient coupled model runs to calculate the effective climate sensitivity (in the manner used here), whilst Stainforth *et al*. (2005) used a many thousand member ensemble of perturbed slab models to perform a $CO_2$ doubling equilibrium experiment. Stainforth *et al*. (2005) do not provide a standard deviation. The range of climate sensitivity from the perturbed ocean ensemble is much smaller than the ranges from other ensembles. The standard deviation is also smaller. The variance of the ocean ensemble is not indistinguishable from that of any of the other ensemble at the 5% confidence level. In conclusion, there is an uncertainty in the effective climate sensitivity caused by ocean model uncertainty, but it is significantly less than from other modelling uncertainties.

## 4.7 Ocean heat uptake efficiency

It has been stated that the two factors determining the rate of global warming are the rate of heat loss to the deep ocean and the rate of heat loss to space. A derivation of the climate feedback parameter, $\Lambda$, was given, but it was not stated how this can be reconciled as a determinant of the rate of heat loss to space. First this will be established, and then an analogous measure for the heat loss into the deep ocean will be introduced.

Newton's law of cooling states that the rate of heat transfer between two objects is directly proportional to the temperature gradient between those objects (Tipler, 1999) (note that this is a linearisation of the true relationship):

$$\frac{dE}{dt} \propto A\frac{T_1 - T_2}{x} \tag{4.12}$$

where $\frac{dE}{dt}$ is the rate of heat transfer, $A$ is the surface area in contact with the two objects, $T_1$ and $T_2$ are temperatures of the two objects and $x$ is the distance between them. An increase in $CO_2$ in the atmosphere will induce a surface warming, $\Delta T$, which will lead to an additional heat loss, $\Delta\frac{dE}{dt}$. Space can be thought of as an infinite heat sink, so its temperature, $T_2$, will not change, hence the additional heat loss to space is directly proportional to the change in surface temperature:

$$\Delta\frac{dE}{dt} = \frac{kA}{x}\Delta T = \Lambda\Delta T \tag{4.13}$$

where $k$ is a constant of proportionality. Therefore the climate feedback parameter is measuring the heat loss into space. This leads to the suggestion that the surface heat loss into the deep ocean should be measured in a similar way. Gregory and Mitchell (1997) observed that the heat flux into the ocean is linearly related to the change in global mean surface temperature with a linearly increasing imposed forcing. They also provide a derivation of this measure of heat loss to the ocean, arriving at:

$$N = \kappa\Delta T \tag{4.14}$$

The constant of proportionality, $\kappa$, is related to the strength of the processes that transfer heat into the ocean (Gregory and Mitchell, 1997). Further work into this measure was performed by Raper

| **Ensemble Member** | **TCR** (°C) | $\kappa$ ($Wm^{-2}°C^{-1}$) | $\Lambda$ ($Wm^{-2}°C^{-1}$) |
|---|---|---|---|
| STD | 2.07 | 0.63 | 1.15 |
| LowISO | 2.17 | 0.57 | 1.12 |
| HighISO | 2.07 | 0.61 | 1.18 |
| MedLAM | 2.11 | 0.62 | 1.13 |
| LowLAM | 2.16 | 0.57 | 1.14 |
| LowVDIFF | 2.28 | 0.55 | 1.06 |
| HighVDIFF | 1.82 | 0.74 | 1.29 |

**Table 4.3** *Global mean values of each ensemble member.* ***TCR*** *is the transient climate response of the ensemble member.* $\kappa$ *is the ocean heat uptake efficiency (eq. 4.16).* $\Lambda$ *is the climate feedback parameter (eq. 4.11).*

*et al*. (2002), who named it the ocean heat uptake efficiency. This is a slight misnomer as an efficiency should be a dimensionless ratio ($\kappa$ has units of $Wm^{-2}°C^{-1}$, and is therefore strictly an area-normalised thermal conductivity). The term shall be used throughout this thesis, along with the symbol, $\kappa$, as it measures how effective ocean processes are at transferring heat. Raper *et al*. (2002) showed that $\kappa$ varies with time (especially as a model approaches equilibrium). However for a constantly increasing forcing $\kappa$ does not vary as rapidly as $\Delta T$, so a substantial amount of variation of the heat flux can be explained by variations in $\Delta T$. This allows us to rearrange eq. 4.8 as

$$\kappa \Delta T = Q - \Lambda \Delta T \tag{4.15}$$

There are several methods to determine the value of the ocean heat uptake efficiency. Raper *et al*. (2002) divided the twenty year average of the ocean fluxes at the time of doubling of $CO_2$ by the twenty year average of the surface air temperature response. Gregory and Mitchell (1997) use linear regression of the global mean change in flux with the global mean surface temperature change to find the slope, whose value is $\kappa$. The Gregory and Mitchell (1997) method removes more of the natural variability by considering more information, however using the Raper *et al*. (2002) method allows comparison to the previous model ensembles studies (Collins *et al*. (2006) also use that method).

The ocean heat uptake efficiency for each of the ensemble members is shown in table 4.3, computed by:

$$\kappa = \frac{\left[\langle 0.7F_{1\%}\rangle_{globe}\right]_{561}^{580} - \left[\langle 0.7F_{cont}\rangle_{globe}\right]_{501}^{580}}{TCR} \tag{4.16}$$

where $F$ is the heat flux into the ocean and 0.7 is the fraction of the Earth's surface covered by the ocean. The range of $\kappa$ from the ocean ensemble is 0.55 - 0.74 $\mathrm{Wm^{-2}{}^{\circ}C^{-1}}$. $N$ could be used instead of $0.7F$, but this definition is used as it is analogous to Raper *et al.* (2002). The results are not changed if $N$ is used instead.

The range of $\kappa$ expected from modelled internal variability must be estimated to determine if the ocean model uncertainty causes detectable spread in $\kappa$. The standard deviation of global mean surface temperature was estimated as 0.05 °C in section 4.4.1. The standard deviation of the global mean heat flux into the ocean is 0.05 $\mathrm{Wm^{-2}}$ (also calculated from eq. 4.7). These two standard deviations can be combined to calculate the standard deviation of $\kappa$:

$$\sigma_\kappa = \frac{0.7\overline{F}}{\overline{TCR}}\sqrt{\left(\frac{\sigma_F}{\overline{F}}\right)^2 + \left(\frac{\sigma_T}{\overline{TCR}}\right)^2} \tag{4.17}$$

where $\sigma_F$ and $\sigma_T$ are the standard deviations of the heat flux and TCR respectively, $\overline{F}$ is the ensemble mean heat flux into the ocean and $\overline{TCR}$ is the ensemble mean TCR (Barlow, 1989). The standard deviation of $\kappa$ found using this method is 0.02 $\mathrm{Wm^{-2}{}^{\circ}C^{-1}}$, which gives a 5-95% range in $\kappa$ due to modelled internal variability of $0.59-0.68$ $\mathrm{Wm^{-2}{}^{\circ}C^{-1}}$. This "natural" range is smaller than the range seen in the ocean ensemble.

There are fewer studies analysing the spread in ocean heat uptake efficiency, than for either climate sensitivity and TCR. However the range in $\kappa$ for the ocean is less than that from the CMIP2 ensemble (0.60 - 0.88 $\mathrm{Wm^{-2}{}^{\circ}C^{-1}}$, Raper *et al.* (2002)). The range of $\kappa$ from atmospheric model uncertainty is 0.54 - 0.73 $\mathrm{Wm^{-2}{}^{\circ}C^{-1}}$ (Collins *et al.*, 2006), which is both similar to that from the ocean ensemble and greater than the estimated range expected from internal variability.

The ocean model uncertainty seems to have a detectable effect on the ocean heat uptake efficiency relative to the internal variability in this quantity. However the effects of ocean model uncertainty are only as large as the effects of atmosphere model uncertainty. This is unexpected, because one would expect the ocean physics to effect the ocean heat uptake more than atmosphere physics.

| | Range of TCR found in ensemble | Assuming standard model's $\Lambda$ | Assuming standard model's $\kappa$ |
|---|---|---|---|
| Ocean | 1.8-2.3 °C | 2.0-2.2 °C | 1.9-2.2 °C |
| Atmosphere | 1.6-2.7 °C | 2.1-2.3 °C | 1.6-2.5 °C |

**Table 4.4** *The range of transient climate response considering uncertainties in the ocean heat uptake efficiency and the climate feedback parameter. "Ocean" values refer to the ensemble described in this thesis, which investigates ocean model uncertainty. "Atmosphere" refers to an ensemble which samples atmospheric model uncertainty, (Collins* et al.*, 2006). The second column shows the range of TCR found in the ensemble, which include changes in both the ocean heat uptake efficiency and the climate feedback parameter. The third column shows the hypothetical TCR range that would be found if only variations in the ocean heat uptake efficiency are considered. The fourth column shows the hypothetical TCR that would be found if only the climate feedback parameter varied.*

## 4.8 Relative importance of factors determining the spread in the global mean surface temperature response

The magnitude of the transient climate response can be described conceptually as being determined by the rate of heat loss to two different heat sinks (space and the deep ocean). The uncertainties in the rate of the heat loss to these sources have been quantified, using the measures of climate sensitivity and the ocean heat uptake efficiency. The ocean model uncertainty causes small, but detectable uncertainty in both of these two measures.

The relative importance of differences in the climate feedback parameter and the ocean heat uptake efficiency to the TCR can be investigated by using a re-arrangement of equation 4.15:

$$TCR_i = \frac{Q_{2xCO_2}}{\Lambda_i + \kappa_i} \tag{4.18}$$

where $i$ refers to an individual ensemble member, and $Q_{2xCO_2}$ is 3.74 $\mathrm{Wm}^{-2}$. Table 4.4 shows the ranges of TCR calculated using eq 4.4. It also shows the hypothetical range of TCR computed when considering only variations in the ocean heat uptake efficiency (calculated by replacing $\Lambda_i$ with the standard model's, $\Lambda_{STD}$) and when considering only variations in the climate sensitivity (calculated by replacing $\kappa_i$ with the standard model's, $\kappa_{STD}$). In both the ensemble described here and in the atmosphere parameter ensemble (Collins *et al.*, 2006), spread in the climate feedback parameter (or climate sensitivity) causes a larger spread in the hypothetical transient response than uncertainty in the

ocean heat uptake efficiency. This is more marked in the atmosphere ensemble. The effect of variations in $\Lambda$ caused by the ocean model uncertainty are of similar magnitude to the effect of variations in $\kappa$.

The ranges in table 4.4 differ slightly from those presented in our publication on this subject, (Collins *et al.*, 2007). In this thesis, the values of $\Lambda_{STD}$ and $\kappa_{STD}$ are taken to be the values of the standard model run presented in this thesis (section 3.2) and the atmosphere ensemble's standard model is taken from the standard model run described along with the atmosphere ensemble in Collins *et al.* (2006). However in Collins *et al.* (2007), we take the $\Lambda_{STD}$ and $\kappa_{STD}$ to be the mean value of an ensemble of 4 standard model versions, most of which are flux corrected. The ocean ensemble's STD has a TCR that is 0.08 °C less than the TCR of the atmosphere ensemble's standard model version. The differences between the ranges presented here and the ranges presented in Collins *et al.* (2007) are only of order 0.01 $Wm^{-2}°C^{-1}$, however this causes some differences when rounded to 1 decimal place. These differences do not affect the conclusions drawn from the work.

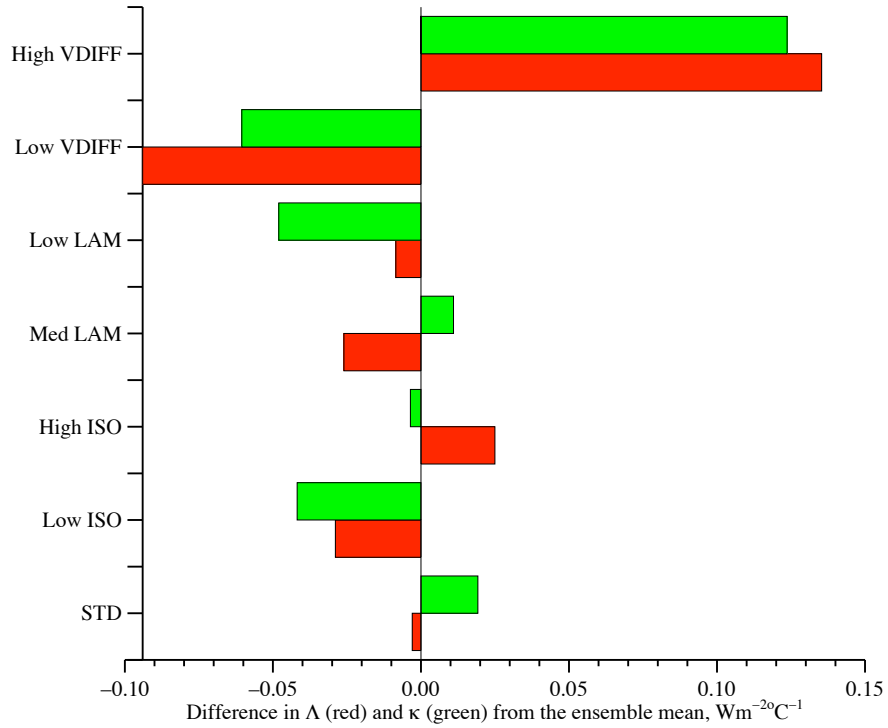


**Figure 4.7** *The change in the climate feedback paramater ($\Lambda$, red) and the ocean heat uptake efficiency ($\kappa$, green) for each ensemble member from the ensemble mean. Compensation is occuring between the two warming processes, if the individual contributions lie on opposite sides of the ensemble mean.*

One of the aims of looking at the climate sensitivity and ocean heat uptake efficiency was to discover if there was any compensation occuring between the two different warming factors. Compensation occurs when the changes in $\kappa$ and $\Lambda$ caused by the ocean parameter perturbations have opposite effects on the TCR. Raper *et al*. (2002) found that this form of compensation was occuring in CMIP2, although they noted that such compensation could be a chance artifact. Collins *et al*. (2006) did not find this type of compensation occuring in the atmosphere ensemble. The deviations in $\Lambda$ and $\kappa$ from the ensemble mean values are shown in figure 4.7 in red and green respectively. Compensation is occuring when the deviations in the two factors are opposite, such as in MedLAM. However, the ensemble members with the largest deviations in $\Lambda$ and $\kappa$ do not show any compensation. As the members with largest deviations are responsible for the TCR range, it can be concluded that there is no compensation between $\Lambda$ and $\kappa$ that acts to reduce the TCR range in the ocean ensemble. It should be noted that for the two most extreme ensemble members (LowVDIFF and HighVDIFF) the changes in $\Lambda$ are larger than the changes in $\kappa$, perhaps showing that changes in the climate feedback parameter dominate the range of TCR in the ocean ensemble, but more probably that the changes are of approximately equal importance.

## 4.9 Conclusions

The uncertainty in global mean surface air temperature response to an incremental increase in $CO_2$ due to ocean model parameter uncertainty in a complex AOGCM has been investigated using a 7 member perturbed physics ensemble. Variations in the transient climate response across the ensemble can be detected above the modelled internal variability at the 5% confidence level. Therefore ocean model uncertainty does cause uncertainty in the global mean temperature response to an increase in $CO_2$. This uncertainty in the transient climate response is small compared to both that caused by atmosphere model uncertainty and from all AOGCM uncertainties combined (as measured by Collins *et al*. (2006) and Cubasch *et al*. (2001) respectively). The ocean ensemble has been created to sample

the maximum extent of ocean model uncertainty. Some possible reasons for its failure to do so have been discussed. It seems likely that the ensemble does encompass most ocean model uncertainty, and hence, that the small relative effects of this uncertainty are a feature of HadCM3.

The loss of the additional imposed heat to both space and the deep ocean have been characterised (by the climate feedback parameter and the ocean heat uptake efficiency respectively). Ocean model uncertainty causes detectable uncertainty in the climate sensitivity, and therefore in the climate feedback parameter. The uncertainty in climate sensitivity due to ocean model uncertainty is an order of magnitude less than that due to atmosphere model uncertainty. There is also detectable uncertainty in the ocean heat uptake efficiency caused by the ocean model uncertainty. This is a similar amount of uncertainty as that caused by atmosphere model uncertainty. There is no compensation occuring between the two measures of heat loss that would explain the relatively small range of transient climate response seen in the ocean ensemble. Variations in the climate feedback parameter are as important, if not more so, than the variations in ocean heat uptake efficiency in determining the ensemble's range of transient climate response.

A summary of the detailed work of this chapter has been accepted for publication by Journal of Climate as Collins *et al*. (2007). This paper is included as appendix A, and also includes analysis of some additional flux-adjusted runs. This chapter has dealt solely with the global mean surface temperature changes that are seen in response to an increase in $CO_2$. Climate change is not spatially uniform, but has a regional pattern. This pattern has uncertainty associated with it (Giorgi *et al*., 2001). The next chapter will describe the spatial patterns of the effects of ocean model uncertainty on the climate change signal.

# CHAPTER 5

# Spatial variations in the climate change signal

## 5.1 Introduction

This thesis has so far documented the creation of a perturbed ocean physics ensemble and analysed the global mean transient climate response to investigate the effects of ocean model uncertainty in time-dependent climate projections. The CMIP2 scenario of an increase in $CO_2$ of 1% per year has been used to allow comparison of this ensemble to work published about other ensembles. Chapter 3 explained the creation of the ensemble and looked at the uncertainty in the preindustrial climate state caused by ocean model uncertainty. Spatial patterns of the preindustrial ensemble spread were investigated. The previous chapter introduced the climate change experiment. It investigated the simplest measure of climate change - the global mean temperature change - and found that the signal spread in the transient climate response was larger than that expected from internal variability, but smaller than that caused by atmosphere model uncertainty and AOGCM uncertainty in general. The previous chapter also invoked a simple diagnostic model to interpret these changes. It was found that uncertainty in the feedback strengths (as measured by the climate feedback parameter) were as important as changes in the effectiveness of vertical heat transfers in the ocean (measured by the ocean heat uptake efficiency). Characterising each ensemble member by its global mean temperature change reduces the ensemble to just seven numbers, and ignores the vast majority of available information.

The spatial pattern of climate change is of great interest. The IPCC devotes only 7 pages to projections of the global mean temperature change, whilst spending a whole chapter of regional climate projections (Giorgi *et al.*, 2001). One reason for this interest is that few individual regions will experience the

global mean change. However, the climate change signal itself must first be understood and explained, before the uncertainty in the climate change signal caused by the effects of ocean model uncertainty can be investigated. Understanding the climate change signal is a large area of ongoing research in the climate community, and many features of the climate change signal are not fully understood or are model-dependent. Therefore, this work will only concentrate on the large-scale and accepted climate change processes. Sections 5.2 - 5.8 are a description of the climate change signal. For the purposes of this chapter, the climate change signal will be computed as the contemporaneous difference of the final 20 years of the experiment (see section 4.3 for further discussion of the merits of different definitions of the climate change signal).

Once the ensemble mean climate change signal has been described, then the signal spread due to the ocean model uncertainty can be investigated. It has been shown in chapter 4 that ocean model uncertainty causes signal spread in the global mean surface temperature response. This signal spread is not spatially uniform. Its pattern will be investigated in section 5.10. The effects of ocean model uncertainty on other surface changes will the be investigated, such as precipitation changes, cloud feedbacks (both in section 5.12) and sea ice changes (section 5.11).

The analysis then moves to look in more depth at the effects of ocean model uncertainty in climate change signal in the ocean, initially with global mean depth profiles, and then moving onto the spatial pattern of heat content changes. Model simulations of the slowdown in the thermohaline circulation differ greatly (Gregory *et al.*, 2005b), and the final section of this chapter will investigate the effects of ocean model uncertainty on the slowdown.

## 5.2 The climate change signal and internal variability

The previous chapter has investigated the effects of parameter perturbations to the global mean response, and found only small effects compared to the effects seen by Collins *et al.* (2006) to atmo-

sphere model perturbations. The ocean parameter perturbations are not expected to cause changes to the model response that are completely uniform. They will have a spatial pattern, in part because the ocean does not cover the whole surface of the earth. Therefore it is expected that there will be changes in the regional pattern of climate change. The comparatively small global mean effects seen in the ensemble might also be explained by looking at the spatial patterns: there could be compensating regional temperature differences and hopefully the important processes can be determined from their regional effects.

However before an investigation into the differences caused by the perturbations can be performed, it is necessary to understand the mean climate change signal upon which these differences occur. The following sections are devoted to describing the ensemble mean climate change signal. This will include comparisons to modelled internal variability to determine where the climate change signal is detectable relative to the the internal variability. This chapter will use the second method of determining the climate change signal described in section 4.3. The signal is calculated as twenty year average of the contemporaneous difference between the 1% run and the control run at the end of the experiment (definition 2 in Cubasch *et al.* (1992)):

$$\Delta V_{2\times CO_2}(x,y) = [V_{1\%}(x,y,t)]_{561}^{580} - [V_{cont}(x,y,t)]_{561}^{580} \tag{5.1}$$

where $\Delta V_{2\times CO_2}(x,y)$ is the spatial climate change signal for variable $V$. $V_{1\%}$ is the 1% run, $V_{cont}$ is the control run and $[V]_{561}^{580}$ means the average between years 561 to 580 (the last 20 years of the increasing $CO_2$ experiment). This section is primarily devoted to describing the ensemble mean climate change signal, but first the modelled internal variability will be investigated, because it will be used to determine the significance of the climate change signal.

### 5.2.1 Modelled internal variability on 20 year timescales

The climate varies at all timescales due to its chaotic, nonlinear nature (Lorenz, 1967). The climate change signal has been defined to remove as much noise (and climate drift) as possible, and still allow

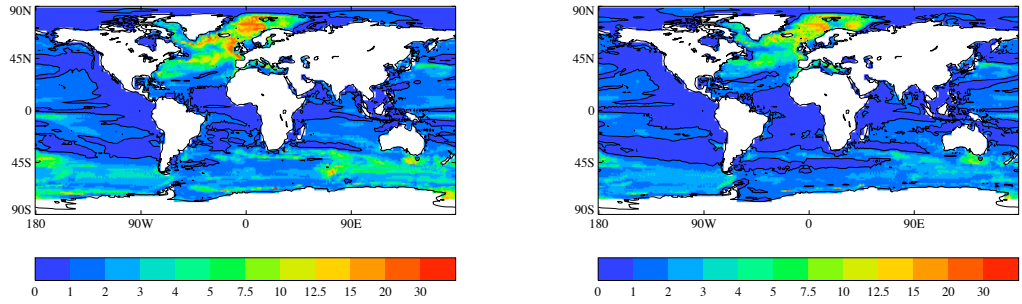


(a) Source: HadCM3 1000yr Control Run

(b) Source: Ocean Ensemble Control Runs

**Figure 5.1** *The standard deviations of modelled internal variability in 20 year mean mixed layer depth (in m), estimated from 2 different sources*

simple computation (section 4.3). Some of the differences between the climate change signals will still arise from modelled internal variability. In the previous chapter, three different methods were used to estimate the modelled internal variability in the global mean annual temperature at 20 year timescales. The results returned from the 3 methods were the same. An estimate of modelled internal variability on 80 year timescales was required to determine the significance of changes between the mean of the 7 control runs, so the independent multi-millenia control run of Collins *et al.* (2001) was utilised (section 3.5.1). Section 3.5.1 also describes the two statistical tests used to detect changes that are significantly larger than modelled internal variability at the 5% confidence level - an f-test and a z-test.

The modelled internal variability for all the diagnostics and at each location can be estimated from the multi-millenia control run of HadCM3 described by Collins *et al.* (2001). This model is set up using the standard configuration, but without the interactive sulphur cycle. Section 3.5.12 has shown that the interannual variability of the different ensemble members varies, but not significantly. Therefore another possible source for an estimate of the modelled internal variability of the ensemble would be the combination of the 20 year anomalies from all the control runs (using eq. 4.7). This estimate would incorporate any changes in the modelled internal variability arising from the parameter perturbations.

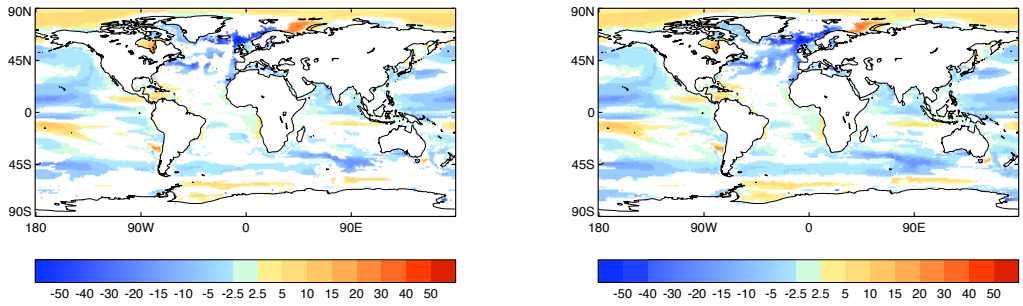


(a) Source: HadCM3 1000yr Control Run

(b) Source: Ocean Ensemble Control Runs

**Figure 5.2** *The detectable climate change signal in annual mean mixed layer depth (in m), when compared to estimates of modelled internal variability from two different sources. (a) is estimated from a millennium long HadCM3 control run and (b) is estimated from the control runs of the ocean ensemble using 4.7.*

for each source, the internal variability is calculated by subdividing the run into a series of independent 20 year long samples, to form a distribution. The standard deviation of the distribution created from both sources are shown in figure 5.1. It can be seen that there are differences, especially in the Southern Ocean and North Atlantic.The differences between these two panels could be caused by the parameter perturbations.

A sample variable has been analysed to test the sensitivity of the future results of this chapter to different estimates of natural variability. Figure 5.2 shows the ensemble mean climate change signal in annual mean mixed layer depth that is detectable from the two estimates of internal variability at the 5% confidence level. Although the exact fraction of the climate change signal that is detectable changes with the different estimates of modelled internal variability, the pattern of the detectable signal is qualitatively similar.

For the rest of this chapter, the modelled internal variability will be estimated from the ensemble control runs using eq. 4.7. Although this choice may have a small impact on fraction of the climate change signal detected, it will not change the shape of the signal, and therefore will not affect the conclusions drawn from investigating the climate change signals. It should be noted that this approach

assumes that increasing $CO_2$ concentrations do not alter the variability of the model, which may not be the case (see Collins (2000) and Timmermann *et al*. (1999) for examples of El-Niño-southern-oscillation variability changes under greenhouse warming, yet e.g. Keeley (2006) suggests this is not the case for winter surface air temperature variability).

## 5.3 Ensemble mean surface temperature changes

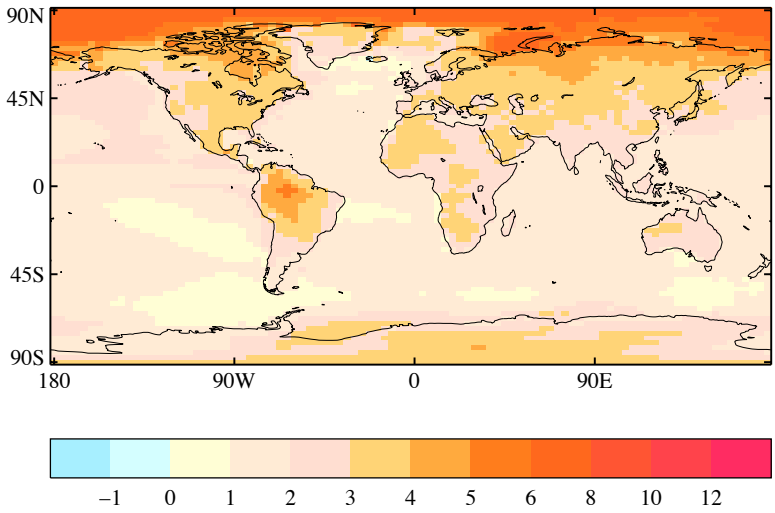


**Figure 5.3** *The ensemble average climate change signal in surface air temperature (difference between the 20 year mean centred on doubling of $CO_2$ and the mean of the control climate).*

Surface temperature is the focus of much work into climate change. Figure 5.3 shows the ensemble mean change in surface air temperature averaged over the twenty years centred on the time of doubling of $CO_2$. It can be seen that the whole globe experiences an increase in temperature, although the magnitude of the warming varies regionally. Before a full description of the spatial pattern is undertaken the significance of the changes must be considered. Figure 5.4 shows the temperature change in terms of the standard deviation of modelled internal variability (calculated from eq. 4.7 and described

in section 5.2.1). It can be seen from this figure that the changes in surface air temperature over the whole globe are greater than 2 standard deviations of modelled internal variability, except for the East Greenland Current (shown in purple). This occurs as a result of a small signal and large variability at these locations. If the variability was normally distributed, then 95% of independent samples would fall within 2 standard deviations, so any signal larger than this is a detectable consequence of the increase in $CO_2$ at the 5% confidence level.

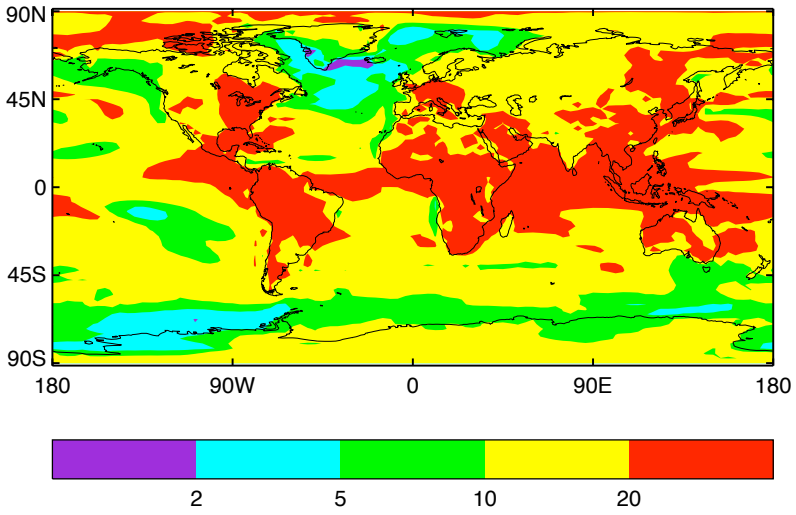


**Figure 5.4** *The ensemble average climate change signal in surface air temperature, expressed in standard deviations of natural variability.*

The temperatures over land increase more than those over the ocean (Washington and Meehl (1989) and Meehl *et al*. (1993)). This is primarily caused by the difference in heat capacity of the two surfaces, but also influenced by differing rates of latent heat loss caused by the different surface moisture contents. The warming is strongest in the northern high latitudes, and weakest in parts of the Southern Ocean and the North Atlantic (Thompson and Schneider (1982) and Bryan *et al*. (1988)). The majority of the Arctic warms by more than 5°C. Holland and Bitz (2003) define the polar amplification as the ratio of the warming of the Arctic north of 75°N to the global mean temperature change, which has a

mean ratio of 2.6 for the ocean ensemble. The equatorial part of South America warms dramatically. This warming is because of a suppression of convection over the area, allowing more solar radiation to be incident on the surface (Timmermann *et al.*, 1999). This warming of Amazonia is a feature of HadCM2 and HadCM3 (Keen and Murphy (1997) and Johns *et al.* (2003) respectively), but is weaker in some other climate models (e.g. Noda *et al.* (2001))

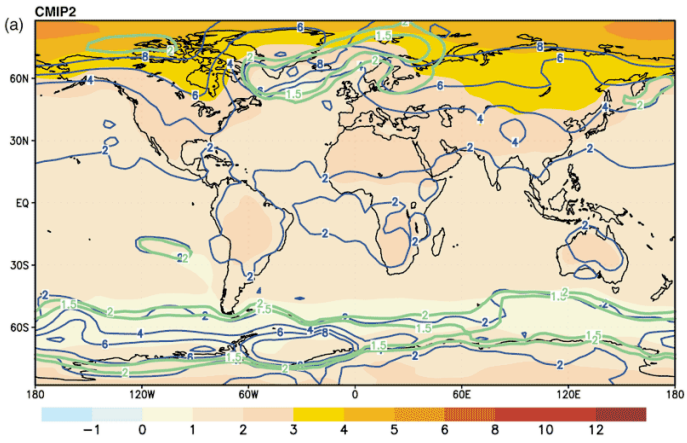


**Figure 5.5** *The CMIP2 ensemble average climate change signal in surface air temperature (figure 9.10a from Cubasch* et al. *(2001)). The blue contours show the range of the multi-model ensemble, and the green contours show the multi-model mean change divided by the multi-model standard deviation (values greater than 1 have a consistent model response).*

The CMIP2 project collated the results from global warming simulations with 20 different GCMs. The ensemble mean spatial pattern is presented by Cubasch *et al.* (2001), and is shown as figure 5.5. The magnitude of the signal seen in the ocean perturbed physics ensemble is spatially consistent with these results over the majority of the globe. Some slight differences occuring in the ocean ensemble are more polar amplification, stronger Amazonian warming and a less zonal pattern in the Southern Ocean. Throughout in the globe, the perturbed physics ensemble falls within the range of the models in the CMIP2 assessment. Although this was expected (HadCM3 is a member of the CMIP2 ensemble), it is reassuring that the ocean ensemble gives a recognisable warming pattern.

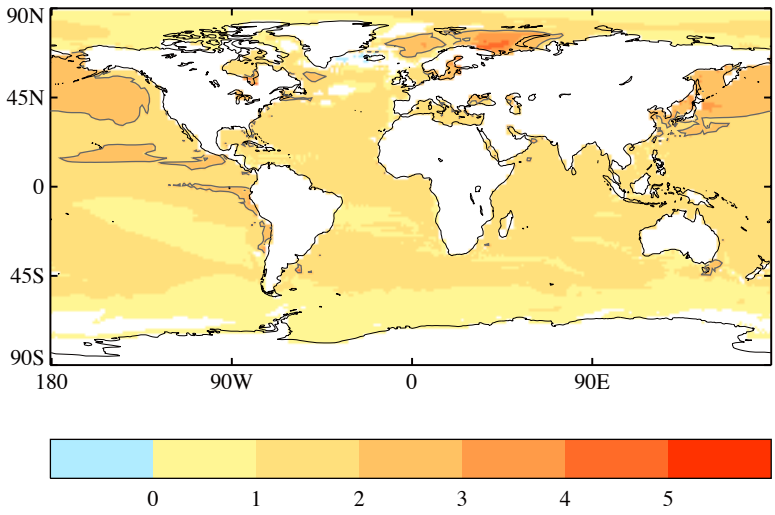


**Figure 5.6** *The ensemble average climate change signal in surface sea temperature (in°C). The black contour shows a climate change signal of 2°C. Ocean areas are shown in white when the climate change signal is not significantly different from modelled internal variability.*

## 5.4 Ensemble mean sea surface changes

The change in sea surface temperature (SST) under climate change is shown in figure 5.6. The changes are very similar to the changes in the surface air temperature. However in the Arctic Ocean and off the coast of Antarctica, the warming is dramatically different from the change in surface air temperature. The sea-ice (which thins under climate change, but keeps a similar fraction of the ocean covered) acts as a barrier disconnecting the atmosphere from the ocean surface in the winter time, which is the season of the greatest climate change warming in the high latitudes (Curry *et al.*, 1995). Both the tropical Atlantic and Pacific show preferential warming to the eastern side of the basin (Collins, 2000). The North Pacific (especially the region of the Kuroshio) shows more warming than the corresponding latitudes in the North Atlantic (Manabe and Wetherald, 1980). This is caused by a reduction in the strength of the thermohaline circulation in the North Atlantic, and the northward heat transport

associated with it.

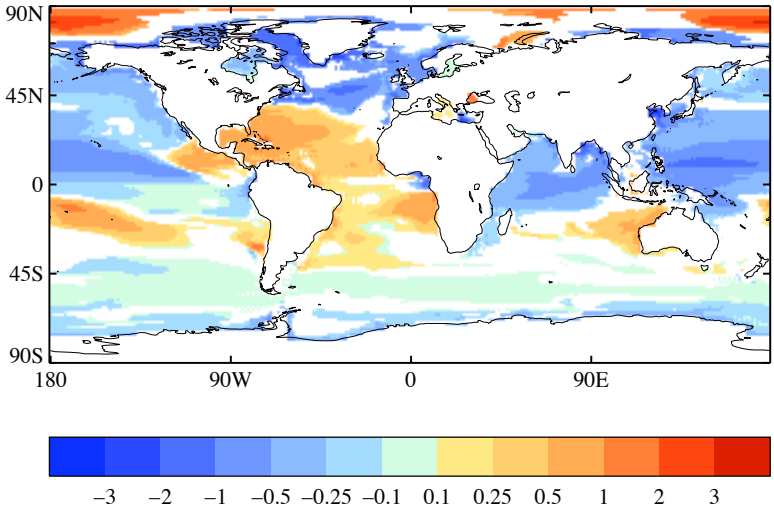


**Figure 5.7** *The ensemble average climate change signal in surface sea salinity (in PSU). Ocean areas are shown in white when the climate change signal is not significantly different from modelled internal variability.*

The changes in sea surface salinity (shown in figure 5.7) are not as uniform as the changes in sea surface temperature. Some areas of the globe freshen significantly compared to modelled internal variability, whilst others become significantly saltier. The North Atlantic freshens, which will have impacts on the meridional overturning circulation (Gregory *et al.*, 2005b). The tropical Atlantic becomes saltier. This saltier water is advected northwards, which may act to slow the reduction of the thermohaline circulation (e.g. Latif *et al.* (2000)).

Freshening occurs in the ITCZ in the West Pacific (although not in the maritime continent itself). Changes in salinity underneath the South Pacific convergence zone are not significant. This freshening, and the salinification of the middle of the South Pacific, are consistent with an increase and extension eastwards of the hydrological cycle in the equatorial Pacific (Timmermann *et al.*, 1999). This can be confirmed by inspecting the change in precipitation caused by an increase in $CO_2$.

## 5.5 Ensemble mean precipitation changes

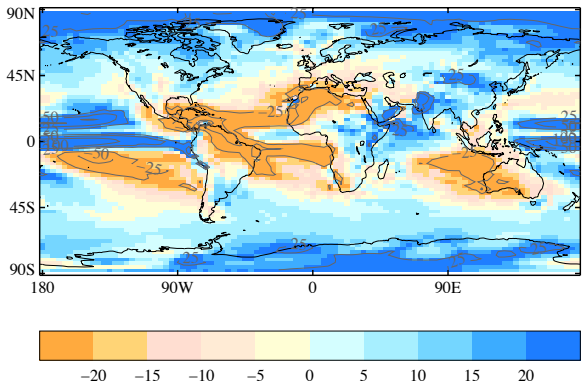


**Figure 5.8** *The ensemble average fractional change in precipitation in the perturbed ocean physics ensemble at the time of doubling of $CO_2$ (as a %). The black contours are placed at -50%, -25%, 25% and 50%.*

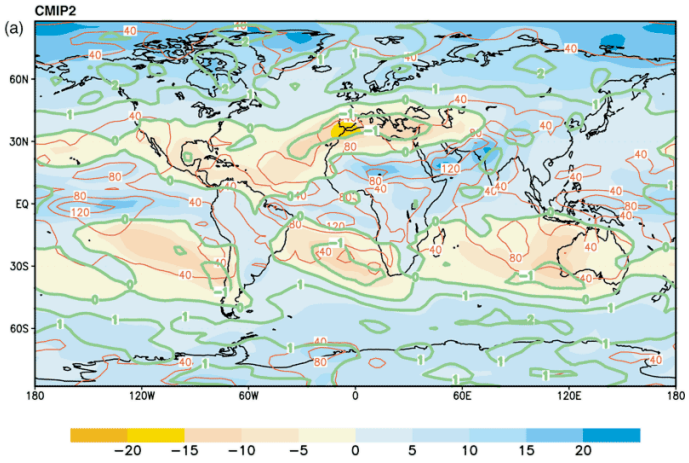


**Figure 5.9** *The ensemble average fractional change in precipitation in the CMIP2 ensemble at the time of doubling of $CO_2$ (as a %). The red lines show the range of the ensemble and the green lines indicate the robustness of the signal (Cubasch* et al.*, 2001).*

The ensemble mean fractional change in precipitation due to increasing $CO_2$ is shown in figure 5.8. There is increased precipitation in the west- to mid-Pacific. This would mean an intensified and eastward shifted Walker circulation, leading to descent and a reduction in precipitation over South America. The reduction in precipitation seen in the Caribbean and northern South America in figure

5.8 explains the increase in salinity seen in fig. 5.7. Figure 5.9 shows the changes in precipitation for the CMIP2 ensemble. The main features of the spatial distribution of changes in precipitation seen in the CMIP2 ensemble compare well with those from the perturbed physics ensemble. There are differences in the synoptic-scale details, but the changes in the CMIP2 ensemble have high levels of uncertainty. The green isolines show the multi-model mean divided by the multi-model standard deviation. Areas where the magnitude of this ratio is greater than 1 show that the majority of models have a consistent direction of signal.

## 5.6 Ensemble mean ocean heat uptake

More heat enters the climate system, because of the increase in $CO_2$. It is slowly absorbed by the ocean. The effectiveness with which the ocean stores heat is an important facet of the climate system's response to an imposed radiative forcing. The ocean heat uptake efficiency, $\kappa$, was used in the previous chapter to diagnose the global mean behaviour of the ocean heat storage. The spatial pattern of the change in heat content can impart information about which processes are moving the most heat.

The ensemble mean spatial pattern of change in heat content is shown in figure 5.10. The change in heat content, $\Delta HC$, is calculated from the changes in potential temperature:

$$\Delta HC(x,y) = \rho c_p \int_{-H}^{0} \Delta\theta(x,y,z)dz \tag{5.2}$$

where $\rho$ is the average density of sea water (1026 kgm$^{-3}$), $c_p$ is the specific heat capacity of sea water at a constant pressure (3988 Jkg$^{-1}$°C$^{-1}$), and $\Delta\theta(x,y,z)$ is the 3D field of the climate change signal in potential temperature. The change in heat content calculated in this way is the amount of additional energy stored in the water column. It can be seen from fig 5.10 that the largest changes in heat content occur in the North Atlantic. These occur in the regions of deep convection in the Labrador and Greenland-Iceland-Norwegian (GIN) seas. The large change in heat content south of Iceland is caused by the warm, deep water being advected over the Iceland-Scotland ridge (which is shallow

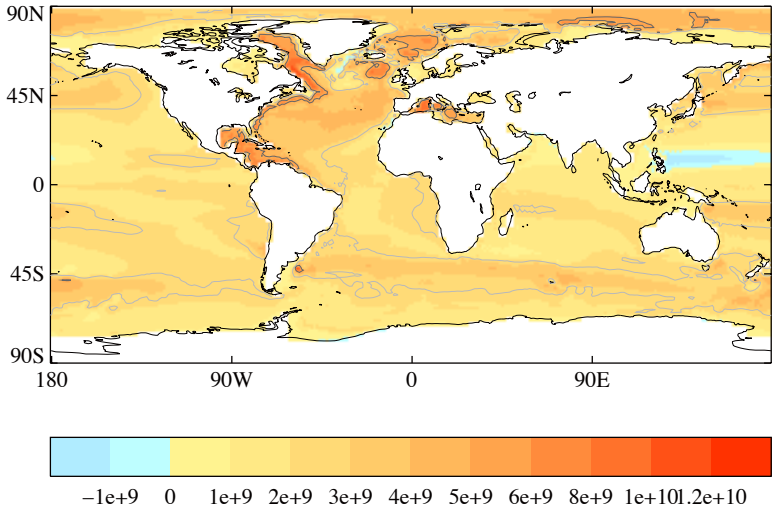


**Figure 5.10** *The ensemble mean change in heat content (unit: $Jm^{-2}$). The light grey contour is at $2.5 \times 10^9 Jm^{-2}$ and the dark grey contour is at $5 \times 10^9 Jm^{-2}$. Note: the colour scale is not linear, and no significance testing has been performed.*

so does not contain as much heat). The deep western boundary current in the North Atlantic can be clearly seen along the coast of North America. It carries the relatively warm, deep waters from the formation regions down to the Caribbean. There is also a change in heat content greater than $2.5 \times 10^9$ $Jm^{-2}$ in the Southern Ocean, and the North Pacific. These are both regions of strong vertical heat transfers, and therefore uncertainty in the preindustrial climate (section 3.5.2). There is a reduction in heat content in the tropical West Pacific that is related to a equatorward shift in the northern extent of the West Pacific warm pool. The large increases in the heat content occur in the Northern Atlantic convection zones, which are also locations of the sinking branch of the thermohaline circulation.

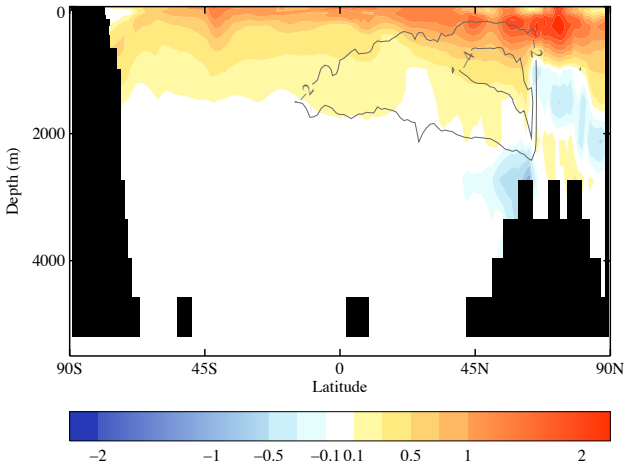


**Figure 5.11** *The ensemble mean change in the zonal mean potential temperature (colours, °C) and meridional streamfunction (contours, Sv) in the Atlantic. The streamfunction changes are only shown north of 30°S to prevent confusion between the Thermohaline circulation and the Ekman driven circulation of the Antarctic Circumpolar Current. Note that the colour scale is not linear and that no significance testing has been performed.*

## 5.7 Ensemble mean thermohaline circulation changes

The thermohaline circulation (THC) is a density-driven circulation, which ventilates most of the ocean's deep water (Toggweiler and Key, 2001). It is therefore important in determining the rate that heat enters the deep ocean. The THC is characterised by sinking in the Labrador and GIN seas, and then a southwards flow at depth throughout the Atlantic (see fig. 1.4 for a schematic of this). The water then upwells in the Southern Ocean (Russell *et al.*, 2006), and returns north as a surface flow.

Figure 5.11 shows the zonal average potential temperature changes in the Atlantic. The majority of the Atlantic ocean above 1000m suffers a warming of 0.25°C or greater. However the strongest warming is confined to a shallow layer near the surface. The largest warming occurs in the North Atlantic (50-80°N) in the subsurface layers (50-500m). The change in the zonally averaged meridional streamfunction is shown by the contours in figure 5.11. The maximum of the thermohaline circulation weakens by 4 Sverdrups, and shallows slightly at 60N (the ensemble mean starting state has a maximum strength of 19 Sv). This is similar to the reduction seen by Wood *et al.* (1999) in HadCM3.

Wood *et al*. (1999) also observed variations in the location of the deep convection leading to regions of localised cooling, such as the surface cooling over west Iceland seen in figure 5.6. Thorpe *et al*. (2001) investigated different mechanisms for the THC reduction in HadCM3. They found that changes in the surface heat fluxes in the North Atlantic are responsible for the THC reduction.

## 5.8 Ensemble mean sea ice changes

It was noted earlier that there are regions in which the climate change signal in SST is different from the changes in the air temperatures at the same location. It was stated that these differences occured in the regions where there was sea-ice cover. However the sea-ice coverage is expected to decrease under increasing $CO_2$ (Curry *et al*., 1995), and observations of reduced of sea-ice coverage are one of the most detectable changes caused by an increase in $CO_2$ (Serreze and Francis, 2006). Sea-ice extent is computed by determining whether a gridbox is covered by sea ice, and then determining the edge of the sea-ice coverage. A gridbox is defined as being covered by sea-ice, if it has a fractional coverage greater than 15% (following McAvaney *et al*. (2001) and Flato and Participating CMIP Modelling Groups (2004)). The minimum sea ice extent surrounds those gridboxes that are icy in every month of the average year and the maximum ice extent surrounds those which are covered for at least one month in the average year. Figure 5.12 shows the changes in maximum and minimum ice extent of the sea ice coverage in the northern hemisphere (left) and the southern hemisphere (right). The blue line shows the sea-ice extent in ensemble mean of the control runs. The red line shows ensemble mean sea-ice extent in the 1% runs at the time of doubling of $CO_2$. There is a reduction in the sea-ice extent in both the Arctic and Antarctic throughout the year. In both hemispheres, there is still a large region of sea-ice cover in their respective winters (the season when most warming occurs). This sea ice cover prevents ocean-atmosphere interactions and explains the differences seen in the air and sea surface temperatures.

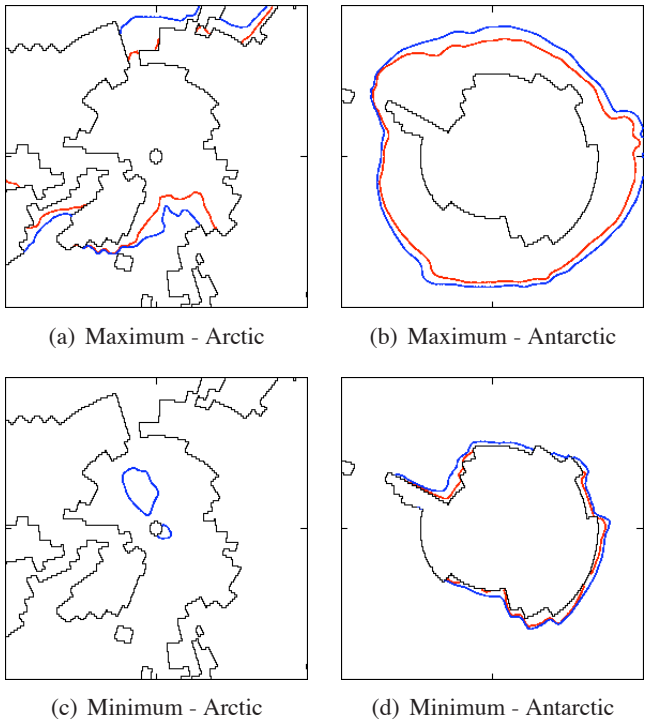

(a) Maximum - Arctic (b) Maximum - Antarctic

(c) Minimum - Arctic (d) Minimum - Antarctic

**Figure 5.12** *Ensemble mean sea ice extent in the respective summer and winters for both hemispheres. The sea ice extent in the ensemble mean of the control runs is shown as a blue line. The red line shows the extent at the time of doubling of $CO_2$.*

The steady increase in $CO_2$ means that there is no permanent sea ice cap in the Arctic at the time of $2\times CO_2$ in any ensemble member (there is minimal coverage in the preindustrial states, see section 3.5.9). This is not the case in the Southern Hemisphere, although there is a reduced amount of permanent ice coverage, especially in the Weddell Sea.

## 5.9 Ensemble spread in the climate change signal (signal spread)

It was noted at the beginning of this chapter that it is necessary to understand the ensemble mean climate change signal, before the ensemble spread can be analysed. The previous sections have been devoted to describing the ensemble mean climate change pattern and putting it in context with other simulations, both from HadCM3 and from other AOGCMs. It has been shown that the whole globe does not warm uniformally. There are minima of warming in the Southern Ocean and the North Atlantic and the warming is amplified in the northern polar regions. Changes in sea surface salinity and

precipitation are mainly consistent with an enhanced hydrological cycle and there is uneven warming of the equatorial Pacific. The surface warming minima occur in regions of large ocean vertical heat transfers, effecting the nature of the circulation in these regions - which can be seen by a slowing down in the thermohaline circulation. These are also the regions, which exhibit the most uncertainty in the preindustrial state (chapter 3), so it could be expected that there would be significant uncertainty in the climate change signal in these regions.

It has previously been shown that there are large regional variations in the pattern of climate change between different AOGCMs (Cubasch *et al*., 2001). The spatial patterns of climate change seen in HadCM3 under varying scenarios are very similar (Johns *et al*., 2003). Hence, the majority of these inter-model variations must arise from model and initial condition uncertainty. Collins *et al*. (2006) have shown that these regional variations are partly due to atmosphere model uncertainty, the regional effects of ocean model uncertainty have not been investigated. The rest of the chapter will look at the range in the climate change signal (calculated using eq. 5.1) that is seen across the ensemble - this shall be termed “signal spread”.

## 5.10 Signal spread in the surface temperature

The range in surface air temperature climate change signal across the ensemble is shown in figure 5.13. This is plotted on the same scale as fig. 3.6, which shows the range in preindustrial surface temperature across the ensemble. The areas for which no values have been presented are those areas which the signal spread is not detectable from the spread expected from modelled internal variability (computed using a one-tailed f-test at the 5% confidence level). The signal spread is smaller than the preindustrial ensemble spread. This is not surprising as the preindustrial spread is the result of 500 years of integration instead of 80 years as for the signal spread. The temporal evolution of the ensemble spread will be discussed in depth in the next chapter.

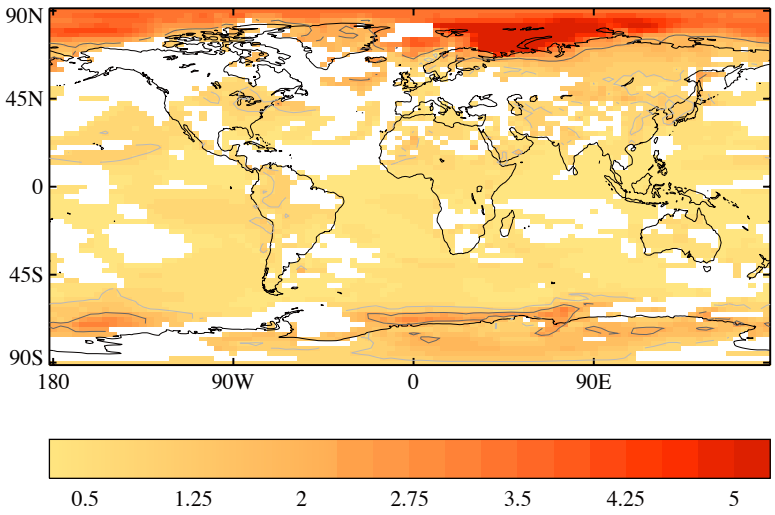


**Figure 5.13** *The ensemble range of the climate change signal in surface air temperature (unit: °C). The range is only shown if detectable from internal variability at the 5% level. The light grey contour is at 1°C and the black contour is at 2.5°C. An analogous plot of spread in the control runs is shown as figure 3.6*

The region of largest signal spread is the Barents Sea, where the range across the ensemble is greater than 5°C. The large spread in this region is related to uncertainty in the sea ice edge, which will be shown later in section 5.11. There is larger signal spread in the northern hemisphere than the southern, and larger signal spread over the land than the ocean. Both of these features can also be seen in the ensemble mean climate change signal (fig. 5.3) - i.e. where the signal is large, the spread is also large.

It is important to relate the signal spread to other factors of relevance. This can be done by comparison to other possible spreads - figure 5.14 shows ensemble spread as a fraction of the modelled internal variability. This comparison is especially interesting as it puts the local signal spread into context of the observable climate for that region. It can be seen that for the vast majority of the globe the range of climate change signals from the ensemble is between two and ten times the magnitude of the modelled internal variability. The ensemble spread is an order of magnitude greater than the internal variability

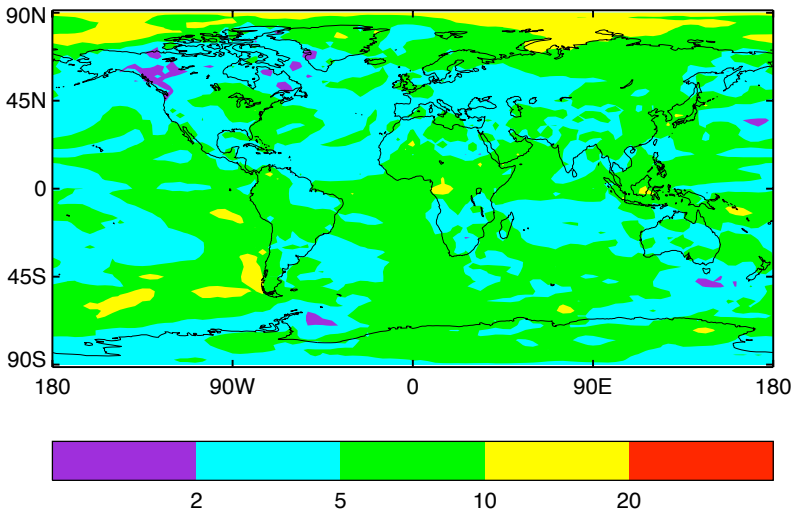


**Figure 5.14** *The ensemble spread from fig. 5.13 expressed as a fraction of modelled internal variability.*

in the Arctic and regions of the Southern Ocean. (It should be noted that the significant regions in fig. 5.13 do not correspond to the regions where the signal spread is more than 2 standard deviations of internal variability in fig. 5.14. This is because fig. 5.13 compares the standard deviation of the climate change signal to that of internal variability using an f-test to determine significance (section 3.5.1), rather than the range as in fig. 5.14.)

Figure 5.15 shows the signal spread as a percentage of the local ensemble mean signal. There are regions where the signal spread is greater than the ensemble mean signal. This does not imply that the sign of the change change signal varies across the ensemble, because the ensemble mean is not necessarily in the centre of the range. The aim of the figure is to give an impression of the relative importance of the uncertainty in the climate change signal. The consistency of the signal could be examined by normalising the ensemble mean climate change signal by the ensemble standard deviation - this ratio is shown as the green lines on fig. 5.5 for the CMIP2 ensemble.

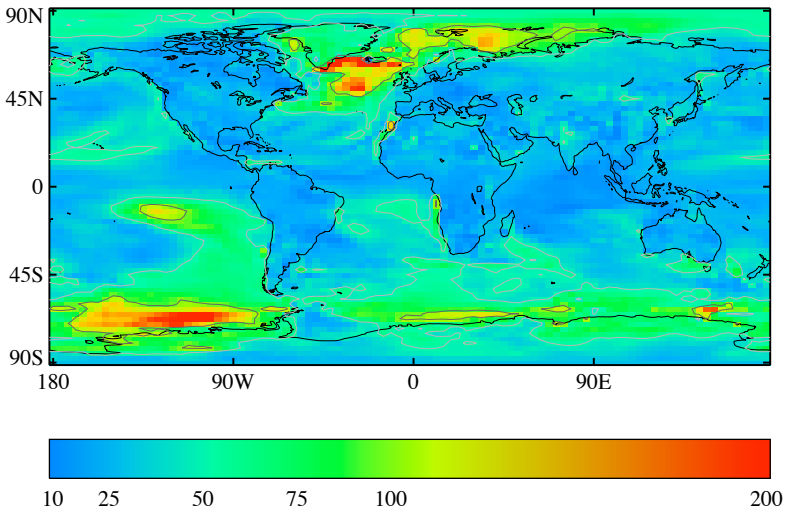


**Figure 5.15** *The range in surface temperature climate change signals seen in the ensemble, expressed as a percentage of the ensemble mean climate change signal. The absolute values of both are shown in figures 5.13 and 5.3 respectively. The light grey contour is at 50%, the dark grey contour is at 100%.*

The spatial pattern in the percentage signal spread (shown in fig. 5.15) is similar to the pattern of preindustrial ensemble spread (fig. 3.6). The largest relative spread occurs in the Ross Sea, North Atlantic and the Barents Sea. The large percentage signal spread in the Ross and Barents Seas are related to uncertainty in the location of the sea ice edge, which will be shown in section 5.11. There is a tongue of large relative uncertainty extending into the South Pacific, although the tongue in the North Pacific is not as well defined. These tongues are reminiscent of the preindustrial ensemble spread (fig. 3.6). In the tropics (30°S - 30°N), there is a correlation coefficient, $r$, of 0.6 between the two patterns. This strongly implies a connection between the percentage signal spread and the preindustrial ensemble spread. Two possible reasons for this connection are that the signal spread is caused by uncertainty in the initial climate state or that the mechanisms that cause the spread in the preindustrial climate state also cause spread in the signal. These two possible links will be examined further in chapter 6.

### 5.10.1 Compensation in the surface temperature responses

The previous chapter has shown that there is less TCR signal spread in the ocean ensemble than in both the atmosphere ensemble of Collins *et al*. (2006) and the ensembles of opportunity of IPCC TAR (Cubasch *et al*., 2001) and IPCC AR4 (presented in Collins *et al*. (2006)). It was suggested that the reason for this could be regional compensation occuring in the ocean ensemble. How compensating regional variations cause a reduction of the global mean spread is perhaps explained best with an example. Suppose there are only 2 ensemble members and that there is inter-hemispheric compensation occuring: in ensemble member $A$ the northern hemisphere is 5°C warmer than in ensemble member $B$, but the southern hemisphere is 4°C cooler. The global mean spread is only 0.5°C, but there are large regional differences.

Testing whether exact regional compensation is occuring in ocean perturbed physics ensemble is complicated, however a simple test is to look for negative correlations between different regions. This does not look into the degree of compensation occuring or whether the two regions exactly cancel. However a negative correlation of some form would always need to exist, if exact compensation was occuring. The Earth's surface was divided into 41 different regions to perform this analysis: the 23 land regions defined Giogri and Francisco (2000) and used in regional climate change section of the IPCC TAR (Giorgi *et al*., 2001), and 18 ocean surface regions. The location of these regions is shown in figure 5.16.

The surface air temperature was averaged for each region for each ensemble member, giving 7 values for each region. Figure 5.17 shows the ensemble correlation coefficients, $r$, between the area-averages for all the regions. Each region is listed on both the horizontal and vertical axis, using the abbreviations from fig. 5.16. Each region must be perfectly correlated with itself, and hence there is a black line (signifying that $r = 1$) on the leading diagonal. The upper, right portion shows the correlation coefficients for the final 20 years of the control integrations. Any correlations in this portion must

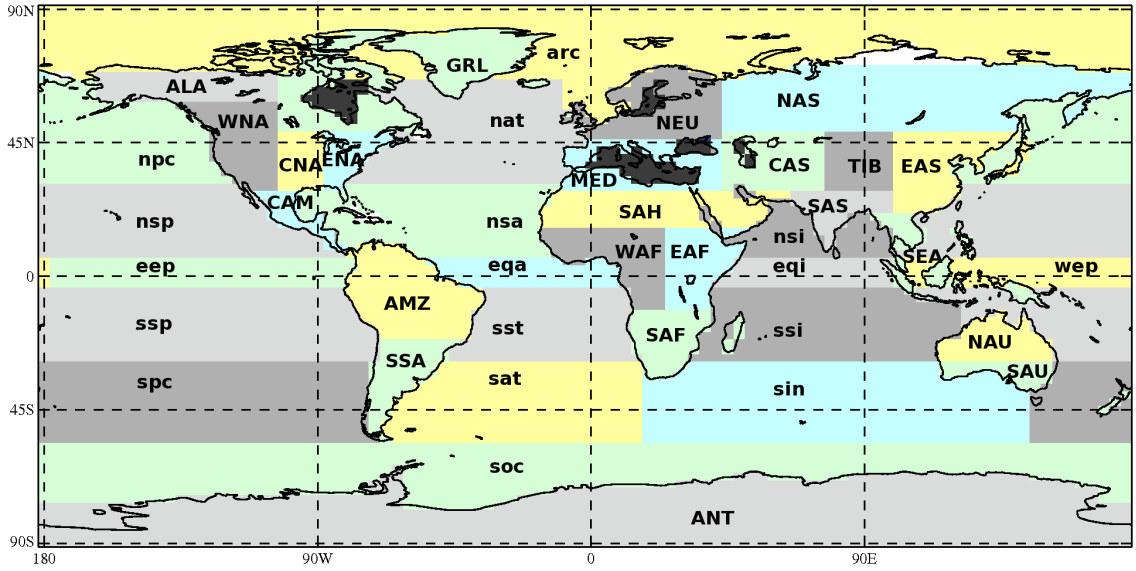


| | | | | | |
|---|---|---|---|---|---|
| ALA | Alaska | SAF | Southern Africa | ssp | S. Subtropical Pacific |
| WNA | Western North America | ANT | Antartic | spc | South Pacific |
| CNA | Central North America | NAS | Northern Asia | soc | Southern Ocean |
| ENA | Eastern North America | TIB | Tibet | nat | North Atlantic |
| GRL | Greenland | EAS | Eastern Aisa | nsa | N. Subtropical Atlantic |
| CAM | Central America | SAS | Southern Asia | eqa | Equatorial Atlantic |
| AMZ | Amazonia | SEA | South East Asia | sst | S. Subtropical Atlantic |
| SSA | Southern South America | NAU | Northern Australia | sat | South Atlantic |
| NEU | Northern Europe | SAU | Southern Australia | nsi | N. Subtropical Indian |
| MED | Mediterranean | arc | Arctic | eqi | Equatorial Indian |
| CAS | Central Asia | npc | North Pacific | ssi | S. Subtropical Indian |
| SAH | Sahara | nsp | N. Subtropical Pacific | sin | Southern Indian |
| WAF | West Africa | eep | E. Equatorial Pacific | mar | Marginal Seas |
| EAF | East Africa | wep | W. Equatorial Pacific | | *(Shown in Black)* |

**Figure 5.16** *The geographical regions used to determine whether compensation is occuring. The land regions (denoted by capital abbreviations) are those of Giogri and Francisco (2000). The ocean regions (lower case abbreviations) have been defined especially for this work. The marginal seas are not labelled, but are shown in black.*

be occuring from natural variability (rather than climate change). There are both positive and negative correlations in the upper, right portion of the figure, so we would expect some naturally occuring compensation. The lower, left portion of the figure shows the correlation coefficient between the regions for the climate change signal. It can be seen that there are no appreciable negative correlations occuring in the climate change signal, and therefore there can be no compensation occuring.

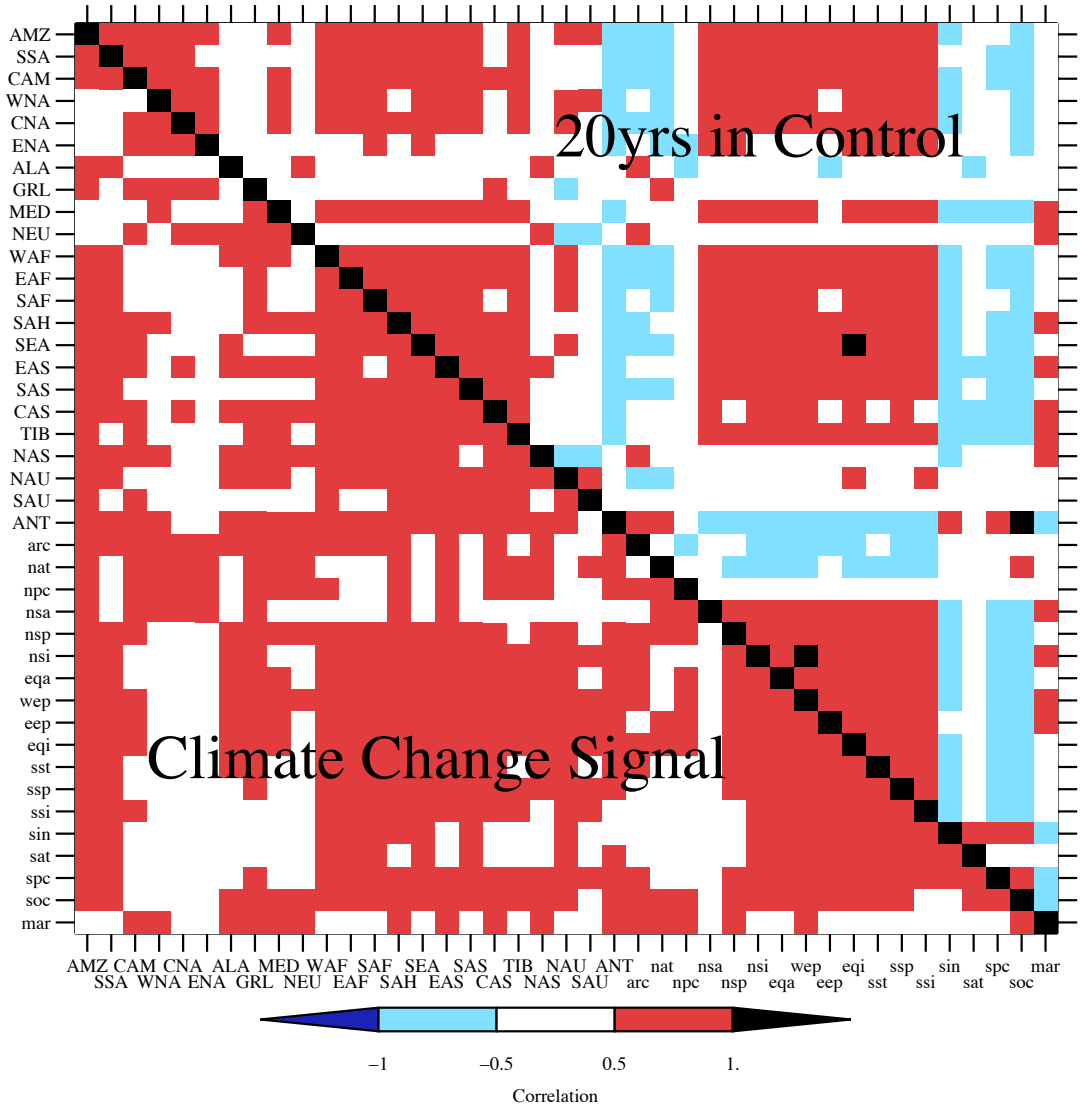


**Figure 5.17** *The correlation between anomalous surface air temperature changes in each of the regions shown in figure 5.16. The figure is divided into two portions. The upper right shows the correlations for a sample 20 years taken from the control runs. The lower left shows the correlations for the climate change signal. Red shows a positive correlation, blue shows a negative correlation. The correlation is measured by the $r$ value (rather than the $r^2$ value) to show the sign of the correlation rather than its significance.*

## 5.11 Signal spread in the sea ice reduction

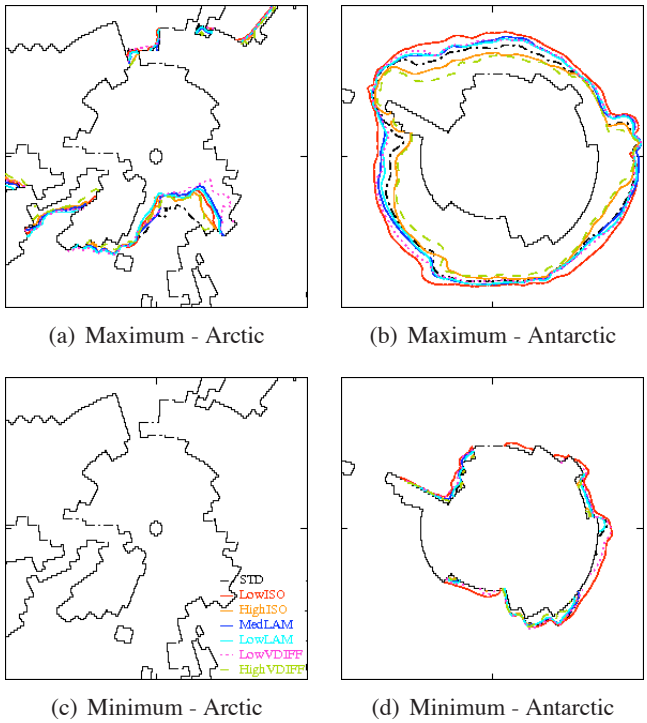


(a) Maximum - Arctic (b) Maximum - Antarctic

(c) Minimum - Arctic (d) Minimum - Antarctic

**Figure 5.18** *Average annual maximum and average annual minimum sea ice extents in the last 20 years of the increasing $CO_2$ run.*

As the globe warms, the quantity of sea ice reduces (section 5.8). It has long been understood, that the reduction in sea-ice cover causes a local positive feedback on the climate change signal (Kellogg, 1975). It was shown that there was large signal spread in the surface temperature of the Barents Sea, and surrounding the Antarctic continent (figure 5.13), and mentioned that this would be related to differences in the sea ice distributions.

Figure 5.18 shows the average annual maximum and annual minimum sea ice extent in the final 20 years of the 1% run for each ensemble member. All the ensemble members show a complete removal of sea ice in the summer in the Northern Hemisphere. The warming occurs mostly in the winter months, when the sea ice is approaching its maximum. It can be seen that the maximum ice extent in the Barents Sea and around the coast of Antarctica show the most variations. These are the same regions as the large uncertainty in the surface air temperature. This strongly suggests that the sea ice feedback amplifies the uncertainty in the surface temperature response to increasing $CO_2$.

The uncertainty in sea ice feedback can be shown directly by analysis of the local surface albedo feedback (Winton, 2006). The outgoing radiation can be subdivided into cloudy and clear sky radiation, as well as shortwave and longwave components. This separation allows individual feedbacks to be defined (Boer and Yu, 2003). Starting from a re-arrangement of the global mean feedback equation (eq. 4.8):

$$\Lambda\Delta T = Q - N. \tag{5.3}$$

The diagnosed values for the clear sky heat flux is written as $N_A$, and be introduced as follows:

$$\Lambda\Delta T = Q - N + (N_A - N_A). \tag{5.4}$$

Now define the changes in net radiative heat flux from clouds as the difference between the total net flux and the clear sky net flux: $N_C = N - N_A$. This now allows eq. 5.4 to be rewritten as:

$$\Lambda\Delta T = Q - N_A - N_C. \tag{5.5}$$

Webb *et al*. (2006) then divides the climate feedback parameter up into a clear-sky and a cloud component, $\Lambda_A$ and $\Lambda_C$ respectively, which combine linearly giving:

$$\Lambda = \Lambda_A + \Lambda_C = \frac{Q - N_A}{\Delta T} - \frac{N_C}{\Delta T}. \tag{5.6}$$

Boer and Yu (2003) convert these global mean quantities into spatially varying fields, by normalising the local flux changes with the global mean temperature change, $TCR$.

$$\Lambda(x,y) = \Lambda_A(x,y) + \Lambda_C(x,y) = \frac{Q(x,y) - N_A(x,y)}{TCR} - \frac{N_C(x,y)}{TCR}. \tag{5.7}$$

Changes in the surface albedo will cause changes in the amount of incoming shortwave radiation reflected back into space. Winton (2006) divides $\Lambda_A$ into a shortwave and longwave component, which allows the surface albedo feedback to be defined:

$$SAF \approx \Lambda_A, sw = \frac{N_A, sw}{TCR}. \tag{5.8}$$

The spread in surface albedo feedback, defined in this way, is shown in figure 5.19. It can be seen that there is spread of up to 10 $\mathrm{Wm}^{-2\circ}\mathrm{C}^{-1}$ in the regions of uncertainty in the sea ice edge. The uncertainty

in the sea ice edge is caused by many factors. The most important factors are probably the magnitude of the TCR and location of the preindustrial sea ice edge. It can also be seen that is uncertainty in the snow cover over the land masses in the northern hemisphere (especially the Himalayas).

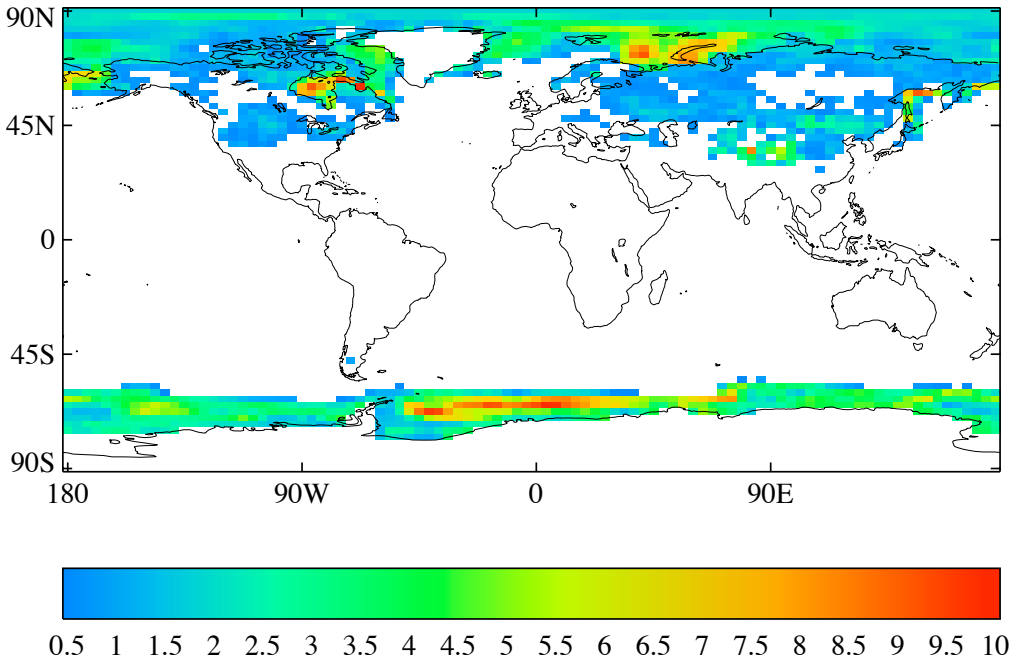


**Figure 5.19** *The signal spread in the surface albedo feedback calculated from eq. 5.8 (in $Wm^{-2}{}^{\circ}C^{-1}$). Regions with an signal spread of less than $0.5Wm^{-2}{}^{\circ}C^{-1}$ are not shaded.*

## 5.12 Signal spread in the surface salinity and precipitation

It has been shown that largest signal spread in surface temperature occurs in the high latitudes. There is little signal spread in the tropics. In the previous chapter, it was shown that the spread in global mean transient climate response (TCR) for the ensemble could only be explained by considering changes in the climate feedback parameter as well as changes in the ocean heat uptake efficiency. It was

suggested that two mechanisms could be responsible for changes in the climate feedback parameter across the ocean ensemble: changes in the surface albedo feedback from different sea ice distributions and changes in the cloud feedbacks due to different underlying SSTs. It has already been shown that there are variations in the surface albedo feedback.

The effects of changes in cloud feedbacks have found to be strongest in the tropics (Barsugli *et al*. (2006) and Boer and Yu (2003)). An indication of changes in clouds and convection in the tropics is the uncertainty in the precipitation, which is shown in figure 5.20(a) as a percentage of the ensemble mean climate change signal. The signal spread is largest in the tropical Pacific, and seems to be associated with location of the inter-convergence zones. The surface temperature signal spread in this region is less than 0.75°C (fig. 5.13), however Barsugli *et al*. (2006) found the global mean temperature to be most sensitive to changes in this region, because of cloud feedbacks.

The signal spread in the precipitation response shown in fig. 5.20(a) is presented without any form of significance testing, to improve its clarity. The spread could occur from internal variability. One method of testing this hypothesis is to use an f-test. Figure 5.20(b) shows the probabilities returned from such a test. The dark grey areas show the locations where such a hypothesis can be rejected at the 5% confidence level, and the signal spread is detectable.

It can be seen that large areas of the Earth do not have a detectable ensemble spread from ocean model uncertainty from fig. 5.20(b). However, the ensemble shows some detectable changes in precipitation in the tropics that could be consistent with changes in the cloud feedback strength. This does not formally prove that are changes in the cloud feedbacks. Boer and Yu (2003) suggest a method of calculating the local cloud radiative feedback parameter directly using the methodology presented in section 5.11. The local cloud feedback parameter, $\Lambda_C(x, y)$ as calculated using eq. 5.7, is shown in figure 5.21.

It can be seen from fig. 5.21 that there is spread in the strength of the cloud feedbacks. It is not possible

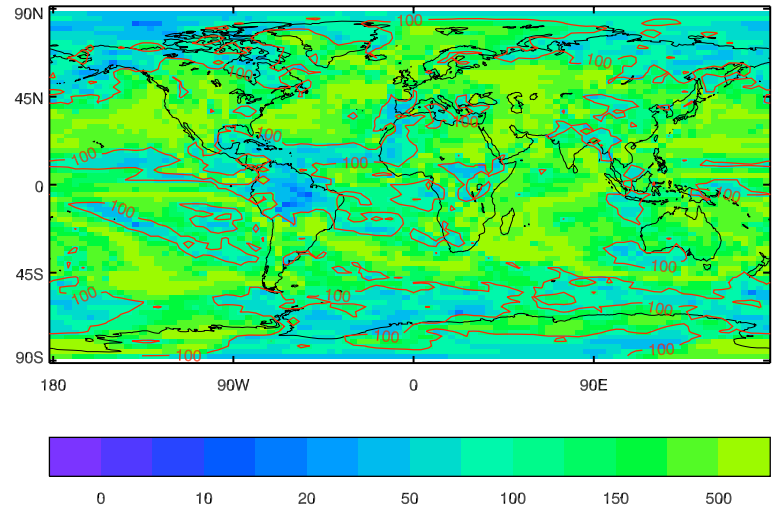


(a)

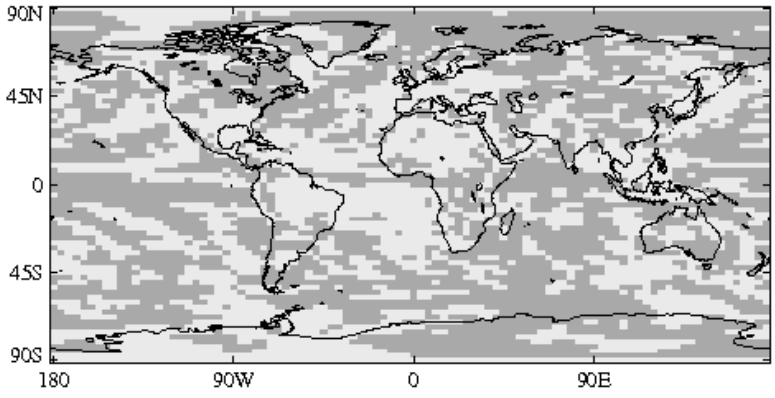


(b)

**Figure 5.20** *Panel (a) shows the ensemble spread of climate change signal in precipitation. The range is expressed as a percentage of the ensemble mean climate change signal. The significance of this range is indicated by panel (b), which shows the probability of the signal spread in precipitation being caused by modelled internal variability computed using an F-test. The dark grey area regions have a probability of less than 5%, so have detectable effects of ocean model uncertainty.*

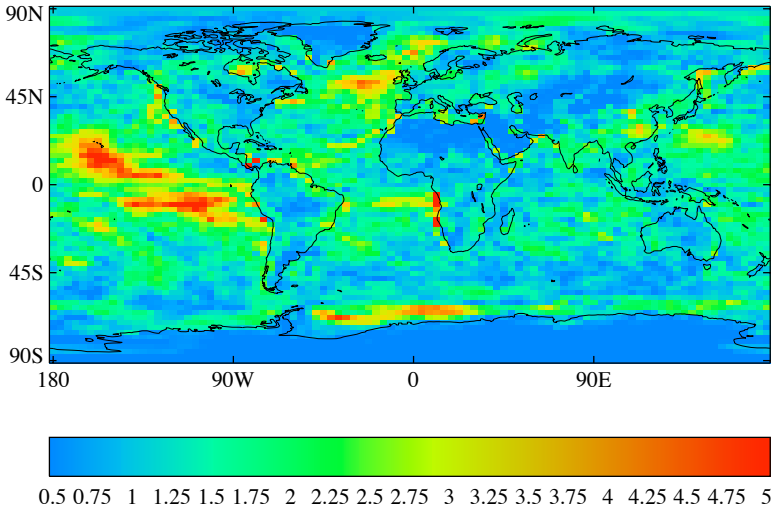


**Figure 5.21** *The range of the local cloud radiative feedback parameter, $\lambda_C(x, y)$, calculated using eq. 5.7 (in $Wm^{-2\circ}C^{-1}$).*

to compare this spread to any form of internal variability, because the calculation to compute the cloud radiative feedback parameter requires an imposed forcing, which would not happen in a control run. However, the largest changes in the cloud feedbacks are occuring in the tropical Pacific. This region has both detectable effects of ocean model uncertainty in the signal spread of precipitation and surface temperature. The SST signal spread is relatively small in the tropics, but small changes in SST can have a large impact on the global circulation (Barsugli *et al.*, 2006). It, therefore, seems highly likely that the uncertainty in the cloud feedbacks are also due to the ocean model uncertainty.

## 5.13 Signal spread in the global mean depth profiles

It was shown in the previous chapter that the signal spread in the TCR arose from variations in both the climate feedback parameter and the ocean heat uptake efficiency. The previous two sections have

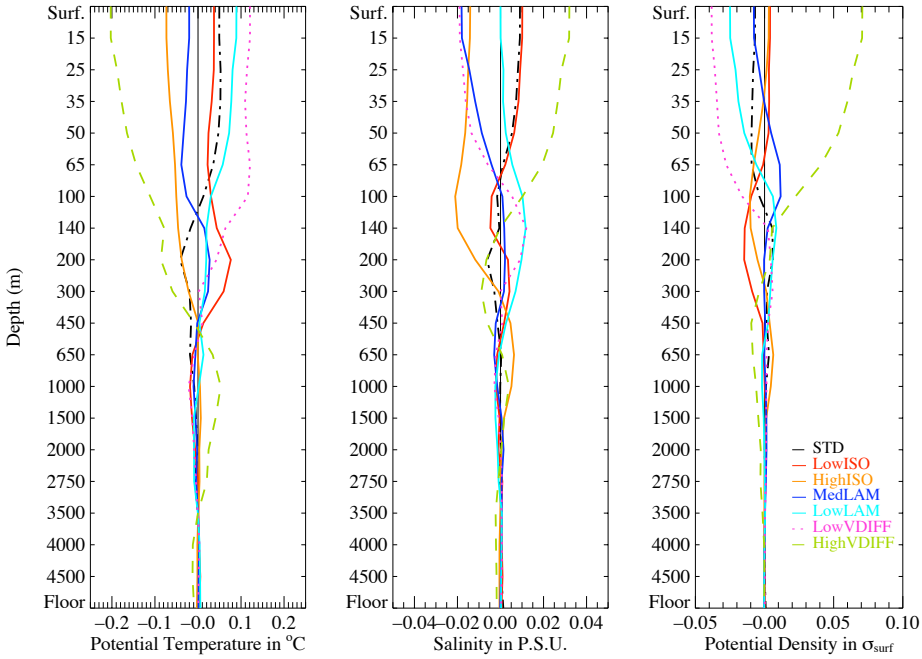


**Figure 5.22** *Variations in the depth profiles of the climate change signal in the ensemble. The 3 quantities are, from left to right, potential temperature, salinity and potential density. The vertical coordinate is not linear in depth, however it does correspond to the model levels.*

shown that the variations in the climate feedback parameter arise from uncertainty in the surface albedo feedback at high latitude (related to the sea ice distribution) and uncertainty in the tropical cloud feedback (caused by sensitivity to the underlying sea surface temperatures). The reasons for the spread in the ocean heat uptake efficiency, $\kappa$, have not yet been investigated. This can be performed with an analysis of the depth variation of the climate change signal. A larger $\kappa$ will mean that more heat is being taken into the deep ocean. Figure 5.22 shows the global mean depth profiles of the climate change signal in potential temperature (left), salinity (middle) and potential density (right). The deviation of each member from the ensemble mean is plotted. If there are positive deviations at some depth and negative deviations at another depth, then it can be said that there is some compensation with depth. There is compensation occuring within the salinity profile, because the total salt content of the ocean is approximately constant. There is also depth compensation occuring in the potential temperature. This is most obvious with HighVDIFF, but all ensemble members show some kind of depth compensation. This is consistent with the variations in $\kappa$ seen in section 4.7. A larger $\kappa$ means more heat will be transmitted to depth, away from the surface. All the ensemble members, apart from

HighVDIFF, have a $\kappa$ of 0.6 $Wm^{-2\circ}C^{-1}$ (see table 4.3) and it can be seen that changes in the deep ocean temperatures between these members below 500m are less than 0.02 °C. Although looking at these global mean climate change signal profiles agrees with a slight spread in $\kappa$, it does not explain how those changes arise.

## 5.14 Signal spread in the process diagnostics

The global mean downwards heat flux from different physics parameterisations can be calculated from the model diagnostics of potential temperature tendency from each parameterisation, using equation 3.5. The ensemble mean climate change signal in the parameterisation's global mean downwards heat fluxes was shown as fig. 4.5 in the retrospective discussion about parameter choice presented in section 4.5. It is presented again as the top left hand panel of figure 5.23. During climate change, the mixed layer scheme is responsible for most of the additional downwards heat transfer in the top 160m, then advection dominates until 350m. The isopycnal diffusion dominates the vertical heat transfer below 350m until 1500m. The additional heat from an increase in $CO_2$ is very low below this (also see fig. 5.11). This is a similar order as that found by Gregory (2000) in HadCM2, however the transitions occur at different heights.

The climate change signal in each of the global mean downwards heat fluxes for each ensemble member are shown in figure 5.23. They are shown as anomalies from the ensemble mean climate change signal. It is surprising that there is nearly always compensation occuring between the different processes. For example LowISO has a reduced downward heat flux from isopycnal diffusivity, which is what was expected from that parameter perturbation. This is, at least partly, compensated for by an increased downwards flux from the Gent and McWilliams (1990) scheme. Various forms of compensation are happening that reduce the impact of the parameter perturbations on the ocean heat uptake under climate change. This nullification of the parameter perturbations explains the small range in $\kappa$

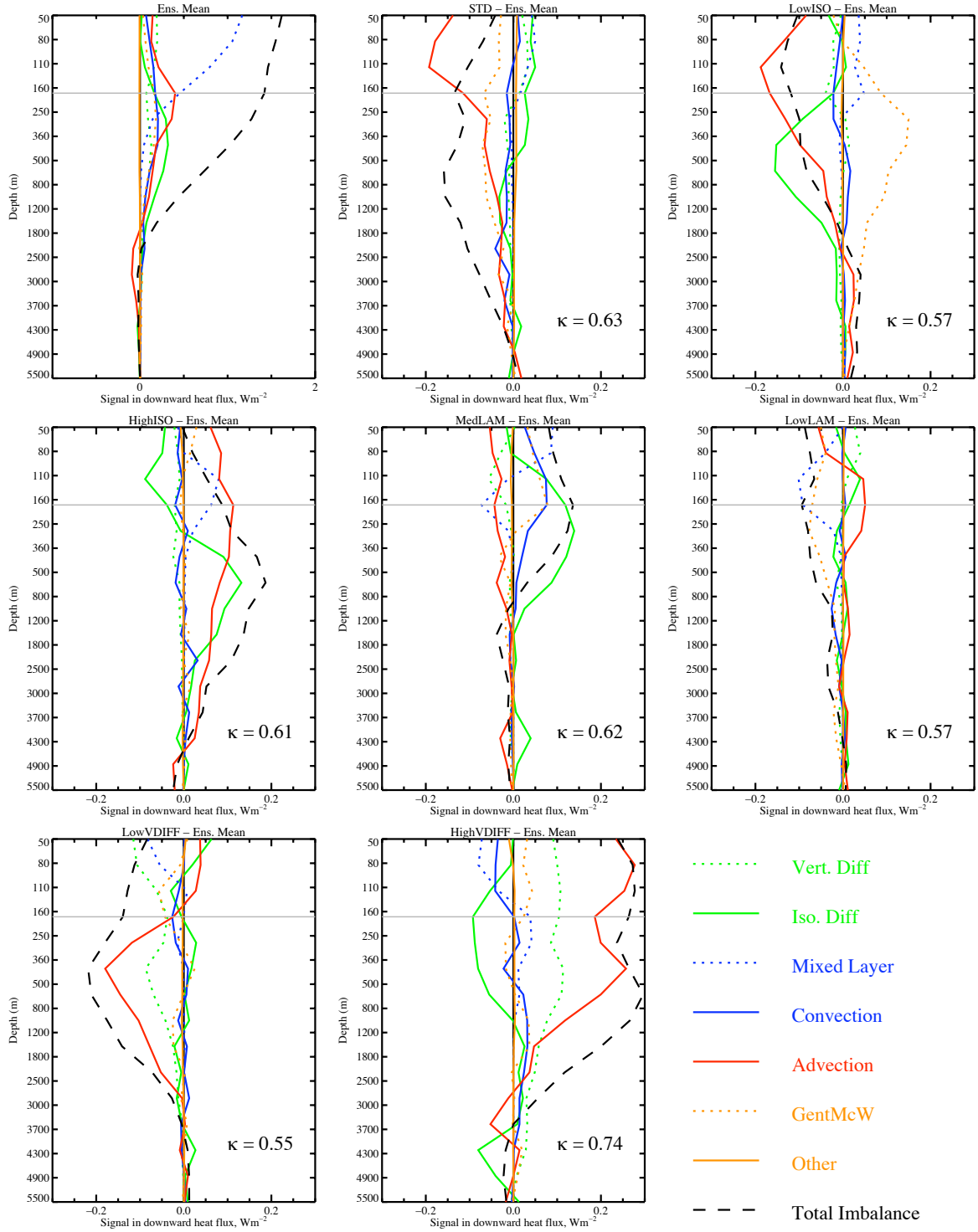


**Figure 5.23** *The climate change signal in the global mean downward heat flux from each physical parameterisation (in Wm$^{-2}$). The top left panel shows the ensemble mean climate change signal. The other panels show the deviations of each ensemble members signal from the ensemble mean. The heat fluxes are computed from diagnosed temperature tendencies using eq. 3.5.*

seen in this perturbed physics ensemble.

It is interesting that the largest variations in the heat balance come about from changes in the amount of heat being advected downwards. This is especially noticeable in HighVDIFF, which is the ensemble member with the largest variation in $\kappa$. The global mean downwards heat flux from advection is a confusing concept as there can be no net vertical velocity. The heat flux from advection must be related to a circulation between regions with different temperature properties, and looking at global mean is at odds with that view. A further discussion about the interpretation of an advective heat flux can be found in appendix B of Gregory (2000). Possible reasons for changes in the global mean downwards heat flux from advection are dynamical changes in the ocean circulation and changes in the local potential temperature profiles. It is not possible to determine which of these effects are occuring from the analysis presented here, but it can be concluded that changes in the global mean downwards heat flux from advection is important.

## 5.15 Signal spread in the heat content change

The previous two sections have looked at the global mean depth profiles of ocean properties, whilst earlier sections have looked at the spatial pattern at the ocean surface. One possible method to look at the spatial pattern of ocean interior properties is to take the vertical integral at each location. The vertical integral of the change in energy stored in the ocean column (computed using eq. 5.2) is shown in figure 5.24 as a percentage of the global mean of the ensemble mean climate change signal ($2.2 \times 10^9$ Jm$^{-2}$ - the spatial pattern from which this global mean is taken is shown as fig. 5.10).

The additional heat caused by an increase in $CO_2$ is moved from the surface to depth by a variety of processes (Williams, 2001). All of them involve either the movement of water that has recently been at the surface (also called ventilated water), or contact with that water. The creation and ventilation of different water masses occur at different spatial locations (Emery, 2001). There is large spread

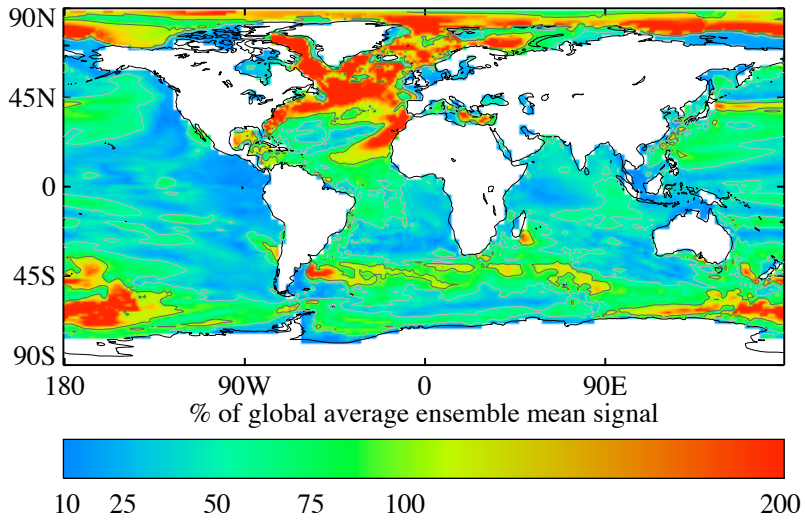


**Figure 5.24** *Signal spread in the vertically integrated ocean heat content increase: expressed as a percentage of the global average ensemble mean increase (unit: %). The light grey contour shows a spread of 50%, and dark grey contour shows a spread of 100% of the global average ensemble mean ($2.2 \times 10^9$ $Jm^{-2}$)*

in the amount of heat stored in the Southern Ocean (greater than 100% of the global mean signal in places). This spread seems to be largest on the edges of the Antarctic Circumpolar Current (ACC). It has been shown in section 3.5.10 that the strength of the ACC varies in the ensemble. The ACC partly determines the amount of water ventilated in the Southern Ocean (Russell *et al.*, 2006), so these variations in the ACC could explain the variation in the change in heat content. However, this is also a region of strong vertical heat transfers that have been intentionally perturbed, which may also explain the uncertainty in the change in heat content. The strength of the ACC and the strength of the vertical heat transfers are not independent.

The largest signal spread is seen in the Arctic and extra-tropical North Atlantic. There is also some large signal spread in the Canary Current off the coast of West Africa, which may be related to the advection of North Atlantic waters southwards in this region. The extra-tropical North Atlantic and

the Arctic overflow is the formation region of North Atlantic Deep Water (NADW, Emery (2001)), which is associated with the sinking branch of the THC. The southwards path of the NADW in the deep western boundary current is clearly visible in fig. 5.10, but the signal spread is not constrained to this region. The northern high latitudes have been shown to have a large signal spread in the surface air temperature (fig. 5.13). Different atmospheric temperatures would change the size of the heat source available for any ocean heat content increases in these regions.

It has been shown that there is signal spread in the ocean heat content, which is largest in the Arctic, North Atlantic and Southern Oceans. Several possible causes for this signal spread have been identified. The possible causes presented are not independent of each other. A much more detailed analysis is required to understand the relative importance of these causes and the degree of their interactions.

## 5.16 Uncertainty in the thermohaline response

The signal spread in heat content is largest in the North Atlantic. One possible cause of this is uncertainty in the response of the thermohaline circulation (THC) to increasing $CO_2$. There is large natural variability in the THC that makes detection of uncertainty a problem. The THC has important variations on time scales greater than 10 years (as well as variations in shorter timescales). A 500 year segment of the multi-year HadCM3 run of Collins *et al*. (2001) has been used to estimate the modelled internal variability, rather than the combined control runs, as in the rest of the chapter (see section 5.2.1).

The climate change signal in the THC is shown in table 5.1. The climate change signal has been constructed in a similar fashion to the TCR (eq. 4.3), which is different from elsewhere in this chapter (which uses eq. 4.4). The internal variability in the THC is much greater than any climate drift in the control. This is not the case for some other variables looked at in this chapter, hence the different definitions. All of the ensemble members have THC reductions that are greater than 1.96 standard

| Ensemble Member | Initial THC Strength, Sv | Signal, Sv |
|---|---|---|
| STD | 18.7 | -3.7 |
| LowISO | 18.4 | -3.0 |
| HighISO | 18.1 | -1.7 |
| MedLAM | 18.2 | -3.7 |
| LowLAM | 18.9 | -4.3 |
| LowVDIFF | 16.5 | -2.0 |
| HighVDIFF | 24.6 | -4.2 |
| Ens. Mean | 19.1 | -3.2 |
| Collins *et al*. (2001) | 18.6 | ±0.5† |

**Table 5.1** *The thermohaline circulation properties across the ensemble. The initial strength is taken as the 80 year mean in the control run. The signal is the difference between the mean of the last 20 years of the increasing $CO_2$ run and the initial strength. The final row shows the mean state and 20yr variability from 500 years of the multi-thousand year control integration of Collins* et al. *(2001). †is a standard deviation of natural variability instead of a modelled change.*

deviations of internal variability, and are therefore detectable changes at the 5% confidence level. The spread across the climate change signal is 3.2 Sv, yet the variance of the ensemble is not significantly different from that expected by internal variability at the 5% confidence level using an f-test. Therefore it is not possible to detect any signal spread that is a consequence of the ocean model uncertainty in the THC.

Analysis of just the climate change signal at the time of doubling of $CO_2$ does not capture possibly interesting temporal behaviour. Figure 5.25 shows the ten year running mean of the change in THC from the long term mean from the control run. The grey region gives an idea of the variations expected from internal variability and is computed using the following method. First the ensemble mean climate change signal was determined as in table 5.1. An ensemble mean linear trend was calculated from this value at the time of doubling of $CO_2$ and the origin (this trend is shown as a solid black line in fig. 5.25). A standard deviation of decadal internal variability was calculated from the HadCM3 control run of Collins *et al*. (2001). This corresponds to the ten year timescale for the running mean. The grey band covers 2 standard deviations of the ensemble mean linear trend: 95% of samples taken from a normal distribution will fall within 2 standard deviations of the mean, so anything outside this grey region could be considered significant at the 5% confidence level.

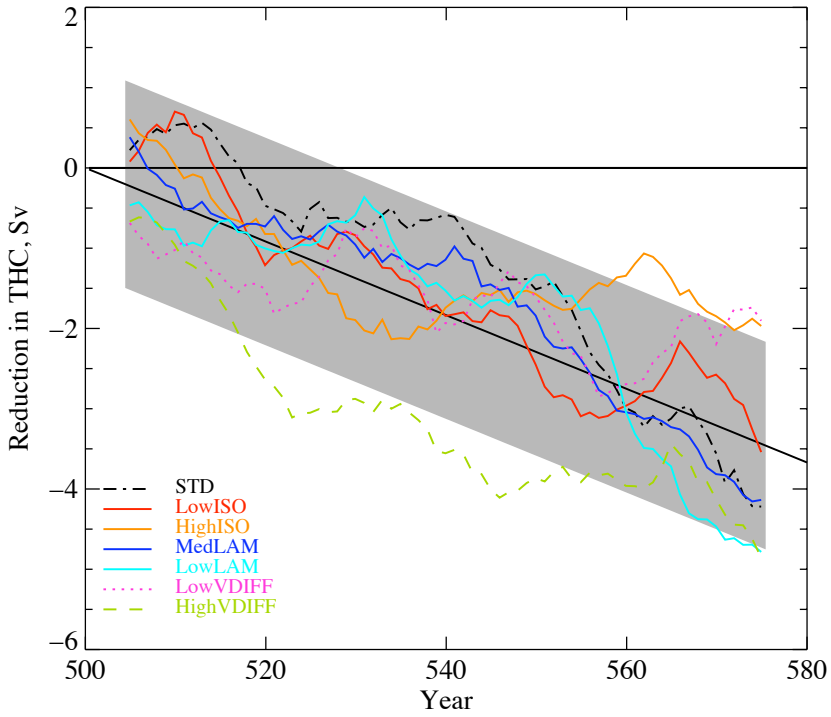


**Figure 5.25** *The ten year running mean change in maximum meridional overturning circulation for each ensemble member. The ensemble mean linear trend is shown as a black solid line. The grey region is ± 2 standard deviations of modelled internal variability from that line.*

Two ensemble members have a temporal evolution of the THC that lies outside the bounds of natural variability - HighVDIFF and HighISO. HighVDIFF seems to drop rapidly in the first 20 years and then reduce at a rate similar to the other ensemble members. This ensemble member has a greater preindustrial THC. Maybe the process controlling the reduction of the THC is proportional to the strength of the initial THC. To investigate this, figure 5.26 shows the THC strength as a fraction of the preindustrial mean state. Figure 5.26 shows that the changes in the THC of HighVDIFF are not detectable as a fractional change. However the smaller reduction seen in HighISO does fall outside the region expected by internal variability for a period, when considered as both an absolute and a fractional change. The reason for this is not clear from the figures. It could be due to some form of stabilisation occuring after approximately 35 years or more likely that HighISO has a slightly smaller reduction in the THC and some large superimposed internal variability.

A variety of attempts have been made to ascertain whether ocean model uncertainty has an effect on

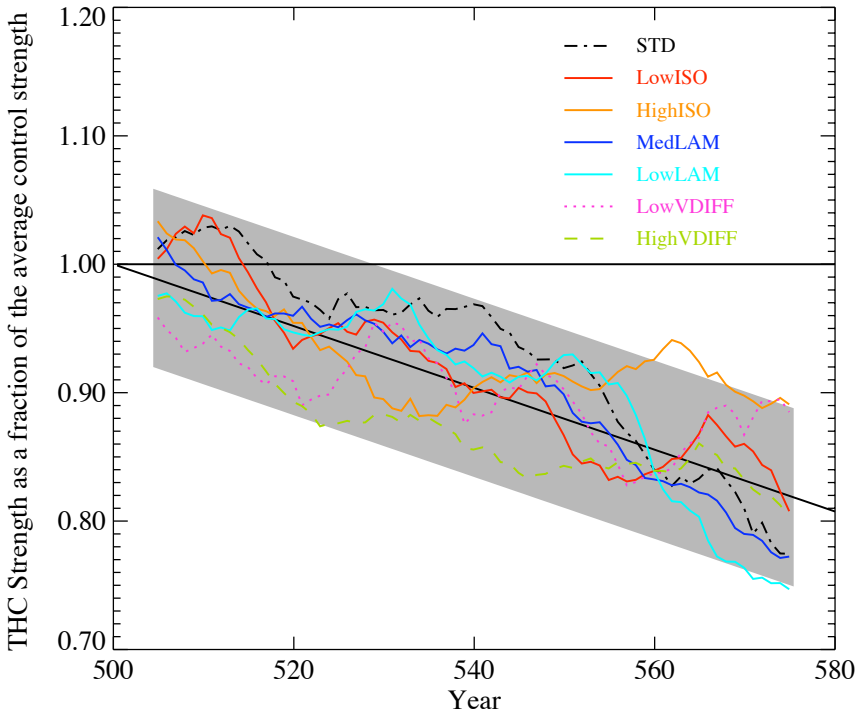


**Figure 5.26** *as fig. 5.25, but with THC strength expressed as a fraction of the initial strength.*

the reduction of the thermohaline circulation. Although there are implications that it might do, there is no conclusive proof that the ocean model uncertainty effects the THC slowdown significantly.

## 5.17 Conclusions

Chapter 4 shows there is uncertainty in the increase in global mean surface temperature response to an increase in $CO_2$. This signal spread was found to be less than in the atmosphere perturbed physics ensemble (Collins *et al.*, 2006), but more than that expected from modelled internal variability. The ensemble spread was found to be caused in approximately equal amounts from variations in the climate feedback parameter, $\Lambda$, which characterises the feedbacks in the system, and the ocean heat uptake efficiency, $\kappa$, which characterises at the effectiveness of vertical transfers at absorbing heat into the deep ocean.

This chapter has taken the analysis a stage further, by looking at regional variations in the climate change signal. The first part of the chapter was devoted to investigating the ensemble mean pattern. Characterising a model's response by looking only at the global mean temperature change neglects many interesting features of climate change. Much work has already published by the community looking at the features of climate change. A series of comprehensive summaries have been produced by the IPCC. The purpose of looking at the ensemble mean spatial patterns in the perturbed ocean ensemble is twofold. Firstly, it is necessary to understand the mean features of the change to place any measures of ensemble spread in the climate change signal (signal spread) in context. Secondly, it shows that the ensemble is providing plausible climate change signal. The ensemble mean pattern falls within the range of previously published AOGCM assessments, which gives confidence that the signal spread of the ocean ensemble will also be realistic.

The rest of the chapter was devoted to examining the spatial pattern of the signal spread. It was shown that ocean model uncertainty causes variations in the surface temperature pattern of climate change that are detectable from internal variability for the majority of the Earth. It was previously suggested the relatively small spread of TCR in the ocean ensemble could be due to regional compensation. A correlation analysis was used to reject this hypothesis.

Variations in the climate feedback parameter (shown in the previous chapter to be responsible for at least half of the TCR signal spread) have been traced to variations in the surface albedo feedback and the cloud radiative feedback. Variations in the surface albedo feedback are caused by uncertainty in the location of the sea ice edge. Variations in the cloud radiative feedback are probably caused by uncertainty in the underlying sea surface temperature patterns. Variations in the ocean heat uptake efficiency were shown to be primarily caused by uncertainty in the vertical advective heat flux. Signal spread in the change of ocean heat content occurs in regions of large vertical heat fluxes, namely the North Atlantic and Southern Ocean.

There are many differing climate projections of the THC response to an increase in $CO_2$ (Cubasch

*et al*., 2001). As the THC is an ocean circulation, it would seem reasonable for its behaviour to be effected by ocean model uncertainty. All of the ensemble members showed a reduction in the thermohaline circulation with increasing levels of $CO_2$. The thermohaline circulation has large internal variability, and it was not possible to conclusively prove that the spread in the THC reduction is a consequence of ocean model uncertainty, rather than from internal variability.

# CHAPTER 6

# Evolution of ensemble spread of the global mean surface temperature

## 6.1 Introduction

The previous three chapters of this thesis have been devoted to the creation of a perturbed ocean physics ensemble and the analysis of ensemble spread in two different quantities. Chapter 3 gave an analysis of the ensemble spread in the preindustrial climate states ($Spread(Var_i)$, where $Var_i$ is the variable under analysis for ensemble member $i$). Henceforth, we shall refer to the range between the modelled climate state of individual ensemble members as the "absolute ensemble spread". Chapters 4 and 5 defined a climate change signal for each ensemble member and then looked at the spread between these signals. This form of spread has been referred to as a "signal spread" ($Spread(signal) = Spread(Var_i(t) - Var_i(t = t_0))$). The climate change signal for each ensemble member is defined to be 0 at the beginning of the 1% per year experiment ($t_0 = 501yrs$) and increases as the levels of $CO_2$ increase. Therefore, there is no signal spread at the beginning of the 1% experiment, and the signal spread increases thereafter. The change in the absolute ensemble spread under increasing $CO_2$ (namely the range in climate state across the the individual ensemble members of the 1% integrations) has not yet been investigated in this thesis. Absolute ensemble spread is not investigated to the same degree in the climate modelling community as signal spread - for example the majority of work relating to uncertainties in predictions in the IPCC report relates to the signal spread.

This chapter will investigate the evolution of the absolute ensemble spread in global mean surface temperature, and find a surprising result - the absolute ensemble spread reduces under increasing $CO_2$. A reducing absolute ensemble spread is not contradictory with an increasing signal spread.

The physical mechanisms that lead to this reduction will be investigated in the context of the climate feedback parameter and the ocean heat uptake efficiency (through a similar methodology to that used in chapter 4). An investigation of the spatial pattern of changes in the absolute ensemble spread strongly implies that the cause of the reduction is the same as the cause of the initial ensemble spread.

## 6.2 Absolute ensemble spread in the global mean surface temperature

A 500 year long spin up integration was performed for each ensemble member, before the increasing $CO_2$ experiment was performed. Each ensemble member was initialised from the same climate state (based on observations), hence there can be no absolute spread at this time. Yet after 500 years, the ensemble members have different global mean surface temperatures. The evolution of the temperature of each ensemble member was shown in figure 3.1, but the absolute ensemble spread was not explicitly shown. It is presented in figure 6.1 as a solid line, for the whole 580 years of integration with a constant $CO_2$ level. The absolute spread of the 1% integrations is shown as a dashed line.

It can be seen that the absolute spread expands rapidly in the first 50 years of the spin up and then reduces for the next 50 years. After 100 years, the absolute spread seems to have settled down to a quasi-stable value of 0.8 °C. The absolute spread starts increasing again after 350 years, and is about 1.0 °C at start of the increasing $CO_2$ experiment ($t = 500$years). The large increase in absolute spread seen at the beginning is due to the ensemble members having different response times to the initial imbalance (caused by inclusion of the interactive sulphur cycle). This can be seen quite clearly in figure 3.1(a). The increase in absolute spread after 350 years is related to the fact that LowISO (the bottom of the range) is very close to being equilibrated, whilst HighVDIFF (top of the range) is still drifting.

The absolute spread of 1.0 °C in the global mean surface temperature at the beginning of the increasing $CO_2$ experiment is comparable to the error estimates of reconstructions of the preindustrial climate.

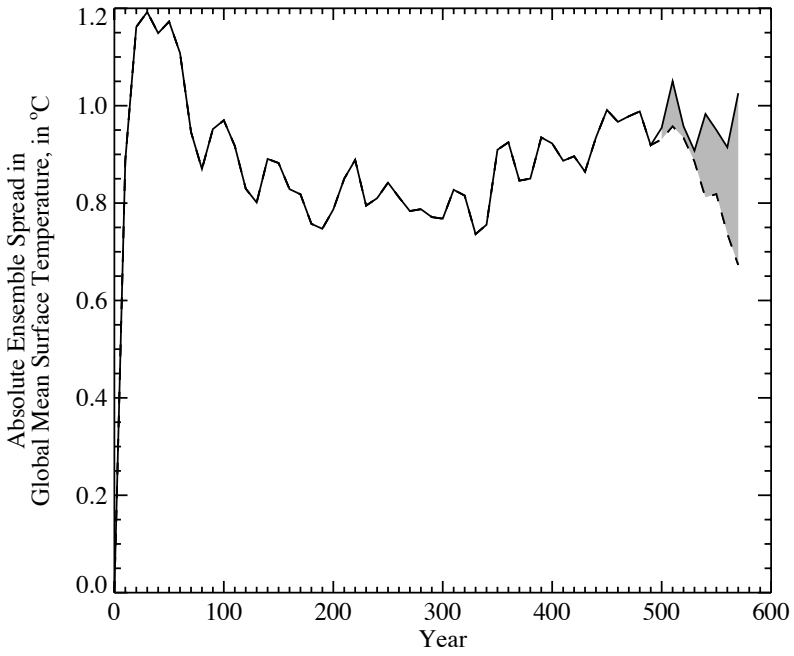


**Figure 6.1** *A 20 year running mean of the absolute ensemble spread in global mean surface temperature. The solid line shows the absolute spread for integration with constant $CO_2$ (the spin up and control), the dashed line shows the absolute spread in the increasing $CO_2$ runs. The shaded region emphasises the reduction in absolute spread caused by the increase in $CO_2$.*

For example, Mann and Jones (2003) find a 5-95% preindustrial range of 0.8 °C and Esper *et al.* (2002) find a range of 1.3 °C. The absolute spread of the ensemble is however greater than the error estimates of observations of the present day climate (Folland *et al.*, 2001b).

The dashed line in fig. 6.1 shows the absolute spread in the increasing $CO_2$ runs. It can be seen that the absolute spread is reducing (this reduction is shown by the grey shaded area). This reduction in absolute spread is not contradictory with the increase in the signal spread, because the signal spread is by definition zero at year 500. The grey shaded area is approximately equal to the signal spread.

To help understand the mechanisms by which the absolute spread reduces (whilst the signal spread increases), figure 6.2 shows the absolute global mean temperature in the 1% and control runs. The dark grey area shows the absolute ensemble spread in the 1% runs. The reason for the reduction in absolute spread is that the colder ensemble members warm more under increasing $CO_2$. In other words, there is an anti-correlation between the initial temperature and the TCR. This is shown in figure

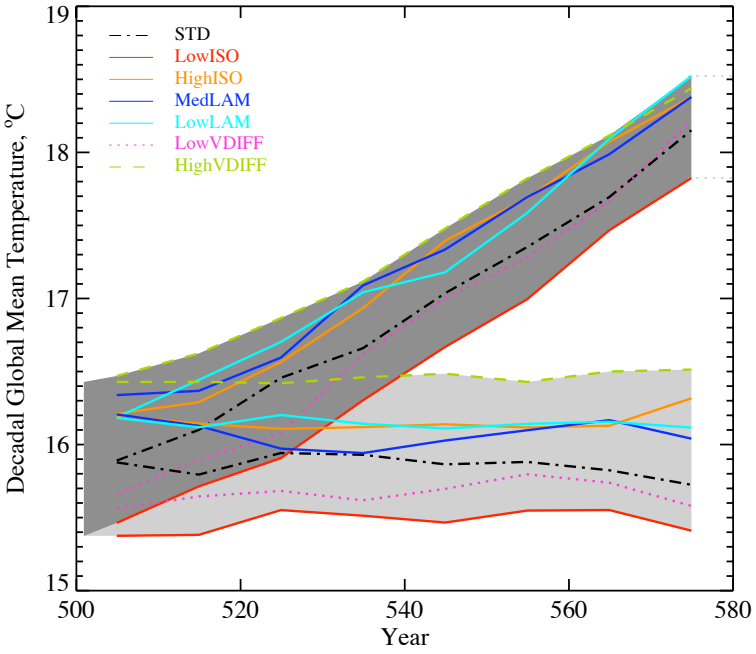


**Figure 6.2** *Decadally averaged global mean temperature for both the increasing $CO_2$ run and the control run for each ensemble member. The absolute spread in temperature in the increasing $CO_2$ run is shown as the dark grey shaded area; whilst the absolute spread in the control run is shown as the light grey shaded area. The initial values of the shaded areas are the maximum and minimum temperatures from the average of each ensemble member's control run.*

6.3, and the correlation coefficient for this relationship is -0.76.

The reduction in absolute ensemble spread from the increasing $CO_2$ is 0.3 °C. The standard deviation of modelled internal variability is 0.05 °C on twenty year timescales (section 4.4.1). The reduction in spread due to the increase in $CO_2$ is 6 standard deviations, and therefore the reduction in spread is significantly greater than that expected from internal variability at the 5% confidence level, and is a detectable feature of the increase in $CO_2$. If the reduction in spread continues there will be a time when the absolute ensemble spread in the 1% $CO_2$ run is reduced to a level where it is indistinguishable from internal variability. This would happen at 220yrs into the run, if the rate of absolute ensemble spread reduction is both linear and constant. However, this is probably not the case, because the ensemble members that determine the range changes with time.

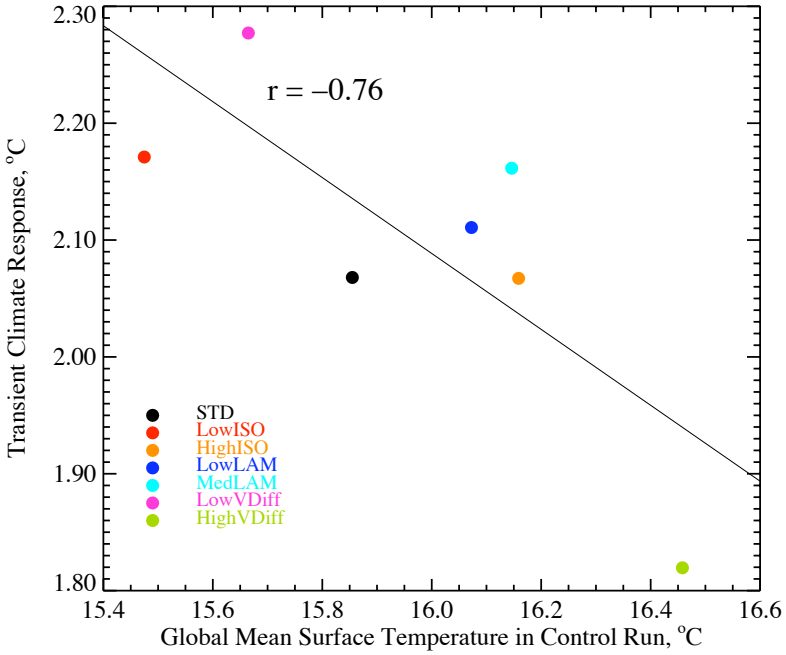


**Figure 6.3** *The relationship between the long-term average global mean surface temperature in the control run (effectively the initial condition) and the transient climate response for the ocean ensemble. The surface temperature of the control run is discussed in section 3.5.2; the transient climate response is defined and calculated in section 4.4. Numerical values for both can be found in table 4.1*

### 6.2.1 Causes of the reduction in spread

The reduction in absolute ensemble spread is manifested by a relationship between the transient climate response and the global mean temperature in the control run. A warmer (colder) long term mean temperature is related to a smaller (larger) TCR. In section 4.8 it was shown that the differences in the TCR arise, in approximately equal measure, from variations in the climate feedback strength and the rate of ocean heat uptake. This does not necessarily mean that the reduction in absolute ensemble spread also arises from changes in both these factors.

Section 4.8 modelled a "hypothetical" TCR to determine the relative importance of $\Lambda$ and $\kappa$ in determining the climate change signal. A similar method can be used to investigate whether the reduction in absolute ensemble spread is caused by changes in either $\Lambda$, $\kappa$ or a combination of both. The hypo-

thetical absolute ensemble spread can be determined as,

$$AS(t) = max\left(T_{cont,i} + \frac{Q(t)}{\Lambda_i + \kappa_i}\right) - min\left(T_{cont,i} + \frac{Q(t)}{\Lambda_i + \kappa_i}\right) \tag{6.1}$$

where $T_{cont,i}$, $\Lambda_i$ and $\kappa_i$ are the diagnosed global mean surface temperature in the control run, the climate feedback parameter and the ocean heat uptake efficiency for the $i$th ensemble member. $max$ and $min$ mean the maximum and minimum of all the ensemble members. Values for $T_{cont,i}$ can be found in table 4.1. $\Lambda_i$ is calculated using eq. 4.11 and $\kappa_i$ is calculated using eq. 4.16. The values for them are given in table 4.3. The hypothetical absolute ensemble spread calculated in this way is shown as the green line in figure 6.4. The crosses show the decadal average values of the actual absolute ensemble spread in global mean surface temperature diagnosed directly from the model simulations. The hypothetical absolute spread is similar to, but sometimes less than, the diagnosed absolute spread. The gradient of the line changes at approximately 565 years. At this point the absolute ensemble spread is determined by the difference between LowISO and LowLAM, rather than LowISO and HighVDIFF as before.

This hypothetical derivation of the absolute ensemble spread allows the influence of changes in $\Lambda$ and $\kappa$ to be isolated individually. For example, the effect of changes in $\kappa$ can be determined by setting $\Lambda$ to be the ensemble mean value, and allowing $\kappa$ to have different values for each ensemble member:

$$AS_\kappa(t) = max\left(T_{cont,i} + \frac{Q(t)}{\overline{\Lambda} + \kappa_i}\right) - min\left(T_{cont,i} + \frac{Q(t)}{\overline{\Lambda} + \kappa_i}\right). \tag{6.2}$$

The red solid line in fig. 6.4 shows the absolute ensemble spread determined using eq. 6.2, which only considers variations in $\kappa$. The absolute ensemble spread considering only changes in $\Lambda$ is constructed in an exactly analogous way and is shown as the blue dotted line. These two lines are almost overlaid and both over-estimate the amount of absolute spread. The two overlaid lines are created from the difference in $\kappa$ and $\Lambda$ for two ensemble members (the two most extreme members). Therefore, the surprising amount of similarity between the two lines could have arisen by chance. However, it does mean that the reduction in absolute spread seen in the 1% run cannot be explained solely by differences in $\Lambda$ or $\kappa$, and therefore a combination of the effects of differences in both measures is required.

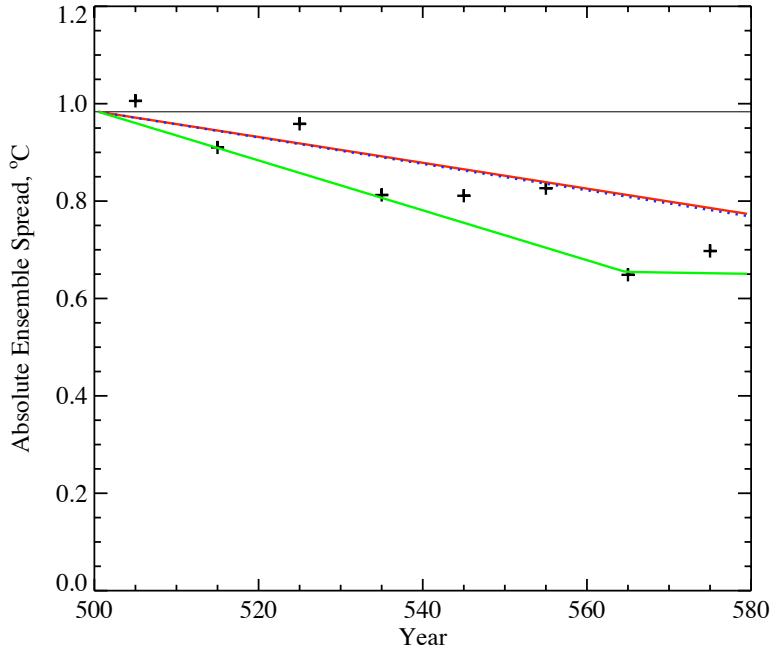


**Figure 6.4** *Hypothetical ensemble spread computed from the diagnosed $\Lambda$, $\kappa$ and knowledge of the imposed radiative forcing. The solid green line is the hypothetical ensemble spread (eq. 6.1). The crosses show the actual spread in decadal temperature in the ensemble. The red line is the spread when only changes in $\kappa$ are considered (eq. 6.2). The blue dotted line is the spread when only changes in $\Lambda$ are considered.*

## 6.3 Relationships to the initial state

The absolute ensemble spread reduces with increasing $CO_2$, and it has been shown by fig. 6.4 that this is caused by changes in both $\Lambda$ and $\kappa$. It also has been shown that the reduction in absolute ensemble spread comes about because of an anti-correlation between the TCR and the initial temperature (fig. 6.3). $\Lambda$ and $\kappa$ are inversely related to the TCR by definition (eq. 4.18). This implies that both $\Lambda$ and $\kappa$ are linearly related to the initial temperature (taken to be the long term average global mean temperature in the control run).

It can be seen in figure 6.5 that both $\Lambda$ and $\kappa$ are linearly proportional to the initial temperature. The slopes of the two lines of best fit (calculated using a least squares regression) are similar, which is consistent with both $\Lambda$ and $\kappa$ being required to explain the reduction in absolute ensemble spread. Although it is interesting to discover that both $\Lambda$ and $\kappa$ are related to the initial climate state, such

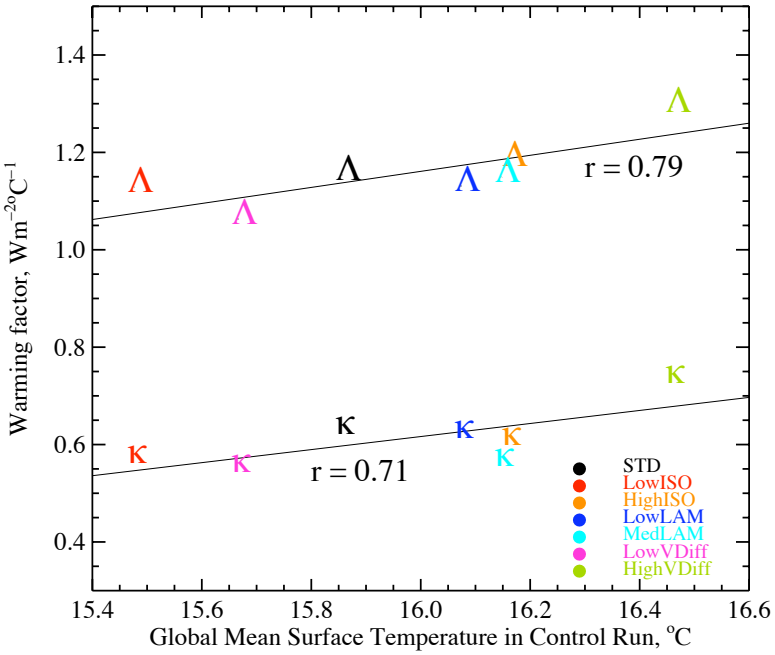


**Figure 6.5** *The relationships between Λ and the initial temperature and κ and the initial temperature. The correlations (r values) for the two relationships are shown on the figure, next to the lines of best fit.*

analysis does not explain the reasons for such relationships. The reasons, if found, will also explain the anti-correlation between the TCR and initial temperature, because variations in both Λ and $\kappa$ have been shown to be important in causing the reduction in absolute spread. The reasons for the two relationships are likely to be different, because of the different nature of Λ and $\kappa$. Therefore, the two relationships will be considered separately.

### 6.3.1 Climate feedback parameter

The climate feedback parameter, Λ, is a measure of the total feedbacks in the climate system, many of which are determined in the atmosphere model. The four main forcings considered by e.g. Colman (2003) are the lapse rate feedback, the water vapour feedback, the surface albedo forcing and the cloud feedbacks. The two largest of these feedbacks are the water vapour feedback (warmer air holds more water vapour) and the lapse rate feedback (a warmer upper troposphere than surface will

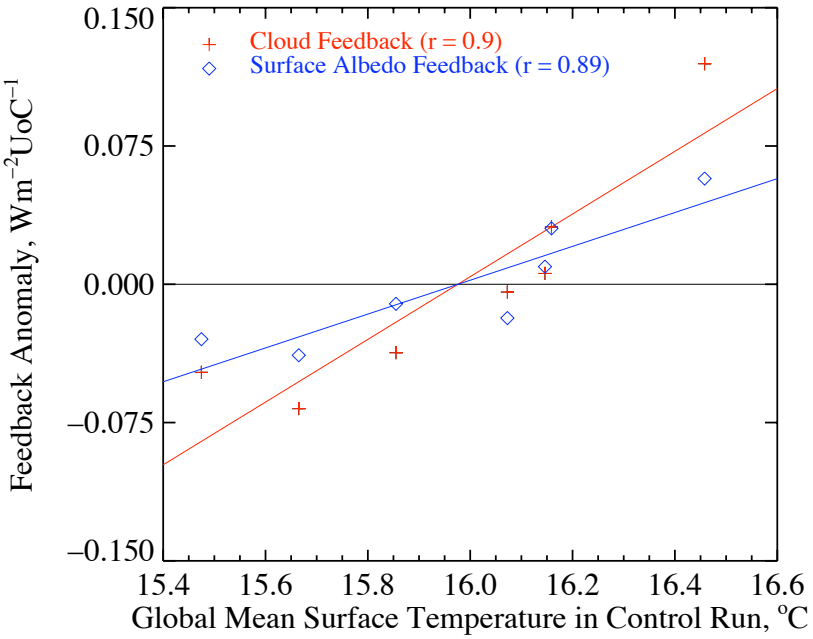


**Figure 6.6** *The relationships between the global mean surface temperature in the control runs and either the cloud feedback (crosses) or the surface albedo feedback (diamonds). The feedback strengths are expressed as anomalies from the ensemble mean values, so that both fit on the same scale - the ensemble mean strength of the surface albedo feedback is 25 times larger than the ensemble mean cloud feedback.*

reduce the temperature gradient, and lessen the greenhouse effect). The review of Bony *et al*. (2006) gives estimates of 1.80 $\pm$ 0.18 Wm$^{-2}$°C$^{-1}$ and -0.84 $\pm$ 0.26 Wm$^{-2}$°C$^{-1}$ respectively for these two feedbacks. Soden and Held (2006) suggest that they are anti-correlated, and should more strictly be considered together. They are both determined by the atmospheric physics and do not change in the ocean ensemble.

There is evidence that the cloud and surface albedo feedbacks can be related to the initial climate state (e.g. Boer and Yu (2003) and Winton (2006)). The surface albedo feedback is dominated by the regions of sea ice and snow cover (Winton, 2006). The maximum extent of sea ice in the models is related to the global mean surface temperature in the control runs (section 3.5.9). Therefore a positive correlation between the strength of the surface albedo feedback and the initial global mean surface temperature is expected. This is shown in figure 6.6 as the diamonds, and shows a significant positive correlation ($r = 0.89$).

It is surprising that there is a similar positive relationship for the cloud feedback (shown as crosses in fig. 6.6, $r = 0.90$). Cloud feedbacks contain the most uncertainty in model predictions (Cubasch *et al*. (2001) and Webb *et al*. (2006)). The strength of the global warming has been shown to be especially sensitive to the sea surface temperature pattern in the tropical ocean (Barsugli *et al*., 2006). This is primarily due to cloud feedbacks.

The magnitude of the surface albedo change (-0.55 $\mathrm{Wm^{-2}{}^{\circ}C^{-1}}$ for the ensemble mean) is over 25 times the magnitude of the cloud feedbacks (-0.04 $\mathrm{Wm^{-2}{}^{\circ}C^{-1}}$). The variations in cloud feedback term are larger however. The gradient of the line of best fit (computed using least squares regression) for cloud feedbacks against the surface temperature (0.17 $\mathrm{Wm^{-2}{}^{\circ}C^{-1}}$) is approximately twice that of the surface albedo feedback (0.09 $\mathrm{Wm^{-2}{}^{\circ}C^{-1}}$). This shows that a sensitivity of the cloud feedback strength to the global mean surface temperature is the dominant process causing the element of reduction in absolute ensemble spread that is attributable to changes in $\Lambda$.

The properties of cloud feedbacks are different in different coupled models (e.g. McAvaney *et al*. (2001)), so the conclusion that the initial global mean surface temperature is a determining factor in the strength of the cloud feedbacks in HadCM3 may not hold true for other coupled models. However, it does highlight the possible influence of systematic biases in the initial surface temperature effecting the modelled climate change signal, through the cloud feedbacks.

### 6.3.2 Ocean heat uptake efficiency

Variations in the ocean heat uptake efficiency, $\kappa$, have been shown to account for about half of the reduction in ensemble spread. Changes in feedbacks can be thought of as caused by changes in the initial state of the model, because the atmospheric physics have not been perturbed in the ensemble. This is not the case with the ocean physics. The ocean physics have been purposely perturbed throughout the ensemble. $\kappa$ is a measure of how effective the ocean physics are at transferring heat to depth under an

increase in $CO_2$. Changes in $\kappa$ are expected as a direct consequence of the parameter perturbations. Therefore, when trying to explain the relationship between the global mean surface temperature and $\kappa$, we are looking for reasons why an ocean with a higher $\kappa$ (i.e. stronger vertical heat transports) should have a higher global mean surface temperature.

The latitudes of the globe with the strongest vertical heat transfers between the upper and lower ocean are in the Southern Ocean in the region of the ACC (50°S-60°S, Gregory (2000)), so the magnitude of $\kappa$ can be expected to be related to the strength of the upward heat transfer in this region. A strong upward heat transfer (and therefore high $\kappa$) would be expected to lead to a warmer surface in this region (and does in the ensemble). The correlation coefficient, $r$, between $\kappa$ and the average surface air temperature between 50°S-60°S in the control run is 0.84. It can be seen from analysis of the control mean SST patterns (section 3.5) that the temperature of the Southern Ocean has the strongest surface temperature changes, and is therefore highly related to the global mean surface temperature (the correlation coefficient is 0.96).

The ocean heat uptake efficiency, $\kappa$, is a diagnostic that only really has a meaning when investigating the time-varying response of the climate to a time-varying forcing (Booth *et al.*, 2006). It is not relevant if the climate system is close to reaching an equilibrium (as it always implies a flux imbalance into the ocean), because the assumption that the deep ocean temperature does not change is false on long timescales after a change in forcing (Gregory, 2000). However, variations in $\kappa$ imply variations in the strength of the vertical heat transfers in the ocean. These variations have implications on the surface temperature of the equilibrium climate state. As $\kappa$ is inversely related to the TCR, this means that the initial temperature must be anti-correlated to the TCR through ocean processes.

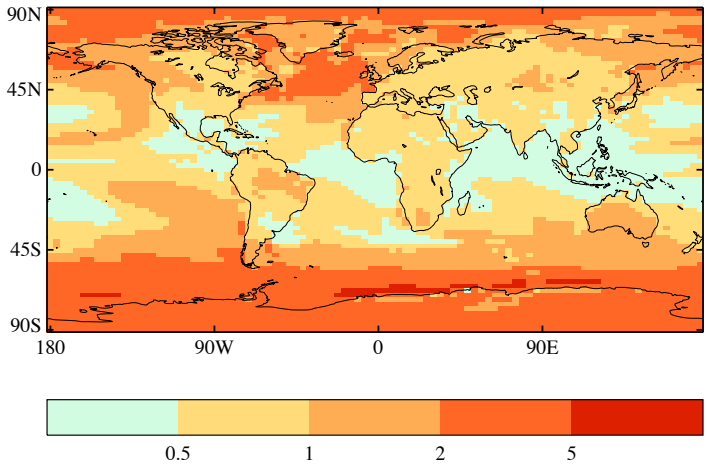


(a) Initial absolute spread (This is shown with significance testing and a finer contour spacing in fig. 3.6)

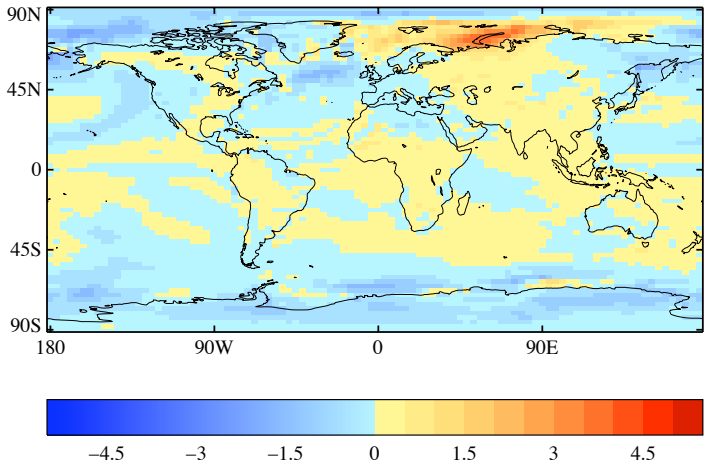


(b) The change in absolute spread caused by increased $CO_2$

**Figure 6.7** *The spatial pattern of absolute ensemble spread in surface air temperature (in°C). (a) shows the absolute spread in the control integrations (the initial conditions). (b) shows the difference in the absolute ensemble spread between the final 20 yrs of the the 1% run and the final 20 years of the control integration.*

## 6.4 Spatial variation of the evolution of spread

Figure 6.7 shows the change in absolute ensemble spread in surface air temperature caused by the increase in $CO_2$ for the last 20 years of the experiment. The absolute ensemble spread in the control run is shown as (a), whilst (b) shows the changes seen in the increasing $CO_2$ run. The absolute spread reduces in those regions with the largest initial spread. These are the regions of largest vertical heat transports in the ocean (section 3.5.3). An obvious exceptions to this is the increase absolute ensemble spread off the coast of Siberia, which is related to the uncertainty in sea ice coverage described in section 5.11. The area has constant sea ice coverage in the control run, but as the climate warms the ice edge retreats into this area.

There is a spatial anti-correlation between these two global patterns ($r = -0.52$). This anti-correlation might imply that the same mechanisms that cause absolute ensemble spread in the control runs, also cause the reduction in absolute spread that occurs when $CO_2$ levels are increased.

## 6.5 Conclusions

There is a detectable reduction in the absolute ensemble spread as a result of increasing the $CO_2$ content of the atmosphere. This reduction can be thought of as being the result of uncertainty in two different factors, the climate feedbacks (characterised by the climate feedback parameter, $\Lambda$) and the strength of the ocean vertical heat transfers (characterised by the ocean heat uptake efficiency, $\kappa$). The importance of the effects of uncertainty in the two factors is approximately equal, both in setting the signal spread (spread in transient climate response, section 4.8), and in the reduction in absolute ensemble spread (section 6.2.1).

The origin of the uncertainty in the two factors is different. The uncertainty in the strength of the ocean vertical heat transfers is caused by the uncertainty in the ocean physics parameterisations and can be

thought of as a direct consequence of the ocean model uncertainty. It causes a negative correlation between the preindustrial surface temperature and the transient climate response. Stronger (weaker) vertical heat transfers causes warmer (colder) surface temperatures at high latitudes in the control state, as well as a reduced (increased) transient climate response.

The uncertainty in the climate feedback parameter occurs because the climate feedbacks are partly a property of the initial climate state. The changes in $\Lambda$ are primarily due to the sensitivity of the cloud feedbacks to the modelled sea surface temperature pattern. There is also a contribution from the differing initial sea ice distributions effecting the surface albedo feedback. Both of these feedback changes can be considered indirect effects of the ocean model uncertainty, because they result from the systematic changes in the ocean surface climate caused by the parameter perturbations.

There is ensemble spread in the initial (preindustrial) climate state of around 1°C (as described in chapter 3). This ensemble spread is much larger than the uncertainty in the instrumental observations of the present day climate (e.g. 5-95% range of 0.06°C for 2000 A.D. from Folland *et al*. (2001b)). However, the initial absolute ensemble spread is consistent with the ranges from proxy data of the pre-industrial climate (Mann and Jones (2003) and Esper *et al*. (2002)). The anti-correlation between the initial temperature and the TCR found in this chapter means that a different ensemble with less spread in the initial conditions might be expected to have a reduced spread in the time-dependent response.

# CHAPTER 7

# Conclusions

## 7.1 Introduction

This chapter summarises the work and findings presented in all the previous chapters. It will concentrate on showing how these findings answer fundamental questions about the influence of ocean model uncertainty. This thesis has presented the first study into the effects of ocean model uncertainty in complex AOGCMs on the projections of climate change. This chapter will conclude with a discussion of the next steps to investigate the effects of ocean model uncertainty more comprehensively, and address some further questions which have been posed by the conclusions of this work.

## 7.2 An overview of the thesis

The uncertainty inherent in climate predictions comes from a variety of sources. This thesis has isolated and investigated one of these sources - the uncertainty in ocean models that arises because of inaccuracies in the values of parameters used in the physical parameterisation schemes (referred to as "ocean model uncertainty" in this work). The effects of this source of uncertainty on time-dependent climate change have never previously been systematically investigated in a complex atmosphere-ocean general circulation model (AOGCM). Version 3 of the Hadley Centre's coupled model (HadCM3) was used for this investigation. Its atmosphere component has recently been used in studies into the effects of atmosphere model uncertainty on the equilibrium response of the climate system to an increase in $CO_2$ (Stainforth *et al*. (2005) and Murphy *et al*. (2004)). Although Collins *et al*. (2006) included an

ocean model to look at the effects of atmosphere model uncertainty on the time-dependent response, they did not include an investigation of the ocean model uncertainty. Thus one of the goals for this work was to examine the relative importance of the ocean model uncertainty and the atmosphere model uncertainty.

### 7.2.1 Creation of a database of ocean physical parameterisations and their uncertainty ranges

To determine the effects of ocean model uncertainty on climate change, it was first necessary to devise a method of sampling the uncertainty. A method similar to that of Murphy *et al*. (2004) was followed. It requires the creation of a database of ocean physical parameterisations and their uncertainty ranges. Twelve parameters and four logical switches have been identified as containing some uncertainty by an expert elicitation exercise (a further description of this process can be found in section 2.2). A range for each parameter was determined, within which the parameterisation is consistent with both observations and our knowledge of the physical processes. Three parameters relating to the isopycnal thickness diffusion parameterisation of Gent and McWilliams (1990) are only relevant for either HadCM3 or HadCM3L. A different database of perturbations has been created for each model; table 2.8 for HadCM3 and table 2.9 for HadCM3L.

These databases contain many possible perturbations. To limit the computational requirement each perturbation has been given a priority depending on its expected impact on time-dependent climate change. The priority was also derived through expert elicitation.

### 7.2.2 Creation of a perturbed ocean physics ensemble

The rest of the thesis describes an assessment of the *maximum* impacts of the ocean model uncertainty on time-dependent climate change, as determined by single perturbations. A perturbed ocean physics

ensemble of HadCM3 was created by perturbing the three most important parameters from the newly created database to their maximum extent. The seven resultant model versions (the standard model is also included) have been brought into a quasi-equilibrium with constant preindustrial levels of $CO_2$ after 500 years of spin up without flux adjustments. A simple model evaluation criteria was defined to test each model version before its inclusion in the ensemble. Some model versions were more realistic than others, but all were considered plausible representations of the climate system.

### 7.2.3 Ensemble spread in the long term pre-industrial climate state

A systematic investigation of the ensemble spread in the long term mean climate state was performed. The ensemble spread is greater than that expected from modelled internal variability alone (as computed from a millenia-long integration of HadCM3) for nearly all variables investigated in both the atmosphere and ocean. All of the perturbations cause changes in the vertical heat budget of the ocean. They do not change the dominance of the different processes though. The largest uncertainty in surface air temperature occurs in the high latitudes, where the vertical heat transports in the ocean are largest. The uncertainty in the high latitudes is amplified by feedbacks with the sea ice edge and snow cover. The surface temperature uncertainty is not confined to the high latitudes. The tropical temperature uncertainty causes significant uncertainty in the precipitation distribution. Therefore the ocean model uncertainty causes uncertainty throughout HadCM3's preindustrial climate.

### 7.2.4 The transient response to an increase in $CO_2$

A climate change experiment was performed with the ensemble. The amount of $CO_2$ in the atmosphere was increased by 1% per year for 80 years (meaning that the $CO_2$ levels were doubled after 70 years).

The ensemble exhibits a range of transient climate responses (TCR, defined as global mean temperature change after 70 years under this scenario) that is detectably larger than that expected from

internal variability alone. The ensemble represents the maximum linear effect that would be caused by ocean model uncertainty, because each of the parameters are perturbed to the limits of their uncertainty ranges. The fact that the TCR is significantly larger than internal variability shows that the ocean physics parameter perturbations (and hence ocean model uncertainty) have an effect on the time-dependent climate change signal.

However, the spread in TCR is over 75% less than that seen in the ensembles comprised of AOGCMs included in the IPCC's third and fourth assessment reports. The spread in the ocean ensemble is also less than half that of the spread seen in a similar experiment performed with a perturbed atmosphere physics ensemble (Collins *et al.*, 2006). The ensemble presented in this thesis attempts to sample the maximum effects of ocean model uncertainty, however the signal spread in TCR is still relatively small compared to non-maximised uncertainty from other sources.

Several possible causes for the ensemble to underestimate the maximum signal spread were investigated. Firstly, the perturbations could have been too conservative and might not express the full uncertainty in each of the parameters. To address this possibility, the experts who provided the ranges were re-consulted and asked if they would revise the ranges in light of the results found. They felt that the ranges could not be extended and still agree with current observations and knowledge. A second possibility investigated was that the perturbed parameters might not control ocean heat uptake and hence might not control the time dependent response of the model. Analysis of global mean ocean vertical heat transfers found that two of the three dominant processes had been successfully perturbed. The other process, advection, is explicitly resolved rather than parameterised.

### 7.2.5 Signal spread caused by ocean model uncertainty

There is detectable signal spread in the climate feedback parameter (related to the climate sensitivity) as well as in the ocean heat uptake efficiency. They are approximately equally important in determin-

ing the TCR range. The ocean model uncertainty affects the climate feedback parameter through both the surface albedo and the cloud radiative feedback.

The largest uncertainties in the surface temperature climate change signal occur in the North Atlantic, Southern Ocean and the south-east tropical Pacific. The signal spread is greater than the ensemble mean warming in these regions. The surface temperature signal spread has a similar spatial pattern to the surface temperature ensemble spread in the preindustrial climate.

All ensemble members show a reduction in the strength of the thermohaline circulation under climate change. There are variations in the strength of the reductions. These cannot be unambiguously attributed to ocean model uncertainty at the 5% confidence level, because of the large natural variability of the thermohaline circulation.

A small global mean signal spread could be masking important regional differences, through a form of compensation. Raper *et al*. (2002) found compensation occuring between the climate sensitivity and ocean heat uptake efficiency in a multi-model ensemble. This form of compensation does not occur in the ensemble. The spatial pattern of the climate change signal was also investigated to discover if regional compensation was occuring. This was performed by examining the correlation of ensemble variations amongst 41 regions. No negative correlations were found between any regions, so no regional compensation is occuring.

### 7.2.6 The temporal evolution of ensemble spread

The effects of ocean model uncertainty on the preindustrial climate can be thought of as providing initial state errors, allowing the error growth due to an increase in $CO_2$ to be investigated. The ensemble spread in the global mean surface temperature reduces significantly as the levels of $CO_2$ increase. This occurs because there is an anti-correlation between the initial global mean surface temperature and the magnitude of the transient climate response. This relationship is caused in part by a dependence of the

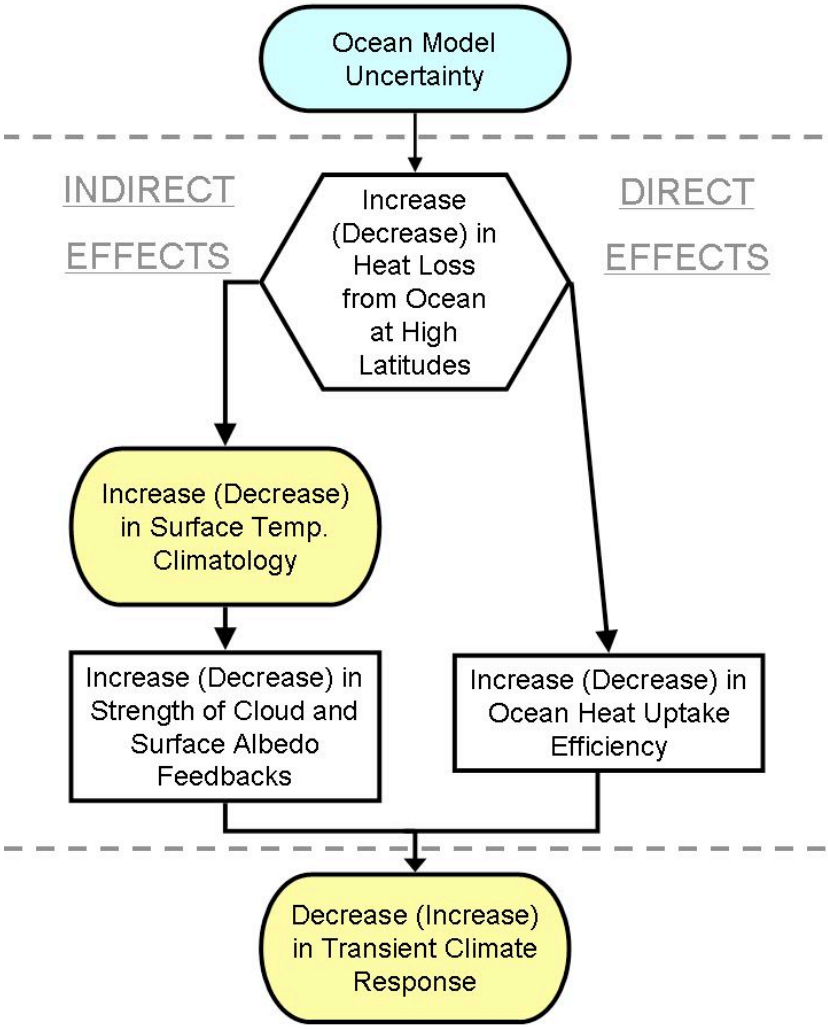


**Figure 7.1** *A flowchart showing the global mean influences of ocean model uncertainty. The blue shape indicates the input - ocean model uncertainty. An arrow means "causes variations in". The diamond shape indicates that the heat loss is not itself a global mean change, but rather a mechanism through which global mean changes occur. Yellow shading indicates that, although the relationships relates to the global mean changes (investigated in chapter 6), the spatial pattern of the temperature changes and changes in other variables have been investigated in this thesis.*

climate feedback parameter on the preindustrial climate (largely related to the cloud radiative feedback, but also to the surface albedo feedback) and in part by a relationship between the ocean heat uptake efficiency and the amount of warming observed in the spin-up (related through the strength of the vertical heat transfers).

These relationships are summarised in figure 7.1. The ocean model uncertainty causes uncertainty in the heat loss from the ocean at high latitudes, that can be seen by the large uncertainty both in the

preindustrial surface temperature and in the climate change signal in the high latitudes. An increased heat loss would indicate stronger vertical heat transfers in the high latitudes, which would mean the model has an increased ocean heat uptake efficiency. An increased ocean heat uptake efficiency leads to a smaller transient climate response. This can be thought of as a direct effect, because the changes in the vertical heat transfers lead directly to a variation in the climate change signal. The increase in the heat loss from high latitudes will also lead to increased surface air temperatures in the preindustrial climate state. An increased preindustrial temperature is also associated with an increase in the strength of the climate feedback parameter, through cloud and surface albedo feedbacks. An increased climate feedback parameter leads to a smaller transient climate response. This can be considered as an indirect effect of ocean model uncertainty on the climate change signal, because it relies on changes in the preindustrial climate state.

If the ocean model uncertainty causes a decrease in the heat loss from the ocean at high latitudes, there would be a reduced ocean heat uptake efficiency and a reduced climate feedback parameter (through a decreased temperature in the preindustrial state). These changes would in turn lead to a larger transient climate response. The preindustrial climate state would also be affected by atmosphere model uncertainties. This may break the link between the climate feedback parameter and the preindustrial global mean temperature, and hence remove the indirect effect of ocean model uncertainty.

The spatial pattern of the reduction in absolute ensemble spread is similar to the pattern of preindustrial ensemble spread. This suggests that the same mechanisms cause the uncertainty in the preindustrial climate and the reduction in ensemble spread.

## 7.3 Discussion

The purpose of this thesis was to investigate ocean model uncertainty and its effects on time-dependent climate change. Ocean model uncertainty, as defined in this thesis, is not the total uncertainty con-

tained in the ocean component of the model. It is solely the uncertainty in the parameter values in the ocean physics parameterisations. This definition of ocean model uncertainty is consistent with the definition of atmosphere model uncertainty used by Murphy *et al*. (2004), Collins *et al*. (2006) and Stainforth *et al*. (2005). Structural uncertainties were not involved as part of the current definition, because of the complexity of investigating them. Structural uncertainties include variations in the model resolution and the basic physical assumptions used in the parameterisation of sub grid scale processes (Harris *et al*., 2006). To investigate them would require a completely modular model, in which all possible assumptions can be adjusted. It is outside the scope of this study to create such an AOGCM.

As the effects of structural uncertainty in time-dependent climate change have not been investigated, it could still be the case that the ocean component of AOGCMs contains a large amount of uncertainty. This thesis has shown that the amount of uncertainty in the parameter settings is relatively small. One possible method of performing an initial investigation into structural uncertainty would be to use an adaptable coupler to join different atmosphere and ocean components together. Guilyardi *et al*. (2004) performed such an exercise to look at El-Niño-southern-oscillation simulations, and found that the largest discrepancies in the El-Niño-southern-oscillation simulation were related to the atmosphere model. It is suspected that there is less total uncertainty in the ocean component of HadCM3 than in the atmosphere component. This cannot be definitively proven from the work presented here.

It is known that multiple parameter perturbations may lead to a much larger response, because of non-linear interactions between the perturbations (Stainforth *et al*., 2005). Only a single parameter has been perturbed in each member of the ensemble presented here. The only method of discovering whether non-linearities of this type exist is to repeat the experiment including multiple parameter perturbations. It should be noted that for the majority of the climate change signal analysis, the range was established solely by the perturbations to the vertical diffusivity. The other perturbations had little detectable effect. Therefore any non-linearities would have to be very substantial to affect changes in the signal spread. The lack of supportive research suggests this is not the case. However, following on

the work presented in chapter 6, it would be expected that the range in the transient climate response would increase if multiple perturbations were included. They are expected to cause a larger absolute spread in the initial climate state and hence a larger reduction in spread under increasing $CO_2$ would be seen. This could mean a larger signal spread.

## 7.4 Further work

The ultimate goal of systematic investigation into uncertainties is to produce probabilistic climate predictions. Quantifying the effects of ocean model uncertainty is a step towards this goal. The work presented in this thesis is an initial quantification of the effects of ocean model uncertainty on time-dependent climate change. Further investigations are required both to provide a more comprehensive knowledge of the effects of ocean model uncertainty itself, and to incorporate ocean model uncertainty into probabilistic forecasting methods.

A more comprehensive knowledge of ocean model uncertainty would be gained by addressing some of the other sources of uncertainty discussed in sections 4.5 and 7.3. A much larger ensemble could be created that incorporates multiple parameter perturbations. It should also consider additional parameters from the perturbation database, in case of misjudgements of the priorities presented in chapter 2. A larger ensemble would be expected to have both an increased signal spread and an increased preindustrial ensemble spread. It is not expected to substantially alter the conclusion that ocean model uncertainty causes smaller uncertainty in the transient climate response than atmosphere model uncertainty.

There are many features of the Earth's climate that involve coupled feedbacks between the atmosphere and ocean. This implies that there will be interactions between atmosphere model uncertainty and ocean model uncertainty. So far these two uncertainties have only been investigated individually in AOGCMs. An ensemble should be created to investigate whether such coupled interactions exist. It

might be the case that atmosphere model uncertainty dominates ocean model uncertainty to such an extent that the ocean model uncertainty is not an important factor. Evidence for this is provided by the fact that the TCR spread caused by atmosphere model uncertainty (as determined by Collins *et al.* (2006)) encompasses the TCR spread seen in the AR4 models.

In the longer term, a method of investigating the effects of structural uncertainty needs to be devised. The OASIS coupler (Valcke *et al.*, 2000) allows different model components to be coupled to each other. It has already been used to couple the atmosphere models of HadAM3 and ECHAM4 to the OPA ocean model (Guilyardi *et al.*, 2004). Use of such a coupler would allow an initial investigation into the importance of structural uncertainties. It would still be restricted to sampling the choices and assumptions made by existing AOGCMs and in the coupler. A single modular AOGCM that allows every assumption to be altered would be required to fully sample structural uncertainty. Such a model would take many man-years to develop, and should not be undertaken unless an initial investigation shows structural uncertainty to be a significant source of uncertainty in climate projections. Collins *et al.* (2006) have shown that atmosphere model uncertainty alone can replicate the full spectra of TCR from models submitted to the IPCC for inclusion into AR4. This implies that the development of a single modular AOGCM may be unnecessary.

The final goal of a probabilistic forecast can only be achieved with a "grand ensemble" (Stainforth *et al.*, 2005). This should sample all forms of uncertainty - model uncertainty, structural uncertainty, scenario uncertainty and initial condition uncertainty. The computer resource required to create this form of prediction is substantial. Climate*prediction*.net are using distributed computing to provide the resources necessary to perform an initial attempt at such a prediction (www.climate*prediction*.net). This approach of using otherwise wasted personal computing resources combined with optimal sampling techniques (Hargreaves and Annan, 2006) provides the most likely source of creating a reliable regional probabilistic prediction, which includes all the uncertainties involved in climate prediction.

# APPENDIX A

# The sensitivity of the rate of transient climate change to ocean physics perturbations

## A paper accepted to be printed in Journal of Climate in 2007

M. Collins[1], C. M. Brierley[2], M. MacVean[3], B. B. B. Booth[1], G. R. Harris[1]

[1]Hadley Centre for Climate Prediction and Research, Met Office, Exeter, UK. [2]Department of Meteorology, University of Reading, Reading, UK. [3]European Centre for Medium-Range Weather Forecasts, Reading, UK.

## Abstract

"Perturbed physics" ensembles of Hadley Centre climate models have recently been used to quantify uncertainties in atmospheric and surface climate feedbacks under enhanced levels of CO2, and to produce probabilistic estimates of the magnitude of equilibrium climate change. The rate of time-dependent climate change is determined both by the strength of atmosphere-surface climate feedbacks and by the strength of processes which remove heat from the surface to the deep ocean. Here we report on the first small ensemble of coupled atmosphere-ocean climate model experiments in which the parameters that control three key ocean physical processes are perturbed. We find that the perturbations have little impact on the rate of ocean heat uptake, and thus have little impact on the time-dependent rate of global warming. Under the idealised scenario of 1% per year compounded CO2 increase, the spread in the Transient Climate Response is of the order of a few tenths of degree, in contrast to the order one degree spread cause by perturbing atmospheric-model parameters.

## Introduction

Uncertainties in the magnitude of future climate change have recently been quantified using "perturbed physics" ensembles of the Hadley Centre climate model (Murphy et al., 2004; Stainforth et al., 2005; Barnett et al., 2006; Webb et al., 2006; Collins et al., 2006; Piani et al., 2006). In these studies, parameters in the atmospheric component of the model are varied within specified ranges, and the atmosphere is coupled either to a simple mixed-layer ocean, or, in one case (Collins et al., 2006) coupled to the same standard-parameter dynamical ocean component. The studies thus explore physical climate feedbacks associated with atmospheric and surface processes of which clouds are the leading-order driver of uncertainty (Webb et al., 2006).

The rate of global-mean time-dependent temperature change under a specified forcing scenario is determined jointly by the strength of the physical feedbacks in the atmosphere and surface components of the climate system and the efficiency of processes which remove heat from the surface of the ocean to depth (Gregory and Mitchell (1997)). We may parameterise the flux of heat through the ocean surface, $F$, as being proportional to a constant, $\kappa$, multiplied by the global mean temperature change; this being a suitable approximation to make under forcing scenarios of increasing greenhouse gases (e.g. common socio-economic scenarios or simple compound increases in CO2) and which is justified *aposteriori* (see fig. 2(b)). Hence we may write,

$$\Delta T = \frac{Q}{\Lambda + \kappa}, \quad (1)$$

where $\Delta T$ is the global mean temperature change at a given time, $Q$ is the radiative forcing in at that time, $\Lambda$ is the atmospheric feedback parameter and $\kappa$ is the ocean heat uptake efficiency (Raper et al., 2002). Uncertainties

in the transient response of the climate system are determined by the physical processes involved in setting both $\Lambda$ and $\kappa$.

Here we report on the first small ensemble of coupled atmosphere-ocean model simulations of climate change in which parameters in the ocean component of the model are systematically varied; thus potentially impacting the rate of ocean heat uptake and the rate of warming. In order to isolate the impact of different oceanic processes, we follow Murphy et al. (2004) by perturbing parameters one-at-a-time. We also focus on global mean quantities in order to understand the leading-order impact of the perturbations on future climate change.

## Experiments and Perturbations

We use version three of the Hadley Centre Coupled Model (Gordon et al., 2000) employed in previous perturbed physics studies (e.g. Collins et al., 2006) with the standard parameter settings in the atmosphere and the inclusion of an interactive sulphur cycle. Experts in ocean modelling were consulted and a list of ocean parameters produced, together with likely ranges (Brierley, 2006). Those experts also indicated the parameters which would be likely to have the greatest impact, leading to the parameters which control three ocean physical processes being perturbed; the diffusivity of tracers along isopycnal surfaces, the calculation of the depth profile of wind-mixing energy in the ocean mixed-layer, and the vertical diffusivity of tracers (table 1).

Figure 1 illustrates the experimental design. In each simulation, the model ocean component was initialised from the Levitus (1994) analysis of the observed temperature and salinity, and a state of no motion. Each member was then run for 500 years in "spin-up" mode with constant preindustrial concentrations of greenhouse gases and sulphate emissions. No flux-adjustments were employed, resulting in a varying degree of drift away from the initial state. The reason for the increase in ocean heat content in comparison with the relatively small drift seen in the original HadCM3 control experiment (Gordon et al., 2000) is the replacement of the prescribed sulphate aerosol distribution with that determined by the interactive sulphur cycle (this was done for consistency with the study of Collins et al., 2006). Because the model then generates its own three dimensional aerosol fields in place of previously prescribed fields, there is a positive top-of-atmosphere (TOA) radiative imbalance, with approximately 1.5 $\mathrm{Wm}^{-2}$ less outgoing than incoming radiation and a corresponding initial warming and drift in each member (see table 1 of Collins et al., 2006). Aerosol emissions remain fixed at preindustrial values in all of the experiments described below and experiments with the atmosphere component of the model coupled to a mixed-layer ocean give climate sensitivities which are indistinguishable with interactive and non-interactive schemes.

Following this spin-up phase, a further 80 years of control experiment was run with constant CO2, together with an experiment with a CO2 increase of 1% per year compounded (hereafter the 1%-scenario). While no experiment is in true equilibrium, the drift in total ocean heat content in the control phase is small in comparison with the signal seen in the 1%-scenario experiments. In addition, the relevant surface and atmosphere global-mean variables show no significant drift (see figure 2 later). The 500 year spin-up attempts to produces control-states with relatively small residual trends and at the same time limit the drift away from the observed initial state, minimising as far as possible the influence of mean-state biases.

For comparison, we also use global-mean quantities from a 16 member HadCM3 ensemble in which atmosphere, surface and sea-ice parameters have been varied (Collins et al., 2006). In this ensemble, flux-adjustments are employed to correct for top-of-the-atmosphere radiation imbalances that result from the physics perturbations, and to improve the credibility of the simulations in terms of their projections of regional climate change. We also perform two more experiments with standard atmosphere and ocean parameter values but with slight modifications to the Haney- phase temperature and salinity relaxation coefficients (this greatly improves the SST biases seen in Collins et al., 2006). The use of this atmosphere-surface physics ensemble allows us to assess the relative importance of uncertainties in the processes that determine $\Lambda$ and $\kappa$ in setting the rate of time-dependent climate change. In what follows, we refer to the Collins et al. (2006) ensemble as the "atmosphere-physics" ensemble, the experiments shown in figure 1 as the "ocean-physics" ensemble and all experiments with standard parameter values (whether flux-adjusted or not) as the "standard-model".

## Impact on Global Mean Climate Change

Figure 2 shows a number of global-mean quantities from both the atmosphere-physics and the ocean-physics ensemble. In terms of the rate of global-mean temperature rise, the perturbations to the ocean parameters appear to have little impact in comparison with atmosphere parameter perturbations. They produce a very small ensemble spread in $\Delta T$, the same being true of the anomalous flux of heat into the ocean, F, and the rate of rise of ocean heat content. The only exception appears to be the experiment with high vertical diffusivity.

The information contained in figure 2 may be quantified by diagnosing the terms in equation 1 over the 20-year period straddling the time of CO2 doubling at year 70 of the 1%-scenario experiments (see e.g. Raper et al., 2002). The feedback parameter is computed as

$$\Lambda = \frac{Q_{2X} - N_{2X}}{\Delta T_{2X}} \text{ , (2)}$$

where $Q_{2X}$ is the radiative forcing at doubled $CO_2$, $N_{2X}$ is the 20-year average TOA flux anomaly and $\Delta T_{2X}$ is often known is the Transient Climate Response or TCR, the 20-year average global-mean temperature anomaly. We assume that $Q_{2X}$ is the same in each experiment, taking the value of 3.8 $Wm^{-2}$ calculated explicitly from an atmosphere-mixed layer experiment. Each model version uses the same radiation component and, as shown in figure 1(a) of Webb et al. (2006), three structurally-different versions of the Hadley Centre model in which this same radiation component is used have near-identical global mean radiative forcing. Anomalies are calculated with respect to the relevant 80-year control average. The ocean heat uptake efficiency is calculated as

$$\kappa = \frac{F_{2X}}{\Delta T_{2X}} \text{ , (3)}$$

where anomalies in the global-mean flux of heat from the atmosphere to the ocean, $F_{2X}$, are expressed per unit area of the Earth's surface. While $\Lambda$ is generally relatively time-invariant in such 80-year experiments (although time-dependence is seen in longer experiments with larger forcing e.g. Senior and Mitchell, 2000; Raper et al., 2002) the $\kappa$ parameter does have a time-dependence that is inversely proportional to the length of time from the start of the experiment. Nevertheless, the $\kappa$-approach provides a conceptually simple metric which facilitates comparison with previous studies. A graphical representation of the variations in TCR, $\Lambda$ and $\kappa$ is presented in figure 3 and numerical values are given in table 1.

As reported in Collins et al. (2006), perturbations to the atmosphere component of the model impact the magnitude of atmospheric and surface climate feedbacks and, as a consequence, the TCR. The range in the atmosphere-physics ensemble shown in figure 3 is similar to the range seen in the most recent group of models collected for the fourth assessment of the Inter-Governmental Panel on Climate Change (see Collins et al., 2006, figure 7). Perturbations to the atmosphere component (with the ocean component fixed) make little change to the ocean heat uptake efficiency and what little spread there is in the magnitude of $\kappa$ makes an almost negligible contribution to the spread in TCR (tables 1 and 2).

Perhaps surprisingly, it is also the case that the perturbations to the ocean component make little impact on the ocean heat uptake efficiency and, as a consequence, the TCR. With the exception of the experiment with high vertical diffusivity (discussed below), figure 3 and tables 1 and 2 show that the range of $\kappa$ is consistent with that seen in the ensemble with perturbed atmosphere parameters. The corresponding spread in the TCR (again, excluding the HighVDiff experiment) is similarly small, of only a few tenths of a degree.

The only perturbation that does seem to have an impact on the TCR is that with high vertical diffusivity. In this experiment, there is an increase of the order of a few tenths of a $Wm^{-2}K^{-1}$ in the ocean heat uptake efficiency, $\kappa$, in comparison with the standard model version but there is also a similar-magnitude increase in the atmospheric feedback parameter, $\Lambda$ (table 1). Both changes contribute to a reduction in the TCR in comparison with the standard model. We hypothesise that the relatively larger drift away from the observed initial state in this experiment (figure 1) results in a significantly different control climate and therefore different magnitudes of atmosphere-surface feedback processes under enhanced $CO_2$. To test this hypothesis, we repeat the high vertical diffusivity experiment using flux-adjustments in order to keep the control-experiment climatology close to that of the standard model. In this experiment, $\Lambda$ is consistent with the standard-model $\Lambda$, and $\kappa$ is closer to

that of the standard model but still marginally higher indicating that the perturbation does have some influence on the processes that determine ocean heat uptake. Nevertheless, the impact of the perturbation on the TCR is still small in comparison with perturbations made to atmospheric parameters.

## Discussion and Future Work

There are three potential caveats to this work: firstly the experts consulted may have may have been overly conservative in their specification of the ranges of the parameters perturbed; secondly there may be other ocean-component parameters which are important; and thirdly the one-by-one nature of the perturbations may mask some non-linear interactions of processes which could produce significant spread in $\kappa$ and the rate of climate change. Re-consultation with the experts and examination of the literature reveals the first of these to be unlikely. The second is possible; although there are no obvious candidates. The third is also possible, and can only be really checked by performing simultaneous parameter perturbation experiments. Nevertheless, the broadening of the frequency distribution of climate sensitivity seen in the simultaneous atmospheric perturbation studies (Stainforth et al., 2005; Webb et al., 2006) in comparison with that in the single-parameter perturbation study (Murphy et al., 2004) is a result of non-linear interactions between individual processes which, on their own, are known to have a significant impact on climate sensitivity. The degree of non-linearity needed to amplify physical processes which, on their own, have little impact on ocean heat uptake efficiency would have to be considerable.

The obvious oceanic process not influenced by the ocean-component parameter perturbations we have chosen is the high-latitude convection which appears (from Gregory 1999 and 2000) to have an important, and possibly controlling, role. Convective instability in HadCM3 is removed using the Rahmstorf (1993) scheme globally with the Roussenov et al (1995) scheme applied in the sills separating the Greenland-Iceland-Norway Seas from the Atlantic (in order to improve the properties of the dense water which overflows these sills). While it may be possible to perturb some of the options associated with this part of the code, the generic effect of ocean convection schemes is to instantaneously mix columns of water which have become unstable (as a result of surface heat loss or salinification through brine release from sea ice). Introducing a time-lag into the ocean convection scheme might improve the representation of that process, but is unlikely to have a large effect on the rate of ocean heat uptake because of the disparate time scales.

The ranges in the key properties discussed in this perturbed-parameter ensemble are smaller than those reported in multi-model studies (Raper et al., 2002; Sokolov et al., 2003), suggesting that structural aspects of ocean models are of leading-order importance. For example, Russell et al. (2006a) and (2006b) assess the role of the southern ocean in recent AOGCMs and find a rather wide range of control-states which affect the storage of heat in this key region under climate change. Using an approach based on optimal detection and attribution, Forest et al. (2006) show that the ocean effective diffusivity in many of the current generation of AOGCMs is inconsistent with observations although in their study, HadCM3 is one of the better models being more consistent with the data than many others. One corollary of this study is that the choices made when building the ocean component of a coupled model, together with mean climate biases, are likely to be of central important in setting the rate of ocean heat content and may not be "tuned out" by changing the input parameters of the model.

Here we only report on the outcome of the study in terms of global mean temperature change. While the impacts of the perturbations are small in comparison with natural variability and atmosphere-model parameter uncertainties, larger ensembles or longer experiments under different forcing scenarios may yet reveal significant impacts. The next stage of the work will be to understand why the simulations show only small changes in ocean heat uptake efficiency and global mean temperature change. In addition, regional patterns of climate change may be impacted by the perturbations and we still have not exhausted the list of parameters which could be perturbed, nor have we examined non-linearities by perturbing parameters simultaneously.

## Acknowledgements

We are very grateful to the input from the Hadley Centre Ocean Group and a number of international experts for their help in determining the parameters and their ranges and in interpreting the results. We are grateful also to Jonathan Gregory and Mark Webb for their insightful comments. The work was supported by the

UK Department of the Environment, Food and Rural Affairs under Contract PECD/7/12/37, by the European Community ENSEMBLES (GOCE-CT-2003-505539) project under the Sixth Framework Programme and by the UK Natural Environment Research Council.

## References

Barnett, D.N., S.J. Brown, J. M. Murphy, D.M.H. Sexton and M.J. Webb (2006). Quantifying uncertainty in changes in extreme event frequency in response to doubled CO2 using a large ensemble of GCM simulations. Climate Dynamics, 26, 489-511.

Brierley, C. (2006) Ocean parameter perturbations for ensemble climate prediction with climateprediction.net and QUMP. Unpublished manuscript.

Collins, M., B.B.B. Booth, G.R. Harris, J.M. Murphy, D.M.H. Sexton, M.J. Webb (2006) Towards Quantifying Uncertainty in Transient Climate Change. Climate Dynamics, 27, 127-147.

Forest, C.E., P.H. Stone and A.P. Sokolov (2006) Estimated PDFs of climate system properties including natural and anthropogenic factors. Geophys. Res. Letts. 33, L01705.

Gregory, J.M. and J.F.B. Mitchell (1997) The climate response to CO2 of the Hadley Centre coupled AOGCM with and without flux adjustment. Geophysical Research Letters, 24, 1943-1946.

Gregory, J.M. (1999) Comparison of heat uptake by the ocean in HadCM2 and HadCM3. Internal Hadley Centre Report.

Gregory, J.M. (2000) Vertical heat transports in the ocean and their effect on time- dependent climate change. Climate Dynamics, 16, 501-515.

Gordon, C., C. Cooper, C. A. Senior, H. Banks, J. M. Gregory, T. C. Johns, J. F. B. Mitchell, R. A. Wood (2000): The simulation of SST, sea ice extents and ocean heat transport in a version of the Hadley Centre coupled model without flux adjustments. Climate Dynamics, 16, 147-168.

Levitus, S. and T. Boyer, World Ocean Atlas 1994. NOAA Atlas NESDIS, U.S. Department of Commerce, Washington, D.C., 1994.

Murphy, J.M., D.M.H. Sexton, D.N. Barnett, G.S. Jones, M.J. Webb, M. Collins and D.A. Stainforth (2004) Quantification of modelling uncertainties in a large ensemble of climate change simulations. Nature, 430, 768-772.

Piani, C., D.J. Frame, D.A. Stainforth, M.R. Allen (2005) Constraints on climate change from a multi-thousand member ensemble of simulations. Geophys. Res. Lett., 32, L23825, doi:10.1029/2005GL024452.

Rahmstorf, S. (1993) A fast and complete convection scheme for ocean models. Ocean Modelling, 101, 9-11.

Raper, S.C.B., Gregory, J.M. and Stouffer, R.J. (2002) The role of climate sensitivity and ocean heat uptake on AOGCM transient temperature response. J. Climate, 15, 124-130.

Roussenov , V.M., E. Stanev, V. Artale, and N. Pinardi (1995) A seasonal model of the Mediterranean Sea general circulation. Journal Geophysical Research , 100 , 13515-13538.

Russell, J.L., R.J. Stouffer and K.W. Dixon (2006) Intercomparison of the Southern Ocean circulations in IPCC coupled model control simulations. J. Climate, in press.

Russell, J.L., K.W. Dixon, A. Gnanadesikan, R.J. Stouffer and J.R. Toggweiler (2006) The Southern Hemisphere Westerlies in a warming world: Propping open the door to the deep ocean. J. Climate, in press.

Senior, C.A. and J.F.B. Mitchell (2000) The time-dependence of climate sensitivity. Geophys Res Letts 27:2685-2688.

Sokolov, A.P., C.E. Forest and P.H. Stone (2003) Comparing oceanic heat uptake in AOGCM transient climate change experiments. J. Climate, 16, 1573-1581.

Stainforth, D. A., T. Aina, C. Christensen, M. Collins, N. Faull, D. J. Frame, J. A. Kettleborough, S. Knight, A. Martin, J. M. Murphy, C. Piani, D. Sexton, L. A. Smith, R. A. Spicer, A. J. Thorpe, M. R. Allen (2005) Uncertainty in predictions of the climate response to rising levels of greenhouse gases. Nature, 433, 403-406.

Webb, M. J. , C. A. Senior, K. D. Williams, M. D. H. Sexton, M. A. Ringer, B. J. McAvaney, R. Colman, B. J. Soden, N. G. Andronova, S. Emori, Y. Tsushima, T. Ogura, I. Musat, S. Bony, and K. Taylor (2006) On uncertainty in feedback mechanisms controlling climate sensitivity in two GCM ensembles. Climate Dynamics, 27, 17-38.

## Tables

## Figures

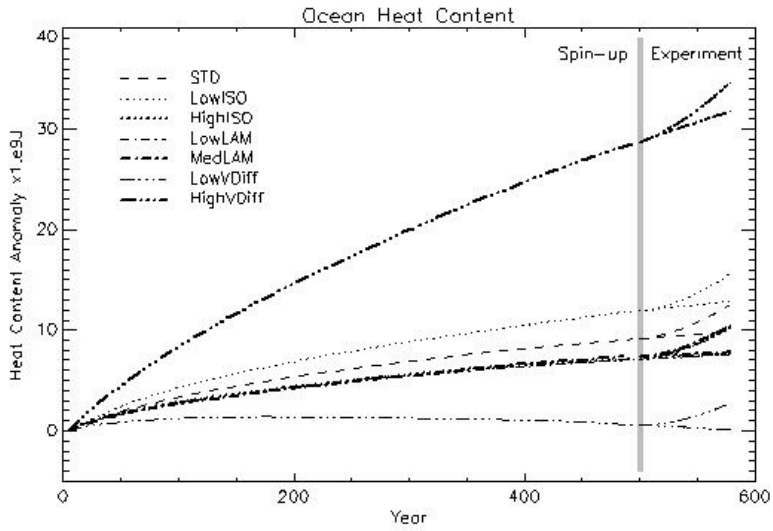


Figure 1: Anomalies in ocean heat content (computed with respect to the Levitus (1994) analysis of ocean temperatures) from the ensemble of ocean-physics ensemble experiments. For each member, 500 years of spin-up was performed with fixed pre- industrial greenhouse gases and other forcing agents. Each spin-up was then extended for 80 years to produce a control experiment and an additional experiment with CO2 increases at a rate of 1% per year compounded was performed. Parameter perturbations are indicated in the figure legend and correspond to those given in table1. For the HighISO, LowLAM and MedLAM experiments, the evolution of the heat content in the spin-up phase is very similar.

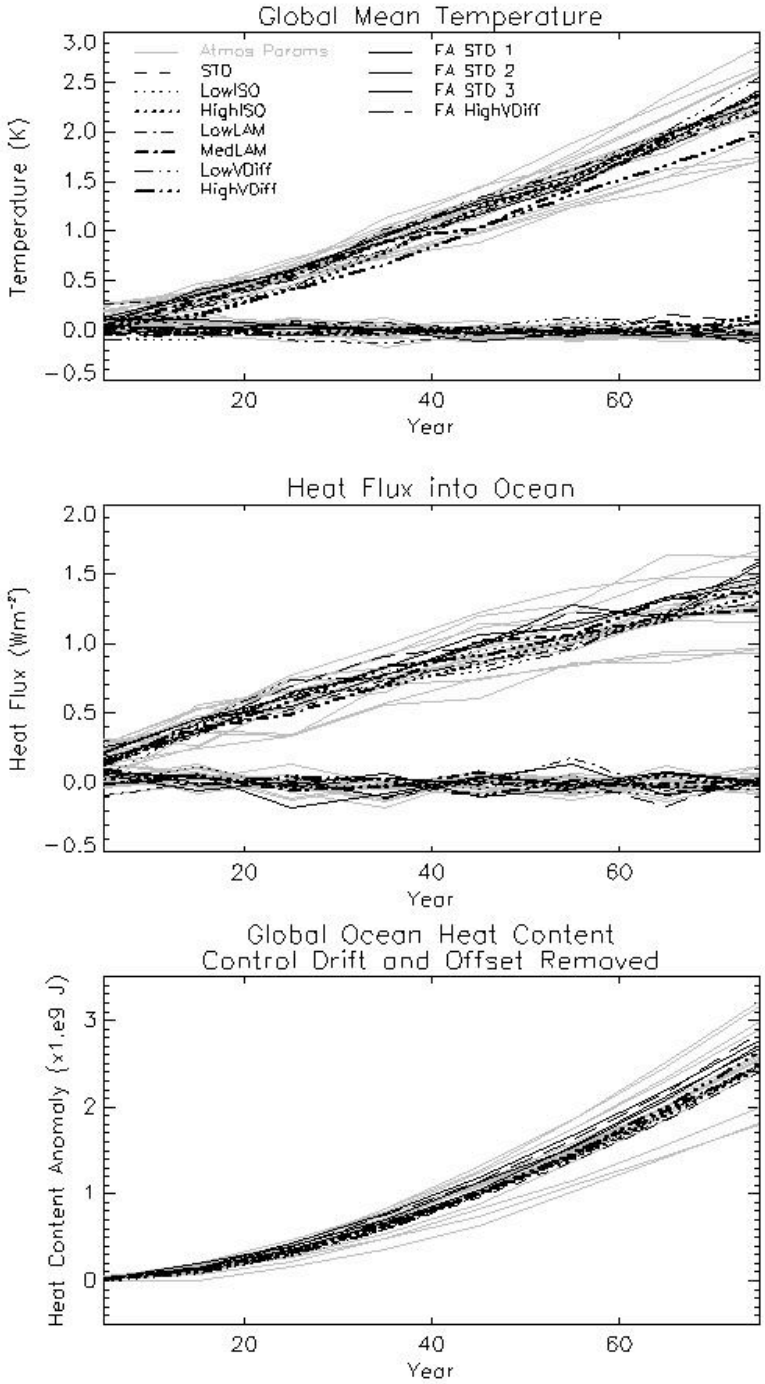


Figure 2: Time series of global-mean quantities taken from the control and 1% experiments. Grey lines are from the atmosphere-physics ensemble and black lines are from standard-model and ocean-physics ensembles with the parameter perturbation indicated in the legend (see table 1). Upper panel: 1.5 m temperature from control and 1% experiments. Middle panel: heat flux per unit area of the earth's surface from the atmosphere into the ocean from control and 1% experiments. Lower panel: ocean heat content from the 1% experiments expressed in terms of anomalies with respect to the corresponding control experiment (thus removing the small impact of control-climate drift).

| | Isopycnal Diffusivity | Background Vertical Diffusivity Profile | Mixed Layer Parameters | | TCR $\sigma$=0.04 | $\Lambda$ $\sigma$=0.02 | $\kappa$ $\sigma$=0.02 | MOC $\sigma$=0.3 |
|---|---|---|---|---|---|---|---|---|
| | | | ratio | depth | | | | |
| | $m^{-2}s^{-1}$ | x$10^{-5}$ $m^{-2}s^{-1}$ | | m | K | $Wm^{-2}K^{-1}$ | $Wm^{-2}K^{-1}$ | Sv |
| STD | 1000 | 1-15 | 0.7 | 100 | 2.07 | 1.17 | 0.63 | 3.7 |
| FA STD1 | | | | | 2.17 | 1.08 | 0.63 | 2.3 |
| FA STD2 | | | | | 2.16 | 1.07 | 0.65 | 1.4 |
| FA STD3 | | | | | 2.13 | 1.10 | 0.64 | 2.0 |
| LowISO | 200 | 1-15 | 0.7 | 100 | 2.17 | 1.14 | 0.57 | 3.0 |
| HighISO | 2000 | 1-15 | 0.7 | 100 | 2.07 | 1.19 | 0.61 | 1.7 |
| MedLAM | 1000 | 1-15 | 0.5 | 50 | 2.11 | 1.14 | 0.62 | 3.7 |
| LowLAM | 1000 | 1-15 | 0.3 | 100 | 2.16 | 1.16 | 0.57 | 4.3 |
| LowVDIFF | 1000 | 0.5-4 | 0.7 | 100 | 2.28 | 1.07 | 0.55 | 2.0 |
| HighVDIFF | 1000 | 2-50 | 0.7 | 100 | 1.82 | 1.31 | 0.74 | 4.2 |
| FA HighVDIFF | | | | | 2.03 | 1.14 | 0.69 | 2.3 |
| Atmosphere Physics | | | | | 1.56-2.61 | 0.85-1.75 | 0.57-0.76 | 0.8-3.1 |

*Table 1: Ocean-model parameter values used in the perturbed physics ensemble experiments and key quantities which determine the rate of global mean warming. The first column indicates the experiment name (FA indicating that flux adjustments are applied). The along-isopycnal diffusion coefficient takes a constant value everywhere in HadCM3 and is indicated in the second column. The background vertical diffusivity (third column) has a vertical profile with the first number in the column indicating the surface value and the second the value at the bottom of the ocean (see table A of Gordon et al., 2000). The HadCM3 mixed-layer scheme is a Kraus-Turner type controlled by the "ratio" parameter (fourth column) which scales the calculation of the wind mixing energy and the depth parameter (fifth column) which controls decay-length for its penetration. These parameters are known to control processes responsible for vertical heat transport in ocean models. The sixth column gives the Transient Climate Response (TCR), the 20-year averaged global mean temperature change at the time of CO2 doubling in the 1%/year CO2 increase experiment. The seventh column gives the effective atmospheric feedback parameter and the eighth column the ocean heat uptake parameter (see equation 1 and text for information on how these are calculated). The ninth column shows the reduction in the strength of the maximum overturning streamfunction in the North Atlantic in Sverdrups. For the last four columns, the standard deviation in the calculation expected from natural variability (computed from all the control experiments) is shown. The values in some columns are shown to 2 decimal places to highlight small difference.*

| | All variations in $\Lambda$ in and $\kappa$ | Assuming standard model $\Lambda$ | Assuming standard model$\kappa$ |
|---|---|---|---|
| Atmosphere | 1.63 - 2.69 | 2.04 - 2.27 | 1.59 - 2.55 |
| Ocean | 1.86 - 2.34 | 2.06 - 2.29 | 1.95 - 2.22 |
| Ocean (excluding HighVDIFF expts) | 2.11 - 2.33 | 2.20 - 2.29 | 2.07 - 2.22 |

*Table 2: Ranges of "hypothetical" TCR in degrees calculated using equation 1, the values of $\Lambda$ and $\kappa$ given in table 1 and a fixed radiative forcing of 3.8 $Wm^{-2}$. Ranges are computed from the atmosphere-physics ensembles (row 1), the ocean-physics ensemble (row 2) and the ocean-physics ensemble excluding the experiments with high vertical diffusivity. Column 2 shows the range calculated using the values of $\Lambda$ in and $\kappa$ computed from the ensemble experiments, column 3 the range calculated by substituting the standard model $\Lambda$ in the calculation, and column 4 by substituting the standard-model $\kappa$. Values are shown to 2 decimal places to highlight small differences.*

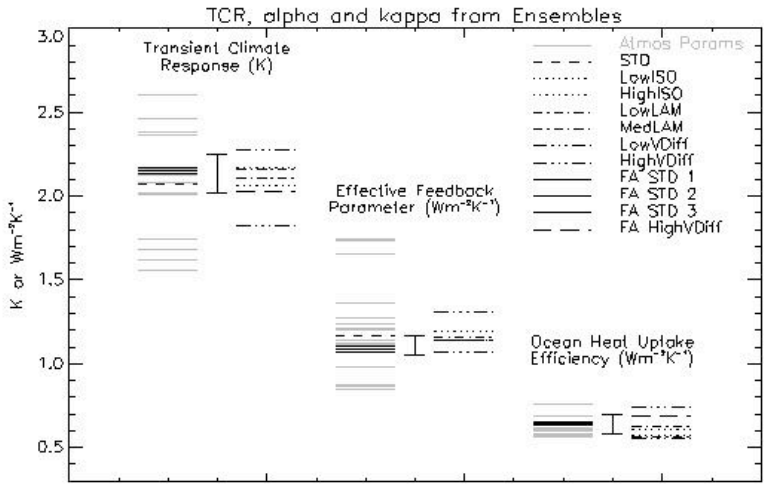


Figure 3: Graphical representation of the range of the terms in equation 1 in the atmosphere- and ocean-physics ensembles (as indicated on the legend). Left hand side: the transient climate response. Middle: the effective feedback parameter, $\Lambda$. Right hand side: the ocean heat uptake efficiency, $\kappa$. In each case the "error bar" indicates the mean and +/- 2 standard deviations of the uncertainty in the estimate of the quantity that would be expected from natural variability. Uncertainty estimates are calculated from non-overlapping 20-year sections of all of the control experiments and are centred on the standard model estimates of the respective quantity.

# APPENDIX B

## Abbreviations and symbols

| | |
|---|---|
| $\alpha_{VIS}$ | The Visbeck coefficient |
| $\beta_{HANEY}$ | Haney coefficient |
| $\delta$ | Exponential decay depth |
| $\Delta T^{eq}_{2\times CO_2}$ | Climate sensitivity |
| $\kappa$ | Ocean heat uptake efficiency |
| $\lambda$ | Wind mixing fraction |
| $\Lambda$ | Climate feedback parameter |
| $\nu_H$ | Horizontal viscosity |
| $\nu_{V,0}$ | Initial vertical viscosity |
| $\nu_{V,bg}$ | Background vertical viscosity |
| $\rho$ | Density |
| $\rho_\theta$ | Potential density (with the surface as a reference pressure) |
| $\sigma_{80}$ | Standard deviation of natural variability on 80 years |
| $\theta$ | Potential temperature (with the surface as a reference pressure) |
| ACC | Antarctic Circumpolar Current |
| AR4 | Assessment Report 4. Currently being written by the IPCC |
| AOGCM | Atmosphere-Ocean General Circulation Model |
| CMIP | Coupled Model Intercomparison Project |
| CMIP2 | The second phase of the Coupled Model Intercomparison Project: the time-dependent climate response to an increase in $CO_2$ |

| | |
|---|---|
| $D_{max}$ | Maximum depth of the boundary layer |
| HadAM3 | Hadley Centre Atmospheric model version 3 |
| HadCM3 | Hadley Centre coupled model version 3 |
| HadCM3L | Lower ocean resolution version of the Hadley Centre coupled model version 3 |
| HadSM3 | Hadley Centre Atmosphere model version 3 coupled to a Mixed Layer Ocean |
| IPCC | Intergovernmental Panel on Climate Change |
| ITCZ | Inter-tropical convergence zone |
| $K_I$ | Isopycnal diffusivity |
| $K_{THK}$ | Thickness diffusivity |
| $K_{THK,bg}$ | Background thickness diffusivity |
| $K_{V,bg}$ | Background vertical diffusivity |
| $N$ | Net radiative imblance at the tropopause |
| PDF | Probability Distribution Function |
| QUMP | The Quantifying Uncertainty in Model Predictions project |
| $Q_{2\times CO_2}$ | Radiative forcing effect of doubling $CO_2$ |
| rms | Root mean squared (error) |
| $RI_{crit}$ | Critical Richardson number |
| SRES | Special Report into Emissions Scenarios (Nakićenović *et al.*, 2000) |
| SST | Sea Surface Temperature |
| TAR | The IPCC's Third Assessment Report |
| TCR | Transient Climate Response (the change in global mean surface air temperature for the 20 years centred on the year of doubling of $CO_2$) |
| THC | Thermohaline Circulation |
| TOA | Top of the Atmosphere |

# APPENDIX C

# Bibliography

# Bibliography

Acreman, D. (2005). The impact of improved vertical resolution and model tuning on mixed layer models. Technical Report 2, National Centre for Ocean Forecasting, Met Office, FitzRoy Road, Exeter, Devon, EX1 3PB, UK.

Allan, R. J. and Ansell, T. J. (2006). A new globally complete monthly historical mean sea level pressure data set (HadSLP2): 1850-2004. *Journal of Climate*, **19**(22), 5816–5842.

Allen, M. (1999). Do-it-yourself climate prediction. *Nature*, **401**, 64.

Allen, M. (2003). Possible or probable? *Nature*, **425**, 242.

Allen, M. R. and Stainforth, D. A. (2002). Towards objective probablistic climate forecasting. *Nature*, **419**, 228.

Arrhenius, S. (1896). On the influence of carbonic acid in the air upon the temperature of the ground. *Philosophical Magazine*, **41**, 237–276. Available from http://web.lemoyne.edu/ğiunta/Arrhenius.html.

Baede, A. P. M., Ahlonsou, E., Ding, Y., Schimel, D., Bolin, B., and Pollinais, S. (2001). *Climate Change 2001: The Scientific Basis. Contribution of Working Group I to the Third Assessment Report of the Intergovernmental Panel on Climate Change*, chapter 1: The Climate System: an Overview, pages 84–98. Cambridge University Press. (ed. J. T. Houghton, Y. Ding, D. J. Griggs, M. Noguer, P. J. van der Linden, X. Dai, K. Maskell and C. A. Johnson).

Barkstrom, B. J. (1984). The Earth Radiation Budget Experiment (ERBE). *Bulletin of the American Meteorological Society*, **65**(11), 1170–1185.

Barlow, R. J. (1989). *Statistics: a guide to the use of statiscal methods in the physical sciences*. The Manchester Physics Series. Wiley.

Barnett, T. P., Pierce, D. W., AchutaRoa, K. M., Glecker, P. J., Santer, B. D., Gregory, J. M., and Washington, W. M. (2005). Penetration of human-induced warming into the world's ocean. *Science*, **309**, 284–287.

Barsugli, J. J., Shin, S., and Sardeshmukh, P. D. (2006). Sensitivity of global warming to the pattern of tropical ocean warming. *Climate Dynamics*. doi: 10.1007/s00382-006-0143-7.

Bell, J., Duffy, P., Covey, C., Sloan, L., and the CMIP investigators (2000). Comparison of temperature variability in observations and sixteen climate model simulations. *Geophysical Research Letters*, **27**(2), 261–264.

Bell, M. J. (1994). Notes on how to choose parameter values for the Cox numerical ocean circulation model. Forecasting Technical Research Note 135, United Kingdom Meteorological Office, FitzRoy Road, Exeter, Devon, EX1 3PB, UK.

Beltrami, H., Smerdon, J. E., Pollack, H. N., and Huang, S. (2002). Continental heat gain in the global climate system. *Geophysical Research Letters*, **29**(8), 1167.

Boer, G. J. and Yu, B. (2003). Climate sensitivity and response. *Climate Dynamics*, **20**, 415–429.

Bony, S., Colman, R., Kattsov, V. M., Allan, R. P., Bretherton, C. S., Dufresne, J., Hall, A., Hallegatte, S., Holland, M. M., Ingram, W., Randall, D. A., Soden, B. J., Tselioudis, G., and Webb, M. J. (2006). How well do we understand and evaluate climate change feedback processes. *Journal of Climate*, **19**, 3445–3482.

Booth, B. B. B., Gregory, J. M., and Allen, M. R. (2006). Simple analogues of ocean heat uptake. *Submitted to Journal of Climate*.

Broecker, W. S., Bond, G., Klas, M., Bonani, G., and Wolfi, W. (1990). A salt oscillator in the glacial North Atlantic? 1. The concept. *Paleoceanography*, **5**, 469–477.

Bryan, F. (1987). Parameter sensitivity of primitive equation ocean general circulation models. *Journal of Physical Oceanography*, **17**, 970–985.

Bryan, K. (1984). Accelerating the convergence to equilibrium of ocean-climate models. *Journal of Physical Oceanography*, **14**, 666–673.

Bryan, K., Manabe, S., and Spelman, M. J. (1988). Interhemispheric assymetry in the tranisent response of a coupled ocean-atmosphere model to a $CO_2$ forcing. *Journal of Physical Oceanography*, **18**, 851–867.

Bryden, H. L., Longworth, H. R., and Cunningham, S. A. (2005). Slowing of the Atlantic meridional overturning circulation at 25$^o$N. *Nature*, **438**, 655–657.

Callendar, G. S. (1949). Can carbon dioxide influence climate? *Weather*, **4**, 310–314.

Carissimo, B. C., Oort, A. H., and Haar, T. H. V. (1985). Estimating the meridional energy transports in the atmosphere and ocean. *Journal of Physical Oceanography*, **15**, 82–91.

Church, J. A., Gregory, J. M., Huybrechts, P., Kuhn, M., Lambeck, K., Nhuan, M. T., Qin, D., and Woodworth, P. L. (2001). *Climate Change 2001: The Scientific Basis. Contribution of Working Group I to the Third Assessment Report of the Intergovernmental Panel on Climate Change*, chapter 11: Changes in Sea Level, pages 639–694. Cambridge University Press. (ed. J. T. Houghton, Y. Ding, D. J. Griggs, M. Noguer, P. J. van der Linden, X. Dai, K. Maskell and C. A. Johnson).

Colling, A. (2002). *Ocean Circulation*. Open University Oceanography Series. Butterworth-Heinemann, 2nd edition.

Collins, M. (2000). The El-Niño southern oscillation in the second Hadley Centre model and its response to greenhouse warming. *Journal of Climate*, **13**, 1299–1312.

Collins, M. and Allen, M. R. (2002). Assessing the relative roles of initial and boundary conditions in interannual to decadal climate predictability. *Journal of Climate*, **15**(21), 3104–3109.

Collins, M. and the CMIP Modelling Groups (2005). El Niño- or La Niña-like climate change? *Climate Dynamics*, **24**, 84–104.

Collins, M., Tett, S. F. B., and Cooper, C. (2001). The internal climate variability of HadCM3, a version of the Hadley Centre coupled model without flux adjustments. *Climate Dynamics*, **17**, 61–81.

Collins, M., Booth, B., Harris, G., Murphy, J., Sexton, D., and Webb, M. (2006). Towards quantifying uncertainty in transient climate change. *Climate Dynamics*. doi:10.1007/s00382-006-0121-0.

Collins, M., Brierley, C. M., MacVean, M., Booth, B. B. B., and Harris, G. R. (2007). The sensitivity of the rate of transient climate change to ocean physics perturbations. *Accepted by Journal of Climate*. included as appendix A.

Colman, R. (2003). A comparison of climate feedback in general circulation models. *Climate Dynamics*, **20**, 865–873.

Cox, P. M., Betts, R. A., Bunton, C. B., Essery, R. L. H., Rowntree, P. R., and Smith, J. (1999). The impact of the new land surface physics on the GCM simulation of climate and climate sensitivity. *Climate Dynamics*, **15**, 183–203.

Cox, P. M., Betts, R. A., Jones, C. D., Spall, S. A., and Totterdell, I. J. (2000). Acceleration of global warming due to carbon-cycle feedbacks in a coupled climate model. *Nature*, **408**, 184–187.

Cubasch, U., Hasselmann, K., Höck, H., Maier-Reimer, E., Mikolajewicz, U., Santer, B. D., and Sausen, R. (1992). Time-dependent greenhouse warming computations with a coupled ocean-atmosphere model. *Climate Dynamics*, **8**(2), 55–69.

Cubasch, U., Meehl, G. A., Boer, G. J., Stouffer, R. J., Dix, M., Noda, A., Senior, C. A., Raper, S., and Yap, K. S. (2001). *Climate Change 2001: The Scientific Basis. Contribution of Working Group*

*I to the Third Assessment Report of the Intergovernmental Panel on Climate Change*, chapter 9: Projections of Future Climate Change, pages 525–582. Cambridge University Press. (ed. J. T. Houghton, Y. Ding, D. J. Griggs, M. Noguer, P. J. van der Linden, X. Dai, K. Maskell and C. A. Johnson).

Cunningham, S. A., Alderson, S. G., King, B. A., and Brandon, M. A. (2003). Transport and variability of the Antarctic circumpolar current in the Drake Passage. *Journal of Geophysical Research*, **108**(C5), 8084.

Curry, J. A., Schramm, J. L., and Ebert, E. E. (1995). Sea ice-albedo climate feedback mechanism. *Journal of Climate*, **8**, 240–247.

Davis, R. E., deSzoeke, R., and Niiler, P. (1981). Variability in the upper ocean during MILE. part II: Modeling the mixed layer response. *Deep Sea Research*, **28A**(12), 1453–1475.

de Boyer Montégut, C., Madec, G., Fischer, A. S., Lazar, A., and Iudicone, D. (2004). Mixed layer depth over the global ocean: An examination of profile data and a profile based climatology. *Journal of Geophysical Research*, **109**(C12). doi:10.1029/2004JC002378.

de la Mare, W. K. (1997). Abrupt mid-twentieth-century decline in Antarctic sea-ice extent from whaling records. *Nature*, **389**, 57–60.

Dong, B. and Sutton, R. T. (2005). Mechanism of interdecadal thermohaline circulation variability in a coupled ocean-atmosphere GCM. *Journal of Climate*, **18**, 1117–1135.

Draper, N. R. and Smith, H. (1998). *Applied Regression Analysis*. John Wiley and Sons, $3^{rd}$ edition.

Edwards, J. M. and Slingo, A. (1996). Studies with a flexible new radiation code I: choosing a configuration for a large-scale model. *Quarterly Journal of the Royal Meteorological Society*, **122**, 689–719.

Edwards, N. R. and Marsh, R. (2005). Uncertainties due to transport-parameter sensitivity in an efficient 3-D ocean-climate model. *Climate Dynamics*, **24**, 415–433.

Emery, W. J. (2001). *Encyclopedia of Ocean Sciences*, volume 6 (T-Z, Index), chapter : Water Types and Water Masses, pages 3179–3187. Academic Press. (ed. J. H. Steele, K. K. Turekian and S. A. Thorpe).

Esper, J., Cook, R., and Schweingruber, F. H. (2002). Low-frequency signals in long tree-ring chronologies for reconstructing past temperature variability. *Science*, **295**, 2250–2253.

Flato, G. M. and Participating CMIP Modelling Groups (2004). Sea-ice and its response to $CO_2$ forcing as simulated by global climate models. *Climate Dynamics*, **23**, 229–241.

Folland, C., Karl, T., Christy, J., Clarke, R., Gruza, G., Jouzel, J., Mann, M., Oerlemans, J., Salinger, M., and Wang, S.-W. (2001a). *Climate Change 2001: The Scientific Basis. Contribution of Working Group I to the Third Assessment Report of the Intergovernmental Panel on Climate Change*, chapter 2: Observed Climate Variability and Change, pages 99–181. Cambridge University Press. (ed. J. T. Houghton, Y. Ding, D. J. Griggs, M. Noguer, P. J. van der Linden, X. Dai, K. Maskell and C. A. Johnson).

Folland, C. K., Rayner, N. A., Brown, S. J., Smith, T. M., Shen, S. S. P., Parker, D. E., Macadam, I., Jones, P. D., Jones, R. M., Nicholls, N., and Sexton, D. M. H. (2001b). Global temperature change and its uncertainties since 1861. *Geophysical Research Letters*, **28**(13), 2621–2624.

Forest, C. E., Stone, P. H., Sokolov, A. P., Allen, M. R., and Webster, M. D. (2002). Quantifying uncertainties in climate system properties with the use of recent climate observations. *Science*, **295**, 113–117.

Forest, C. E., Stone, P. H., and Sokolov, A. P. (2006). Estimated PDFs of climate system properties including natural and anthropogenic forcings. *Geophysical Research Letters*, **33**(L01705). doi:10.1029/2005GL023977.

Frame, D. J., Booth, B. B. B., Kettleborough, J. A., Stainforth, D. A., Gregory, J. M., Collins, M.,

and Allen, M. R. (2005). Constraing climate forecasts: The role of prior assumptions. *Geophysical Research Letters*, **32**. doi:10.1029/2004GL022241.

Gent, P. R. and McWilliams, J. C. (1990). Isopycnal mixing in ocean circulation models. *Journal of Physical Oceanography*, **20**, 150–155.

Gibson, J. K., Kaallberg, P., Uppala, S., Hernandez, A., Nomura, A., and Serrano, E. (1999). ERA-15 description. ECMWF Re-analysis project report series 1, European Centre for Medium-range Weather Forecasting.

Gill, A. E. (1982). *Atmosphere-Ocean Dynamics*, volume 30 of *International Geophysics Series*. Academic Press.

Giogri, F. and Francisco, R. (2000). Evaluating uncertainties in the prediction of regional climate change. *Geophysical Research Letters*, **27**, 1295–1298.

Giorgi, F., Hewitson, B., Christensen, J., Hulme, M., von Storch, H., Whetton, P., Jones, R., Mearns, L. O., and Fu, C. (2001). *10: Climate Change 2001: The Scientific Basis. Contribution of Working Group I to the Third Assessment Report of the Intergovernmental Panel on Climate Change*, chapter Regional Climate Information - Evaluation and Projections, pages 583–638. Cambridge University Press. (ed. J. T. Houghton, Y. Ding, D. J. Griggs, M. Noguer, P. J. van der Linden, X. Dai, K. Maskell and C. A. Johnson).

Gnanadesikan, A. (1999). A simple predictive model for the structure of the oceanic pycnocline. *Science*, **283**, 2077–2079.

Gordon, C., Cooper, C., Senior, C. A., Banks, H., Gregory, J. M., Johns, T. C., Mitchell, J. F. B., and Wood, R. A. (2000). The simulation of sst, sea ice extents and ocean heat transports in a version of the Hadley Centre coupled model without flux adjustments. *Climate Dynamics*, **16**, 147–168.

Gregory, J. M. (2000). Vertical Heat Transports in the Ocean and their Effect on Time-Dependent Climate Change. *Climate Dynamics*, **16**, 501–515.

Gregory, J. M. and Mitchell, J. F. B. (1997). The climate response to $co_2$ of the Hadley Centre coupled AOGCM with and without flux adjustment. *Geophysical Research Letters*, **24**(15), 1943–1946.

Gregory, J. M., Ingram, W. J., Palmer, M. A., Jones, G. S., Stott, P. A., Thorpe, R. B., Lowe, J. A., Johns, T. C., and Williams, K. D. (2004a). A new method for diagnosing radiative forcing and climate sensitivity. *Geophysical Research Letters*, **31**. doi:10.1029/2003GL018747.

Gregory, J. M., Banks, H. T., Stott, P. A., Lowe, J. A., and Palmer, M. D. (2004b). Simulated and observed decadal variability in ocean heat content. *Geophysical Research Letters*, **31**. doi:10.1029/2004GL020258.

Gregory, J. M., Dixon, K. W., Stouffer, R. J., Weaver, A. J., Driesschaert, E., Eby, M., Fichefet, T., Hasumi, H., Hu, A., Jungclaus, J. H., Kamenkovich, I. V., Levermann, A., Montoya, M., Murakami, S., Nawrath, S., Oka, A., Sokolov, A. P., and Thorpe, R. B. (2005a). A model intercomparison of changes in the Atlantic thermohaline circulation in response to increasing atmospheric $CO_2$ concentration. *Geophysical Research Letters*, **32**(12). doi:10.1029/2005GL023209.

Gregory, J. M., Dixon, K. W., Stouffer, R. J., Weaver, A. J., Driesschaert, E., Eby, M., Fichefet, T., Hasumi, H., Hu, A., Junclaus, J. H., Kamenkovich, I. V., Levermann, A., Montoya, M., Murakami, S., Nawrath, S., Oka, A., Sokolov, A. P., and Thorpe, R. B. (2005b). A model intercomparison of changes in the atlantic thermohaline circulation in response to increasing atmospheric $co_2$ concentration. *Geophysical Research Letters*, **32**. doi: 10.1029/2005GL023209.

Griffies, S. M. (2004). *Fundamentals of Ocean Climate Models*. Princeton University Press.

Griffies, S. M. and Bryan, K. (1997). A predictability study of simulated North Atlantic multidecadal variability. *Climate Dynamics*, **13**, 459–487.

Griffies, S. M., Gnanadesikan, A., Pacanowski, R. C., Larichev, V. D., Dukowicz, J. K., and Smith, R. D. (1998). Isoneutral diffusion in a z-coordinate ocean model. *Journal of Physical Oceanography*, **28**(5), 805–830.

Griffies, S. M., Harrison, M. J., Pacanowski, R. C., and Rosati, A. (2004). A technical guide to MOM4. GFDL Ocean Group Technical Report 5, NOAA/Geophysical Fluid Dynamics Laboratory.

Guilyardi, E., Madec, G., and Terray, L. (2001). The role of lateral ocean physics in the upper ocean thermal balance of a coupled ocean-atmosphere GCM. *Climate Dynamics*, **17**, 589–599.

Guilyardi, E., Gualdi, S., Slingo, J., Navarra, A., Delecluse, P., Cole, J., Madec, G., Roberts, M., Latif, M., and Terray, L. (2004). Representing El Niño in coupled ocean-atmosphere GCMs: The dominant role of the atmospheric component. *Journal of Climate*, **17**, 4623–4629.

Hansen, J., Johnson, D., Lacis, A., Lebedeff, S., Lee, P., Riley, D., and Russell, G. (1981a). Climate impact of increasing atmospheric carbon dioxide. *Science*, **213**(4511), 957–966.

Hansen, J., Russell, G., Lacis, A., Fung, I., Rind, D., and Stone, P. (1981b). Climate response times: Dependence on climate sensitivity and ocean mixing. *Science*, **229**, 857–859.

Hansen, J., Ruedy, R., Glascoe, J., and Sato, M. (1999). GISS analysis of surface temperature changes. *Journal of Geophysical Research*, **104**, 30997–31022. Data available from http://data.giss.nasa.gov/gistemp/.

Hargreaves, J. C. and Annan, J. D. (2006). Using ensemble prediction methods to examine regional cliamte variation under global warming scenarios. *Ocean Modelling*, **11**, 174–192.

Harris, G. R., Sexton, D. M. H., Booth, B. B. B., Collins, M., Murphy, J. M., and Webb, M. J. (2006). Frequency distributions of transient regional cliamte change from perturbed physics ensembles of general circulation model simulations. *Climate Dynamics*, **27**, 357–375.

Holland, M. M. and Bitz, C. M. (2003). Polar amplification of climate change in coupled models. *Climate Dynamics*, **21**, 221–232.

Holland, M. M., Bitz, C. M., and Tremblay, B. (2006). Future abrupt reductions in the Summer Arctic sea ice. *Geophysical Research Letters*, **33**(23). doi:10.1029/2006GL028024.

Houghton, J. (2002). *The Physics of Atmospheres*. Cambridge University Press.

Huang, B., Stone, P. H., and Sokolov, A. P. (2003). Ocean heat uptake in transient cliamte change: Mechanisms and uncertainty due to subgrid-scale eddy mixing. *Journal of Climate*, **16**, 3344–3356.

Hulme, M., Jenkins, G. J., Lu, X., Turnpenny, J. R., Mitchell, T. D., Jones, R. G., Lowe, J., Murphy, J. M., Hassell, D., Boorman, P., McDonald, R., and Hill, S. (2002). *Climate Change Scenarios for the United Kingdom: The UKCIP02 Scientific Report*. Tyndall Centre for Climate Change Research, School of Environmental Sciences, University of East Anglia, Norwich, UK.

Jerlov, N. G. (1968). *Optical Oceanography*. Elsevier.

Johns, T. C., Carnell, R. E., Crossley, J. F., Gregory, J. M., Mitchell, J. F. B., Senior, C. A., Tett, S. F. B., and Wood, R. A. (1997). The second Hadley Centre coupled ocean-atmosphere GCM: model description, spinup and validation. *Climate Dynamics*, **13**, 103–134.

Johns, T. C., Gregory, J. M., Ingram, W. J., Johnson, C. E., Jones, A., Lowe, J. A., Mitchell, J. F. B., Roberts, D. L., Sexton, D. M. H., Stevenson, D. S., Tett, S. F. B., and Woodage, M. J. (2003). Anthropogenic climate change for 1860 to 2100 simulated with the HadCM3 model under updated emissions scenarios. *Climate Dynamics*, **20**, 583–612.

Jones, A., Roberts, D. L., Woodage, M. J., and Johnson, C. E. (2001). Indirect sulphate aerosol forcing in a climate model with an interactive sulphur cycle. *Journal of Geophysical Research*, **106**(D17), 20293–20310.

Jones, C. (2003). A fast ocean GCM without flux adjustments. *Journal of Atmospheric and Oceanic Technology*, **20**(12), 1857–1868.

Jones, C. D. and Palmer, J. R. (1998). Spinup Methods for HADCM3L. Climate Research Technical Note 84, Hadley Centre for Climate Prediction and Reseach, Met Office, FitzRoy Road, Exeter, Devon, EX1 3PB, UK.

Jones, P. D., New, M., Parker, D. E., Martin, S., and Rigor, I. G. (1999). Surface air temperature and its variations over the last 150 years. *Reviews of Geophysics*, **37**, 173–199.

Keeley, S. P. E. (2006). *Climate Variability: Effects of Doubling Carbon Dioxide and Uncertainty in Model Predictions*. Ph.D. thesis, Department of Meteorology, University of Reading.

Keen, A. B. and Murphy, J. M. (1997). Influence of natural variability and the cold start problem on the simulated transient response to increasing $CO_2$. *Climate Dynamics*, **13**, 847–864.

Kellogg, W. W. (1975). *Climate of the Arctic: 24th Alaska Science Conference 1973*, chapter : Climatic feedback mechanism involving polar regions. University of Alaska geophysical institute. Weller G. and Bowling S. A. (ed.).

Killworth, P. D. (1987). Topographic instabilities in level model OGCMs. *Ocean Modelling*, **75**, 9–12.

Kraus, E. B. (1990). *Climate-ocean interaction*, chapter : Diapycnal mixing, pages 269–293. Kluwer, Amsterdam, Netherlands. Schlesinger M.E. (ed).

Kraus, E. B. and Turner, J. S. (1967). A one-dimensional model of the seasonal thermocline II. the general theory and its consequences. *Tellus*, **19**(1), 98–105.

Large, W. G., McWilliams, J. C., and Doney, S. C. (1994). Oceanic vertical mixing: A review and a model with a nonlocal boundary layer. *Reviews of Geophysics*, **32**(4), 363–403.

Latif, M., Roeckner, E., Mikolajewicz, U., and Voss, R. (2000). Tropical stabilization of the thermohaline circulation in a greenhouse warming simulation. *Journal of Climate*, **13**, 1809–1813.

Ledwell, J. R., Watson, A. J., and Law, C. S. (1993). Evidence for slow mixing across the pycnocline from an open-ocean tracer-release experiment. *Nature*, **364**, 701–703.

Legates, D. R. and Willmott, C. J. (1990). Mean seasonal and spatial variability in global surface air-temperature. *Theoretical & Applied Climatology*, **41**, 11–21.

Levitus, S. and Boyer, T. (1994). *World Ocean Atlas 1994*. NOAA Atlas NESDIS. U.S. Department of Commerce, Washington, D.C.

Levitus, S., Antonov, J. I., Wang, J., Delworth, T. L., Dixon, K. W., and Broccoli, A. J. (2001). Anthropogenic warming of Earth's climate system. *Science*, **292**, 267–270.

Levitus, S., Antonov, J. I., and Boyer, T. (2005). Warming of the world ocean, 1955-2003. *Geophysical Research Letters*, **32**(L02604). doi:10.1029/2004GL021592.

Lorenz, E. N. (1967). *The Nature and Theory of the General Circulation of the Atmsopere*. Number 218. World Meteorological Organization, Geneva, Switzerland.

Manabe, S. and Wetherald, R. T. (1967). Thermal equilibrium of the atmosphere with a given distribution of relative humidity. *Journal of the Atmospheric Sciences*, **24**(3), 241–259.

Manabe, S. and Wetherald, R. T. (1975). The effects of doubling the $CO_2$ concentration on the climate of a general circulation model. *Journal of the Atmospheric Sciences*, **32**(1), 3–15.

Manabe, S. and Wetherald, R. T. (1980). On the distribution of climate change resulting from an increase in $CO_2$ content of the atmosphere. *Journal of the Atmospheric Sciences*, **37**(1), 99–118.

Mann, M. E. and Jones, P. D. (2003). Global surface temperatures over the past two millenia. *Geophysical Research Letters*, **30**(15). doi:10.1029/2003GL017814.

Marotzke, J. and Stone, P. (1995). Atmospheric transports, the thermohaline circulation, and flux adjustments in a simple coupled model. *Journal of Physical Oceanography*, **25**, 1350–1264.

McAvaney, B., Covey, C., Joussaume, S., Kattsov, V., Kitoh, A., Ogana, W., Pitman, A., Weaver, A., Wood, R., and Zhao, Z.-C. (2001). *Climate Change 2001: The Scientific Basis. Contribution of Working Group I to the Third Assessment Report of the Intergovernmental Panel on Climate Change*, chapter 8: Model Evaluation, pages 471–524. Cambridge University Press. (ed. J. T. Houghton, Y. Ding, D. J. Griggs, M. Noguer, P. J. van der Linden, X. Dai, K. Maskell and C. A. Johnson).

Mearns, L., Hulme, M., Carter, T., Leemans, R., Lal, M., and Whetton, P. (2001). *Climate Change 2001: The Scientific Basis. Contribution of Working Group I to the Third Assessment Report of the Intergovernmental Panel on Climate Change*, chapter 13: Climate Scenario Development, pages 739–768. Cambridge University Press. (ed. J. T. Houghton, Y. Ding, D. J. Griggs, M. Noguer, P. J. van der Linden, X. Dai, K. Maskell and C. A. Johnson).

Meehl, G. A., Washington, W. M., and Karl, T. R. (1993). Low-frequency variability and $CO_2$ transient climate change. *Climate Dynamics*, **8**, 117–133.

Meehl, G. A., Boer, G. J., Covey, C., Latif, M., and Stouffer, R. J. (1997). Intercomparison makes for a better climate model. *Eos: Transactions of the American Geophysical Union*, **78**, 445–446, 451.

Meehl, G. A., Boer, G. J., Covey, C., Latif, M., and Stouffer, R. J. (2000). The Coupled Model Intercomparison Project (CMIP). *Bulletin of the American Meteorological Society*, **81**, 313–318.

Molteni, F., Buizza, R., Palmer, T. N., and Petroliagas, T. (1996). The new ECMWF ensemble prediction system: methodology and validation. *Quarterly Journal of the Royal Meteorological Society*, **122**, 73–119.

Murphy, J. M., Barnett, D. N., Jones, G. S., Sexton, D. M. H., and Webb, M. J. (2003). Database of atmosphere model (HadAM3) parameters and their uncertainty ranges. Report to DEFRA 15d/1/02, Hadley Centre for Climate Prediction and Reseach, Met Office, FitzRoy Road, Exeter, Devon, EX1 3PB, UK.

Murphy, J. M., Sexton, D. M. H., Barnett, D. N., Jones, G. S., Webb, M. J., Collins, M., and Stainforth, D. A. (2004). Quantification of modelling uncertainties in a large ensemble of climate change simulations. *Nature*, **430**, 768–772.

Nakićenović, N., Alcamo, J., Davis, G., de Vries, B., Fenham, J., Gaffin, S., Gregory, K., Grübler, A., Jung, T. Y., Kram, T., Rovere, E. L. L., Michaelis, L., Mori, S., Morita, T., Pepper, W., r, H. P., Price, L., Raihi, K., Roehrl, A., Rogner, H.-H., Sankovski, A., Schlesinger, M., Shukla, P., Smith,

S., Swart, R., van Roojen, S., Victor, N., and Dadi, Z. (2000). *Emissions Scenarios, A Special Report of Working Group III of the Intergovernmental Panel on Climate Change*. Cambridge University Press. 599 pp.

Noda, A., Yukimoto, S., Maeda, S., Uchiyama, T., Shibata, K., and Yamaki, S. (2001). A new Meteorological Research Institute coupled GCM (MRI-CGCM2): Transient response to greenhouse gas and aerosol scenarios. CGER's supercomputer monograph report 7, National Institute for Environmental Studies, Tsukhuba, Japan.

Pacanowski, R. C. and Philander, S. G. H. (1981). Parameterization of vertical mixing in numerical models of tropical oceans. *Journal of Physical Oceanography*, **11**, 1443–1451.

Palmer, J. R. and Totterdell, I. J. (2001). Production and export in a global ocean ecosystem model. *Deep-Sea Research*, **48**(Part I-Oceanographic Research Papers), 1169–1198.

Palmer, T. N. (2000). Predicting uncertainty in forecasts of weather and climate. *Reports on Progress in Physics*, **63**, 71–116.

Palmer, T. N., Alessandri, A., Andersen, U., Cantelaube, P., Davey, M., Délécluse, P., Déqué, M., Díez, E., Doblas-Reyes, F., Feddersen, H., Graham, R., Gualdi, S., Gurmy, J.-F., orn, R. H., Hoshen, M., Keenlyside, N., Latif, M., Lazar, A., Maisonnave, E., Marletto, V., Morse, A. P., Orfila, B., Rogel, P., Terres, J.-M., and Thomson, M. C. (2004). Development of a European multi-model ensemble system for seasonal to inter-annual prediction (DEMETER). *Bulletin of the American Meteorological Society*, **85**, 853–872.

Parkinson, C. L., Cavalieri, D. J., Gloersen, P., Zwally, H. J., and Cosimo, J. (1999). Arctic sea ice extents, areas, and trends. *Journal of Geophysical Research*, **104**, 20837–20856.

Paulson, C. and Simpson, J. (1977). Irradiance measurements in the upper ocean. *Journal of Physical Oceanography*, **7**, 952–956.

Peixoto, J. P. and Oort, A. H. (1992). *Physics of Climate*. AIP Press.

Peters, H., Gregg, M. C., and Toole, J. M. (1988). On the parameterization of equatorial turbulence. *Journal of Geophysical Research*, **93**(C2), 1199–1218.

Plass, G. N. (1956). The carbon dioxide theory of climatic change. *Tellus*, **8**, 140–154.

Pope, V. D., Gallani, M. L., Rowntree, P. R., and Stratton, R. A. (2000). The impact of new physical parametrizations in the Hadley Centre climate model: HADAM3. *Climate Dynamics*, **16**, 123–146.

Rahmstorf, S. (1993). A fast and complete convection scheme for ocean models. *Ocean Modelling*, **101**, 9–11.

Rahmstorff, S. (2002). Ocean circulation and climate during the past 120,000 years. *Nature*, **419**, 207–214.

Ramaswamy, V., Boucher, O., Haigh, J., Hauglustaine, D., Haywood, J., Myhre, G., Nakajima, T., Shi, G., and Solomon, S. (2001). *Climate Change 2001: The Scientific Basis. Contribution of Working Group I to the Third Assessment Report of the Intergovernmental Panel on Climate Change*, chapter 6: Radiative Forcing of Climate Change, pages 349–416. Cambridge University Press. (ed. J. T. Houghton, Y. Ding, D. J. Griggs, M. Noguer, P. J. van der Linden, X. Dai, K. Maskell and C. A. Johnson).

Raper, S. C. B., Gregory, J. M., and Stouffer, R. J. (2002). The role of climate sensitivity and ocean heat uptake on AOGCM transient temperature response. *Journal of Climate*, **15**, 124–130.

Rayner, N. A., Parker, D. E., Horton, E. B., Folland, C. K., Alexander, L. V., Rowell, D. P., Kent, E. C., and Kaplan, A. (2003). Global analyses of sea surface temperature, sea ice, and night marine air temperature since the late nineteenth century. *Journal of Geophysical Research*, **108**(D14), 4407. doi:10.1029/2002JD002670.

Revelle, R. and Suess, H. E. (1957). Carbon dioxide exchange between atmosphere and ocean and the question of an increase of atmospheric $co_2$ during the past decades. *Tellus*, **9**, 18–27.

Rickard, G. (1999). Ocean models and the implementation of vertical diffusion and vertical mixing. Unified Model Documentation 59, United Kingdom Meteorological Office, Met Office, FitzRoy Road, Exeter, Devon, EX1 3PB, UK.

Rothrock, D. A., Yu, Y., and Maykutt, G. A. (1999). Thinning of the Arctic sea-ice cover. *Geophysical Research Letters*, **26**, 2469–3472.

Roussenov, V. M., Stanev, E., Artale, V., and Pinardi, N. (1995). A seasonal model of the Mediterranean Sea general circulation. *Journal of Geophysical Research*, **100**, 13515–13538.

Russell, J. L., Dixon, K. W., Gnanadesikan, A., Stouffer, R. J., and Toggweiler, J. R. (2006). The Southern Hemisphere westerlies in a warming world: Propping open the door to the deep ocean. *Journal of Climate*, **19**(24), 6382–6390.

Schmitz, W. J. (1996). On the world ocean circulation: Volume I. Some global/north atlantic circulation. Technical Report WHOI-96-03, Woods Hole Oceangraphic Institution.

Serreze, M. C. and Francis, J. A. (2006). The Arctic on the fast track of change. *Weather*, **61**(3), 65–69.

Simonot, J.-Y. and le Treut, H. (1986). A climatological field of mean optical properties of the world ocean. *Journal of Geophysical Research*, **91**(C5), 6642–6646.

Soden, B. J. and Held, I. M. (2006). An assesment of climate feedbacks in coupled ocean-atmosphere models. *Journal of Climate*, **19**, 3354–3360.

Sokolov, A. P. and Stone, P. H. (1998). A flexible climate model for use in integrated assessments. *Climate Dynamics*, **14**, 291–303.

Sprintall, J. and Cronin, M. F. (2001). *Encyclopedia of Ocean Sciences*, volume 6 (T-Z, Index), chapter : Upper Ocean Vertical Structure, pages 3120–3128. Academic Press. (ed. J. H. Steele, K. K. Turekian and S. A. Thorpe).

Stainforth, D. A., Aina, T., Christensen, C., Collins, M., Frame, D. J., Kettleborough, J. A., Knight, S., Martin, A., Murphy, J., Piani, C., Sexton, D., Smith, L. A., Spicer, R. A., Thorpe, A. J., Webb, M. J., and Allen, M. R. (2005). Uncertainty in predictions of the climate response to rising levels of greenhouse gases. *Nature*, **433**(7024), 403–406.

Stommel, H. (1948). The westward intenstification of wind-driven ocean currents. *Transactions, American Geophysical Union*, **29**(2). Reprinted in Volume II p. 11-15 of the Collected Works of Henry M. Stommel (ed. N. G. Hogg and R. X. Huang).

Stommel, H. (1961). Thermohaline convection with two stable regimes of flow. *Tellus*, **13**, 224–230.

Storkey, D. (2001). Treatment of penetrating solar radiation in FOAM. Technical report, United Kingdom Meteorological Office, Met Office, FitzRoy Road, Exeter, Devon, EX1 3PB, UK.

Sverdrup, H. U. (1947). Wind-driven currents in a baroclinic ocean; with application to the equatorial currents of the eastern pacific. *Proceedings of the National Academy of Sciences*, **33**, 318–326.

Thompson, P. D. (1957). Uncertainty of initial state as a factor in the predictibility of large scale atmospheric flow patterns. *Tellus*, **9**, 257–295.

Thompson, S. L. and Schneider, S. H. (1982). Carbon dioxide and climate: The importance of realistic geography in estimating the transient temperature response. *Science*, **217**, 1031–1033.

Thorpe, A. J. (2005). Climate change prediction: a challenging scientific problem. Technical report, Institute of Physics, www.iop.org.

Thorpe, R. B., Gregory, J. M., Johns, T. C., Wood, R. A., and Mitchell, J. F. B. (2001). Mechanisms determining the Atlantic thermohaline circulation response to greenhouse gas forcing in a non-flux-adjusted coupled climate model. *Journal of Climate*, **14**, 3102–3116.

Timmermann, A., Oberhuber, J., Bacher, A., Esch, M., Latif, M., and Roeckner, E. (1999). Increased El Niño frequency in a climate model forced by future greenhouse warming. *Nature*, **398**, 694–696.

Tipler, P. A. (1999). *Physics for scientists and engineers*. Freeman and Worth, 4th edition.

Toggweiler, J. R. and Key, R. M. (2001). *Encyclopedia of Ocean Sciences*, volume 6 (T-Z, Index), chapter : Thermohaline Circulation, pages 2941–2947. Academic Press. (ed. J. H. Steele, K. K. Turekian and S. A. Thorpe).

Tracton, M. S. and Kalnay, E. (1993). Operational ensemble forecasting at the National Meteorological Center: practical aspects. *Weather and Forecasting*, **8**, 379–398.

Tyndall, J. (1865). *Heat considered as a mode of motion: being a course of twelve lectures delivered at the Royal institution of Great Britain in the season of 1862*. D. Appleton and co. Available from http://www.hti.umich.edu/.

Valcke, S., Terray, L., and Piacentini, A. (2000). The OASIS coupler user guide version 2.4. Technical Report TR/CMGC/00-10, CERFACS.

Vellinga, M. and Wood, R. (2002). Global climatic impacts of a collapse of the atlantic thermohaline circulation. *Climatic Change*, **54**(3), 251–276.

Vellinga, M. and Wu, P. (2004). Low latitude freshwater influence on centennial variability of the atlantic thermohaline circulation. *Journal of Climate*, **17**, 4498–4511.

Visbeck, M., Marshall, J., Haine, T., and Spall, M. (1997). Specification of eddy transfer coefficients in coarse resolution ocean circulation models. *Journal of Physical Oceanography*, **27**, 381–402.

von Storch, H. and Zwiers, F. (1999). *Statistical Analysis in Climate Research*. Cambridge University Press.

Washington, W. M. and Meehl, G. A. (1989). Climate sensitivity due to increased $CO_2$: experiments with a coupled atmosphere and ocean general circulation model. *Climate Dynamics*, **4**, 1–38.

Weart, S. R. (2004). *The Discovery of Global Warming*. Harvard University Press. A more detailed version is available at http://www.aip.org/history/climate.

Webb, M. J., Senior, C. A., Sexton, D. M. H., Ingram, W. J., Williams, K. D., Ringer, M. A., McAvaney, B. J., Colman, R., Soden, B. J., Gudgel, R., Knutson, T., Emori, S., Ogura, T., Tsushima, Y., an d B. Li, N. A., Musat, I., Bony, S., and Taylor, K. E. (2006). On the contribution of local feedback mechanisms to the range of climate sensitivity in GCM ensembles. *Climate Dynamics*, **27**, 17–38.

Weeks, W. F. (2001). *Encyclopedia of Ocean Sciences*, volume 5 (S), chapter : Sea Ice / Overview, pages 2574–2582. Academic Press. (ed. J. H. Steele, K. K. Turekian and S. A. Thorpe).

Whitworth, T. and Petersen, R. (1985). Volume transport of the Antarctic circumpolar current from bottom pressure measurements. *Journal of Physical Oceanography*, **15**, 810–816.

Williams, K. D., Senior, C. A., and Mitchell, J. F. B. (2001). Transient climate change in the Hadley Centre models: The role of physical processes. *Journal of Climate*, **14**(12), 2659–2674.

Williams, R. G. (2001). *Encyclopedia of Ocean Sciences*, volume 4 (N-R), chapter : Ocean Subduction, pages 1982–1993. Academic Press. (ed. J. H. Steele, K. K. Turekian and S. A. Thorpe).

Winton, M. (2006). Surface albedo feedback estimates for the AR4 climate models. *Journal of Climate*, **19**, 359–365.

Wood, R. A. (1998). Time step sensitivity and accelerated spinup of an ocean GCM with a complex mixing scheme. *Journal of Atmospheric and Oceanic Technology*, **15**, 482–495.

Wood, R. A., Keen, A. B., Mitchell, J. F. B., and Gregory, J. M. (1999). Changing spatial structure of the thermohaline circulation in response to atmospheric $CO_2$ forcing in a climate model. *Nature*, **399**, 572–575.

Xie, P. and Arkin, P. A. (1996). Analyses of global monthly precipitation using gauge observations, satellite estimates, and numerical model predictions. *Journal of Climate*, **9**, 840–858.

Yao, M.-S. and Del Genio, A. D. (2002). Effects of cloud parameterization on the simulation of

climate changes in the GISS GCM. part II sea surface temperature and cloud feedbacks. *Journal of Climate*, **15**, 2491–2503.